UC Berkeley

Title

First-principles calculations of thermodynamics and kinetics in spinel oxides for battery materials

Permalink

https://escholarship.org/uc/item/25z2410n

Author

Chen, Tina Joan

Publication Date

2022

First-principles calculations of thermodynamics and kinetics in spinel oxides for battery
materials

by

Tina J. Chen

A dissertation submitted in partial satisfaction of the

requirements for the degree of

Doctor of Philosophy

in

Materials Science and Engineering

in the

Graduate Division

of the

University of California, Berkeley

Committee in charge:

Professor Gerbrand Ceder, Chair
Professor Mark Asta
Professor Kristin Persson

Summer 2022

Abstract

First-principles calculations of thermodynamics and kinetics in spinel oxides for battery
materials

by

Tina J. Chen

Doctor of Philosophy in Materials Science and Engineering

University of California, Berkeley

Professor Gerbrand Ceder, Chair

Spinel-based materials have historically been one of the most promising frameworks for
Li-ion cathodes since the discovery of $LiMn_2O_4$ in 1983. The material was first proposed
due to the diamond network of face-shared unoccupied tetrahedral and octahedral sites in
Mn_2O_4, which offers a three-dimensional pathway for Li-ion transport. Since then, much
work has been spent on $LiMn_2O_4$ and its Ni-substituted derivative due to their use of Mn,
which is more abundant and less expensive than the Co used in the layered-based Li-ion
cathodes that dominate the portable electronic and electric vehicle industries. Furthermore,
the three-dimensional Li-ion conduction pathway in spinel has made the spinel framework
appealing for more applications than just Li-ion cathodes. Various spinel oxides and sulfides
have been proposed as potential Mg-ion cathodes, and a low voltage Ti-based spinel has
been proposed as a "zero-strain" Li-ion anode. The addition of spinel-like partial order has
also been proposed to aid the voltage profile and Li transport in the disordered rock salt
materials, which are a more recently-discovered class of high energy density Li-ion cathodes.

In this dissertation, I utilize first-principles techniques based on density functional theory cal-
culations and cluster expansion methods to investigate intercalation in a number of promising
spinel-based electrodes. In Chapter 1, I introduce in detail the spinel structure and the pos-
sible ways working ions can intercalate in the structure, as well as the techniques that will
be used in the following studies.

In Chapter 2, I investigate the barriers to Mg intercalation into the spinel-$Mg_xCr_2O_4$ sys-
tem. Using first-principles calculations in combination with a cluster expansion model and
the nudged elastic band theory, I calculate the voltage curve for Mg insertion at room tem-
perature and the activation barriers for Mg diffusion at varying Mg concentrations in the
Cr_2O_4 structure. Our results identify a potential limitation to Mg intercalation in the form
of stable Mg-vacancy orderings in the Cr_2O_4 lattice, which exhibit high migration barriers
for Mg diffusion in addition to a steep voltage change. Additionally, we propose cation

1

substitution as a potential mechanism that can be used to suppress the formation of stable Mg-vacancy orderings, which can eventually enable the practical usage of Cr_2O_4 as a Mg-ion cathode.

In Chapter 3, I delve into understanding the kinetics of Li transport in spinel $Li_4Ti_5O_{12}$, which is a Li-ion anode exhibiting extraordinary rate capability. The rate capability of $Li_4Ti_5O_{12}$ is especially surprising given its two-phase reaction and slow diffusion within the endmembers, in contrast to the typical fast-charging battery electrodes that are capable of accommodating lithium continuously via solid-solution transformation. Through real-time tracking of Li^+ migration using operando electron energy-loss spectroscopy (EELS) combined with first-principles investigation of the Li configurations, their simulated EELS spectra, and Li migration barriers, it is revealed that the kinetic pathway that enables facile ionic transport in lithium titanate consists of distorted Li polyhedra in metastable intermediate states. This study highlights that the rate capability of fast-charging electrodes may not be controlled solely by the intrinsic ionic diffusivity of macroscopic phases, but also by transport via kinetically accessible low-energy landscapes. These findings may open new avenues for designing fast-charging electrodes.

In Chapter 4, I investigate the thermodynamic effects of disordering the spinel framework of $LiMn_2O_4$ towards understanding the partially disordered Li-excess spinels, a promising class of high energy density Li-ion cathodes with good discharge rate capability. To elucidate where in the partially disordered space the optimal materials lie, we investigate the configuration space of spinel with Mn disordered over the 16c and 16d sites. Using a cluster expansion in conjunction with Monte Carlo simulations, we find that disorder shortens the deleterious $\sim$3V plateau between $LiMn_2O_4$ and $Li_2Mn_2O_4$ by raising the energy landscape and stabilizing the motifs found in solid-solution configurations, and the plateau is completely removed with 25% Mn 16c occupancy. We expect partially disordered spinels with this level of disorder to exhibit both solid-solution behavior as well as good rate due to the remaining spinel character. We also identify Ti-doping and Li-excess as potential ways to facilitate 16c/16d disordering.

Contents

List of Figures

Acknowledgments

To my advisor, Prof. Gerbrand Ceder, thank you for all of the guidance you have provided over my many years in the group. You've been a great role model, and I hope to inherit your broad vision of the research field, your high standards towards scientific rigor and communication, and your passion for obtaining deeper scientific understanding. It has also been such a gift having long discussions with you in the office. Not only did I receive great scientific advice and insight into academia but also some great wine recommendations. My journey started with your willingness to take on a bright-eyed undergraduate at MIT, and I will always be thankful for your role in this priceless experience.

I also want to thank my first mentors in the Ceder group for the generous help from Prof. Alexander Urban when I first began learning first-principles calculations and the close guidance of Gopalakrishnan Sai Gautam when I began working on my first major project. Thank you for helping me gain the essential skills to become the researcher that I am today.

I have had many friends in the Ceder group, some of whom have moved on to new things, but I appreciate all of them for enriching my PhD experience. Thank you to Yaosen Tian and Tan Shi, who began their journeys at Berkeley at the same time as me; Jaechul Kim, my cubicle neighbor who brightened the aisle with his stories; Julia Yang, who I worked closely with throughout my entire PhD; Wenxuan Huang and Dong-hwa Seo, for their helpful collaboration; Daniil Kitchaev and Wenhao Sun, for both scientific and academic advice; Piero Canepa and Dan Hannah, for discussions and collaboration on multivalent battery projects; Yihan Xiao, Howie Tu, and Valentina Lavicita for welcoming me during my brief stint in the solid-state group; Zinab Jadidi, Luis Barroso-Luque, Bin Ouyang, Peichen Zhong, and Fengyu Xiao, for their theoretical work on the disordered rock salts and our cluster expansion package; and Huiwen Ji, Zhengyan Lun, and Zijian Cai, for their experimental efforts on the disordered rock salts. I'm also grateful to my collaborators, Prof. Wei Zhang, who is now at Nankai University, and Dr. Feng Wang, from Brookhaven National Lab.

Thank you also to Prof. Phillip Geissler, who offered insightful advice on my research. His joy for teaching and love of science was inspiring.

I would also like to thank my parents, Long-Qing Chen and Fannie Mui, for their steadfast belief in me throughout this long journey. In addition to their unconditional love and support these past 29 years, they have always provided guidance—academic, scientific, and personal—at every opportunity they could. Thank you also to Ben Sheng and Rose Sheng, my parents-in-law, for your patience and support despite an ever-changing finish line.

Finally, thank you to my husband, Nathan Sheng. We met, dated, became engaged, and got married, all during my PhD at Berkeley, and your love and support have been unwavering. I'm so lucky to have you in my life, and thank you for being here with me through all of this.

Chapter 1

Introduction

In this chapter, I briefly review the conventional Li-ion cathodes and anodes and a few appealing alternatives, as well as Mg-ion batteries as a battery technology with the potential for significantly higher energy density. As spinel-structured oxides show promise across many different systems, I discuss the spinel structure, intercalation in the spinel framework, and the challenges and questions remaining for some spinel oxide electrodes. Following an introduction of first-principles methods for studying the thermodynamics and kinetics of intercalation systems, Chapters 2, 3, and 4 present the investigations of three spinel oxides of interest.

1.1   Intercalation batteries

Rechargeable batteries based on ion intercalation are used as the energy storage device in nearly all portable electronics from smartphones to laptops. They are also the energy storage device of choice in electric vehicles.[1] As the widespread replacement of fossil fuel-powered cars with electric vehicles presents both economic and environmental benefits, improvements to ion-intercalation batteries are needed to propel the electrification of transportation. Batteries with higher capacities would increase the driving distance of electric vehicles; faster
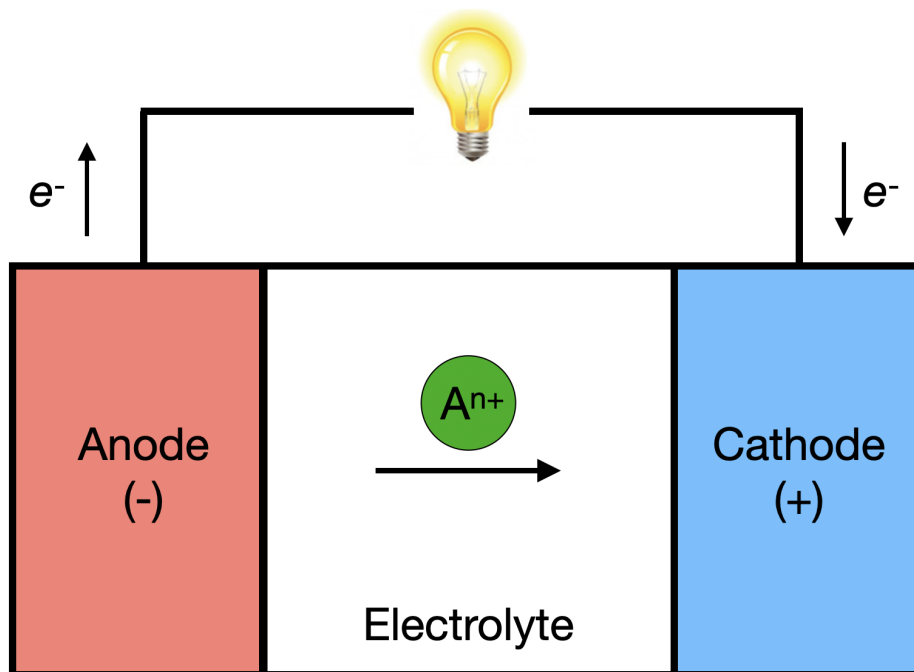
Figure 1.1: **Schematic of intercalation battery** Representation of the major components of an intercalation battery. Arrows show the direction of electron (e^-) and working ion (A^{n+}) motion during discharge. During charge (energy storage), the directions are reversed.

rate capability would lead to shorter charging times; and improved cycle life would give rise to longer lasting batteries. Lithium-ion (Li-ion) batteries are the leading technology in terms of energy density, but the highest energy density Li-ion batteries use cobalt, which is both expensive and resource-scare.[2] Thus, it is imperative to develop alternative batteries or battery components that can not only provide higher energy density and increased rate capability but also accommodate the expected increase in demand for energy storage.

Batteries based on the intercalation of ions store chemical energy through an electrochemical oxidation-reduction (redox) reaction. During discharge, "working ions" (e.g., Li^+) are shuttled from an anode to a cathode through an electrolyte, driven by the difference in the working ion's chemical potential between the two electrodes (Figure 1.1). In the process, the anode is oxidized, delivering electrons to the external circuit, while the cathode accepts electrons and is reduced. The electrolyte separating the two electrodes is generally an electronically-insulating non-aqueous liquid. In charge, an external potential is applied to reverse the reaction. The remainder of this section discusses some electrodes currently implemented in or being researched for Li-ion batteries and introduces Mg-ion batteries as an alternative technology.

1.1.1 Electrodes in Li-ion batteries

Li-ion cathodes

Currently, the Li-ion cathode industry is dominated by well-ordered layered materials, such as $LiCoO_2$ in the portable electronics industry and $Li(Ni,Mi,Co)O_2$ (NMC) and $Li(Ni,Co,Al)O_2$ (NCA) in the electric vehicle industry. With their two-dimensional pathways enabling facile Li transport, these layered materials display impressive electrochemical performance but require Co or Ni, which are both expensive and resource-scarce as shown in Figure 1.2 [2, 3], to remain chemically stable in octahedral environments.[4] With demand for Li-ion batteries expected to grow nearly 5-fold in the upcoming decade [5], further development of high energy density cathodes with alternative structures that can utilize broader chemistries is needed.

One prime example of such an alternative structure is the spinel structure, which can employ redox in less expensive transition metals (TM), such as Mn and Fe. Spinel $LiMn_2O_4$ and its Ni-substituted derivatives are promising alternatives to layered Co-based materials [6–8], but a two-phase transition associated with significant non-homogeneous volume change nearly halves its practical capacity.[9, 10] The disordered rock salt Li-excess (DRX) materials are another class of materials that has shown potential as high energy density cathodes that can accommodate more earth-abundant and less costly TM, such as Mn, Fe, and Cr.[11–13] However, although DRX materials can achieve capacities up to 300-350 mAh g^{-1} [14–18], such high capacities are only obtainable by cycling to extreme voltages (down to 1.5 V and up to 4.8-5.0 V) where current Li-ion electrolytes are usually no longer stable.

Price and Abundance of First-Row TM
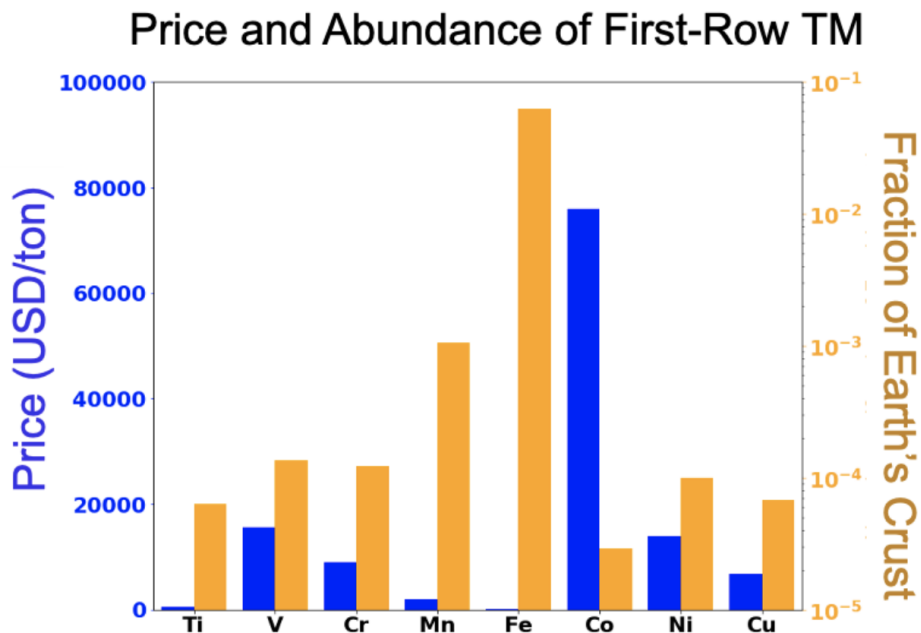
Figure 1.2: **Price and abundance of first-row transition metals** Prices are for metals, except for the Ti price which was obtained from the metal oxide, and abundance is based on fraction of the earth's crust. From data published in Nitta, *et al.* [3] and Clément, *et al.* [2].

Li-ion anodes

The most widely used anode in Li-ion batteries is graphite, which can accommodate Li between its layers of carbon. Due to its low cost, theoretical capacity (372 mAh g^{-1}) above most cathodes, and good cycling stability, it has remained prevalent since its first use in Li-ion batteries in 1994.[19] However, some safety concerns still remain due to graphite's low lithium potential (between 0.25 V and 0.1 V [19]), which causes the formation of a solid-electrolyte interphase (SEI) between the graphite and electrolyte and can potentially cause Li plating [20]. The decomposition of the SEI, which can occur at temperatures as low as 60°C [21, 22], can lead to thermal runaway [23, 24], while Li dendrites can form during fast charging [25] or at low temperatures [26], leading to short-circuiting [27, 28].

One potential alternative Li-ion anode is Li$_4$Ti$_5$O$_{12}$, a spinel oxide operating at ~ 1.55V [29], high enough to avoid the potential safety issues of graphite. Furthermore, it has high power [30, 31], good thermal stability, fast-charging capability [32–34], and undergoes very small volume change during lithiation [35], providing it with long cycle stability [36]. The main drawback of Li$_4$Ti$_5$O$_{12}$ is its low theoretical capacity (175 mAh g^{-1}). Li metal is another potential anode, with the advantage of exceedingly high theoretical capacity (3860 mAh g^{-1}). However, it is also plagued by dendrite formation [37], which can cause short circuiting and

has prompted research into all solid-state batteries that use fast Li-ion conductors as solid electrolytes.

1.1.2   Mg-ion batteries as an alternative to Li-ion batteries

Mg-ion batteries offer significant improvements in energy density compared to conventional Li-ion batteries because they can be utilized directly with a Mg metal anode. The more uniform Mg deposition during electrochemical cycling leads to greater suppression of dendrite formation compared to Li metal anodes.[39] However, Mg-ion batteries currently face challenges in the form of incompatible electrolytes with limited anodic stability [40] and cathodes
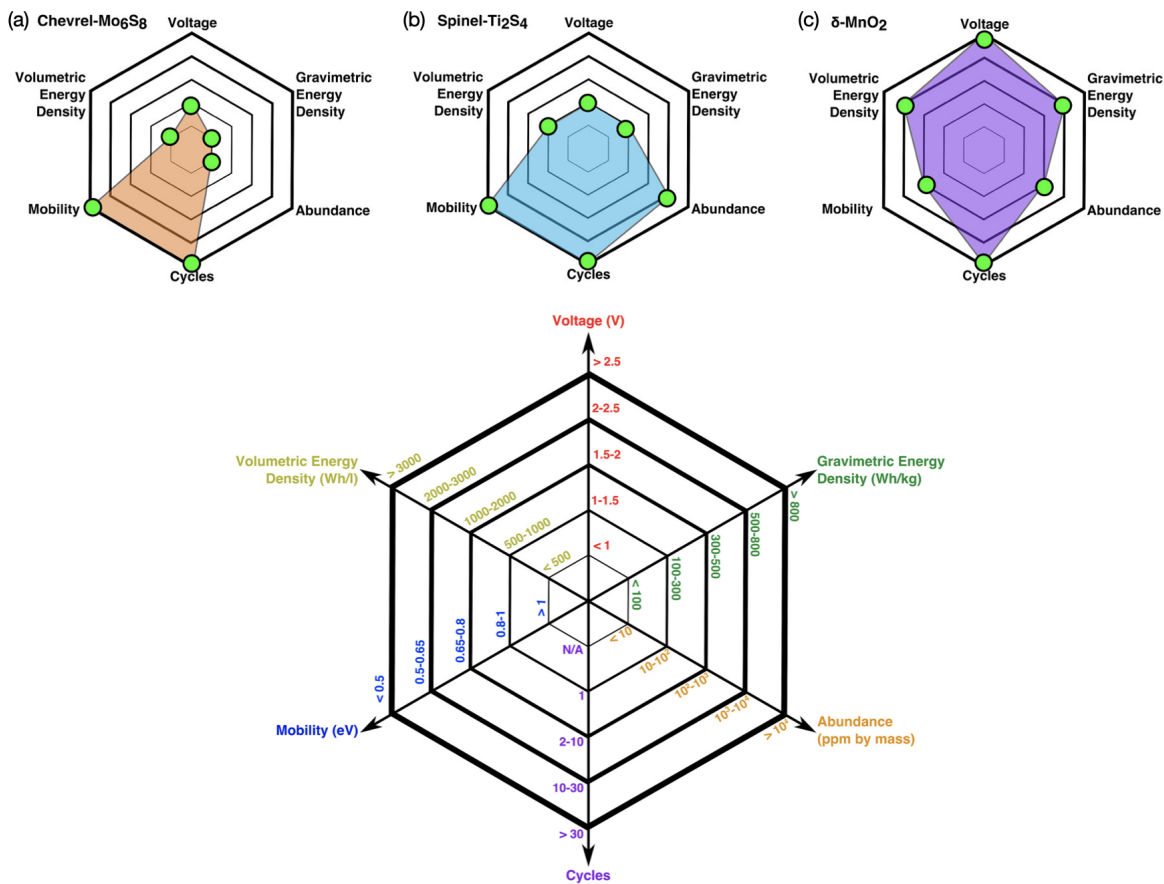
Figure 1.3: **Comparison of Mg spinel oxide with current Mg-ion cathodes** Voltage, gravimetric energy density, volumetric energy density, Mg-ion migration barrier, cyclability, and abundance of transition metal in the earth's crust for the state-of-the-art chevrel Mo_6S_8 and spinel Ti_2S_4 Mg-ion cathodes compared with those of spinel $MgMn_2O_4$. Data and plots originally published in Canepa, *et al.* [38]

5

with either poor Mg-ion mobility or low energy density [38, 41]. For example, the state-of-the-art Mg-batteries employ low-voltage sulfide cathodes, such as Chevrel-Mo_6S_8 [42] or spinel-Ti_2S_4 [43–45]. Oxide-based Mg-ion cathodes, on the other hand, offer the possibility of high energy density due to their higher average voltages but tend to have generally poor Mg-ion mobility [46], as shown in Figure 1.3, and potential conversion side-reactions [38, 47, 48]. One pathway to improving Mg-ion mobility in oxides is finding frameworks that host Mg-ion ions in an "un-preferred" coordination environment. Migrating from an "un-preferred" coordination environment and through a transition state with the "preferred" environment serves to decrease the site energy contribution to the associated migration barrier.[46] Based on this criterion, spinel is a structure expected to have reasonable Mg migration because it hosts Mg in a tetrahedral environment instead of the preferred octahedral environment.[49, 50] Indeed, a recent study has demonstrated facile Mg-transport in ternary chalcogenide spinels, with potential applications as Mg solid electrolytes.[51, 52]

1.2 Spinel materials as electrodes

Materials with the spinel structure have arisen as promising candidates for the various systems described thus far. For example, $LiMn_2O_4$ presents a cheaper alternative for high energy density Li-ion cathodes, $Li_4Ti_5O_{12}$ a potential safer high power Li-ion anode, and Mg spinel oxides a class of possible high voltage Mg-ion cathode. Given the general effectiveness of spinel systems as electrodes, insight into the structure and in what manner it is intercalated is useful for understanding its success as well as directions for improvement.

1.2.1 The structure of spinel AB_2O_4

The AB_2O_4 spinel structure, as shown in Figure 1.4a, is composed of A cations occupying tetrahedral 8a sites (orange polyhedra) and B transition metal cations occupying the octahedral 16d sites (blue polyhedra) within a cubic close-packed O lattice (32e, vertices of orange and blue polyhedra). In a polyhedral representation, the structure consists of B-octahedra that are edge-sharing with other B-octahedra and vertex-sharing with A-tetrahedra. The A-tetrahedra are separated by octahedral interstices (the unoccupied 16c sites). In any given $\langle 110 \rangle$ direction, the spinel structure can be visualized as tunnels, which intersect at regular intervals allowing 3-D diffusion of A atoms through the structure via hops through the empty 16c site.

1.2.2 Intercalation in spinel oxides

In the Li-ion and Mg-ion oxide systems, intercalation up to a stoichiometry of AB_2O_4 involves insertion into the 8a-tetrahedra. In the case of Li, this is due to Li's preference for tetrahedral coordination.[49] For Mg, which generally prefers 6-fold coordination, the tetrahedral occupancy is driven by the nearest-neighbor pair interactions [53], as evidenced by
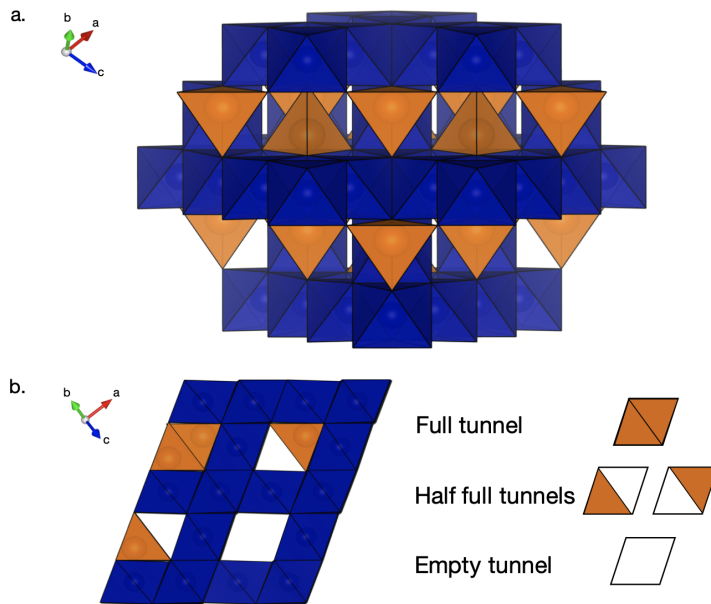
Figure 1.4: **Structure of spinel** Structure of AB_2O_4 spinel conventional cell, with A in tetrahedral (orange) and B in octahedral (blue) coordination. All vertices of polyhedra are occupied by O (not shown). (b) AB_2O_4 spinel structure demonstrating full, half full, and empty tunnels, as viewed along the $\langle 110 \rangle$ direction.

Mg octahedral occupancy in spinels with S^{2-} [44, 54], which is more polarizable and thus better shields charge.[55] Low energy $A_xB_2O_4$ configurations where $x < 1$ often consist of combinations of fully-occupied, half-occupied, and empty tunnels (Figure 1.4b).

When x in $A_xB_2O_4$ exceeds 1, most spinel systems with tetrahedral A occupancy up to $x_A = 1$ undergo a two-phase transition between AB_2O_4 and $A_2B_2O_4$, during which insertion of A into AB_2O_4 causes the collective transition of A-ions from tetrahedral 8a sites to neighboring octahedral 16c sites. The endmembers of this transition, spinel (a) and lithiated spinel (b), are shown in Figure 1.5 for the case of $Li_xMn_2O_4$. Due to the proximity between the A-occupied 8a tetrahedra and the unoccupied 16c sites, any A ion inserted into a 16c site of AB_2O_4 experiences face-sharing with two A-occupied 8a tetrahedra and the concomitant electrostatic repulsion. The connectivity of the 8a-16c network, in which each 8a site face-shares with four 16c sites and each 16c site face-shares with two 8a sites as depicted in Figure 1.6a for AB_2O_4, then prohibits the local rearrangement of A from removing the face-sharing environments, as shown in the two configurations of $A_{1+\delta}B_2O_4$ in Figure 1.6b-c.

Mg-intercalation in spinel oxides have generally been limited to $0 < x_{Mg} < 1$ (in $Mg_xB_2O_4$). While recent works have shown that electrochemical intercalation through the spinel-lithiated spinel phase transition is possible in some spinel oxides [56, 57], such interca-
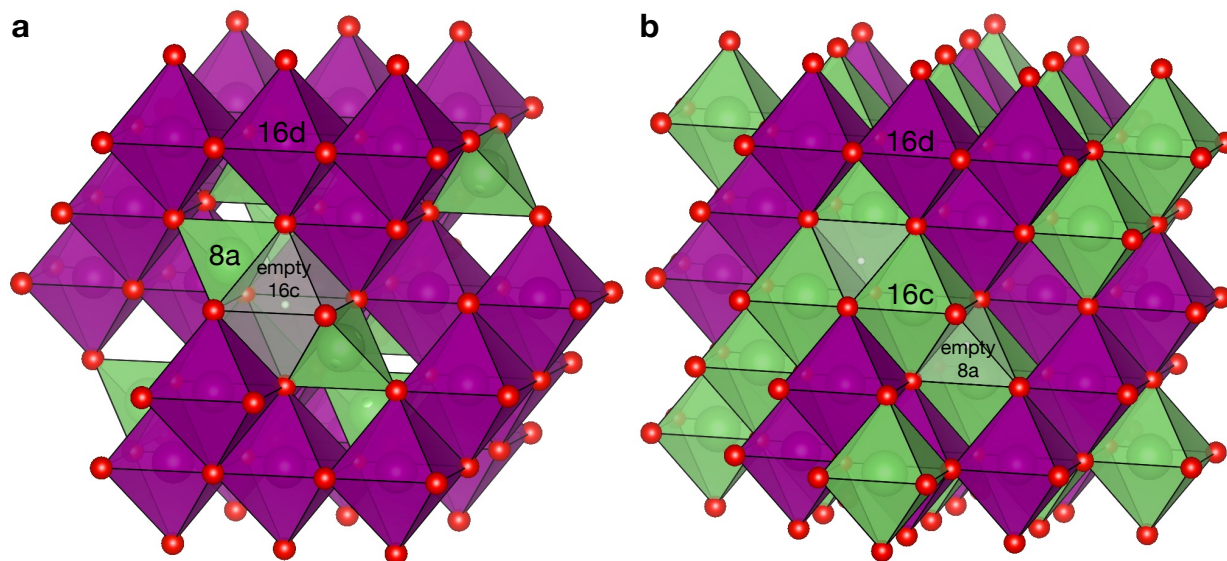
Figure 1.5: **Endmembers of LiMn$_2$O$_4$-Li$_2$Mn$_2$O$_4$ phase transition** Structure of spinel LiMn$_2$O$_4$ (a) and the lithiated spinel (tetragonal rock salt-like) Li$_2$Mn$_2$O$_4$ (b). Li and Mn are shown in green and purple polyhedra, and the O framework is shown as red spheres. The 8a tetrahedral (16c octahedral) Li and 16d octahedral Mn are shown in spinel LiMn$_2$O$_4$ (lithiated Li$_2$Mn$_2$O$_4$), and the empty (i.e., unoccupied) 16c (8a) is shown with a small white sphere and transparent polyhedra to show their respective locations to the filled 8a (16c).
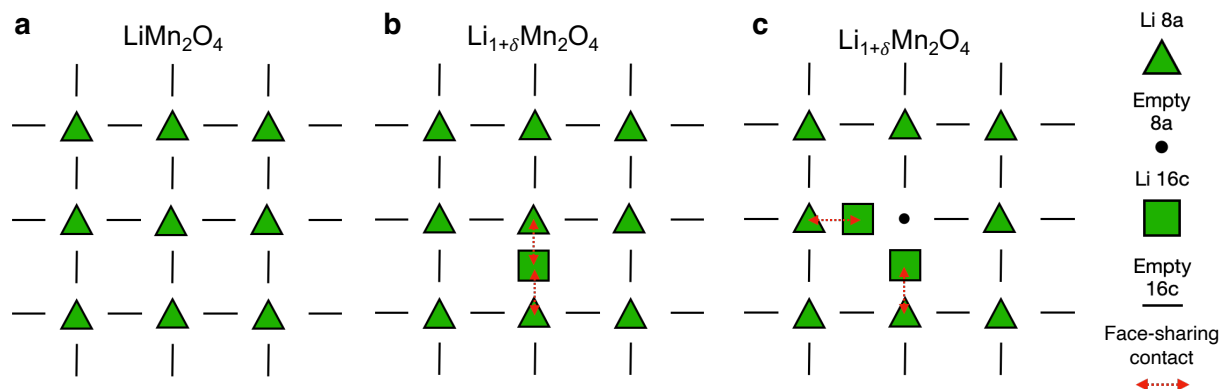
Figure 1.6: **2-D depictions of tetrahedral 8a-octahedral 16c network** for LiMn$_2$O$_4$ (a) and two configurations of Li$_{1+\delta}$Mn$_2$O$_4$ (b,c). Occupied 8a and 16c are shown as green triangles and squares, while unoccupied 8a and 16c are shown as long dashes and dots. Face-sharing contacts with occupied 8a and 16c sites are highlighted by dashed red arrows.

8

lation requires elevated temperatures up to 150°C [58], and the reversibility of such reactions have not yet been proven. Large polarization is also seen during magnesiation across the phase transition.[59] Such difficulties observed with the intercalation of $x_{Mg} > 1$ are indicative of sluggish Mg mobility, which can stem from Mg sitting in octahedral 16c sites in the lithiated spinel phase that appears when $x_{Mg} > 1$, rather than the tetrahedral 8a sites when $x_{Mg} < 1$. Because Mg in octahedral 16c sites do not benefit from the "un-preferred" coordination that leads to reasonable Mg mobility when $x_{Mg} < 1$, they are unlikely to be particularly mobile without the shielding effects of more polarizable anions such as S^{2-} and Se^{2-}. Thus, we consider here only Mg intercalation in the tetrahedral 8a sites of $Mg_2B_2O_4$.

1.2.3 Challenges and questions in spinel oxide electrodes

Mg-based spinel oxides

Although the spinel oxides are especially promising due to their high voltage and "un-preferred" Mg coordination environment, few have successfully been shown to intercalate Mg. One of the few oxides that can intercalate Mg^{2+} electrochemically, albeit poorly, is Mn_2O_4.[60–62] It also exhibits a good average voltage ($\sim$2.9 V), high theoretical capacity ($\sim$270 mAh/g), and reasonable Mg migration barriers ($\sim$500-600 meV in the dilute vacancy limit).[63, 64] However, a major issue with Mn_2O_4 is the tendency of the spinel to undergo "inversion", which is the exchange of the cations in octahedral sites (i.e., $Mn^{3+/4+}$) with the cations in tetrahedral sites (i.e., Mg^{2+}).[65–68] Inversion is especially evident in Mg-based systems compared to Li-based systems due to Li's preference for tetrahedral coordination [49] and thus lower propensity for inversion. As a consequence of Mn 8a occupation, inversion in the spinel structure can cause blockage of Mg percolation paths, which can severely limit both the macroscopic transport of Mg through the cathode particle and the practical capacity that can be extracted.[50] Notably, the facile disproportionation of Mn^{3+} to Mn^{4+} and Mn^{2+} has been attributed by previous studies to aid inversion in Mn-spinels.[69] Thus, in addition to the general challenge of sluggish Mg-ion mobility in oxides, any spinel oxides considered for potential Mg-ion cathodes must also be resistant to inversion.

Fast-charging in $Li_4Ti_5O_{12}$

$Li_4Ti_5O_{12}$ is a spinel anode that can fast-charge at $\sim$1.55V [32, 35], above the potential of the Li plating and SEI formation to which graphite anodes are susceptible. In contrast to most of the AB_2O_4 spinel oxides, where A is the working ion and B is the transition metal that is reduced/oxidized during cycling, $Li_4Ti_5O_{12}$ is a Li-excess spinel, in which Li is substituted in 1/6 of the Ti 16d sites, and intercalates 1 Li across the phase transition from $Li_3^{(8a)}(LiTi_5)^{(16d)}O_{12}$ to $Li_6^{(16c)}(LiTi_5)^{(16d)}O_{12}$. Because intercalation through a two-phase region is generally associated with the additional kinetic barriers of nucleation and growth of the second phase, most commercial electrodes (e.g., layered $LiCoO_2$ [70] and spinel $LiMn_2O_4$ [71]) generally intercalate through solid solution with only a few weak phase transitions

due to Li/vacancy ordering. Thus, the fast-charging ability of $Li_4Ti_5O_{12}$ is contrary to the slower kinetics expected during intercalation through a phase transformation. $LiFePO_4$ is another electrode that appears to intercalate at high rate [72] across a two-phase region. However, rather than its equilibrium phase transformation, it intercalates through solid-solution configurations accessible by a small overpotential during (dis)charge.[73] A similar level of insight on fast-charging in $Li_4Ti_5O_{12}$ may provide guidance on developing more spinel electrodes with high rate capability.

Spinel LiMn$_2$O$_4$

Although $LiMn_2O_4$ holds promise as a potential cheaper high energy density Li-ion cathode, a strong two-phase transition severely limits its practical accessible capacity. This two-phase transition occurs from spinel $LiMn_2O_4$ to the lithiated spinel $Li_2Mn_2O_4$ at $\sim$3 V, and the addition of Li^+ is accompanied by the reduction of Mn from an average oxidation state of 3.5^+ to 3^+. The d^4 configuration of Mn^{3+} causes Jahn-Teller distortion of its octahedral complex in which one axis elongates to break the degeneracy of the e_g states. Due to the 16d ordering in spinel, the Mn^{3+} experience collective Jahn-Teller distortion and elongate along the same axis.[9, 74] The non-homogeneous distortion causes cracking of the $Li_xMn_2O_4$ particles and a drastic decrease in cyclability compared to $Li_xMn_2O_4$ cycled above the voltage at which the two-phase transition occurs (3.0-4.3 V).[75] Cycling in $Li_xMn_2O_4$ is thus practically limited to $0 < x_{Li} < 1$, which has a theoretical capacity of $\sim$148 mAh g^{-1} compared to a theoretical capacity of $\sim$285 mAh g^{-1} when 2 Li can be cycled in Mn_2O_4. Significant effort has been dedicated to investigating strategies based on doping (by e.g., Ni, Cr, Mg) [76–78], particle morphology (nanoparticles) [79–81], and defects (Mn interstitials, edge dislocations) [82, 83] to suppress the collective Jahn-Teller distortion. However, doping has mainly been applied to stabilize the $LiMn_2O_4$ structure for cycling between Mn_2O_4 and $LiMn_2O_4$, and nanoparticles tend to have increased surface reactions such as Mn^{2+} dissolution due to the increased surface area and are more difficulty to coat.[84] The defect-based strategies and other strategies that alter the structure of spinel $LiMn_2O_4$, on the other hand, may provide a basis for suppressing not only the collective Jahn-Teller distortion but also the two-phase reaction and its associated rate-limiting kinetics.

1.3 First principles methods for intercalation batteries

1.3.1 Density functional theory for battery materials

With the increase in computing power and capability of computational methods, atomistic simulations have become integral to guiding materials design and providing insight into mechanisms on the atomic scale. One of the main methods used in atomistic simulations is density functional theory (DFT), which is an approach introduced by Hohenberg, Kohn,

and Sham [85, 86] to solving the 0K ground state and internal energy of a many-electron system at the first-principles level. The energies and local ground state structures from DFT can be used to calculate the thermodynamic stability of orderings or polymorphs while properties such as magnetic moments, charge distributions, and electronic density of states can be obtained from the electronic ground states. In this dissertation, we use DFT as implemented in the Vienna ab initio simulation package (VASP) [87] with the plane-wave basis set [88] and wave functions constructed using the projector augmented wave (PAW) theory [89] with a well-converged energy cut-off of 520 eV.

While exact in its formulation, the application of DFT requires a number of approximations and corrections. In particular, an approximation must be made on the exchange-correlation energy (E_{xc}), which includes the energy associated with enforcing antisymmetry of the wavefunction upon electron exchange (exchange) and the error in energy from excluding interactions between individual electrons such as screening (correlation).[90] Because the true form of E_{xc} is unknown, it is generally approximated by assuming local points of the electron density have the exchange-correlation energy density of a homogeneous electron gas of the same density (local density approximation). The generalized gradient approximation (GGA) also takes into account the gradient of the density.[91] Recently, the Strongly Constrained and Appropriately Normed (SCAN) meta-GGA functional [92] has been gaining popularity; due to its semilocal nature and appropriate parametrization of the medium-range van der Waals interactions, SCAN predicts ground states better than GGA while being less computationally expensive than hybrid functionals and most other meta-GGA's.[93, 94] Another correction sometimes required for DFT is the Hubbard U correction, which helps to localize electron density to transition metals and approximately treat the self-interaction problem of d electrons. In Chapter 2, we use the Perdew–Burke-Ernzerhof (PBE) GGA functional with a Hubbard U correction, while Chapter 3 uses PBE without a U correction due to the delocalized nature of Ti electrons, and Chapter 4 uses the SCAN functional.

With appropriately-chosen approximations and corrections, it is possible to calculate many properties relevant to intercalation systems. The average intercalation voltage of a battery can be obtained solely from the total DFT energies of the intercalated and deintercalated structures and the metal anode.[95, 96] This result can be obtained from the description of voltage as the chemical potential difference of working ion A between the cathode and an anode of metal A

$$V(x_{\mathrm{A}}) = -\frac{\mu_{\mathrm{A}}^{cathode}(x_{\mathrm{A}}) - \mu_{\mathrm{A}}^{anode}}{nF} \tag{1.1}$$

where $V(x_{\mathrm{A}})$ is the voltage as a function of the concentration of working ion A, $\mu_{\mathrm{A}}^{cathode}$ and μ_{A}^{anode} are the chemical potentials of A in the cathode and anode, n is the charge transferred by a single A ion, and F is Faraday's constant. The average voltage can then be deduced by finding that the total electrical energy E from discharging between $\mathrm{A}_{x_2}\mathrm{BO}_2$ and $\mathrm{A}_{x_1}\mathrm{BO}_2$ is the total reaction free energy change ΔG_r. This result can be obtained by recalling that the

chemical potential of A in the cathode is its change in free energy with x_A and integrating the voltage from equation 1.1 times displaced charge.[95] From the Nernst equation, the average intercalation voltage $\bar{V}$ is then

$$\bar{V} = -\frac{\Delta G_r}{nF}.$$

Assuming minimal entropic contribution, ΔG_r can be approximated as the total reaction change in internal energy ΔE_r, and the average intercalation voltage associated with $A_{x_2}BO_2 \rightarrow A_{x_1}BO_2 + (x_2 - x_1)A$ can then be written as

$$\bar{V} = -\frac{E(A_{x_2}BO_2) - E(A_{x_1}BO_2) - (x_2 - x_1)E(A)}{nF} \tag{1.2}$$

where $E(A_{x_2}BO_2)$ and $E(A_{x_1}BO_2)$ are the internal energies of the intercalated and deintercalated materials, and $E(A)$ is the internal energy of the bulk metal A. Average voltage calculations can be performed between the fully intercalated and deintercalated materials to obtain the overall average voltage of the material or between ground state A/vacancy orderings (adjacent in composition) to approximate the $0\,K$ voltage curve.[95, 96]

The stable A/vacancy orderings can be found from a set of configurations and their energies (e.g., from DFT) by comparing their formation energies. The formation energy with respect to the fully intercalated and deintercalated reference phases (E_f) of a configuration with intermediate composition (A_xBO_2 between BO_2 and ABO_2) can be written as [96]

$$E_f(A_xBO_2) = E(A_xBO_2) - xE(ABO_2) - (1-x)E(BO_2). \tag{1.3}$$

The stable phases are then the members forming the lower convex hull of the formation energies of the configurations, and phases above the convex hull have thermodynamic driving force (equal to their energy above the hull) to decompose into the stable phases or combinations of the stable phases. An example convex hull for Li in layered Li_xNiO_2 from Arroyo y de Dompablo, *et al.* [97] is shown in Figure 1.7a. Such convex hulls can be constructed in binary systems, as in intercalation, or ternary and more complex systems, although the difficulty of visualization increases with dimension.

Connections between the voltage curve and the phase diagram are apparent when considering the calculation of the $0\,K$ voltage curve based on A/vacancy orderings from the convex hull. Voltage drops are associated with A/vacancy stable orderings, while voltage plateaus indicate two-phase regions between stable orderings. Stronger orderings, i.e., orderings much lower in formation energy than the tie-line between adjacent orderings, result in longer voltage drops. Configurational entropy at non-zero temperatures tends to smooth out the voltage curve by adding solubility to stable orderings and creating solid-solution behavior in areas with many stable or nearly-stable orderings. This effect can be seen in the simulated room-temperature voltage curve in Figure 1.7b from Arroyo y de Dompablo, *et*

12
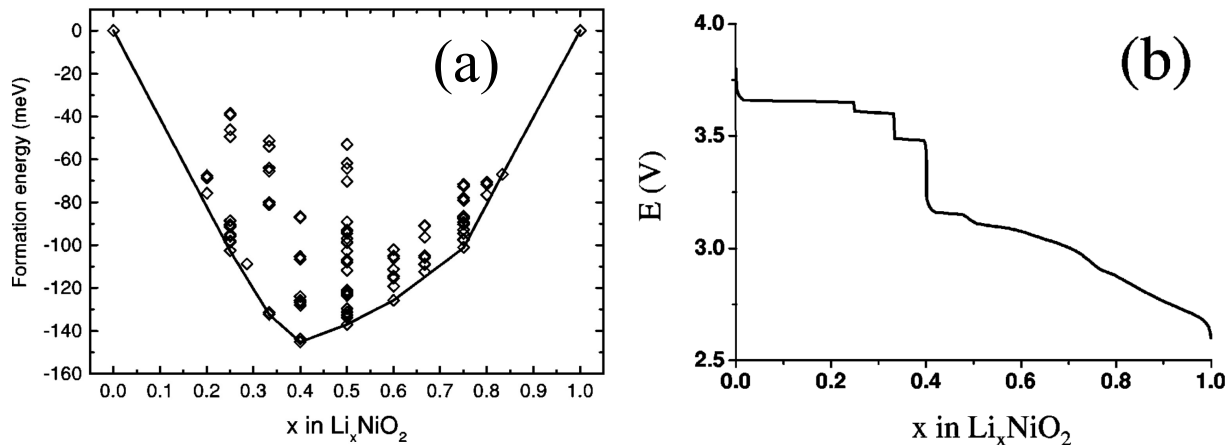
Figure 1.7: **Calculated convex hull and voltage profile of Li$_x$NiO$_2$** (a) Convex hull from calculated formation energies of ordered Li$_x$NiO$_2$ configurations, and (b) voltage-composition curve simulated at room temperature by cluster expansion Monte Carlo methods. Data and plots originally published in Arroyo y de Dompablo, *et al.* [97].

al. [97]. Such effects from configurational entropy at non-zero-temperature can be obtained by combining a cluster expansion, which parametrizes the total energy of configurations in terms of site occupancies on the lattice and is fit to the interactions of clusters of sites, with Monte Carlo simulations.

1.3.2 Cluster expansion and Monte Carlo methods

A cluster expansion (CE) models the configurational energetics of the system, which can be used in conjunction with Monte Carlo (MC) methods to simulate finite-temperature thermodynamics.[98–101] Specifically, the CE is a model mapping lattice configurations to their energies, where the Hamiltonian can be expressed as:

$$E(\sigma) = \sum_{\beta} m_{\beta} J_{\beta} \langle \Phi_{\alpha}(\sigma) \rangle_{\beta}. \tag{1.4}$$

Here, E is the energy as a function of the occupation string σ; β is a collection of symmetrically-equivalent clusters α; m_{β} is the number of clusters in that collection, properly normalized; J_{β} is the effective cluster interaction (ECI); and Φ_{α} is the cluster function, whose average over the crystal is called the correlation function. The cluster function is the product of single-site basis functions, for which we use $\sigma_i = +1(-1)$ when i is occupied by Mg (vacancy) in Chapter 2 and the sinusoidal basis functions described in Van de Walle, *et al.* [102] for disorder beyond the binary level in Chapter 4. An additional electrostatic term can be used to help capture electrostatic interactions that aid in maintaining long-range charge neutrality

13

in MC simulations [103, 104], as in Chapter 4. Though the summation in the Hamiltonian in 1.4 is performed over all possible clusters of the lattice, in practice clusters are truncated, usually to include clusters only up to triplets or quadruplets up to a maximum distance. Such CE have previously been used to model Li-vacancy disorder in layered Li_xCoO_2 [105] and Li_xNiO_2 [97] and cation disorder in DRX compounds [103, 106, 107].

The cluster interactions of the CE can be fit by methods such as compressive sensing [108], quadratic programming, l_1-norm regularization, l_0-l_2 regularization [109], sparse group lasso [110], etc. Due to the increasing number of clusters with the system complexity, the total number of clusters is often much larger than the number of energies that can be calculated with DFT, even after truncation. In ionic systems where species are given explicit oxidation states, linear dependencies due to charge-neutrality constraints can arise between correlation functions.[110] For both these reasons, most fitting methods apply regularization to reduce the effects of overfitting and linear dependencies.

The fitted CE in conjunction with MC methods enable the calculation of finite-temperature thermodynamics that include the effects of configurational entropy. Voltage curves can be calculated through constant-temperature scans in chemical potential of the working ion by applying Equation 1.1, as shown in Figure 1.7b. Phase diagrams of temperature and composition can also be obtained by a series of constant-temperature scans in the relevant chemical potential at varying temperatures and detecting phase transitions through discontinuities in composition and energy.[97, 103, 105, 111] Disordered structures of a known composition can be simulated through high-temperature constant-composition equilibration.[107, 112]

For some phase transitions that cause significant numerical hysteresis in MC simulations, free energy integration is necessary to determine the equilibrium chemical potential and composition of the transition. Such a method involves integrating — from reference states whose free energy is known — either along a constant-temperature path or a constant-chemical potential path to obtain a free energy, namely the grand potential in the grand canonical ensemble. Along a fixed temperature (T_0) scan of chemical potential (μ), the grand potential $\Phi(T, \mu) = \langle E \rangle - TS - \mu \langle N \rangle$ can be integrated via

$$\Phi(T_0, \mu) = \Phi(T_0, \mu_0) - \int_{\mu_0}^{\mu} \langle N(T_0, \mu) \rangle \, d\mu \tag{1.5}$$

while integration along a fixed chemical potential (μ_0) scan of temperature (T) involves

$$\beta \Phi(T, \mu_0) = \beta_0 \Phi(T_0, \mu_0) + \int_{T_0}^{T} (\langle E(T, \mu_0) \rangle - \mu_0 \langle N(T, \mu_0) \rangle) \, d\beta \tag{1.6}$$

where N is the concentration, $\beta = 1/k_B T$, $\beta_0 = 1/k_B T_0$, and k_B is the Boltzmann constant.[113] For example, the equilibrium voltage through the phase transition between spinel AB_2O_4 and lithiated spinel $A_2B_2O_4$ can be calculated through (constant-temperature) scans in increasing μ_A from the $x_A = 1$ spinel-ordered reference state and decreasing μ_A from the
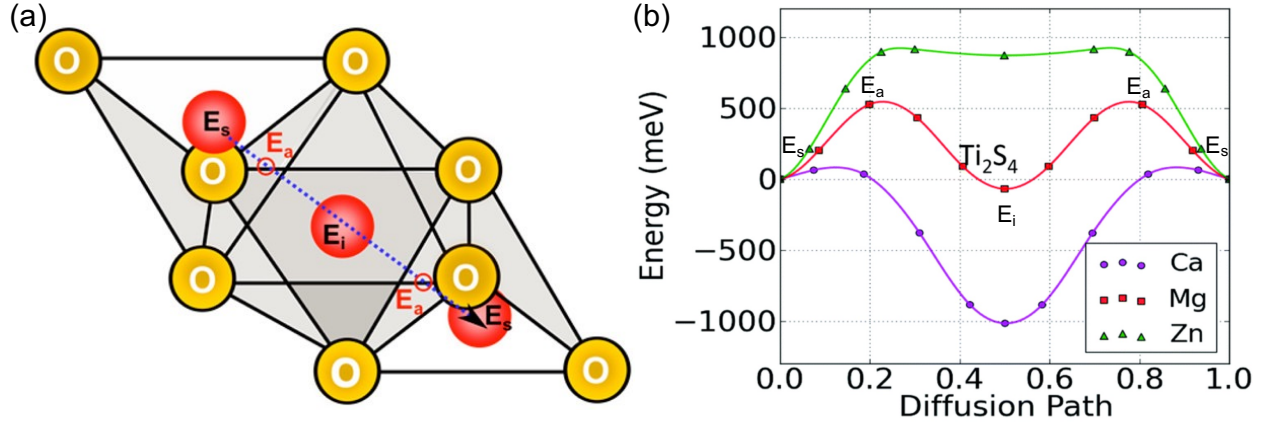
Figure 1.8: **Example migration path and energy profile of minimum energy path in Ti$_2$S$_4$** (a) Example migration path in spinel from a tetrahedral site (E$_s$) through a triangular face (E$_a$) to an intermediate octahedral site (E$_i$) and back through a triangular face to a tetrahedral site. Originally published in Rong, *et al.* [46] (b) Energy profiles of the minimum energy paths (MEP) of Ca, Mg, and Zn in spinel Ti$_2$S$_4$, with Mg MEP labeled with the respective energies of the tetrahedral, activated triangular, and intermediate octahedral sites. Originally published in Liu, *et al.* [115]

$x_A = 2$ lithiated spinel-ordered reference state. The equilibrium pathway and voltage is then determined by taking the lower envelope of the grand potentials obtained by applying Equation 1.5 in both scans, as described in [113, 114].

1.3.3 Migration barriers using the nudged-elastic band method

The diffusion of ions in intercalation materials can be modeled based on the probabilities of individual ion hops through the application of transition state theory (TST). From TST, the rate of a given ion hop can be obtained from only the energies of the ion in its initial state (which is a local energy minimum) and the activated transition state (which is a saddlepoint in the energy) and is given by

$$r^{TST} = \nu e^{-\frac{E_a}{k_B T}}$$

where ν is the attempt frequency, which is generally on the order of 10^{12} to 10^{13} in solids [116]; E_a is the activation barrier, which is the difference between the energies of the activated and initial states; k_B is the Boltzmann constant; and T is the temperature at which the process occurs.[117] The activation barrier, or the migration barrier in the case of ion migration, can be estimated using the nudged-elastic band (NEB) method. In NEB, a band is generated consisting of a chain of images (replicas) of the system along a path including the activated state between two locally stable endpoint configurations. The potential energy of the band

and its images are optimized simultaneously. To control spacing between the images along the band and avoid corner-cutting of the path, the optimization includes spring forces between the images and projects out the forces perpendicular to the band.[118, 119] The result is a discrete representation of the path and the energies and forces along it, as shown in the energy profiles of the minimum energy paths (MEP) in Figure 1.8b. Because energies in the energy profile are referenced to the initial state, the barrier to migration is given by the maximum of the energy profile. A representation of the migration paths of Figure 1.8b marked with the stable and activated states is shown in Figure 1.8a.

1.4   Motivation and outline

The advantages of the spinel structure, namely the 3-D pathways open to facile ion motion, the ability to use more earth-abundant transition metals, and the coordination environments favorable for Mg-ion migration, when applied to Li-ion and Mg-ion electrodes present opportunities to develop new potential intercalation materials. Further understanding of the mechanisms behind successful spinel electrodes such as $Li_4Ti_5O_{12}$ can also be utilized to guide the search for other high-performance materials. Based on the previously discussed gaps in (1) high voltage Mg-ion cathodes, (2) understanding of the high-rate in $Li_4Ti_5O_{12}$, and (3) full utilization of the theoretical capacity in $LiMn_2O_4$, we perform a series of investigations on the thermodynamics and kinetics of intercalation in three spinel systems by leveraging the first-principles methods described in Section 1.3. From the combination of these studies, we aim to obtain a broader perspective on the barriers to intercalation and mechanisms for fast transport in spinel materials as well as pathways to engineer the spinel structure. The remainder of the dissertation is organized as follows.

Chapter 2 presents an evaluation of the spinel $Mg_xCr_2O_4$ system as a potential high voltage Mg-ion cathode. We examine potential thermodynamic barriers to Mg intercalation and kinetic barriers to Mg migration by simulating the voltage profile and assessing Mg mobility at varying Mg concentration. We also consider the potential for Mg-Cr inversion due to Cr disproportionation. **Chapter 3** examines the origins of fast Li-ion mobility in $Li_4Ti_5O_{12}$ through a combined experimental and computational study. We identify features amplified at high (dis)charge rate in operando electron energy-loss spectra, and correlate those features with local Li-Li face-sharing environments that enable facile Li-ion migration. We also present a hypothesis regarding the nature of the phase transformation in $Li_{4+x}Ti_5O_{12}$. **Chapter 4** explores the disorder of Mn from the 16d sites onto the 16c sites in $Li_xMn_2O_4$ as a route to removing the problematic two-phase region between $LiMn_2O_4$ and $Li_2Mn_2O_4$. Simulated voltage curves of the disordered spinels demonstrate a closing of the two-phase region with greater levels of disorder. We also identify the mechanisms behind the changes in the voltage curve. In addition to recommendations on levels of disorder for the partially disordered spinels, we also propose compositional changes to facilitate reaching such levels of disorder. **Chapter 5** concludes the dissertation with the main findings and suggestions for avenues for further development of spinel-based materials for intercalation batteries.

Chapter 2

Magnesium chromate spinel as a potential Mg cathode

While Mg-ion batteries have the potential for higher energy density and better safety, the search for high voltage Mg-ion cathodes is hindered by the higher charge state of Mg^{2+} and thus its more sluggish mobility compared to Li^+ in oxides. The spinel structure where Mg occupies the 8a sites is appealing because it sits in an "un-preferred" tetrahedral coordination environment and passes through its "preferred" octahedral coordination during migration. Mg is thus expected to have lower barriers to migration and reasonable mobility within the spinel structure when it occupies the 8a sites.[46, 49] Compared to Li intercalation, Mg intercalation in the spinel framework presents a number of other obstacles unique to Mg. Due to its higher charge state, Mg may form stronger orderings within the framework. Mg is also more prone to inversion (swapping with the transition metal on the 16d site) as seen in $Mg_xMn_2O_4$ due to Mg's preference for octahedral coordination [49]. In this chapter, we investigate Mg intercalation in a promising spinel oxide, $Mg_xCr_2O_4$, which is expected to have reasonable migration barriers and should be less prone to inversion than $Mg_xMn_2O_4$.

2.1 Introduction

Mn_2O_4 is one of the few oxides that has demonstrated electrochemical Mg intercalation [60–62]. However, inversion in Mn_2O_4 can block percolation, limiting the practical capacity that can be extracted.[50] Spinel-Cr_2O_4 is another promising oxide cathode, exhibiting similar theoretical capacity to Mn_2O_4 ($\sim$280 mAh/g), a significantly higher voltage ($\sim$3.6 V), and comparable migration barriers ($\sim$600-650 meV).[63] Furthermore, Cr^{3+}/Cr^{4+} ions tend to strongly prefer 6-fold coordination [4, 49] owing to large crystal field stabilization energies [120, 121], resulting in $Mg_xCr_2O_4$ being less prone to invert upon Mg (de)intercalation. However, previous studies have reported Cr^{4+} disproportionation into Cr^{3+} and Cr^{6+} [122, 123], the latter of which tends to prefer 4-fold coordination [122, 124]. Additionally, even though previous work has suggested the prevalence of conversion reactions in oxide cathodes [38, 47, 48], the $MgCr_2O_4$ system is unlikely to undergo conversion reactions upon discharge due to the thermodynamic stability of spinel-$MgCr_2O_4$, as determined by the 0 K Mg-Cr-O ternary phase diagram.[123, 124]

Spinel $MgCr_2O_4$ has previously been studied for its magnetic properties.[125–132] In this chapter, we investigate the properties of Mg intercalation in the tetrahedral 8a sites of Cr_2O_4 spinel in detail using first principles calculations. To evaluate the free energy and Mg chemical potential in the material we use the cluster expansion approach, which has been previously used to calculate phase diagrams in Li [97, 105, 133], Na [113], and Mg [134] intercalation compounds.[96] The cluster expansion is an expansion on site occupation variables, fit to energies from first principles calculations. The cluster expansion is then combined with Monte Carlo simulations to include configurational entropy in the finite temperature free energy. In this chapter, we calculate the voltage curve of the $Mg_xCr_2O_4$ system at room temperature (293 K) as well as at 60°C (333 K) since full cell Mg batteries occasionally employ elevated temperatures up to 60°C.[42, 44] Additionally, we evaluate the tendency of the $Mg_xCr_2O_4$ spinel to invert at intermediate Mg concentrations. We also calculate migration barriers at

several Mg concentrations in $Mg_xCr_2O_4$ to evaluate the kinetics of the system throughout the intercalation process. Our results indicate the formation of stable Mg-vacancy orderings at cathode compositions of $Mg_{0.33}Cr_2O_4$ and $Mg_{0.5}Cr_2O_4$, which can severely limit Mg (de)intercalation owing to steep changes in the voltage and high Mg migration barriers at these compositions. To eventually enable Cr_2O_4 to be used in practical Mg batteries, we propose a few strategies, such as cation substitution, to suppress the formation of the stable orderings at $Mg_{0.33}Cr_2O_4$ and $Mg_{0.5}Cr_2O_4$.

2.2 Methods

2.2.1 Phase stability from DFT calculations

To construct the 0 K phase diagram of the $Mg_xCr_2O_4$ system, we use density functional theory (DFT) [85, 86] as implemented in the Vienna Ab initio Simulation Package (VASP) [87, 135], using the Perdew-Burke-Ernzerhof (PBE) parametrization [91] of the generalized gradient approximation (GGA) to describe the electron exchange and correlation. We add a Hubbard U correction of 3.5 eV to the GGA Hamiltonian to remove the spurious self-interaction of the chromium d-electrons.[136–138] The wave functions are constructed using the projector augmented wave (PAW) theory [89], using a well-converged energy cut-off of 520 eV, and sampled on a Monkhorst [139] k-point mesh of density 1000/atom. Additionally, we include the semicore $3p$-electrons along with the valence $4s$ and $3d$ electrons to construct the chromium pseudopotential. Each calculation is converged to within 0.01 meV/formula unit.

2.2.2 Voltage profile via CE-MC simulations

To obtain the room-temperature voltage curve, we perform Grand-canonical Monte Carlo (GMC) simulations on a cluster expansion (CE) Hamiltonian, where the CE is an expansion of the total energy of the system in terms of the occupancies on a topology of sites, as described in Section 1.3.2.[98, 140, 141]

The CE is fit to the total internal energies of 249 Mg-vacancy (Va) configurations, as obtained via DFT calculations. The Mg-Va configurations are enumerated using the Pymatgen library up to supercells of 64 oxygen at 25%, 50%, and 75% Mg, 24 oxygen at 33% and 66% Mg, and 48 oxygen at 16% and 83%.[142, 143] For the 50% Mg concentration, we took only the 50 configurations with the lowest electrostatic energy, as evaluated by the Ewald sum of the supercell [144], due to the large number of enumerations for the 64-oxygen supercell at 50% Mg. We use the split-Bregman algorithm [108, 145] to identify the set of relevant ECIs and fit them to the total internal energies. Convergence of the CE is verified using an in-house algorithm, as described by Huang, *et al.* [146], in combination with canonical Monte Carlo simulations. The root mean squared error (RMSE) and the leave-one-out cross-validation (LOOCV) scores are used to quantify the fit quality and the predicative ca-

pability, respectively, of the CE. Note that the set of Mg-Va configurations is built assuming no inversion of the spinel, i.e., the Mg/Va occupies only the 8a tetrahedral sites.

We perform GMC calculations on 12x12x12 supercells of the primitive rhombohedral spinel cell (corresponding to 3,456 Mg/Va sites), using the Clusters Approach to Statistical Mechanics (CASM) package.[147, 148] The GMC simulations are equilibrated for 40,000 steps and sampled for 100,000 steps. The voltage curve at each temperature is calculated from the chemical potential μ_{Mg} in the GMC simulations using equation 1.1.[95] Additionally, we perform thermodynamic free-energy integration as described in Section 1.3.2 and by Hinuma[113] and Van de Walle[149] to correct for hysteresis in the Monte Carlo scans. Specifically, we perform the free energy integration between 0% Mg and 100% Mg and between 25% Mg and 50% Mg (see Appendix A.3).

2.2.3 Migration barriers via nudged-elastic band method

We calculate the activation barriers to Mg migration in structures with 33% and 50% Mg concentration as well as in the dilute Mg and dilute vacancy limits using DFT-based Nudged Elastic Band (NEB) calculations [118, 119] described in Section 1.3.3, with forces converged within 50 meV/Å. For the dilute Mg and dilute vacancy cases, we consider a single Mg (vacancy) migrating to a nearby empty (occupied) Mg site. For the 33% Mg and 50% Mg cases, we consider two cases, namely addition of a vacancy (+Va) and an interstitial Mg atom (+Mg) to the stable ordered structure. For +Va, we create a vacancy in one of the Mg-occupied 8a sites within the 33% and 50% Mg structures and consider the migration of the vacancy to an equivalent Mg-occupied 8a site. For +Mg, we insert an additional Mg in an 8a site that is unoccupied in the ground state ordering. In the case of the 33% Mg structure with +Mg, we consider specifically the migration of the +Mg in an empty tunnel so that +Mg moves to an adjacent unoccupied 8a site. For +Mg in the 50% Mg structure, the +Mg moves to an adjacent Mg-occupied 8a site concurrently with the migration of the Mg in the occupied 8a site to an interstitial 8a site (see Appendix A.6).

For the DFT-based NEB calculation, we use both the GGA functional and the GGA+U (GGA with Hubbard U correction) functional. Convergence of GGA+U NEB calculations can be problematic due to the possible metastability of electronic states along the migration path in GGA+U, which is a functional that enforces electron localization. As an ion moves along the migration path the specific transition metal ion where the electron localizes may change. The transition of the electron from one state to another is typically not adiabatic in GGA+U and due to the metastability of electron occupation in the method. In some cases, the electron even fails to localize which leads to a very large positive energy contribution from the +U term. These problems with metastable charge density in GGA+U can make convergence of NEB with this functional problematic. Nominally, the barriers for electrons to migrate across redox centers is lower compared to ionic migration [150, 151], indicating that ionic migration is the kinetic rate-limiting step, especially in multivalent systems [38, 63, 152], giving some support for an adiabatic approach to the ion migration problem. Here we

have successfully converged NEB calculations for the Mg-Cr$_2$O$_4$ system using the GGA+U functional and consider both the GGA and GGA+U barriers in the discussion.

2.3   Results

2.3.1   Cluster expansion of Mg$_x$Cr$_2$O$_4$

Figure 2.1a plots the DFT (green circles) and CE-predicted (yellow circles) formation energies ($E_{\text{formation}}$) of all DFT-calculated 249 Mg-Va configurations at different x_{Mg}. The energies in Figure 2.1a are calculated with equation 1.3, referenced to the energies of the empty-Cr$_2$O$_4$ and magnesiated-MgCr$_2$O$_4$ configurations. As indicated by the convex ground state hull from DFT calculations (solid black line in Figure 2.1a), there are several stable DFT ground states (green circles with a black outline) at various Mg concentrations. The convex hull is mainly shaped by the ground states at 33% Mg and 50% Mg (see configurations in insert of Figure 2.2 and more detailed crystallographic information in Appendix A.2), with both configurations exhibiting $E_{\text{formation}}$ of –120 to –130 meV/f.u. There are also numerous ground states that appear to lie near the linear interpolation between the 16% and 33% Mg ground states and between the 50% and 83% Mg ground states (see Figure 2.2). The Mg$_x$Cr$_2$O$_4$ CE, described with 29 clusters, predicts a similar convex hull as compared to the DFT calculations (solid red line in Figure 2.1a), resulting in a root mean squared error (RMSE) of 8 meV/f.u. and a leave-one-out cross-validation (LOOCV) error of 13 meV/f.u., indicating both good quality and predictive capability of the CE fit. The CE-predicted and DFT energies and ground state hulls match relatively well, with the CE convex hull matching 6 out of the 10 ground states in the DFT convex hull. Further, of the DFT ground states that are not CE ground states and the CE ground states that are not DFT ground states, the CE predicts the $E_{\text{formation}}$ of the configurations with an error < 3 meV except for configurations with Mg concentration $< 10\%$.

We further evaluate the performance of the cluster expansion by calculating the error between the CE-predicted and DFT $E_{\text{formation}}$ and plot it against the energy above hull in Figure 2.1b. The energy above hull (E^{hull}) of a structure is given by the energy of decomposition into stable ground states. Structures with $E^{\text{hull}} = 0$ are stable, while structures with low E^{hull} are most important for the excitation spectrum at finite temperatures. From Figure 2.1b, the energies of structures within 50 meV/f.u. of the convex hull are generally predicted by the cluster expansion with an error of < 10 meV/f.u. Notably the CE predicts $E_{\text{formation}}$ of a majority of high E^{hull} (up to 100 meV/f.u.) structures with an error of less than 20 meV/f.u. Additionally, the CE tends to underestimate $E_{\text{formation}}$ of structures at low Mg concentration (Figure 2.1a).

Figure 2.2 shows the energy below the tie-line ($E_{\text{tie-line}}$) for each ground state configuration, where the $E_{\text{tie-line}}$ of a ground state is given by the $E_{\text{formation}}$ of the ground state referenced to the stable states at adjacent Mg compositions. For example, the adjacent sta-
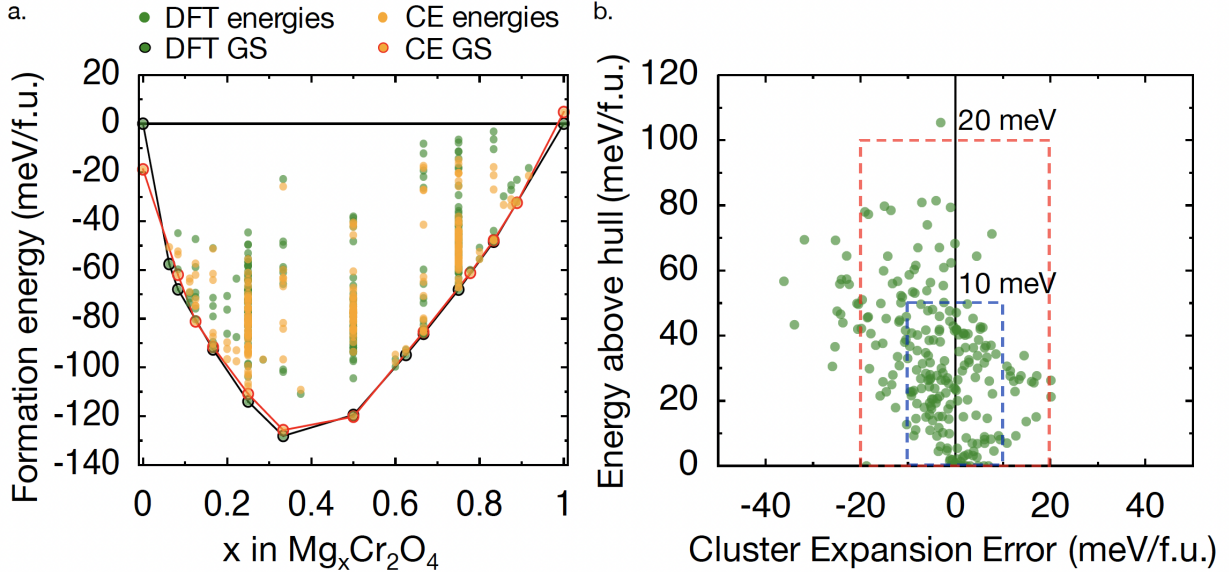
Figure 2.1: **DFT vs. CE convex hull comparison** (a) DFT (green) and CE-predicted (yellow) formation energies and convex hulls, with the DFT convex hull delineated by a black line and the CE-predicted convex hull by a red line. The ground states are outlined in black (DFT GS) or red (CE GS). (b) Plot of CE error and DFT energy above hull per formula unit (f.u.). The blue dashed box encloses structures within 10 meV CE error and 50 meV off the convex hull, while the red dashed box encloses structures within 20 meV CE error and 100 meV off the convex hull.

ble states for the 33% Mg ground state (with $E_{\text{formation}} \sim -128$ meV/f.u.) are the 25% Mg ($E_{\text{formation}} \sim -114$ meV/f.u.) and the 50% Mg ($E_{\text{formation}} \sim -119$ meV/f.u.) ground states. Consequently, $E_{\text{tie-line}}$ of the 33% Mg is given by the difference between $E_{\text{formation}}$ of the 33% Mg ground state and the weighted-sum of the $E_{\text{formation}}$ of 25% Mg and 50% Mg ground states, so -128 meV/(f.u.)-(-114 meV/(f.u.)*(50%-33%)/(50%-25%))-(-119 meV/(f.u.)*(33%-25%)/(50%-25%)) = 12.3 meV/(f.u.). Thus, the $E_{\text{tie-line}}$ quantifies the "depth" of a ground state since it indicates the driving force to form the ground state instead of the stable states at adjacent Mg concentrations. For example, the 33% Mg and 50% Mg ground states with $E_{\text{tie-line}} > 10$ meV/f.u. would be considered "deep" ground states, while the 25% Mg and 66% Mg ground states with $E_{\text{tie-line}} < 5$ meV/f.u. are considered "shallow" ground states.

Indeed, the data in Figure 2.2 indicate that the deepest ground states are at 33% Mg ($E_{\text{tie-line}} \sim 13$ meV/f.u. with respect to the 25% Mg and 50% Mg ground states) and 50% Mg ($E_{\text{tie-line}} \sim 10$ meV/f.u. with respect to the 33% Mg and 62.5% Mg ground states). Additionally, there are numerous shallow ($E_{\text{tie-line}} < 5$ meV) Mg-vacancy orderings such as the 16% Mg and 25% Mg orderings as well as the orderings above 50% Mg in both the DFT and CE convex hulls. Shallower ground states are more likely to disappear at elevated
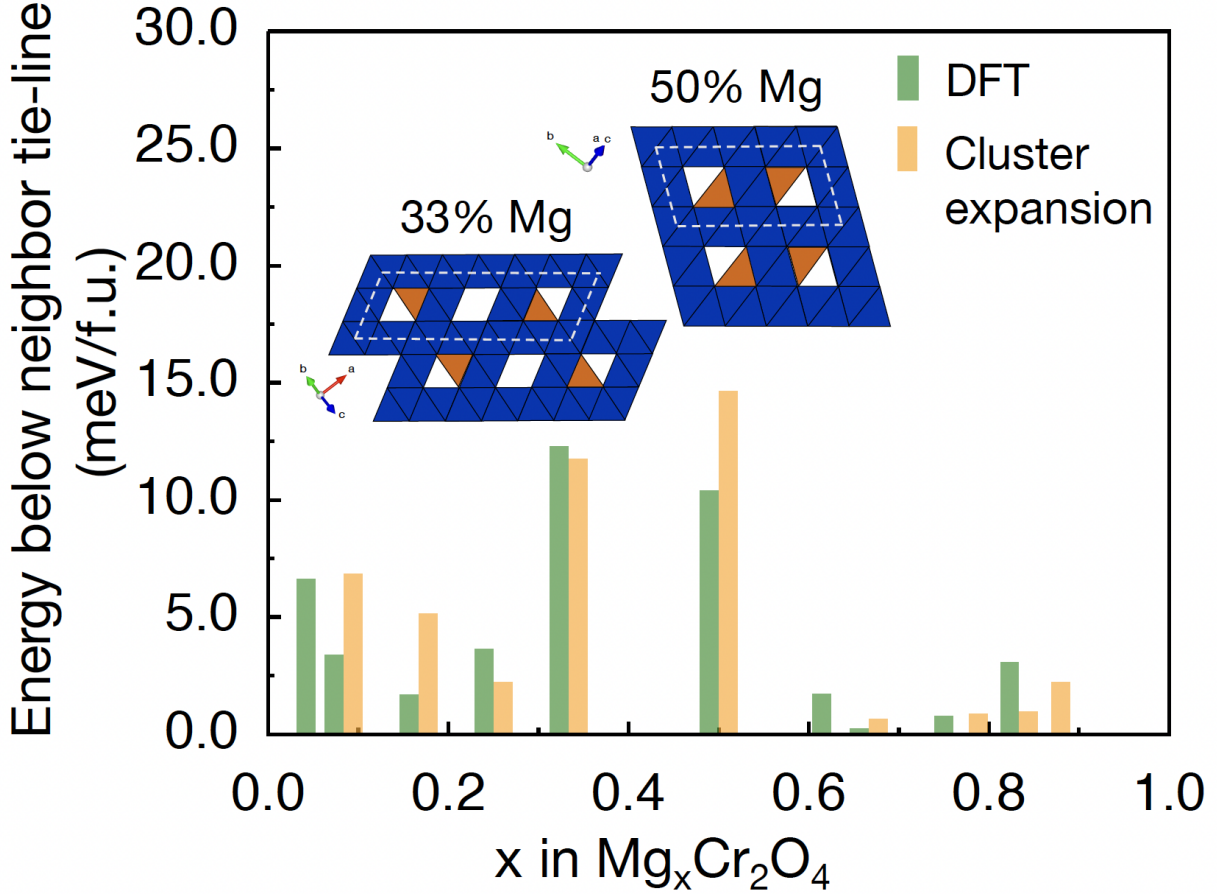
Figure 2.2: **Stability of ground states in DFT and CE** Plot of $E_{\text{tie-line}}$, which is given by the energy difference between a ground state's $E_{\text{formation}}$ and the tie-line connecting neighbor ground state configurations. The $E_{\text{tie-line}}$ of CE ground states are shown in yellow, and the $E_{\text{tie-line}}$ of DFT ground states are shown in green. The configurations of the ground states at 33% Mg and 50% Mg are also shown, with Cr octahedra and Mg tetrahedra indicated by blue and orange polyhedra, respectively, in the $\langle 110 \rangle$ direction. The repeating unit of the ground state configurations are outlined by the dashed white line.

temperature unless they have higher entropy than the structures that define their tie-line. The Figure 2.2 inserts show the structures of the ground states at 33% Mg and 50% Mg, along the $\langle 110 \rangle$ direction, with the repeating unit outlined with the white dashed line.

Using Figure 2.2 to further analyze the performance of the CE vs. DFT, it is shown that the CE is generally able to predict the $E_{\text{tie-line}}$ of ground states within 2-3 meV/f.u. of the DFT values. In all ground states common between the CE and DFT convex hulls, the CE predicts $E_{\text{tie-line}}$ that are within 5 meV of the DFT $E_{\text{tie-line}}$. Notably, the CE does

not predict the DFT ground states at 6.25% Mg, 62.5% Mg, and 75% Mg, as indicated by the lack of yellow bars at those concentrations in Figure 2.2, while the CE predicts spurious ground states at 78% Mg and 89% Mg. Because the voltage curve depends primarily on the shape of the convex hull, i.e., changes in slope of $E_{\text{formation}}$ with respect to x_{Mg}, we choose to trade error in prediction of the exact ground state orderings for lower absolute errors in the ground state $E_{\text{formation}}$.

We additionally investigate the change in volume in the $Mg_xCr_2O_4$ system associated with (de)intercalation in Appendix A.4.

2.3.2   Investigating the possibility of Mg-Cr inversion

In building the convex hull and CE, only the non-inverted normal-$MgCr_2O_4$ spinel is considered. However in oxide spinels such as $Mg_xMn_2O_4$, the structure can invert during Mg (de)intercalation whereby the Mn moves to the 8a tetrahedral sites and can block the percolation of Mg through the structure.[50] Analogously in $Mg_xCr_2O_4$, inversion will involve the movement of a Cr in a 16d site to an 8a site. We briefly investigate the possibility of the $Mg_xCr_2O_4$ spinel inverting during intercalation, which is likely either by the migration of the Cr^{4+} to the 8a tetrahedral site [49] or by disproportionation of Cr^{4+} to Cr^{3+} and Cr^{6+} and the subsequent migration of Cr^{6+} to the 8a tetrahedral site.[122, 124]

Since inversion tends to occur commonly at intermediate intercalant concentrations [50, 153] with disproportionation in Cr_2O_4 requiring the presence of Cr^{4+}, a likely ground state configuration that might be susceptible to inversion is $Mg_{0.33}Cr_2O_4$. As a result, we investigate the energies of potential inverted configurations [50, 154] and the kinetic barriers to Cr migration to the 8a site at the 33% Mg ground state. For the 33% Mg ground state, we calculate the energies of all symmetrically distinct configurations in a unit cell with 24 oxygen ions whereby one Cr^{4+} exchanges with either a vacancy or a Mg^{2+} in a vertex-sharing 8a site. We also calculate the migration barrier using the nudged-elastic band (NEB) method for Cr diffusion to the lowest energy structure among the structures resulting from a Cr^{4+} exchange.

We additionally consider the possibility of Cr^{4+} disproportionation ($3Cr^{4+} \rightarrow 2Cr^{3+} + Cr^{6+}$) as the resulting Cr^{6+} ions prefer tetrahedral coordination. To this end, we initialize the Cr atom in the 8a site with a low magnetic moment ($\sim$0 Bohr-Magneton) in our calculations, which indicates a Cr^{6+} ion. In all calculations of the inverted structures, the magnetic moment on the inverted Cr in the tetrahedral site relaxed to $\sim$2.3 Bohr-Magnetons, suggesting a 4+ charge indicating that disproportionation does not occur.

Figure 2.3a compares $E_{\text{formation}}$ of the non-inverted 33% Mg ground state (black) with the configurations resulting from all possible exchanges of a single Cr^{4+} with either an empty (green) or a Mg-occupied (yellow) 8a site. Structures where Cr^{4+} moves into a Mg-occupied 8a site have $E_{\text{formation}} \sim 60$ meV/f.u. higher than that of the non-inverted ground state, while structures where Cr^{4+} moves into an empty 8a site have $E_{\text{formation}} \sim 20$-40 meV/f.u.

24
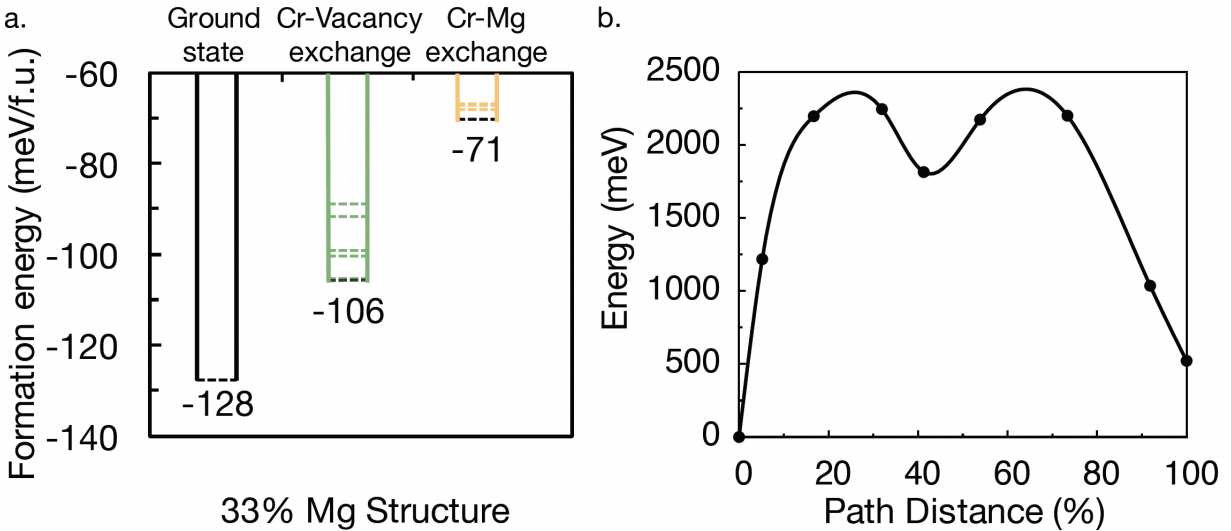
Figure 2.3: **Energetic changes and migration barrier of Cr inversion** (a) Comparison of $E_{\text{formation}}$ of the 33% Mg ground state (black) and structures with a single exchange of a Cr^{4+} to an empty 8a site (green) or a Mg-occupied 8a site (yellow). The lowest Cr-Va and Cr-Mg exchanged configurations are shown in black in their respective column while higher-energy structures are shown in color. (b) Energy profile for Cr diffusion in the 33% Mg configuration (Figure 2.2 insert) to the lowest-energy tetrahedral vacancy. The configuration resulting from the Cr diffusion corresponds to the black dashed line in the Cr-Vacancy exchange column in (a). The migration barrier is given by the maximum of the energy along the path in (b).

higher than that of the ground state. Thus, inversion due to exchange between a Cr^{4+} and an occupied Mg site is unlikely to occur in the 33% Mg ordering, but the inverted structure in which Cr^{4+} moves to an empty Mg site may be slightly more thermodynamically accessible at room temperature.

Figure 2.3b shows the NEB-calculated energy profile for Cr^{4+} diffusing from an octahedral site to a low energy vacant 8a site. The energies in Figure 2.3b are referenced to the initial ground state configuration (0% path distance), with the migration barrier of the given trajectory indicated by the maximum in the corresponding energy profile. From Figure 2.3b, the migration barrier for Cr diffusion is $\sim$2240 meV. In general, at room temperature, it is unlikely that there are any hops with migration barriers over 2 eV, so Cr inversion is not expected at the 33% Mg concentration based on kinetics. Thus, despite the small energy difference ($\sim$ 20 meV/f.u.) between the 33% Mg ground state and the same configuration with an additional Cr^{4+} exchanged with an 8a vacancy, the high kinetic barrier to Cr inversion makes Cr inversion unlikely.

25

2.3.3 Simulated voltage curve of Mg in Cr_2O_4

Figure 2.4 plots the voltage for Mg intercalation as a function of x_{Mg} in the Cr_2O_4 lattice at 0 K (dashed lines in Figure 2.4) and 293 K (solid black line). For comparison, we plot the 0 K voltage curve as obtained directly through DFT calculations (green dashed line) and our CE model (yellow dashed line) in Figure 2.4. Note that the voltage plateaus (such as between 33% and 50% Mg) in Figure 2.4 correspond to 2-phase regions while voltage steps (at 50% Mg for example) correspond to specific ground state configurations. Also, the magnitude of the voltage step at a specific Mg concentration corresponds loosely to the depth of the ground state configuration (see Figure 2.2).
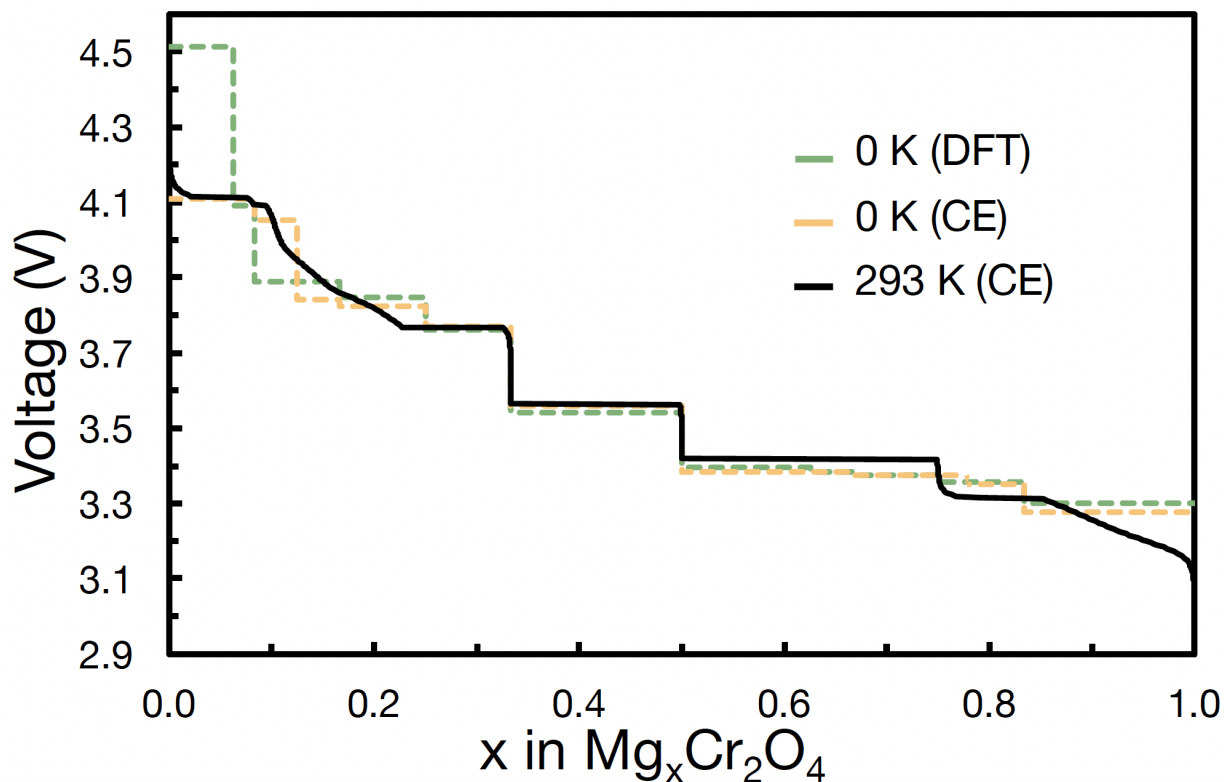
Figure 2.4: **GMC-calculated voltage curves** Calculated voltage curves for Mg (de)intercalation in $Mg_xCr_2O_4$, including the theoretical DFT (0 K) voltage curve, the CE-predicted 0 K voltage curve, and the room temperature (293 K) Monte Carlo-calculated voltage curve, given by the dashed green, dashed yellow, and solid black lines, respectively.

The DFT voltage curve has a multitude of voltage steps, with the small steps (< 0.05 V) originating from the numerous shallow ground state orderings and the largest steps of 0.42 V, 0.20 V, 0.22 V, and 0.15 V originating from the 6.25% Mg, 8.3% Mg, 33% Mg, and 50% Mg ground state configurations, respectively. The large voltage steps at 33% Mg and

50% Mg are in agreement with the deep 33% Mg and 50% Mg ground states and suggest that the 33% and 50% Mg ground states may limit intercalation.[152] The 0 K voltage curve calculated by the CE agrees broadly with the DFT curve except for absent voltage steps at 6.25% Mg, 62.5% Mg, and 75% Mg and spurious voltage steps at 78.9% Mg and 88.9% Mg, consistent with the data from Figure 2.1 and Figure 2.2.

At 293 K, the voltage curve essentially follows the trends displayed by the 0 K CE curve, with noticeable differences at low Mg ($< 20\%$) and high Mg ($> 85\%$) concentrations. For example, between 10% Mg and 22% Mg, the voltage steps at 8.33% and 16.67% Mg are smoothed into a continuous curve. The smoothing behavior comes from the increase in configurational entropy as temperature increases, which disorders the weakly-ordered ground states, leading to a solid-solution behavior. Additionally, an artificial ground state appears at 75% Mg in the Monte Carlo at 293 K, indicated by the sharp voltage step at 75% Mg concentration. Specifically, the Monte Carlo calculation discovers a new CE ground state at 75% Mg that is not a part of the set of configurations used to fit the CE. Upon DFT calculation, the new 75% Mg configuration is near the convex hull ($E^{\text{hull}} \sim 4$ meV/f.u.) but not a real DFT ground state and is actually over-stabilized by the CE by ~ 10 meV/f.u., which is within the 13 meV/f.u. LOOCV error of the CE. Due to the small $E_{\text{tie-line}}$ of the ground states between 50% Mg and 83% Mg, the overstabilization of the new 75% Mg configuration causes that configuration to become a strong ground state in the CE. Thus, the 75% Mg voltage jump is an artifact of our cluster expansion. From Figure 2.4, we calculate the average voltage for Mg intercalation to be 3.6 V in Cr_2O_4, consistent with previous theoretical studies.[63] Also, the voltage curve at 333 K (60°C), as shown in Appendix A.5, appears largely unchanged from the 293 K voltage curve. Notably, the 33% and 50% Mg steps are retained even at an elevated temperature of 60°C. We subsequently investigate Mg mobility within the Cr_2O_4 framework by calculating the migration barriers for Mg diffusion within the deep 33% and 50% Mg ground states, which will be encountered during Mg intercalation.

2.3.4   Mg migration in $Mg_xCr_2O_4$

To analyze the ease of Mg mobility in the Cr_2O_4 lattice at different levels of (de)intercalation, we perform NEB calculations at several Mg concentrations, including 0% Mg (dilute Mg limit), 33% Mg, 50% Mg, and 100% Mg (dilute Va limit). In each of the cases, we consider the migration path typical of Mg in tetrahedral sites of the spinel (Figure 2.5a). In the path depicted in Figure 2.5a, the Mg migrates from a tetrahedral site (A) through a triangular face (B) shared by the tetrahedral with an empty octahedral site (C) to the empty octahedral site and then through another triangular face (B', not shown in Figure 2.5a) to the final tetrahedral site (D). In the dilute Mg (Va) limit, we consider a single Mg (Va) diffusing through the empty (magnesiated) Cr_2O_4 host, along the trajectory shown in Figure 2.5a-b. To evaluate Mg migration in the 33% and 50% Mg configurations, we considered the ground state configurations (Figure 2.2 insert and Appendix A.2) and introduce either an
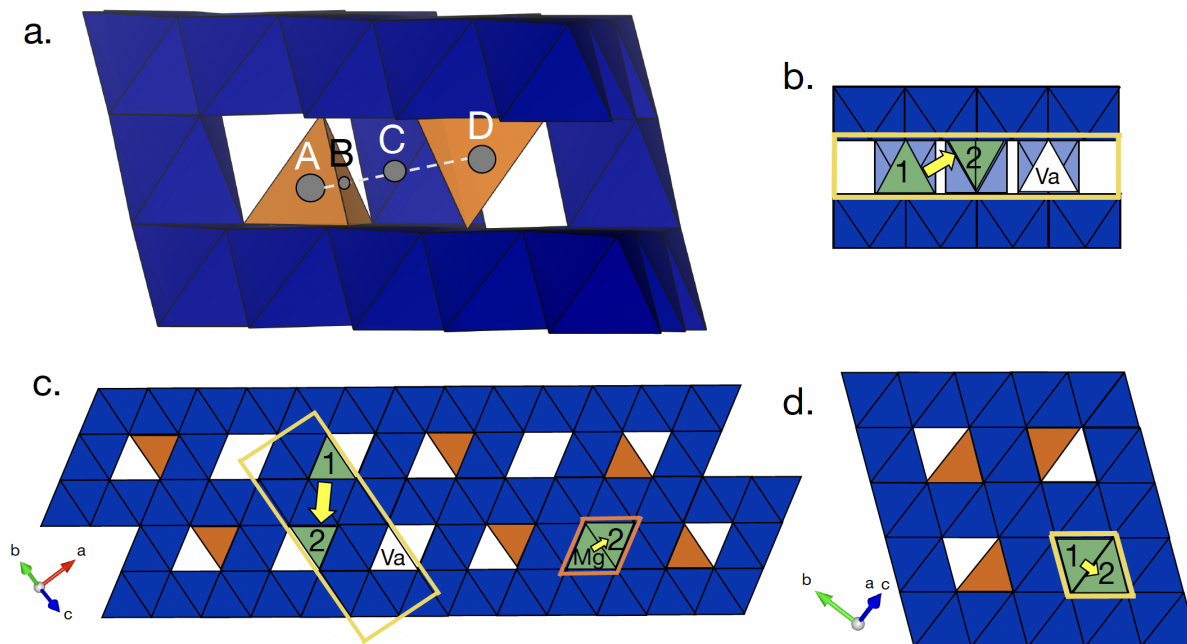
Figure 2.5: **Mg migration pathways in Cr_2O_4** (a) The typical migration path between tetrahedral Mg is indicated by the white dashed line, and positions of note are marked by gray circles. Mg moves from the tetrahedral site (A) through a triangular face (B) shared between the tetrahedral site and an empty octahedral site (C) to the empty octahedral site. It then migrates from the empty octahedral site through another triangular face (B', not shown) leading to the final tetrahedral site (D). (b) The migration barriers are calculated based on the path from the initial (1) to the final (2) endpoints, indicated by green labeled triangles, and represent half of the migration path. (c) The 33% Mg and (d) 50% Mg structures are shown with example migration paths, with yellow arrows in each panel indicating the direction of Mg movement. Migration paths involving an added vacancy are outlined in yellow with the added vacancy labeled 'Va', and migration paths involving an added Mg are outlined in orange with the added Mg labeled 'Mg'.

additional vacancy (+Va) in the Mg-occupied 8a sites (Figure 2.5c-d, yellow-outlined path) or an additional Mg (+Mg) in one of the unoccupied 8a sites (Figure 2.5c orange-outlined path and Appendix A.6). In the case where +Va is added, we evaluate the barrier for a Mg to migrate to the vacant 8a-site added to the ground state configuration. In the case where +Mg is added, for the 33% Mg ground state, we evaluate the barrier for the +Mg to migrate to an adjacent vacant 8a-site in the empty tunnel (see insert in Figure 2.2). Because the paths are symmetric (i.e., (1) to (2) is equivalent to (2) to (Va) in Figure 2.5b-d), we perform an NEB calculation on half of the full migration path (from (1) to (2)). For the above calculations 7 images are used to represent the migrating Mg along the diffusion paths.

28

For the 50% Mg with +Mg, the path is slightly more complex and is explained further in Appendix A.6.

Figure 2.6 shows the NEB DFT-calculated migration barriers for all configurations (dilute Mg, 33% Mg with +Va, 33% Mg with +Mg, 50% Mg with +Va, 50% Mg with +Mg, and dilute Va) using the GGA functional (in green in Figure 2.6) and the GGA+U functional (in yellow in Figure 2.6). Additionally, a direct comparison between NEB barriers and energy profiles calculated using GGA and GGA+U for each configuration is shown in Appendix A.7. From Figure 2.6, the GGA barriers of ∼730 meV and ∼600 meV at the dilute Mg and dilute Va limits agree with the literature values of ∼600-700 meV.[63] The 33% Mg and 50% Mg NEB barriers, which have not been previously reported, are ∼920 and ∼790 meV with +Va and ∼670 meV and ∼970 meV with +Mg, respectively. Further, the energy profiles (Appendix A.7) are in agreement with previous studies regarding the shape of the energy profile, with maxima at the triangular faces (B and B' in Figure 2.5a).[63]

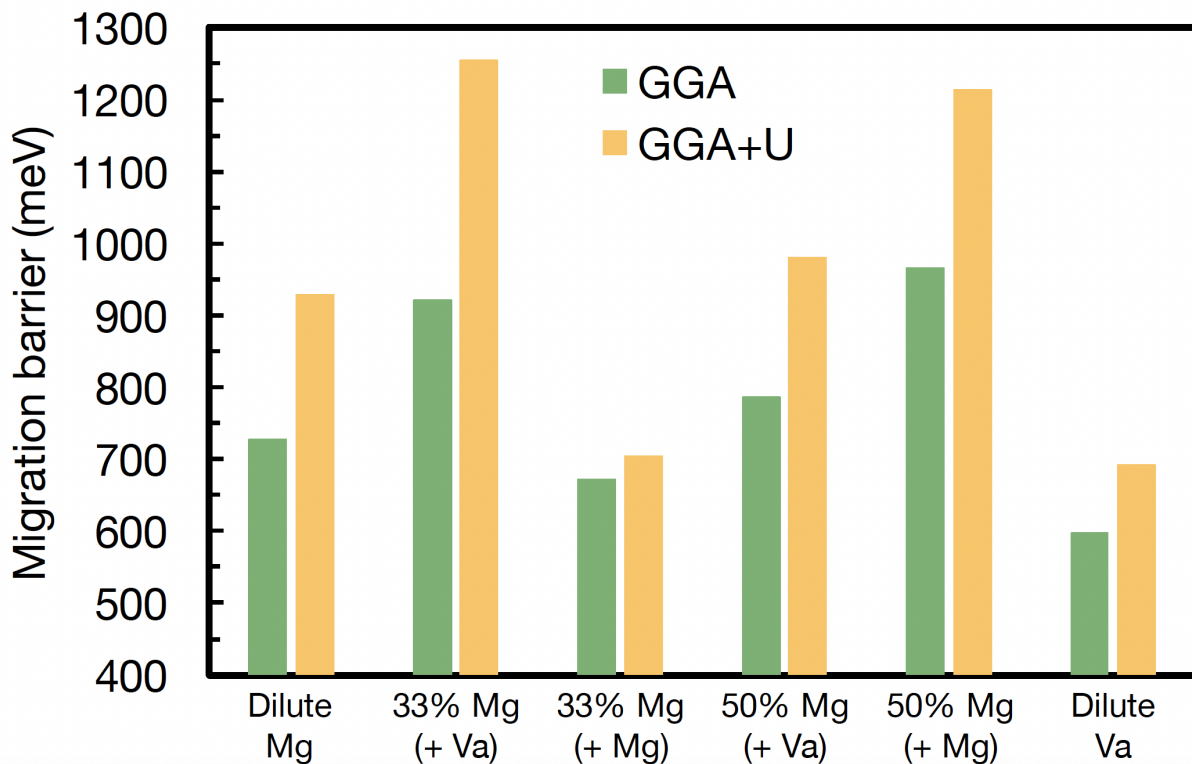Figure 2.6: **Mg diffusion barriers in GGA and GGA+U** The activation barriers for Mg diffusion in the dilute Mg, 33% Mg with additional vacancy (+Va), 33% Mg with additional Mg (+Mg), 50% Mg with additional vacancy (+Va), 50% Mg with additional Mg (+Mg), and dilute vacancy configurations are displayed. NEB barriers calculated in GGA are given by green bars while those calculated in GGA+U are colored in yellow.

Based on the NEB energy profiles calculated using the GGA+U functional in Figure 2.6, the dilute Va limit and 33% Mg with +Mg have the lowest barrier ($\sim$690 meV and $\sim$700 meV, respectively) among the GGA+U migration barriers calculated (similar to the $\sim$600 meV and 670 meV migration barriers calculated in GGA). In the dilute Mg, 33% Mg with +Va, and 50% Mg with +Va and with +Mg configurations, GGA+U predicts a significantly higher Mg migration barrier than GGA. Specifically, GGA+U predicts barriers of $\sim$930 meV for the dilute Mg configuration, $\sim$1250 meV for the 33% Mg configuration with +Va, $\sim$980 meV for the 50% Mg configuration with +Va, and $\sim$1200 meV for the 50% Mg configuration with +Mg, which are respectively $\sim$200 meV, $\sim$320 meV, $\sim$200 meV, and $\sim$250 meV higher than their GGA counterparts. Further comparing the GGA and GGA+U energy profiles in Appendix A.7, it is notable that the end states of the 33% Mg with +Va and 50% Mg with +Va paths in GGA are $\sim$300-350 meV higher than the initial states in GGA+U, reflecting the fact that GGA+U and GGA tend to give quite different ordering profiles (further shown in Appendix A.8). Because of the forced charge localization in GGA+U, screening is not as effective as in GGA, and ordering is more pronounced, leading to stronger effective ordering interactions. Similar effects have also been seen in Na_xCoO_2.[113] In general, GGA orderings seem to be closer to experimental observations, except in systems where electron localization is very pronounced.[155]

To contextualize the magnitude of migration barriers, previous work has shown that barriers around 600-750 meV and below can yield reasonable diffusivity for a 100 nm cathode particle under Mg-electrochemical conditions.[38] Based on the range of reasonable migration barriers (600-750 meV), the dilute Va and 33% Mg with +Mg migration barriers are within the limits of reasonable diffusion in both GGA and GGA+U, indicating that initial Mg deintercalation from a chemically-synthesized $MgCr_2O_4$ should be facile under electrochemical conditions. However, both GGA and GGA+U migration barriers at lower Mg concentrations, specifically for 50% Mg with +Mg and with +Va and 33% Mg with +Va are above the upper limit of 750 meV, signifying that Mg extraction will be difficult beyond $Mg_{0.5}Cr_2O_4$.

2.4   Discussion

2.4.1   Evaluation of $Mg_xCr_2O_4$ as a potential Mg cathode

The $Mg_xCr_2O_4$ system is an appealing system due to its high theoretical capacity ($280\,\text{mAh/g}$) and high average voltage (3.6 V). The NEB calculations and room temperature voltage curve suggest that initial deintercalation until the system is 50% deintercalated is largely uninhibited based on the reasonable ($\sim$690 meV in GGA+U) migration barrier and the smooth voltage profile at $x_{Mg} > 0.5$. Significant barriers to deintercalation appear at the 33% Mg and 50% Mg concentrations in the form of > 900 meV diffusion barriers (in GGA+U) and large voltage jumps of 0.22 V and 0.14 V, respectively. Similar thermodynamic barriers in the form of stable orderings have been shown to inhibit intercalation in analogous systems,

such as Li in Li_xCoO_2 [156], Mg in layered-V_2O_5 [134, 152], and Mg in a Chevrel phase cathode Mo_6S_8 [157]. Thus, while Mg migration may be feasible upon initial charging from the fully-magnesiated state, Mg becomes virtually immobile after $\sim$50% of the Mg is removed. Further, the 33% and 50% Mg configurations remain stable at elevated temperatures, as the voltage steps do not decrease at their respective concentrations at 333 K (Appendix A.5). Thus, while operating at elevated temperatures is one way to improve cation mobility, the operating temperature will need to be raised significantly higher than 60°C to destabilize the 33% Mg and 50% Mg ground states, which may be beyond the stability limits of current organic Mg-electrolytes. Additionally, there are difficulties associated with charging $Mg_xCr_2O_4$ to low Mg concentrations (< 33%) as the voltage extends beyond the electrolyte cathodic stability limit ($\sim$3-3.5 V) typical in Mg-systems.[38, 40]

2.4.2   Instability of spinel Cr_2O_4

Another potential issue is the instability of demagnesiated states of the $Mg_xCr_2O_4$ system. Based on the ternary Mg-Cr-O phase diagram calculated by the Materials Project,[142, 158] the demagnesiated spinel-Cr_2O_4 has a relatively high E^{hull} at $\sim$187 meV/atom with respect to rutile CrO_2, which is a ground state of the Mg-Cr-O phase diagram.[158] Further, the intermediate $Mg_xCr_2O_4$ phases lie on the rutile CrO_2-spinel $MgCr_2O_4$ tie-line, indicating that they have a driving force to decompose to those ground state phases. We calculated the intermediate $Mg_{0.33}Cr_2O_4$ and $Mg_{0.5}Cr_2O_4$ ground state orderings to have E^{hull} of $\sim$100 meV/atom and $\sim$68 meV/atom with respect to the rutile CrO_2 and spinel $MgCr_2O_4$ phases. Thus, while the fully magnesiated $MgCr_2O_4$ is a stable ground state, the high E^{hull} of Cr_2O_4 and intermediate $Mg_xCr_2O_4$ states indicate potential thermodynamically unstable states that can lead to structural transformations into rutile CrO_2 and spinel $MgCr_2O_4$ during deintercalation.[159] However, cathodes with metastable deintercalated states have successfully been used as intercalation compounds, such as delithiated $FePO_4$ with an $E^{hull} \sim$ 26 meV/atom and demagnesiated spinel Mn_2O_4 with an $E^{hull} \sim$ 32 meV/atom.[142, 158]

To more accurately address the potential instability of demagnesiated Cr_2O_4, we calculated its energy as well as that of the ground state rutile CrO_2 using the recently developed non-empirical strongly constrained and appropriately normed (SCAN) functional, which has been shown to improve ground state predictions over the GGA (PBE) and GGA+U functionals.[93] Based on the SCAN calculations, spinel Cr_2O_4 is 260 meV/atom higher in energy than the rutile CrO_2 ground state. For context, we can compare the spinel vs. rutile energy difference of CrO_2 to that of MnO_2, in which the rutile form is similarly the ground state but the spinel can easily be retained at room temperature and no conversion to rutile is ever observed.[160, 161] In the case of MnO_2, the spinel Mn_2O_4 phase is $\sim$110 meV/atom above the rutile ground state using the SCAN functional, which is significantly lower than the 260 meV/atom spinel vs. rutile energy difference in CrO_2.[106] While the driving force to convert the empty spinel to rutile is much higher in CrO_2 than in MnO_2, based on the metastability of the spinel Mn_2O_4 phase, it is difficult to make a definite prediction about

the stability or lack thereof of spinel Cr_2O_4.

2.4.3   Potential pathways to improve $Mg_xCr_2O_4$

A potential approach to improve the Mg migration in the $Mg_xCr_2O_4$ spinel system is destabilizing (or lowering the depth of) the 33% Mg and/or 50% Mg configurations via substitution of the anion, tetrahedral Mg, or octahedral transition metal sites. Of the possible substitutions, cation-substitution or doping on the transition metal octahedral site, such as Mn or Ni on the Cr octahedral site, appears the most promising due to the success and improved electrochemical properties of transition metal doping in Li spinel oxides.[162, 163] Further, the migration barriers at the dilute vacancy limits of the $MgMn_2O_4$ and $MgNi_2O_4$ spinels are lower (∼400 meV with GGA) than that of $MgCr_2O_4$ (∼600 meV with GGA and ∼690 meV with GGA+U). Thus, doping with Mn or Ni on the Cr site may result in paths with lower migration barriers. Other potential substitutions to consider are fluorine or sulfur, which have been successfully doped on the oxygen site in the $LiMn_{1.5}Ni_{0.5}O_4$ spinel [164–166] or Zn on the tetrahedral Mg sites [167, 168]. We note however that cation doping on the Mg sites runs the risk of blocking the Mg percolation pathways.

Chapter 3

Lithium titanate spinel as a fast-charging Li anode

In the previous chapter, we considered Mg intercalation in $Mg_xCr_2O_4$, which occurs as Mg fills/empties the tetrahedral 8a sites in the spinel. Here, we consider Li intercalation in $Li_4Ti_5O_{12}$ (LTO), which occurs through the transition of Li in the 8a sites to the 16c sites. $Li_4Ti_5O_{12}$ is of particular interest as a potential Li anode as it undergoes minimal volume change during this transition. It is also remarkable in its fast-charging capability despite undergoing a two-phase reaction (from the 8a-filled $Li_4Ti_5O_{12}$ to the 16c-filled $Li_7Ti_5O_{12}$) because two-phase reactions are typically associated with slow kinetics due to the barriers associated with nucleation and growth of a second phase. Contrary to this, LTO demonstrates high Li mobility at intermediate concentrations despite apparently undergoing a two-phase reaction. In this chapter, we investigate the origins of the Li-ion kinetics at high (dis)charge rate towards uncovering new mechanisms for fast Li-ion conduction.

Some results presented in this chapter were obtained by a collaborative effort. Contribution from collaborators are made explicit in relevant results.

3.1   Introduction

In commercial LIBs, especially those for fast-charging applications in electric vehicles, electrode materials capable of accommodating Li^+ continuously via solid-solution transformation are preferentially employed because they have few kinetic barriers apart from Li^+ diffusion in the solid state.[73, 169] An exception is lithium titanate (LTO), an appealing anode capable of fast charging without the Li plating observed in graphite.[33] LTO accommodates Li^+ through a two-phase process, during which the initial disordered spinel phase ($Li_4Ti_5O_{12}$; space group $Fd\bar{3}m$) transforms directly into a rock salt phase ($Li_7Ti_5O_{12}$; $Fm\bar{3}m$) with negligible volume change (i.e., zero-strain).[170–172] Microscopically, Li^+ insertion into the octahedral 16c sites is accompanied by Li^+ migration from the tetrahedral 8a to the 16c sites. However, because Li-ion mobility is poor in the two endmembers, a model in which these two phases coexist macroscopically conflicts with the high Li-ion mobility observed at intermediate concentrations.[173–175]

This puzzling behavior has recently been attributed to the existence of an intermediate phase ($Li_{4+x}Ti_5O_{12}$; $0 \leq x \leq 3$) with Li^+ ions simultaneously occupying face-sharing 8a and 16c sites, in the form of either a homogenous solid solution or a mixture of phase-separated nanometer-sized domains.[174, 176] In situ x-ray absorption spectroscopy studies provided evidence of the metastable $Li_{4+x}Ti_5O_{12}$ phase, which emerges upon Li^+ insertion even at low rates.[177] Computational studies also predicted that face-sharing 8a and 16c local motifs are stabilized at the $Li_4Ti_5O_{12}/Li_7Ti_5O_12$ phase boundaries due to the presence of defective Li^+ ions occupying the 16d sites.[176] However, because of numerous possible configurations of $Li_{4+x}Ti_5O_{12}$ and the non-equilibrium nature of the ionic transport,[176, 177] the kinetic pathways and underlying mechanisms enabling facile ionic transport in LTO remain unresolved.

With available characterization techniques, it has been challenging to determine the

atomic configuration of the metastable intermediates ($Li_{4+x}Ti_5O_{12}$) and the associated Li^+ transport pathways.[170, 177, 178] Li K-edge electron energy-loss spectroscopy (Li-EELS), more specifically the energy-loss near edge structure, shows promise for probing the site occupancy of Li^+ in lithiated electrodes due to its high sensitivity to the local environment surrounding Li^+.[179] In this chapter, we demonstrate an ionic liquid electrolyte (ILE)-based electrochemical cell developed for operation inside a TEM, with a configuration resembling that of a real battery, enabling operando Li-EELS probing of Li^+ occupancy and transport in LTO upon galvanostatic (dis)charging at varying rates. Through combined operando Li-EELS and first-principles studies, we identified representative metastable $Li_{4+x}Ti_5O_{12}$ configurations, consisting of distorted Li polyhedra at the reaction front that provide distinct Li^+ migration pathways with significantly lower activation energy than that in the end-members. Our study provides direct evidence that the kinetic accessibility of intermediate states, which are fundamentally different from the thermodynamic equilibrium, dominates fast Li-ion transport in LTO.

3.2   Results and Discussion

3.2.1   Tracking of Li-ion migration by operando Li-EELS

Figure 3.1A[1] shows the configuration of the electrochemical cell for operando Li-EELS measurements, adapted from a TEM-grid based cell.[180] The cell uses ILE, a non-flammable electrolyte that has been increasingly employed for batteries.[181] Because of its low vapor pressure, ILE is compatible with the high-vacuum environment in the TEM column, thereby removing the need for the thick membranes generally required in liquid cells. By controlling the ILE thickness (to 10 nm or less) and collection angle (below 1.0 mrad), plural plasmon excitation can be largely suppressed (Figure B.18 in Appendix B.10), which is crucial to recording high quality low-energy lying Li-EELS spectra.[182] The electrochemical functionality of the cell was tested via galvanostatic cycling of LTO electrodes, with rates spanning from 0.8 to 8 C (C-rate of 1C defined as one-hour (dis)charge). The electrochemical performance, with flat voltage plateaus at ∼1.55 V and sharp redox peaks in the cyclic voltammetry curves (Figure 3.1B and B.19 in Appendix B.10), is comparable to that in regular LIB cells. Such an ILE-based electrochemical cell was employed in operando Li-EELS experiments to track Li-ion migration in LTO nanoparticles with well-defined structure and morphology (Figure B.20 in Appendix B.10). Li-EELS in the pre-edge region provides key information about local site occupancy and migration of Li^+ ions among different sites (e.g., 8a in $Li_4Ti_5O_{12}$, 16c in $Li_7Ti_5O_{12}$, and other polyhedral sites associated with $Li_{4+x}Ti_5O_{12}$), as illustrated in Figure 3.1C.

---

[1]In operando electrochemical cell design and construction, electrochemical tests, and Li K-edge electron energy-loss spectroscopy performed by Prof. Wei Zhang (College of Chemistry, Nankai University).
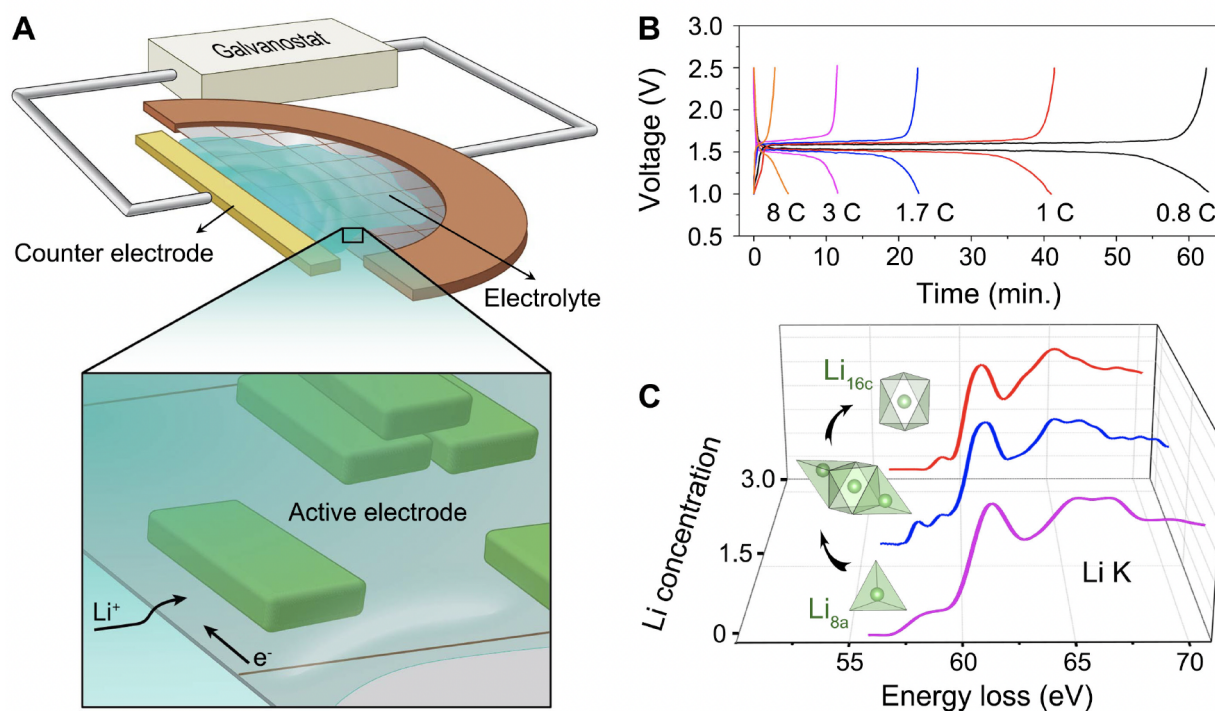
Figure 3.1: **Design of an electrochemically functional cell for operando character-ization of battery materials inside a TEM.** (A) Schematic of the ILE-based electro-chemical cell designed for operation inside a TEM, with a configuration similar to that of lithium batteries with the active electrode (e.g., LTO nanoparticles marked by green color; inset) loaded on a carbon film (gray) as a working electrode, matched with Li metal (yellow) immersed in ILE (light green). (B) Voltage profiles of LTO nanoparticles in the ILE-based electrochemical cell during galvanostatic discharge/charge at different rates (see also Fig-ure B.19 in Appendix B.10 for comparison with cycling tests in regular coin-type cells). (C) Representative Li-EELS spectra as a function of Li concentration obtained from LTO nanoparticles during discharge under galvanostatic conditions, revealing the migration of Li^+ from the initial tetrahedral 8a sites in $Li_4Ti_5O_{12}$ to polyhedral sites in an intermediate to the final octahedral 16c sites in $Li_7Ti_5O_{12}$ (as illustrated in the inset).

Figure 3.2[2] presents the time-resolved Li-EELS spectra obtained from a few selected nanoparticles (Figure 3.2A and Figure B.21 in Appendix B.10) during the 1st cycle at a rate equivalent to 2C. EELS spectra of the Ti L- and O K-edges were also obtained before and after (dis)charge (Figure B.1 in Appendix B.3), confirming active Ti redox. As shown in Figure 3.2C, the main peak position in the Li-EELS spectra remained constant (at ~ 61.5 eV) during cycling. Nonetheless, subtle but clear changes occurred within the pre-edge region, as shown in the intensity map of the spectra in Figure 3.2D. In the spectrum of $Li_4Ti_5O_{12}$, a broad peak in the pre-edge region (called pre-peak hereafter) appeared at ~ 58.9 eV (labelled by "S"; see also Figure B.22 in Appendix B.10), which mainly comes from the inelastic scattering of Li in 8a sites ($Li_{(8a)}$).[179] The pre-peak from Li in 16c sites—$Li_{(16c)}$— in $Li_7Ti_5O_{12}$ appears somewhat surprisingly at the same energy, despite the different local Li^+ environment in the two endmembers (Figure B.22 in Appendix B.10).

Upon discharging and subsequent charging, the pre-peak S remained at nearly the same position. However, a new pre-peak emerged at ~ 58.0 eV (labelled by "M"), which is absent in the spectra of the two endmembers (Figure 3.2D) as well as the partially-lithiated LTO electrodes in ex situ measurements (Appendix B.4). Pre-peak M was commonly observed across the electrode, and its intensity was found to be strongly rate-dependent (Figure B.3). The ratio of integrated intensity of the two pre-peaks M and S (defined as I_M/I_S) as a function of Li concentration (x) was plotted in Figure 3.2E. At low rates (1C and 2C), I_M/I_S values are small (only ~ 0.2) but increase abruptly (to ~ 2.0) at high rates (3C and 8C) (see quantitative analysis in Appendix B.5). As shown later on, the evolution of features in the Li-EELS spectra (e.g., I_M/I_S ratio) provides key information about Li^+ occupancy and migration in the metastable intermediates ($Li_{4+x}Ti_5O_{12}$) and its rate-dependent behaviors.

3.2.2 Atomic configurations of the intermediates ($Li_{4+x}Ti_5O_{12}$)

To understand the origin of the pre-edge features in the Li-EELS spectra and their evolution during charge/discharge, the local configurations of Li^+ ions in the two endmembers ($Li_4Ti_5O_{12}$ and $Li_7Ti_5O_{12}$) and the intermediates ($Li_{4+x}Ti_5O_{12}$, $x = 1$ and 2) were studied using density functional theory (DFT). We considered configurations of $Li_{4+x}Ti_5O_{12}$ at selected Li concentrations ($x = 0$, 1, 2, and 3). To predict the stable and possible metastable Li configurations in $Li_{4+x}Ti_5O_{12}$ ($x = 0$, 1, 2, and 3), we considered various Li/vacancy orderings at the 8a and 16c sites and Li/Ti orderings at the 16d site of $Li_{4+x}Ti_5O_{12}$ ($x = 0$, 1, 2, and 3). We calculated the DFT energies of $Li_4Ti_5O_{12}$ with various Li/Ti orderings at 16d sites within a supercell of $[Li_6]^{tet(8a)}[Ti_{10}Li_2]^{oct(16d)}O_{24}$. The Li/Ti ordering with the lowest formation energy is shown in the $Li_4Ti_5O_{12}$ composition in Figure 3.3B. This Li/Ti ordering on the 16d sites was fixed for the $Li_5Ti_5O_{12}$, $Li_6Ti_5O_{12}$, and $Li_7Ti_5O_{12}$ configurations because Ti is immobile during electrochemical cycling at room temperature [172]. We further calculated the

---

[2]In operando Li K-edge electron energy-loss spectroscopy performed by Prof. Wei Zhang (College of Chemistry, Nankai University).
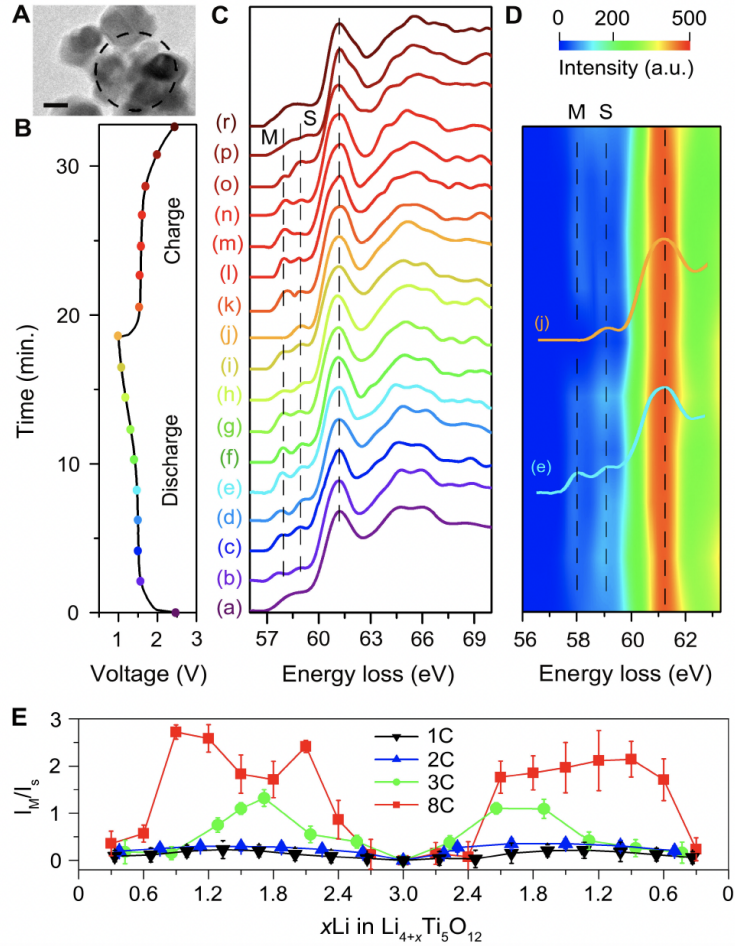
Figure 3.2: **Real-time probing of Li-ion transport in LTO during discharge/charge using operando Li-EELS** (A) Bright-field TEM image showing the LTO nanoparticles selected for obtaining Li-EELS spectra (marked by a black dash circle). Scale bar: 50 nm. (B, C) Voltage profiles of LTO nanoparticles and the corresponding EELS spectra selected with an interval of 120 s during the first cycle at 2C rate (marked by color-coded dots in B, and letters in C). The vertical dashed black lines indicate the energy positions of the main peaks at $\sim$61.5 eV and pre-peaks M (related to metastable configurations of the intermediate compositions) and S (related to stable configurations in $Li_4Ti_5O_{12}$ and $Li_7Ti_5O_{12}$). (D) Intensity map of the Li-EELS spectra at 2C rate (see also Figure B.3 for the EELS spectra and intensity maps at 1C, 3C, and 8C rates in Appendix B.5). Two representative spectra (e) and (j) are displayed to show the pre-edge features, M and S. (E) Intensity ratio of the pre-peak M to that of S (I_M/I_S) as a function of Li concentration (x) at different rates (1C, 2C, 3C, and 8C), where I_M and I_S are the integrated intensities of pre-peaks M and S, respectively.

38

DFT energies of 1,600 different Li/vacancy orderings at 8a and 16c sites in the intermediates $Li_5Ti_5O_{12}$ and $Li_6Ti_5O_{12}$ within a supercell of $[Li_x]^{tet(8a)}[Li_y]^{oct(16c)}[Ti_{10}Li_2]^{oct(16d)}O_{24}$.

To validate the most stable predicted configurations, the voltage was calculated from the DFT energies [95] using equation 1.2. The calculated average voltage of $Li_{4+x}Ti_5O_{12}$ was 1.503 V, which is very close to the experimental value ($\sim$1.55 V) (Figure B.19 in Appendix B.10), indicating that our most stable configurations reasonably represent the structures of $Li_4Ti_5O_{12}$ and $Li_7Ti_5O_{12}$.

Figure 3.3A shows the formation energies of the $Li_5Ti_5O_{12}$ and $Li_6Ti_5O_{12}$ configurations using equation 1.3 referenced to $Li_4Ti_5O_{12}$ and $Li_7Ti_5O_{12}$, with configurations corresponding to the circled points shown in Figure 3.3B-I. The lowest-energy $Li_{4+x}Ti_5O_{12}$ ($x = 0, 1, 2$) are shown in Figure 3.3B-D. Configurations with large domains of only $Li_{(8a)}$ or $Li_{(16c)}$ are considered interfacial-like (orange triangles, e.g., Figure 3.3E,H), while those with large areas of mixed Li site occupancy are considered fully mixed solid solution configurations (blue circles, e.g., Figure 3.3F,I). Also considered solid-solution configurations are those with only 16c occupancy (Figure 3.3G), as they can be accessed by continuous removal of $Li_{(16c)}$ from $Li_7Ti_5O_{12}$ rather than the formation of $Li_4Ti_5O_{12}$ in $Li_7Ti_5O_{12}$. To visualize $Li_4Ti_5O_{12}$ and $Li_7Ti_5O_{12}$ phases in the configurations, domains are colored transparent purple (green) if only 8a (16c) are occupied to indicate the presence of the $Li_4Ti_5O_{12}$ ($Li_7Ti_5O_{12}$) phase. We highlight only the $Li_7Ti_5O_{12}$ ($Li_4Ti_5O_{12}$) phase in $Li_5Ti_5O_{12}$ ($Li_6Ti_5O_{12}$) configurations.

The investigation of $Li_5Ti_5O_{12}$ configurations below 100 meV/O_4 revealed that the most stable $Li_5Ti_5O_{12}$ configuration has a formation energy of -23 meV/O_4 and consists solely of separate domains of $Li_4Ti_5O_{12}$ and $Li_7Ti_5O_{12}$, even within the small supercell containing only 2 formula units of $Li_{4+x}Ti_5O_{12}$ (Figure 3.3C). The small but negative formation energy is consistent with previous computational results [176]. At $\sim$40 meV/O_4 above the $Li_4Ti_5O_{12}$-$Li_7Ti_5O_{12}$ tie-line, configurations in both the $Li_5Ti_5O_{12}$ and $Li_6Ti_5O_{12}$ compositions (Figure 3.3E and H) still display domains of $Li_4Ti_5O_{12}$ and $Li_7Ti_5O_{12}$. However, the smaller domain based on composition ($Li_7Ti_5O_{12}$ in $Li_5Ti_5O_{12}$ and $Li_4Ti_5O_{12}$ in $Li_6Ti_5O_{12}$) has expanded into the larger domain ($Li_4Ti_5O_{12}$ in $Li_5Ti_5O_{12}$ and $Li_7Ti_5O_{12}$ in $Li_6Ti_5O_{12}$), creating a region of intermixed $Li_4Ti_5O_{12}$ and $Li_7Ti_5O_{12}$, which we refer to as an interfacial solid solution (ISS). In the $Li_5Ti_5O_{12}$ composition, at $\sim$60 meV/O_4, we see a configuration in which the $Li_7Ti_5O_{12}$ domain disappears as the $Li_{(16c)}$ are distributed throughout the configuration, and we refer to this as a fully mixed solid solution (Figure 3.3F). In comparison, in the $Li_6Ti_5O_{12}$ composition, a delithiated rock salt-like solid solution phase with no $Li_{(8a)}$ (only 16c site occupied) appears at much lower energies ($\sim$20 meV/O_4) (Figure 3.3G). Of note is that in general, the number of face-sharing Li polyhedra in configurations with ISS regions is larger than that in the phase-separated configurations with sharp phase boundaries.

Surprisingly, even in the low-energy structures of $Li_{4+x}Ti_5O_{12}$, one of the $Li_{(8a)}$ tetrahedra shares a three-coordinated oxygen face with a $Li_{(16c)}$ octahedron at the domain boundary between $Li_4Ti_5O_{12}$ and $Li_7Ti_5O_{12}$ (Figure 3.3C–D). The face-sharing $Li_{(8a)}$ and $Li_{(16c)}$ polyhedra are highly distorted compared to the unperturbed $Li_{(8a)}$ and $Li_{(16c)}$ polyhedra in $Li_4Ti_5O_{12}$

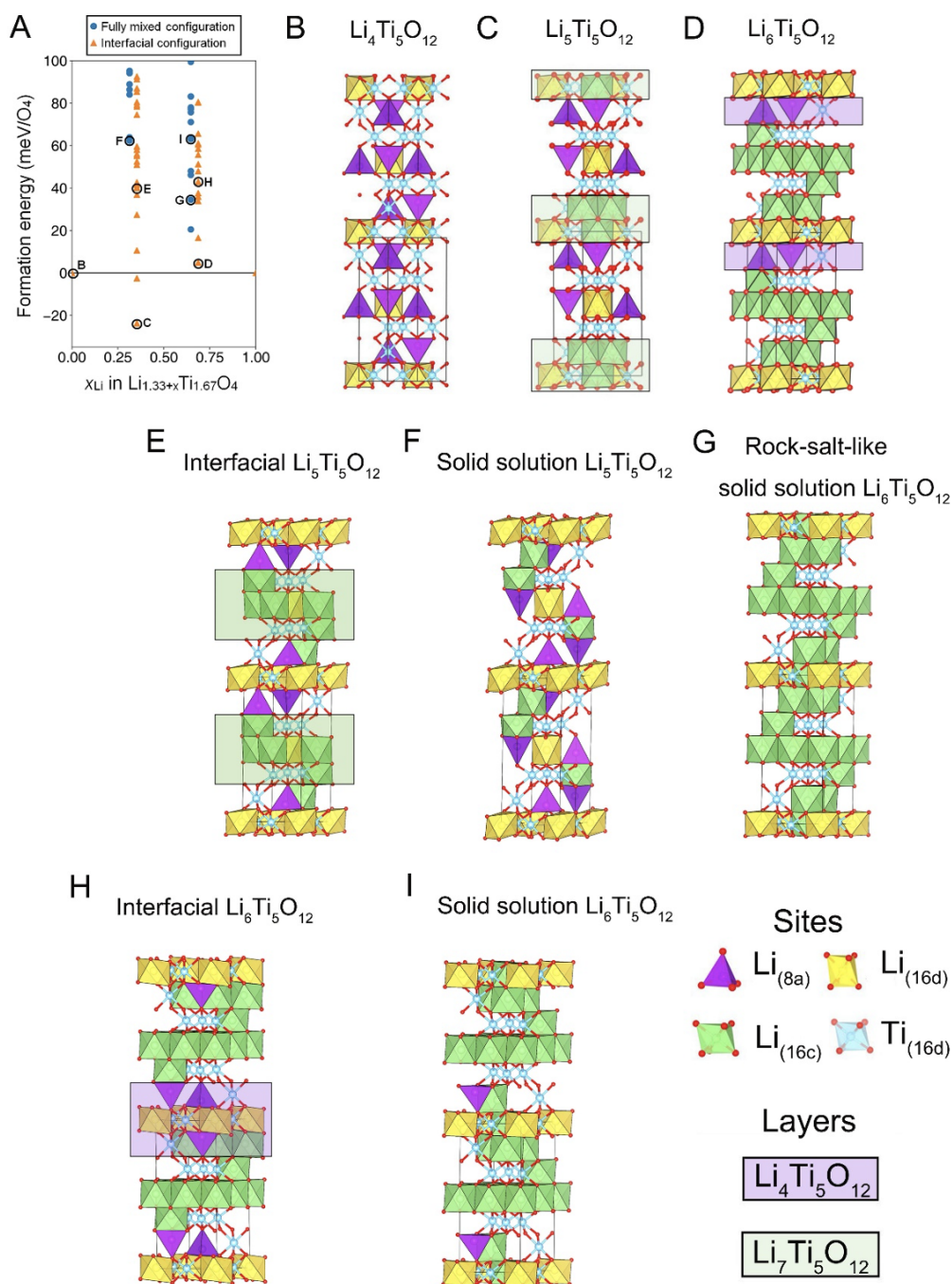Figure 3.3: **LTO convex hull and configurations** (A) Convex hull of $Li_4Ti_5O_{12}$-$Li_7Ti_5O_{12}$ system with labeled circles shown in (B)-(I). In (B)-(I), configurations have sites depicted by polyhedra surrounded by red oxygen and regions with either $Li_{(8a)}$, indicative of the $Li_4Ti_5O_{12}$ phase, or $Li_{(16c)}$, indicative of the $Li_7Ti_5O_{12}$ phase, depicted in transparent purple and green, respectively.

and $Li_7Ti_5O_{12}$ and are stabilized by neighboring $Li_{(16d)}$ octahedra (as described in Appendix B.7), which is consistent with recent DFT calculations [176]. Within 100 meV/O_4, a large number of relevant atomic configurations exist with different local environments, especially local motifs of $Li_{(8a)}/Li_{(16c)}$ face-sharing polyhedra with various levels of distortion (Figure B.11 in Appendix B.7). The DFT-based sampling of the $Li_{4+x}Ti_5O_{12}$ potential landscape in Figure 3.3 reveals that a very large configuration space can be accessed, even within formation energies of 100 meV/O_4, allowing the system to follow the most kinetically facile pathway (discussed further in Section 3.2.5).

3.2.3 Key local structure motifs from Li-EELS fingerprint

After establishing the structural models of $Li_{4+x}Ti_5O_{12}$ at different Li concentrations ($x = 0$, 1, 2, and 3), we calculated the corresponding Li-EELS spectra for Li at the 8a, 16c, and 16d sites for the most stable configurations of $Li_{4+x}Ti_5O_{12}$ using the $Z+1$ approach to model the core-hole effect. Because the pre-edge peaks originate predominantly from the intra-atomic Li $1s$ to $2p$ transition, this level of description is adequate. The good agreement in the near-edge region of the endmembers between the $Z+1$ method and the Bethe-Salpeter equation (BSE)-based method supports our choice of method (Figure B.4 in Appendix B.6). The energy positions of pre-peak S in the computed spectra and their relative intensities compared with those of the main peak for both $Li_4Ti_5O_{12}$ and $Li_7Ti_5O_{12}$ are in good agreement with the experimental results (Figure B.5A), validating the $Z+1$ method used for computing the Li-EELS spectra. The Li-EELS spectra of $Li_{(8a)}$ in the most stable $Li_5Ti_5O_{12}$ and $Li_6Ti_5O_{12}$ configurations are almost the same as those of $Li_{(8a)}$ in $Li_4Ti_5O_{12}$, especially near the pre-peak region (Figure 3.4A[3]).

However, a new pre-peak appears at ~58 eV in the EELS spectra of face-sharing $Li_{(16c)}$ that is absent in the computed spectra of $Li_{(16c)}$ in $Li_7Ti_5O_{12}$ and $Li_{(16d)}$ at any composition (Figure 3.4B, Figure B.5B-C, Figure B.8). Since this new pre-peak coincides in energy with pre-peak M observed in the operando EELS measurements (Figure 3.2B), we assign pre-peak M in the Li-EELS spectra at low rates to the inelastic scattering from distorted face-sharing $Li_{(16c)}$ in the metastable configurations. Due to the distortion of face-sharing $Li_{(16c)}$, several Li-O bonds are elongated, which breaks the degeneracy of Li-O coupling. A representative configuration is shown in Figure 3.4C demonstrating elongated Li-O bond lengths of 2.33-2.50 Å in $Li_5Ti_5O_{12}$, significantly longer than those in $Li_7Ti_5O_{12}$ (2.06-2.20 Å). The weakened Li-O bonds effectively pull the anti-bonding Li-O states to lower energy and cause the pre-peak to split, giving rise to pre-peak M in the EELS spectra. The corresponding partial charge densities are shown in the iso-surface plot in Figure 3.4C. While the partial charge density associated with pre-peak M concentrates more heavily on O atoms with longer Li-O bonds,

---

[3]Simulated electron energy-loss spectroscopy, charge density calculations, and distortion analysis performed by Prof. Donghwa Seo (School of Energy and Chemical Engineering, Ulsan National Institute of Science and Technology).
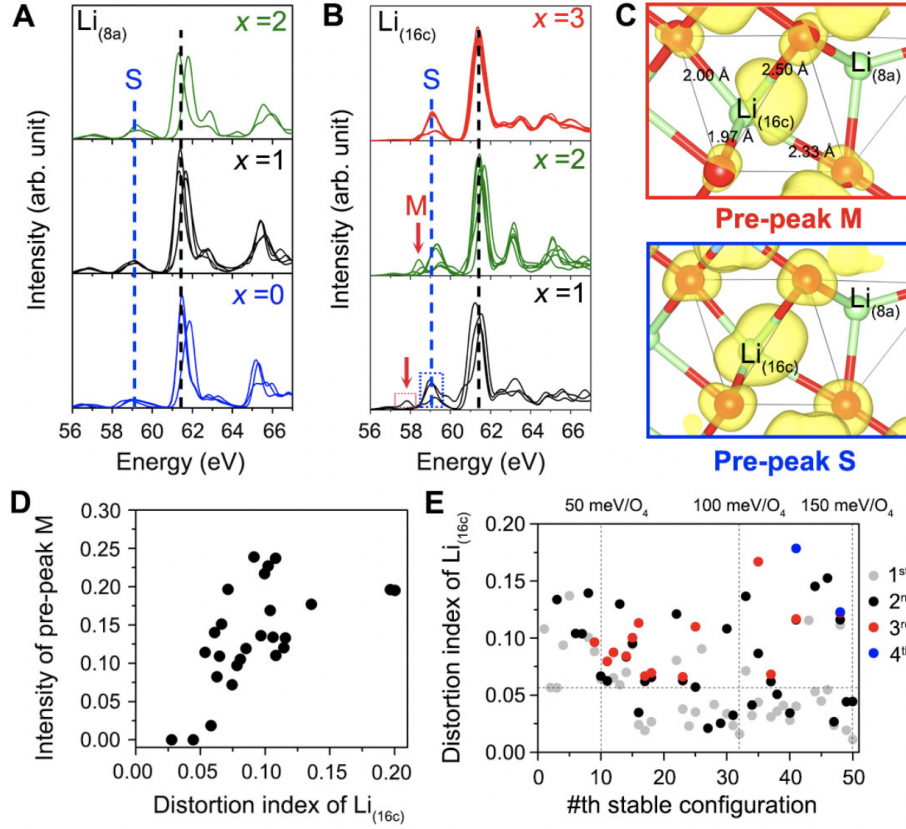
Figure 3.4: **Identification of Li-EELS fingerprints for Li-polyhedral configurations in $Li_{4+x}Ti_5O_{12}$ ($0 \leq x \leq 3$) by DFT calculations** (A, B) Calculated Li-EELS spectra of $Li_{4+x}Ti_5O_{12}$ ($x = 0$, 1, and 2) for Li at 8a sites, and $Li_{4+x}Ti_5O_{12}$ ($x = 1$, 2 and 3) for Li at 16c sites respectively. The black and blue dashed lines in (A and B) mark the energy positions of the main peaks and pre-peak S, respectively. The red arrows in (B) indicate the pre-peak M from face-sharing $Li_{(16c)}$ in $Li_5Ti_5O_{12}$ and $Li_6Ti_5O_{12}$ which is not observed for $Li_{(16c)}$ in $Li_7Ti_5O_{12}$. (C) Iso-surface of partial charge density around face-sharing $Li_{(16c)}$ in $Li_5Ti_5O_{12}$ within the energy range of pre-peak M and pre-peak S, as marked with dashed red and blue boxes respectively in (B), with iso-value of 0.05. Bond lengths between $Li_{(16c)}$ and O ions are labeled. (D) Intensity of the pre-peak M as a function of distortion index (d) of face-sharing $Li_{(16c)}$ for various Li configurations in $Li_5Ti_5O_{12}$ and $Li_6Ti_5O_{12}$. (E) d of face-sharing $Li_{(16c)}$ in the nth stable configuration of $Li_5Ti_5O_{12}$. The horizontal and vertical dashed lines indicate the approximate value of d above which pre-peak M appears and the formation energy of the nth stable configuration at 50, 100, and 150 meV/O_4. When a single configuration contains multiple face-sharing $Li_{(16c)}$, the different face-sharing $Li_{(16c)}$ are labeled as different colored points according to their d values in the ascending order: grey (first lowest distortion index), black (second), red (third), and blue (fourth).

the partial charge density of pre-peak S is distributed evenly on all O atoms regardless of Li-O bond lengths (see also the projected density of states in Figure B.7 in Appendix B.8).

To understand the effect of high (dis)charge rate on pre-peak M in the Li-EELS spectra (Figure 3.2E), the Li-EELS spectra of $Li_5Ti_5O_{12}$ and $Li_6Ti_5O_{12}$ configurations with higher formation energies (which are accessible at higher current rates or large overpotential) were also computed. Figure B.11 shows that the distortion of face-sharing $Li_{(16c)}$ and $Li_{(8a)}$ polyhedra is affected by the presence of neighboring $Li_{(16d)}$ or $Ti_{(16d)}$. The varying local environment results in different intensities and energy levels of pre-peak M (Appendix B.8). Face-sharing $Li_{(16c)}$ and $Li_{(8a)}$ polyhedra in various $Li_{4+x}Ti_5O_{12}$ with distortion index (d; see Eq. B.1 in Appendix B.8) larger than ~ 0.06 result in the appearance of pre-peak M, whose intensity rapidly increases with d (Figure 3.4D, Figure B.12, and Appendix B.8). Such high distortion levels reduce the effective coordination number of $Li_{(16c)}$ and $Li_{(8a)}$. Based on the coordination number weighting scheme of [183], $Li_{(16c)}$ and $Li_{(8a)}$ with $d \sim 0.06$ are found to be under-coordinated with effective coordination numbers of 4.7 and 3.6 (Figure B.13 in Appendix B.8), respectively, rather than the expected 6 and 4. Similar trends showing a more pronounced pre-peak with under-coordinated local environments are well established in transition-metal K-edge x-ray absorption near-edge structures.[184] As observed in Figure 3.4E and Figure B.14 in Appendix B.8, highly distorted face-sharing $Li_{(16c)}$ and $Li_{(8a)}$ polyhedra with d higher than 0.06 appear more frequently as the formation energy of the intermediate $Li_5Ti_5O_{12}$ and $Li_6Ti_5O_{12}$ increases. This is consistent with the presence of more face-sharing $Li_{(16c)}$ and $Li_{(8a)}$ polyhedra in $Li_5Ti_5O_{12}$ configurations with higher formation energies, as indicated by the points with different colors in Figure 3.4E. Note that highly distorted face-sharing $Li_{(8a)}$ tetrahedra are observed much less often than highly distorted $Li_{(16c)}$ octahedra in configurations with formation energy less than 100 meV/O_4 (Figure 3.4E, Figure B.14). Non-face-sharing Li polyhedra, on the other hand, generally tend not to be highly distorted ($d > 0.06$) except for some $Li_{(16c)}$ in $Li_5Ti_5O_{12}$ in configurations with formation energy above 100 meV/O_4 (Figure B.15 in Appendix B.8). Therefore, the appearance of pre-peak M is mainly attributed to face-sharing $Li_{(16c)}$ octahedra at low current rates but to both face-sharing $Li_{(16c)}$ and $Li_{(8a)}$ polyhedra at high current rates.

3.2.4   Kinetic pathways and energetics of Li-ion migration

A structural transformation through a solid-solution path is favorable for high-rate performance.[73, 169] However, the macroscopic solid-solution is found to be largely inaccessible in LTO due to the associated high formation energy (Figure 3.3). Instead, (de)lithiation proceeds via a two-phase reaction, involving face-sharing $Li_{(8a)}$-$Li_{(16c)}$ local motifs at the nano-sized $Li_4Ti_5O_{12}/Li_7Ti_5O_{12}$ phase boundaries[176, 177]. Our results are generally consistent with the two-phase model[176, 177], as we observed mainly interfacial-type configurations at lower energy (see Appendices 3.2.2 and 3.2.5). However, our results further reveal a large variety of face-sharing $Li_{(8a)}$-$Li_{(16c)}$ local motifs in the intermediate $Li_{4+x}Ti_5O_{12}$ configurations. These local motifs, whose number and distortion index display rate dependence, may
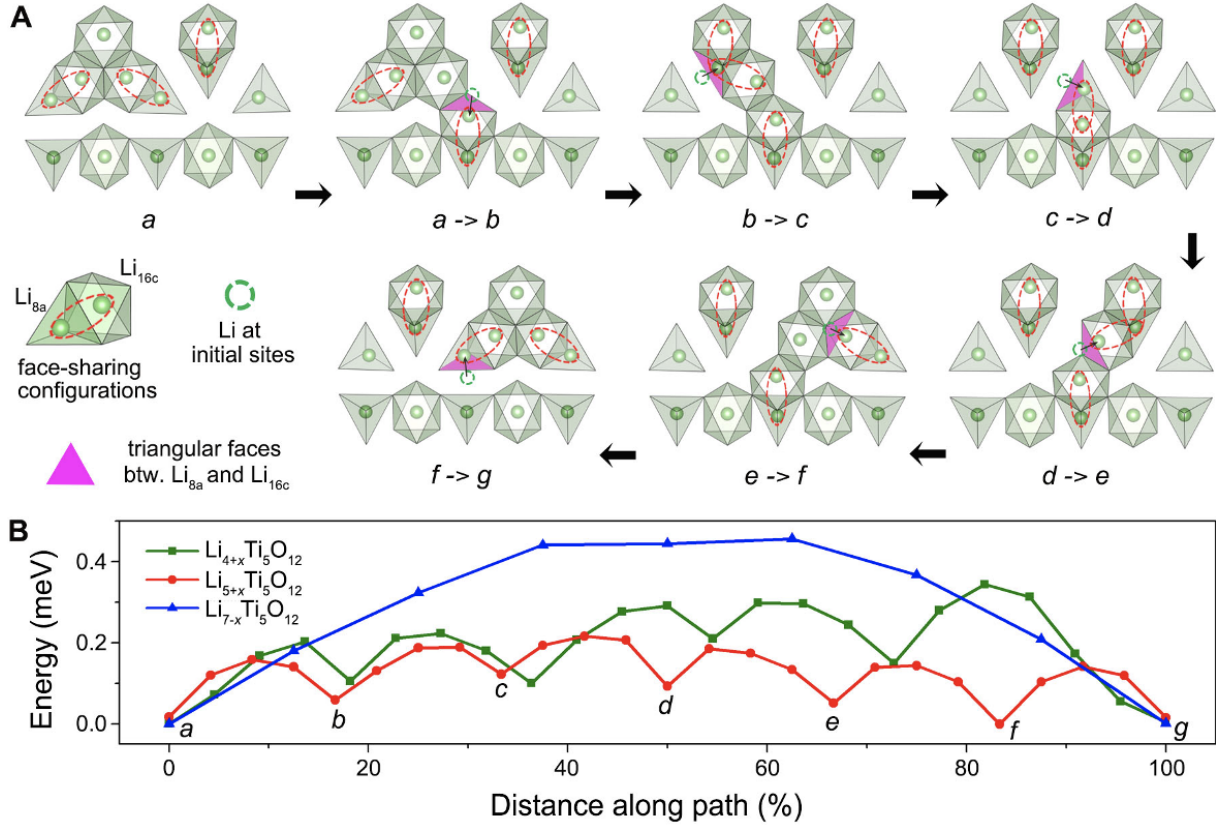
Figure 3.5: **Li-ion migration pathways and energy profiles in the intermediates** (A) Migration pathways involved for each step, from a to g, in one representative intermediate, $Li_{5+x}Ti_5O_{12}$. The translucent green spots mark the initial Li sites during each sub-step of migration. The black arrows indicate the migration direction of each sub-step. The three-coordinated oxygen face through which the Li^+ migrates from a Li_{8a} tetrahedron to a Li_{16c} octahedron is colored purple. The Li-ion migration pathways in $Li_{4+x}Ti_5O_{12}$ and $Li_{7-x}Ti_5O_{12}$ are provided in Figure B.16 and B.17 in Appendix B.9. (B) Energy profile of the pathways in $Li_{4+x}Ti_5O_{12}$ (green), $Li_{5+x}Ti_5O_{12}$ (red), and $Li_{7-x}Ti_5O_{12}$ (blue) as a function of distance along the paths.

strongly affect the kinetics in intermediate compositions.

To obtain a mechanistic understanding of fast Li diffusion in LTO, we performed nudged-elastic band [118, 119] calculations that account for distorted face-sharing Li polyhedra (Figure 3.5 and Figures B.16 and B.17 in Appendix B.9). The activation energies of Li^+ migration in $Li_4Ti_5O_{12}$ and $Li_5Ti_5O_{12}$ (with an interstitial Li^+) and Li7Ti5O12 (with a vacancy) are $\sim$343, $\sim$216, and $\sim$455 meV, respectively (Figure 3.5B). The low activation energy of $Li_5Ti_5O_{12}$ is in line with the low migration barriers previously obtained from NMR measurements[174] and ab initio molecular dynamics[176]. In general, the Li diffusion

44

pathway involves Li hopping from face-sharing tetrahedral (octahedral) Li sites to octahedral (tetrahedral) Li sites (Figure 3.5A, Figure B.16B–H in Appendix B.9). Along this path, while face-sharing Li^+ ions change position, the number of face-sharing Li^+ (3-4) remains nearly constant in the $Li_4Ti_5O_{12}$ (always 2) and $Li_5Ti_5O_{12}$ (from 3 to 4 to 3) pathways. As a result, there is no abrupt increase of the energy of the system. In the higher energy pathway in $Li_7Ti_5O_{12}$, however, the number of face-sharing Li^+-ions changes drastically from 0 to 2 and back to 0 (Figure B.17B-D in Appendix B.9). Clearly, the low migration barrier for Li^+ in LTO system can be attributed to two important factors.

- The number of face-sharing Li polyhedra is smaller in the transition state (when the migrating Li^+ is in the triangular face in Figure 3.5A) than in the initial and final states within each step (e.g., there are three instances of face-sharing in states a and b but only two between a and b in Figure 3.5A). The reduction in Li^+–Li^+ repulsion in the transition state can lower the activation barrier.

- Because local distortion helps to reduce the effective coordination number of Li^+ (Figure B.13), the change in Li^+ coordination is minimized during Li^+ migration through the three-coordinated oxygen face, further lowering the activation barrier [46].

Both factors minimize changes in the energy and thus result in a relatively flat energy landscape, as described in Figure 3.5B. Our analysis implies that the improved kinetics at high rates results from the increased amount of face-sharing Li^+, and thus mobile carriers, and the more highly distorted Li^+ polyhedra seen in the high energy $Li_{4+x}Ti_5O_{12}$ configurations accessible at high rates.

3.2.5 Phase transformation in $Li_{4+x}Ti_5O_{12}$

Although the fully solid-solution phase does exist within a formation energy of 100 meV/O_4, the majority of the configurations are phase-separated with a sharp phase boundary or contain interfacial solid-solution-like (ISS) regions, especially at low formation energies (Figure 3.3A). For example, solid solution configurations do not appear until $\sim$60 meV/O_4 in $Li_5Ti_5O_{12}$ and until $\sim$20 meV/O_4 in $Li_6Ti_5O_{12}$. This is in stark contrast to the well-known LFP system, in which metastable solid-solution structures are only $\sim$0-10 meV/$Li_xTi_{1.67}O_4$ above the two-phase tie-line and can appear at small overpotentials of 20 mV [73]. This difference is likely in part due to the vastly different interfacial energies and kinetic barriers for nucleation and growth. LFP possesses a larger interfacial energy (0.06 eV/A^2) [185] than that of LTO (0.02 eV/A^2) [186]. Considering only the difference in the interfacial energy, the critical nucleation barrier of LFP is 27 time larger than that of LTO, based on the equation $\Delta G = 16\pi \cdot \gamma^3 \cdot v^2 / 3(|\Phi| - \Delta g_s)$ [73], where ΔG is the critical nucleation barrier, γ is the interfacial energy, v is the molar volume, Φ is the applied overpotential, and Δg_s is the coherent strain energy. In addition, LFP has a high coherent strain energy at the boundaries (0.033 eV/Li) [73], but LTO has much lower energy penalties than LFP to form phase boundaries
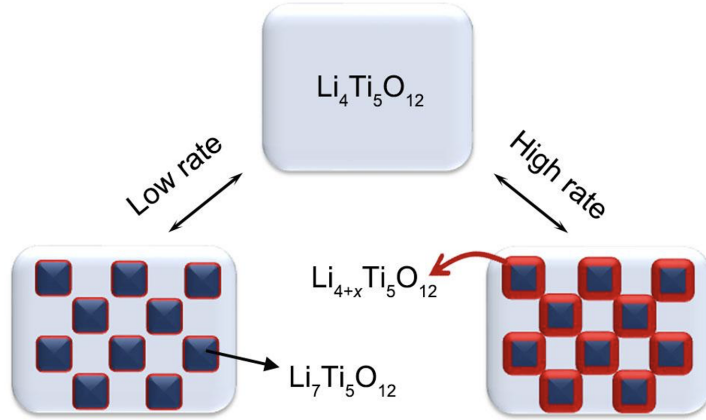
Figure 3.6: Schematic illustration of the rate dependence of the phase boundaries (red color) during the transformation from $Li_4Ti_5O_{12}$ to $Li_7Ti_5O_{12}$, changing from a sharp phase boundary at low rates (left) to a thick interfacial solid solution (ISS).

because of the "zero strain" property [186]. All these features make the two-phase reaction thermodynamically accessible in LTO. It is likely that, in line with observations in the literature [177], the numerous two-phase configurations and configurations containing ISS regions between nano-sized domains of LTO and $Li_7Ti_5O_{12}$ appear during charge/discharge rather than the fully solid-solution configuration seen in LFP under non-equilibrium condition. Therefore, the number of face-sharing Li polyhedra in a sample will be determined by the interfacial area between the nano-sized $Li_4Ti_5O_{12}$ and $Li_7Ti_5O_{12}$ domains in the particle.

Based on the DFT calculations that show a large number of interfacial configurations with increasing interfacial thickness (Figure 3.3) and polyhedral distortion at increasing formation energies (Figure 3.4E and Figure B.14 in Appendix B.8), we speculate an ISS that emerges and can grow in thickness at high rates (Figure 3.6) rather than a strict two-phase system with sharp phase boundaries or a true solid solution system. This model is in line with the domain model of Ganapathy, *et al.* [176], who propose that the $Li_{4+x}Ti_5O_{12}$ system consists of nano-sized $Li_4Ti_5O_{12}$ (with $Li_{(8a)}$) and $Li_7Ti_5O_{12}$ (with $Li_{(16c)}$) domains that are separated by sharp phase boundaries at low rates. However, compared to a sharp phase boundary, the existence of the ISS, which contains a larger number of face-sharing motifs and more highly distorted polyhedra (associated with higher I_M intensity), is more consistent with the observation of large intensity ratios of I_M/I_S in Li-EELS spectra at high rates. To emphasize this point, we show a comparison in Figure B.6 in Appendix B.6 of the computational EELS spectra of $Li_{(16c)}$ from the most stable $Li_5Ti_5O_{12}$ (representative of sharp phase boundaries between $Li_{(8a)}$ and $Li_{(16c)}$ domains) and a $Li_5Ti_5O_{12}$ configuration at higher energy (by 0.102 eV/O_4) with more strongly distorted $Li_{(8a)}$. The I_M/I_S ratios of $Li_{(16c)}$ are 0.30 (most stable $Li_5Ti_5O_{12}$) and 1.48 (metastable $Li_5Ti_5O_{12}$), while the I_M/I_S ratios of the corresponding $Li_{(8a)}$ are 0 and 1.15, respectively. These results suggest that

46

highly distorted Li polyhedra seen in the ISS are responsible for the higher I_M/I_S ratio observed in the EELS measurements. Thus, we build on the well-supported domain model proposed by Ganapathy, *et al.* [176] by suggesting the rate-dependent ISS, which reconciles our experimental observations with the domain model.

In this study, face-sharing Li polyhedral motifs with different local distortion were identified as a key feature at high rate by directly probing the Li site occupancy with operando Li-EELS and identifying the relevant motifs with simulated Li-EELS. These features, which may not be as readily observable by NMR spectroscopy, neutron diffraction, or other techniques[174, 187], were shown to have low activation energy of Li migration. The low migration barrier of the face-sharing motifs appearing in intermediate $Li_{4+x}Ti_5O_{12}$ configurations along with the low interfacial energy of the endmembers reconciles the apparent contradiction between the high-rate capability of LTO and the poor Li-ion conductivity of its endmember phases.

Chapter 4

Adding disorder to lithium manganese oxide spinels toward improved Li cathodes

In the previous chapters, we investigated how intercalation can occur in the 8a sites of spinel from B_2O_4 to AB_2O_4 through the case of Mg in $Mg_xCr_2O_4$ and through the 8a-to-16c transition from AB_2O_4 to $A_2B_2O_4$ through the case of Li in $Li_4Ti_5O_{12}$. In this chapter, we return to the spinel $LiMn_2O_4$ system first discovered in 1983, which is particularly appealing as a cheaper high energy density Li-ion cathode. Compared to the previous spinel systems investigated, spinel $LiMn_2O_4$ can in theory be intercalated from the empty spinel framework Mn_2O_4 to the fully lithiated $Li_2Mn_2O_4$. In practice however, the system undergoes collective Jahn-Teller distortion of the Mn^{3+} [9], resulting in particle cracking and severely limited cyclability.[75] It also results in a symmetry change from cubic to tetragonal (along the direction of Jahn-Teller distortion [6]) that is generally associated with a first-order transition [188], limiting the kinetics of lithiation compared to that through a solid-solution mechanism. One way to mitigate these issues is avoiding or reducing the two-phase region between $LiMn_2O_4$ and $Li_2Mn_2O_4$ by lithiating at least partially through a solid-solution pathway. In this chapter, we demonstrate that it is possible to reduce and even completely remove this two-phase region by imposing disorder between the transition metal-occupied 16d sites (B in AB_2O_4) and the unoccupied octahedral 16c sites, which the working ion fills in the fully lithiated spinel (A in $A_2B_2O_4$).

4.1 Introduction

Given the expected multi-fold increase in demand for Li-ion batteries [5], it is vital to design alternative cathodes that are less expensive and more earth-abundant than the Co and Ni needed for current layered Li-ion cathodes. The only $3d$ transition metals (TM) that generate a reasonable voltage and are produced in large enough quantities to support a multi-TWh annual production of Li-ion batteries are Cr, Mn, and Fe. The recently developed class of Li-excess cation-disordered rock salt materials (DRX) can activate any of these metals as redox centers and has generated several high-energy density cathodes.[11, 12, 189] Reasonable transport is achieved in these materials through the addition of Li-excess (i.e., greater than one Li per two anions), which creates percolating 0-TM channels with low Li migration barriers.[14–18] But the lack of any long-range cation order in these materials creates a highly sloping voltage profile, and a wide voltage window is required to achieve their maximal energy density. Hence, it would be advantageous to combine the benefits of cation-disordered materials (compositional flexibility [13, 18], low volume change [190, 191], no phase transitions, high capacity, capability to fluorinate [103, 192]) with the less-sloped voltage profile of ordered materials, by creating materials with states of order that are intermediate between well-ordered cathodes and fully cation-disordered DRX compounds.

Spinel $LiMn_2O_4$ is a promising compound to implement this strategy due to its good inherent properties: excellent rate capability, use of earth-abundant Mn, and the excellent thermal stability of Mn^{4+} in the charged state.[6, 74, 193, 194] While its theoretical capacity is 285 mAh g^{-1}, in commercial use its Li cycling has been restricted to the 4 V range from Mn_2O_4 to $LiMn_2O_4$ which provides only about half the theoretical capacity. The re-

maining capacity cannot be accessed because cycling the additional Li between $LiMn_2O_4$ and $Li_2Mn_2O_4$ occurs at 3 V through a strong two-phase reaction.[6] Such first order transitions proceed with a strong compositional inhomogeneity in cathode particles leading to large stresses and concomitant capacity degradation.[75] Guided by the general concept that disorder can disrupt the Li/vacancy orderings, and thus reduce the strength, of two-phase reactions, recent experiments on heavily ball-milled cation-excess Li-Mn-O-F spinels confirm that disorder indeed removes the 3 V plateau and leads to a high rate, high energy density cathode material.[195, 196] In this chapter, we model the complex structural arrangements that occur when a spinel is forced to undergo 16c/16d site disorder (where the 16d TM are disordered onto the 16c sites) and investigate its electrochemical voltage profile and lithiation behavior. We demonstrate that even with modest amounts of disorder the solid solution region of spinel can be extended, leading to a much smaller two-phase region. At larger levels of disorder, the two-phase region can be fully transformed into a solid-solution regime, consistent with experiments, pointing at cathode materials that can combine very high rate with very high capacity.

4.2   Methods

4.2.1   Building a cluster expansion to the relevant system

The ordered $LiMn_2O_4$ spinel system has face-centered cubic oxygen packing, in which Li can occupy the tetrahedral (tet) 8a or octahedral (oct) 16c sites, and Mn occupies the oct 16d sites.[6, 9] When Mn is allowed to disorder over the oct 16c and 16d sites, other tet sites (8b and 48f) that are inaccessible in the ordered spinel due to their face-sharing with Mn-occupied 16d sites become open to Li occupation. To investigate the large configurational space of the system, we build a CE with Li^+-Mn^{2+}-Mn^{3+}-Mn^{4+}-Ti^{4+}-Vacancy (Va) as allowed species on the oct sites (16c and 16d Wyckoff sites in the spinel, 4a in rock salt) and Li^+-Mn^{2+}-Mn^{3+}-Va on the tet sites (8a, 8b, and 48f Wyckoff sites in the spinel, 8c in rock salt) of a primitive cell of rock salt and its interstitial tetrahedral sites. Mn^{4+} is not allowed on the tet site as its d^3 configuration results in strong octahedral preference.[4] There is no anion disorder, as all anions are O^{2-}. We also investigate the effects of Ti substitution, as it is a non-redox active TM used in DRX systems to help stabilize the structure.[197]

The cluster expansion (CE) implemented here models the configurational energetics of a system as described in Section 1.3.2 and is used for rapid energy evaluations in Monte Carlo (MC) calculations at finite-temperature.[98–101] An additional term is included to capture long-range electrostatic interactions.[103, 104]

We fit the cluster expansion to the total energies of structures relaxed in first-principles density functional theory (DFT) [85, 86]. Due to its ability to better predict ground states,[94, 198] we perform these DFT calculations using the meta-GGA functional SCAN [92] as implemented in the Vienna ab initio simulation package (VASP) [87] with the project-

augmented wave (PAW) and plane-wave basis set.[88, 89] For structural calculations, we use a plane-wave cutoff of 520 eV and reciprocal space discretization of 25 k-points per Å, and converge to 10^{-6} eV in total energy and 0.02 eV/Å on atomic forces. To help convert relaxed structures to their relevant occupancy string, we use methods described in Yang, *et al.* [110] to obtain optimal $Mn^{2+}/Mn^{3+}/Mn^{4+}$ magnetization cut-offs for charge assignment of Mn (Li, Ti, and O are assumed to be in 1^+, 4^+, and 2^- charge states) and map highly relaxed atomic positions to the relevant lattice sites.

The initial training set for the CE consists of charge-balanced structures from MC-CE searches for ionic configurations with low electrostatic (Ewald) energy. The search is performed in all supercells (varying in shape and size) up to 4 oxygen and simple supercells (varying only in size) up to 24 oxygen. The initial training set is supplemented by Li-Mn-Ti-O-containing structures scraped from an internal database. With a CE trained on the initial data set, we perform the typical iterative approach of fitting, adding further MC-sampled structures, and re-fitting to converge to the final CE.[199] The final converged CE is fit as proposed in [110]: we fit the zeroth basis function (J_0) to the average energy of the training set; to explicitly handle the dimension reduction associated with the charge-neutrality constraint of ionic systems, the point basis functions are fit with lasso regression to the residuals of the zeroth term regression; and, we fit higher order terms to the residuals of predictions using the zeroth and point term fits with l_1-norm regularized regression and selecting the regularization parameter that minimizes the 5-fold cross-validation (CV) error.[108]

To handle the complexity of the system and make the problem better numerically conditioned, we include several additional procedures. We weigh structures by their energy above the hull (i.e., $\exp(-E^{hull}/k_BT)$ with T = 2000K) and by whether the structures contain Li in both octahedral and tetrahedral sites. The weighing improves the fit for low-energy structures and structures with both oct and tet Li, which we expect to see in the disordered spinel space. Additionally, CE are truncated to make the problem tractable. In our truncation, we exclude quadruplet clusters, as the inclusion of so many higher-order terms often worsened the fit. Instead, we include only pair clusters truncated to 7.0Å and triplet clusters to 4.1Å based on a rock salt lattice with a cubic lattice parameter $a = 3.0$Å. Finally, to ensure that the fitting problem is better conditioned [200], we only use the clusters in the feature matrix whose submatrix is full rank. These are the geometric clusters for which the number of unique, symmetrized decorations on the cluster in the training set is equal to the number of the random set of configurations of that cluster on the lattice.[110]

4.2.2 Performing Monte Carlo simulations

We perform sgc MC simulations in a $4 \times 3 \times 3$ supercell of the spinel $Li_2Mn_4O_8$ primitive (a 288-oxygen supercell) at a simulation temperature of 300K. The Li chemical potential is scanned by sweeping from μ_{Li} = -8.5 to μ_{Li} = -3.7 in intervals of 50 meV to sample Li-Va orderings over the cation sites within the Mn-disordered framework. Perturbations for the Metropolis algorithm are "multi-flips", consisting of a pair of flips between Li^+ and Va and

between Mn oxidation states, chosen with the following algorithm to ensure charge balance.

1. Choose either a $(Li^+ + Mn^{2+} \leftrightarrow Va + Mn^{3+})$-type perturbation or a $(Li^+ + Mn^{3+} \leftrightarrow Va + Mn^{4+})$-type perturbation. An $(A_1 + B_1 \leftrightarrow A_2 + B_2)$-type perturbation implies a perturbation of A_1 to/from A_2 and a perturbation of B_1 to/from B_2.

2. Choose two sites randomly.

3. If the identities of the species on the sites match one side of the perturbation type, the perturbation is flipping each species on the matching side to the species on the opposite side of the reaction. For sites with species matching A_1 and B_1, the perturbation is setting the occupation variable of the site with A_1 to A_2 and setting that of the site with B_1 to B_2.

4. Else, discard the perturbation, and go to (1).

At each Li chemical potential, we perform 800k perturbations for equilibration and 800k perturbations for sampling. For sampling perturbations, step (4) returns no perturbation in order to ensure detailed balance in the MC sampling.

We obtain topotactic voltage curves from the sgc MC simulations by converting between $\mu_{Li}(x_{Li})$ and $V(x_{Li})$ using the relation in equation 1.1.[96] The voltage is referenced to that of bcc Li metal. While the CE training set uses the standard Li pseudopotential for its lower computational costs, additional semi-core electrons in the Li_sv pseudopotential are necessary to properly model metallic bcc Li. The use of the Li_sv pseudopotential rather than the Li pseudopotential for the ground states in a simple spinel $LiMn_2O_4$ voltage profile causes minimal change, as seen in Figure C.1 in Appendix C.1. Thus, we use the Li_sv pseudopotential only for the energy of bcc Li to obtain a spinel voltage profile with the ~ 3 V plateau at the appropriate voltage.

Because there tends to be significant hysteresis around the phase transition between $LiMn_2O_4$ and $Li_2Mn_2O_4$, we determine the equilibrium voltage and compositions at that transition through free energy integration. This involves integrating upward in temperature at $x_{Li} = 0.0$ ($x_{Li} = 1.0$) then in increasing (decreasing) μ_{Li}, and taking the lower envelope of the grand potential, as described in Section 1.3.2 and [113, 114].

We also perform canonical MC of the disordered spinels in the same 288-oxygen supercell at varying composition. To simulate Li-excess and Ti-doping, we explore the systems where Li is added to 16c octahedral sites and where Mn^{4+} is substituted for Ti^{4+} in spinel $LiMn_2O_4$. The canonical simulations consist of temperature scans from 100 to 3100K in steps of 100K. At each temperature, we perform 500k equilibration perturbations and 500k sampling perturbations, where each perturbation in the Metropolis algorithm is a swap of the occupation variables between two chosen sites. To isolate the temperature at which 16c/16d TM disordering occurs, we suppress inversion – another type of disorder seen in spinels [201–203] –

by only allowing TM redistribution over oct sites and Li and Va distribution over both tet and oct sites.

We build the CE and perform MC calculations using the statistical mechanics on lattices (smol) package, which is a publicly released package available on Github at `https://github.com/CederGroupHub/smol`.

4.3 Results

4.3.1 Evaluating the cluster expansion

The CE, fit to a final training set of $\sim$1100 energies of structures, has 180 non-zero ECI, an RMSE of 70 meV/prim (35 meV/site), and a 5-fold CV error of 84 meV/prim (42 meV/site). The errors seen in this high-component system are consistent with those seen in [110]. In addition to evaluating the traditional RMSE and CV error, we compare the performance of the CE with the DFT training data for a set of physically relevant properties.

To ensure that the CE reproduces most of the DFT ground states, we compare the DFT (top) and CE-predicted (bottom) Li_2O-MnO-Mn_2O-TiO_2 phase diagrams in Figure 4.1a. Ground states (green) in DFT that are not reproduced by the CE are circled in red. New ground states introduced by the CE, but that do not appear in the DFT phase diagram are circled in blue. The CE misses only the $Li_4Ti_5O_{12}$ phase (a defected spinel with Li substitution on the 16d sites) due to the stabilization of $Li_2MnTi_3O_8$, which is another defected spinel (with Li and Mn on the 8a sites and Li and Ti on the 16d sites). The CE also predicts a few new ground states that are not in the DFT phase diagram, including spinel $LiMn_2O_4$, a rock salt-like $LiMn_2O_3$, and a rock salt-like $TiMn_2O_4$. Thus, while the CE does a relatively reasonable job of finding most of the ground states, it tends to overstabilize some additional Mn-containing spinels and (partially delithiated) rock salts that are not ground states in the DFT phase diagram.

To ensure the CE describes well the transition of Li occupancy from the tet 8a to the oct 16c sites in spinel, we also build a simple 0K voltage curve for topotactic lithiation in spinel $Li_xMn_2O_4$ using well-known Li-Va orderings, and compare the CE-predicted 0K voltage curve with that from DFT (Figure 4.1b). The well-known orderings include the fully delithiated Mn_2O_4, the half-lithiated spinel $Li_{0.5}Mn_2O_4$, the spinel $LiMn_2O_4$, and the fully lithiated $Li_2Mn_2O_4$ (shown in in-sets), with the average voltage between adjacent orderings calculated as in [96, 204]. While the DFT voltage curve has a plateau at $\sim$2.8 V that is comparable with that in experiments, the voltage drop to $\sim$2.8 V at $LiMn_2O_4$ is approximately $\sim$0.5 V smaller than in experiments.[6, 9, 74] Furthermore, the voltage drop at $Li_{0.5}Mn_2O_4$ is much larger ($\sim$0.5 V) than in experiments ($\sim$0.1 V). The discrepancies with experiment appear to be caused by self-interaction errors of Mn in SCAN, which also occur in GGA and are usually rectified using the Hubbard U correction (GGA+U).[205] Indeed, as seen in Figure C.2, DFT with GGA+U with a U-value of 3.9 correctly produces the wider voltage jump at
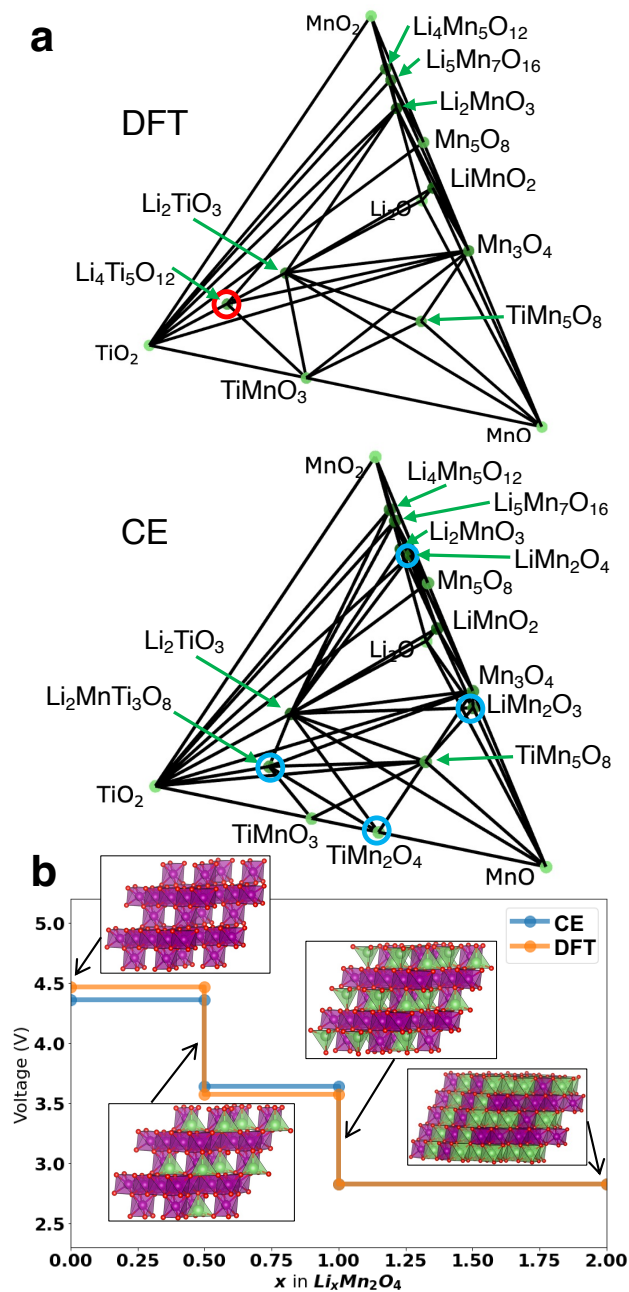
Figure 4.1: **Evaluation of CE-predicted phase diagram and LiMn₂O₄ voltage curve**
(a) Phase diagrams of the Li₂O, MnO, MnO₂, TiO₂ system in DFT vs. predicted by CE.
Ground states (green) in DFT that are not reproduced by the CE are circled in red, while
new CE ground states that do not appear in the DFT phase diagram are circled in blue.
(b) DFT voltage curve vs. CE-predicted 0K voltage curve of spinel LiMn₂O₄ using selected
ground states, shown in in-sets.

~2.8 V of >1 V and the smaller jump at $Li_{0.5}Mn_2O_4$ of ~0.1 V.[206, 207] SCAN+U using the same U-value also reproduces voltage drops with the correct heights, but the average voltage appears ~1 V too high. This indicates that, contrary to some previous works [208] and despite SCAN's ability to obtain correct ground states, DFT-SCAN may still require properly calibrated U-corrections to accurately reproduce voltage curves for some systems.

The CE appears to predict the DFT 0K voltage curve of spinel relatively well, especially the ~3 V plateau. However, the plateau between the half-8a-filled spinel $Li_{0.5}Mn_2O_4$ and spinel $LiMn_2O_4$ appears ~0.1 V lower while the plateau between $Li_{0.5}Mn_2O_4$ and Mn_2O_4 is ~0.1 V higher than in the DFT voltage curve. This indicates that the CE predicts the $Li_{0.5}Mn_2O_4$ ground state to be slightly less stable relative to adjacent ground states compared to the DFT. Because the average CE and DFT voltages between delithiated Mn_2O_4 and spinel $LiMn_2O_4$ appear similar (~4.1 V), the relative energies of these two phases are consistent between DFT and the CE, and only the half-8a-filled $Li_{0.5}Mn_2O_4$ spinel is understabilized while all remaining phases are predicted well.

4.3.2 Exploring the 16c/16d disordered spinel space

In this work, we aim to model configurations in the PDS space. As PDS is generally considered to be disordered rock salt with spinel-like order, the extremes of the space are the ordered spinel and the fully disordered rock salt. Disorder of the 16d Mn onto the 16c sites (16c/16d disorder) is one way to traverse the space between the ordered ($d = 0$) and disordered ($d = 0.5$) extremes. Thus, we use the level of Mn 16c/16d disorder as a handle between the ordered spinel and disordered rock salt.

Furthermore, Mn disorder over the 16c and 16d sites is also of interest because it can potentially remove the two-phase region of the ordered spinel. A two-phase region can be removed by raising the energies of the stable phases (in this case spinel $LiMn_2O_4$ and lithiated spinel $Li_2Mn_2O_4$). 16c/16d disorder can increase the energy of the spinel phase because Mn occupation on 16c sites raises the site energies of Li in the face-sharing 8a sites due to electrostatic repulsion. A two-phase region can also be removed by lowering the energies of the solid-solution phases. 16c/16d disorder can result in Li occupancy of non-Mn-occupied 16d sites, which has been shown to lower the energy of face-sharing environments seen in solid-solution configurations in spinel $Li_4Ti_5O_{12}$, as seen in Chapter 3.[176, 209]

Thus, because it spans the PDS configurational space and can potentially remove the two-phase region of spinel, we investigate the effects of the level of Mn 16c/16d disorder on the voltage profile of the model system $LiMn_2O_4$. We generate Mn disorder over the 16c and 16d sites by starting from ordered $LiMn_2O_4$ spinel and swapping randomly chosen Mn on the 16d sites of the ordered spinel to randomly selected 16c sites, as in [210]. The amount of disorder, d, indicates the proportion of Mn swapped from 16d sites to 16c sites. In the $LiMn_2O_4$ system, d is also equivalent to the 16c Mn occupancy and varies from $d = 0$ – equivalent to the ordered system with 1.0 Mn occupancy in 16d sites and 0.0 Mn occupancy

in 16c sites – to $d = 0.5$ – equivalent to the fully disordered system with 0.5 Mn occupancy of 16d sites and 0.5 Mn occupancy of 16c sites.

4.3.3   Modeling the electrochemical effects of disorder

Based on the hypothesis that 16c/16d disorder can remove the two-phase region between spinel and lithiated spinel, we expect to see similar effects on the associated $\sim$3 V plateau in the voltage profile. To confirm this, we investigate the effects of disorder on the voltage curve by performing μ_{Li} scans in semi-grand canonical (sgc) Monte Carlo (MC) to simulate topotactic (de)lithiation at 300K within frameworks with varying Mn 16c/16d disorder. Figure 4.2 shows the calculated voltage profiles from sgc MC simulations of the disordered
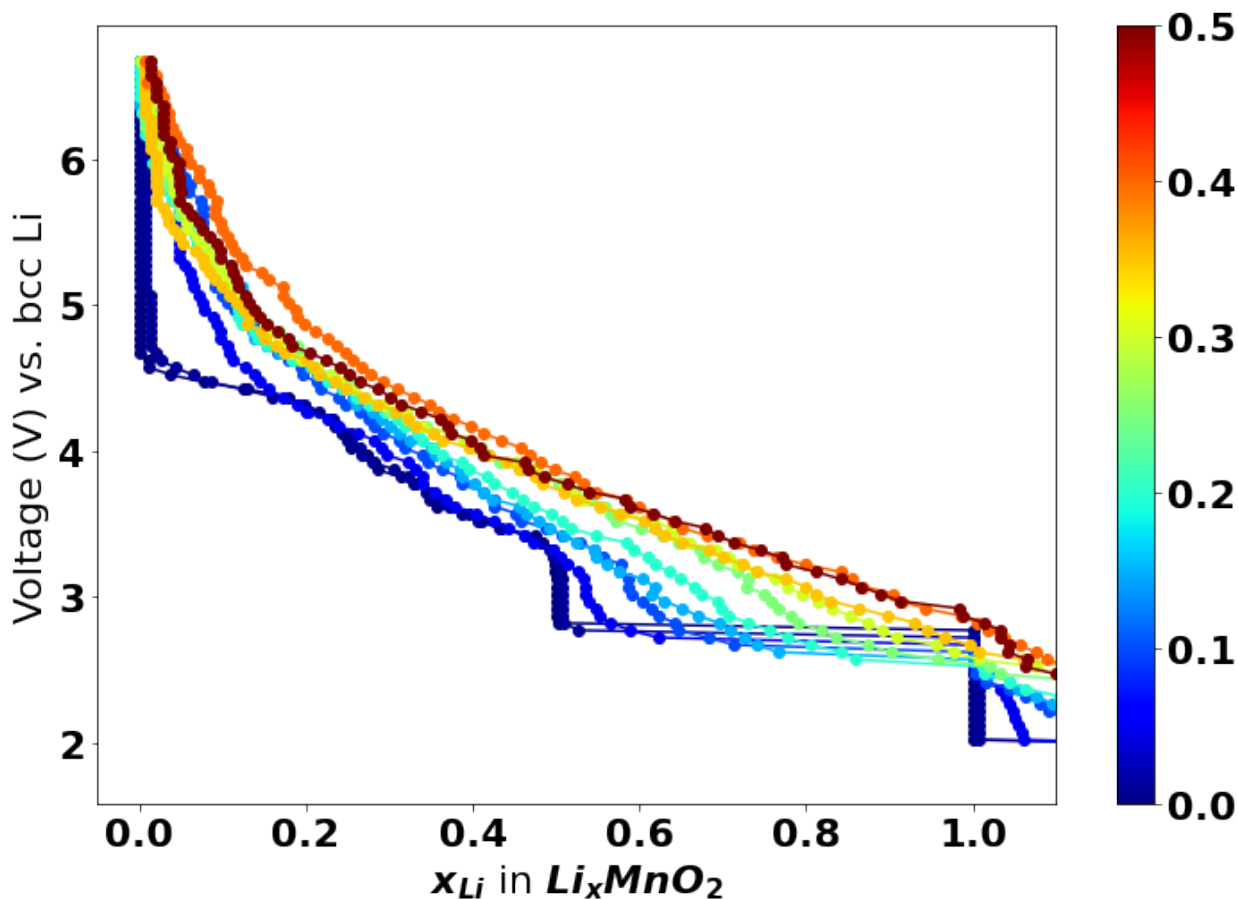

Figure 4.2: **Simulated disordered spinel LiMn$_2$O$_4$ voltage curves** sgc MC-simulated voltage curves of spinel LiMn$_2$O$_4$ with varying amounts of Mn disordered from the 16d site onto the 16c sites from $d = 0.0$ (ordered spinel, shown in dark blue) to $d = 0.5$ (fully disordered spinel, shown in dark red).

spinels, with increasing 16c/16d disorder visualized through color gradation from blue to red.

The dark blue curve shows the voltage profile of the ordered spinel phase, which includes the characteristic spinel plateaus at $\sim$3 V and $\sim$4.3 V. As the Mn disorder over the 16c/16d sites (d, defined as the amount of Mn on the 16c sites) increases, the $\sim$3 V plateau shortens starting from $d = 0.05$ and completely disappears when $d = 0.25$. The shortened $\sim$3 V plateau is a result of increased solubility on the $x_{\text{Li}} = 0.5$ side. The system also reaches higher voltages at dilute limits of Li, with the calculated voltage to extract the final Li (and oxidize the final Mn^{3+}) increasing from $\sim$4.5 V in the ordered spinel to $\sim$6 V in the highly disordered spinel. Overall, while disorder can shorten and even eliminate the $\sim$3 V voltage plateau, it also appears to result in Li and/or Mn in extreme environments that require voltages ($>$5V) above the stability range of most electrolytes to delithiate or oxidize.

In actuality, oxygen will generally begin to oxidize before ($\sim$4.5V) the Mn^{3+} that are in extreme environments, resulting in lower experimental voltages at dilute Li content.[17, 196, 211] Because the O^- anion is not explicitly included in the CE, the sgc MC calculations do not simulate the effects of oxygen oxidation. To account for the oxygen oxidation, we perform DFT-SCAN calculations of structures sampled from sgc MC simulations in O_{60} supercells. For each level of 16c/16d disorder, we obtain the set of lowest-energy structures at each μ_{Li} as well as 5 randomly sampled Li-Va configurations at μ_{Li} corresponding to $x_{\text{Li}} = 0.1, 0.2,$ and 0.3. The estimated voltage curve is then obtained by taking the convex hulls at each level of disorder and calculating the average voltages between configurations adjacent in x_{Li} using equation 1.2.[95, 96]

The DFT-SCAN-estimated voltage curve with oxygen oxidation (blue) is compared alongside the sgc MC simulated voltage curve in O_{60}-supercell without explicit oxygen oxidation treatment (orange) for the Mn framework with $d = 0.1$ in Figure 4.3. The curves for other levels of disorder are shown in Figure C.3. The sgc MC-simulated voltage curve indicates that $\sim$6 V is needed to delithiate to very dilute x_{Li}. In contrast, the DFT-SCAN-estimated voltage curve shows a maximum voltage of 5.2 V. In the low x_{Li} configurations that constitute the DFT-SCAN voltage curve, oxygen oxidation is observable through the increase in magnetic moment on the O and magnetic moments on the Mn indicative of remaining Mn^{3+} even at full delithiation. Thus, the DFT-SCAN calculations appear to properly treat the oxygen oxidation, resulting in less extreme voltages at low x_{Li}. Furthermore, most Li ($>$ 90%) can be extracted by 4.7-4.8 V, consistent with experiments on the partially disordered spinel.[195, 196]
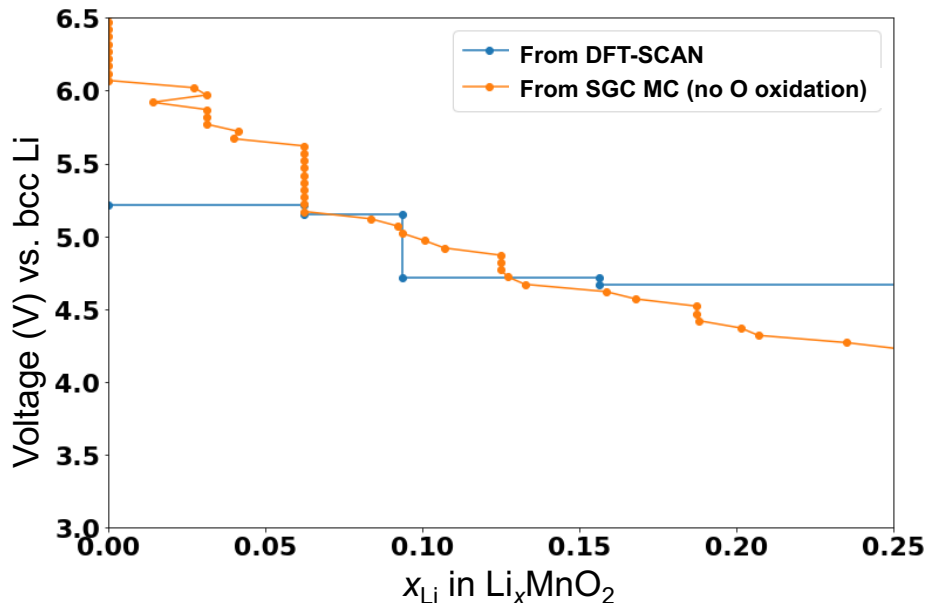
Figure 4.3: **Effect of oxygen oxidation on voltage curve** Comparison between voltage curve simulated using sgc MC in O_{60} supercell (orange) and DFT-SCAN-calculated average voltages from sgc MC sample configurations at disorder $d = 0.1$.

4.4 Discussion

4.4.1 Rationalizing the removal of the two-phase region by 16c/16d disorder

In this work, we demonstrated that partial disorder of Mn over both the 16c and 16d sites in $LiMn_2O_4$ spinel reduces the width of the two-phase region between $LiMn_2O_4$ and $Li_2Mn_2O_4$, shortening the associated voltage plateau. At a critical level of $d = 0.25$, the plateau fully disappears. We hypothesized that the mechanism by which 16c/16d disorder may remove the two-phase region is raising the energy of the spinel phase and lowering the energies of the solid-solution configurations at intermediate Li composition. Using the CE and MC simulations, we confirm our hypothesis and obtain additional mechanistic understanding by sampling the configurations observed along the phase transition.

To confirm that the energies of the spinel and lithiated spinel increase with the addition of 16c/16d disorder, we evaluate the configurational energies of 100 partially disordered $LiMn_2O_4$ and $Li_2Mn_2O_4$ using the CE. For a given partially disordered Mn arrangement, the Li configurations of the $LiMn_2O_4$ are generated by filling any non-face-sharing tetrahedral sites, before non-face-sharing octahedral sites are occupied. If additional Li are required to maintain the $LiMn_2O_4$ stoichiometry, they fill minimally face-sharing empty sites. The Li
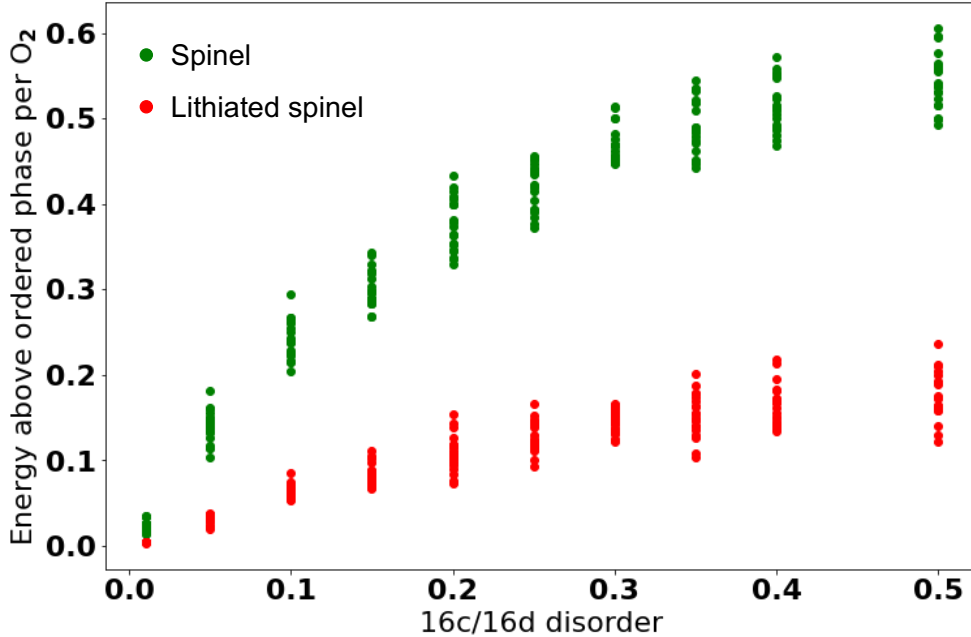
Figure 4.4: **Energies of disordering spinel LiMn$_2$O$_4$ and Li$_2$Mn$_2$O$_4$** CE-calculated energies associated with disordering an increasing number of 16d Mn in spinel LiMn$_2$O$_4$ (red) and lithiated spinel Li$_2$Mn$_2$O$_4$ (blue) onto the 16c sites. Energies are calculated with respect to the ordered spinel (for the disordered spinels) and the ordered lithiated spinel (for the disordered lithiated spinels).

configurations of the Li$_2$Mn$_2$O$_4$ are generated by filling the unoccupied oct sites. The CE-evaluated disordered spinel (green) and disordered lithiated spinel (red) energies are shown with respect to the ordered spinel and lithiated spinel in Figure 4.4. Both spinel and lithiated spinel energies increase with disorder and level out around disorder levels of $d = 0.35$. The spinel energy increases more than twice as much with disorder compared to the lithiated spinel due to the decrease in tet Li in LiMn$_2$O$_4$ with disorder (see Figure C.4). Thus Figure 4.4 confirms that the endmember phases of the two-phase region in ordered spinel become less stable with disorder, but the effect is more pronounced on the LiMn$_2$O$_4$ side of the two-phase region.

To investigate how disorder stabilizes solid-solution configurations relative to the spinel and lithiated spinel, we analyze the configurations sampled by the MC within the x_{Li} range of the two-phase region to understand how (de)lithiation occurs in the disordered spinel compared to the ordered spinel. Figure 4.5 shows the concentration of tet and oct Li environments (a,b) and tet environments categorized by the presence of any face-sharing nearest neighbor cations (c,d) in the ordered ($d = 0.0$) system and a disordered ($d = 0.1$) system. The concentration of tet-occupied and oct-occupied Li are shown in green and red in Figures
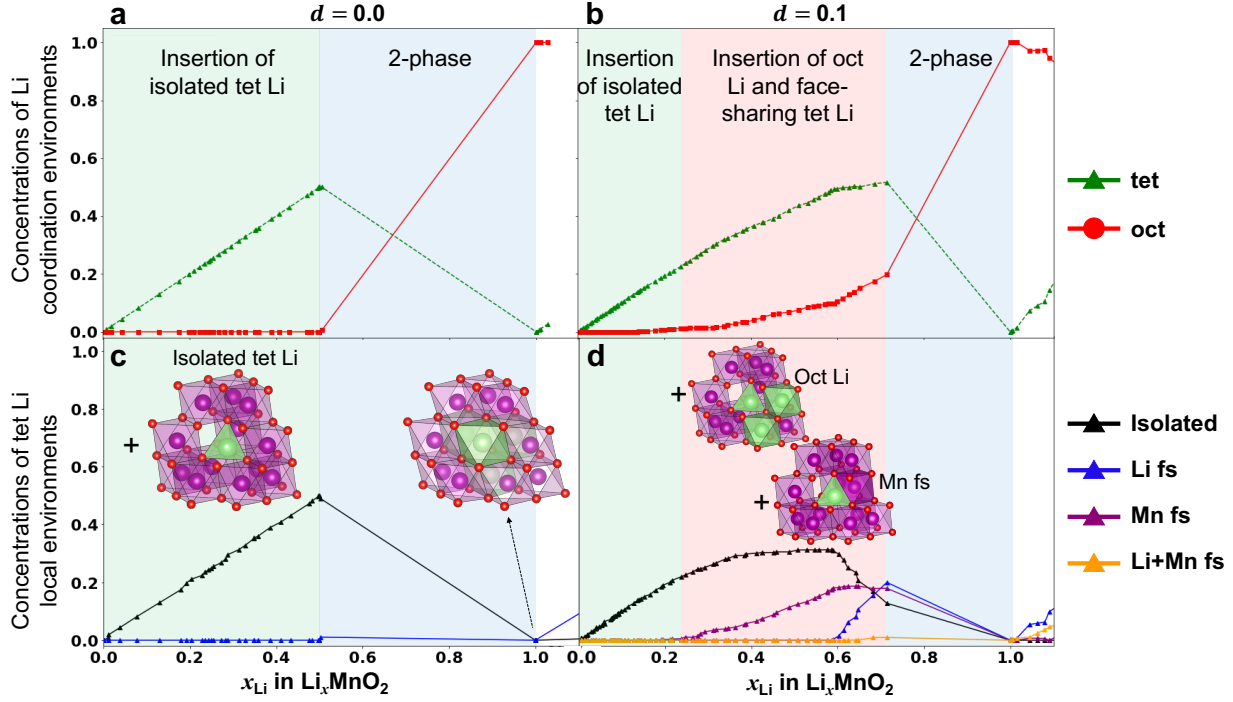
Figure 4.5: **Local environments in simulated disordered LiMn$_2$O$_4$** Averaged concentrations (per O$_2$) of Li in tet (green triangles) and oct (red circles) coordination environments for the ordered spinel with $d = 0.0$ (a) and the slightly disordered spinel with $d = 0.1$ (b); and averaged concentrations of tet Li categorized by the species in their face-sharing nearest neighbor oct sites, including isolated with no face-sharing (black triangles), face-sharing with Li (blue), face-sharing with Mn (purple), and face-sharing with both Li and Mn (orange) in the ordered spinel (c) and the slightly disordered spinel (d). Lithiation is split into regimes based the type of environment Li is inserted, beginning with the insertion of isolated tet Li (transparent green), followed by the insertion of oct Li and face-sharing tet Li (transparent red), and ending in a two-phase region between a spinel-like phase and the lithiated spinel (in which all Li occupy the non-Mn-occupied oct sites). In-sets show examples of local Li environments, such as isolated tet Li inserted during the green regime of lithiation in (a,c), the fully lithiated spinel's oct Li in (a,c), and oct Li and face-sharing tet Li inserted during the red regime in (b,d).

4.5a and b, and the isolated (non-face-sharing) tet Li, Li-face-shared tet Li, Mn-face-shared tet Li, and both Li- and Mn-face-shared tet Li are shown in black, blue, purple, and orange, respectively, in Figures 4.5c and d.

The results in Figures 4.5a and 4.5c demonstrate that in the ordered system ($d = 0.0$), Li is inserted into isolated tet sites (8a sites, left in-set in Figure 4.5c) until they are fully occupied (transparent green regime). The sudden jump in x_{Li} indicates a phase transition

60

(transparent blue regime) along with the shift from tet to oct occupancy (right in-set in Figure 4.5c). Lithiation in the disordered system ($d = 0.1$) initially proceeds as in the ordered system, with the insertion of isolated tet Li. From $\sim x_{Li} = 0.2$ to $\sim x_{Li} = 0.6$, Li begins to occupy oct sites (left in-set in Figure 4.5d) – as evidenced by the rise in oct Li concentration (red in Figure 4.5b) – and Mn-face-sharing tet sites (right in-set in Figure 4.5d) – as evidenced by the rise in the tet Li with Mn-face-sharing environments (purple in Figure 4.5d). Besides a flattening of the isolated tet occupancy, no particular behavior characterizes the typical $Li_{0.5}MnO_2$ spinel stoichiometry even for this moderate level of disorder. Instead, further lithiation until $\sim x_{Li} = 0.7$ involves Li occupying Li-face-sharing tet sites (blue in Figure 4.5d). The regime involving more complex solid-solution insertion of Li into oct sites and face-sharing tet sites is highlighted in transparent red. The two-phase region in the $d = 0.1$ disordered spinel appears between $\sim x_{Li} = 0.7$ and $x_{Li} = 1.0$.

At intermediate Li content, face-sharing tet sites and oct sites in the disordered system are not accessible in the ordered spinel but are energetically competitive enough to appear in the disordered system. This is in line with a previous study showing a decrease in the energy associated with adding face-sharing Li to spinel-like configurations when 16c/16d disorder is present. While only doubly face-sharing oct environments are available in the ordered spinel, the disordered system contains oct environments with only one face-sharing contact; thus the energy required for Li insertion into oct sites in the disordered system is lower than in the ordered system.[210] The additional occupation of the face-sharing tet sites and oct sites allows solid-solution insertion of additional Li past the spinel composition ($x_{Li} = 0.5$) to $\sim x_{Li} = 0.7$. Because the lithiated spinel ($x_{Li} = 1.0$) is still a stable phase, possibly because disorder raises the $LiMnO_2$ energy to a lesser degree than it does $Li_{0.5}MnO_2$ (as shown in Figure 4.4), the length of the overall two-phase region and the associated voltage plateau is shortened from 0.5 Li/MnO_2 to 0.3 Li/MnO_2.

From the configurational energies of the disordered spinel and lithiated spinel (Figure 4.4) and the configurations sampled from MC (Figure 4.5), we find that disorder reduces the two-phase region by destabilizing the spinel and lithiated spinel phases and stabilizing solid-solution configurations. These two effects can be clearly observed in Figure 4.6a which shows the MC-averaged energies for the ordered and partially disordered ($d = 0.1$) systems. Whereas for the ordered spinel the energy of sampled solid solution configurations (dashed blue) turns concavely downwards for $x_{Li} > 0.5$ due to the high energy of creating face-sharing cation interstitials in the ordered spinel, the partially disordered material allows for significantly more solid solubility past $x_{Li} = 0.5$. Between $x_{Li} = 0.5$ and $x_{Li} = 0.7$ these solid-solution configurations are stabilized by disorder compared to the lowest-CE energies of solid-solution configurations sampled in the ordered phase (dashed blue) (see Appendix C.5 for sampling details). A second, more general effect, already highlighted in Figure 4.4 is the general energy increase of the $LiMn_2O_4$ and $Li_2Mn_2O_4$ compositions (connected by dashed maroon) which are raised with respect to the intermediate solid solution compositions. The net effect of these changes in the energy of the system is a shortened two-phase region in the partially disordered systems (dotted maroon), which is also raised with respect to the

two-phase region of the ordered phase (dotted blue).

Disorder also widens the site energy distributions of both the tetrahedral and octahedral sites. In addition to stabilizing some octahedral environments for Li insertion [210], disorder also destabilizes some 8a sites via electrostatic interaction with Mn on the 16c sites. The widening of the site energy distributions can be observed in Figure 4.6b, which shows the distribution of CE energies (relative to the empty Mn framework) associated with inserting a Li into each vacant site in the $d = 0.0$ ordered (top) and $d = 0.1$ disordered (bottom) empty Mn frameworks. It is clear that disorder at dilute x_{Li} causes wider site energy distributions and thus an increasing possibility of overlapping distributions. The closer energetic competition between tet and oct sites then facilitates a more gradual insertion and removal of Li between the two types of sites, indicative of solid-solution behavior, compared to the abrupt 8a-to-16c transition in the ordered system.
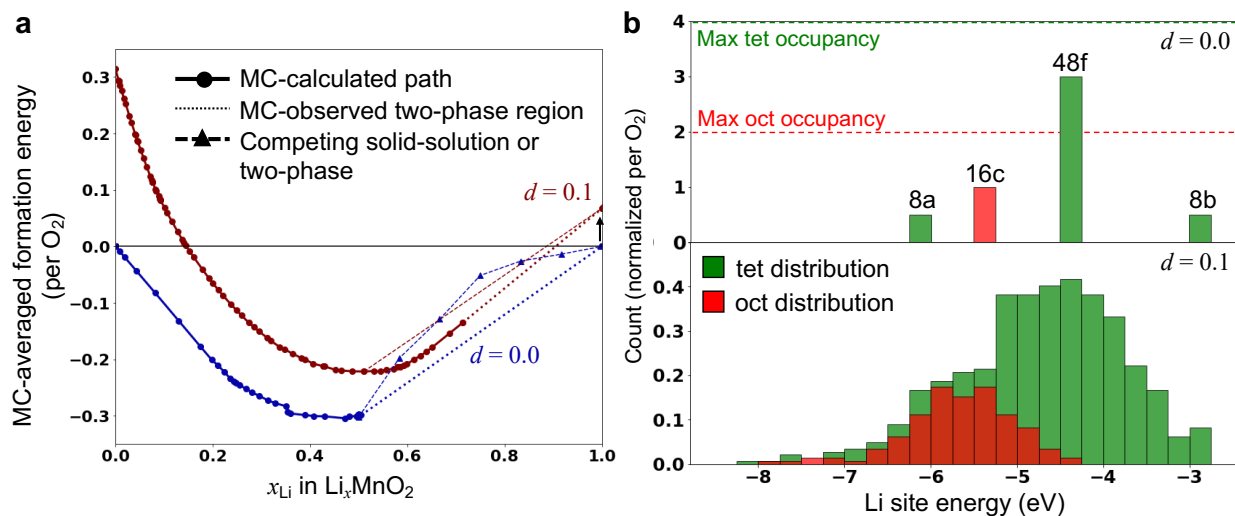
Figure 4.6: **Formation energies and Li site energies in ordered vs. disordered LiMn$_2$O$_4$** a) Averaged formation energies of sampled configurations from sgc MC for the $d = 0.0$ ordered spinel (blue) and the $d = 0.1$ disordered spinel (maroon), with two-phase regions observed by the MC displayed as dotted lines. The dashed maroon line connects the disordered LiMn$_2$O$_4$ and disordered Li$_2$Mn$_2$O$_4$ phases while the dashed blue line signifies the solid-solution pathway in the ordered system. b) Distributions (normalized per O$_2$ cell) of the CE energies associated with inserting a single Li in each vacant tet (green) and oct (red) site in the $d = 0.0$ ordered spinel (top) and $d = 0.1$ disordered spinel (bottom). The site energies in the ordered spinel are labeled by their Wyckoff site, and the maximum level of tetrahedral and octahedral occupancy are delineated by green and red dashed lines.

4.4.2   Pathways to induce and better control disorder in PDS

From our simulations, disordering 16d Mn onto the 16c sites of spinel shortens the ~3 V plateau by increasing solubility of Li in $Li_{0.5}MnO_2$, achieving solid-solution behavior at $d = 0.25$. However, because the energy of spinel $LiMn_2O_4$ increases with disorder (Figure 4.4 and Figure 4.6a), 16c/16d disorder may be difficult to produce experimentally. Potential paths to facilitate disorder include 1) adding d^0 elements, which are more flexible in their coordination environments and thus can better accommodate distortions [197], and 2) synthesizing at off-stoichiometry compositions, as the stability of the 16d ordering at $LiMn_2O_4$ is associated with Li tet occupancy. Because the 16d ordering enables 8a ordering, at which non-face- and edge-sharing tet Li are equidistant to other Li, adding Li-excess that disturbs the 8a ordering may reduce the stability of 16d TM ordering.

To confirm whether these compositional changes can facilitate spinel disordering, we perform canonical MC heating to investigate at what temperature the 16d TM ordering is broken with 1) the substitution of Ti^{4+} for Mn^{4+} and 2) the addition of Li-excess to the 16c sites of spinel $LiMn_2O_4$. We substitute only up to 0.2 Ti per O_2 because Ti does not provide any redox, and we explore Li-excess levels at the same cation to anion ratios as synthesized in PDS in previous experimental work [195]. Figure 4.7 shows the averages of sampled 16c (teal) and 16d (red) TM occupancies as the Ti-substituted (left column) and Li-excess (right column) systems are heated up to 3000K. The shaded extension signifies the standard deviation of the sampled occupancies. Dashed black lines indicate the temperature at which the average 16c TM occupancy $\langle x_{16c}^{TM} \rangle$ exceeds 0.2, and the dashed green line indicates the same for the ordered, non-substituted $LiMn_2O_4$ (TM occupancies for spinel $LiMn_2O_4$ shown in Figure C.5 in Appendix C.4).

Substituting an increasing amount of Ti (from 0.05 to 0.1 to 0.2 Ti per O_2) results in small decreases in the temperature at which the 16d TM ordering is disrupted. This is reflected in the decrease in the temperature at which $\langle x_{16c}^{TM} \rangle > 0.2$ from 2300K to 2000K to 1900K. In the Li-excess systems, we see a more significant decrease in disordering temperature, with the temperatures at which $\langle x_{16c}^{TM} \rangle$ exceeds 0.2 decreasing from 2200K to 1600K to 600K with $x_{Li}=1.07$, $x_{Li}=1.28$, and $x_{Li}=1.60$. Based on the canonical MC heating simulations, we suggest that both the substitution of Ti (up to 0.2 Ti/O_2) and Li-excess can decrease the annealing temperature at which 16c/16d disordering occurs. In particular, Li-excess seems to have a stronger effect compared to Ti substitution, indicating that a deviation from the spinel structure (with the addition of Li 16c) is more critical to reducing the 16c/16d disordering temperature than a deviation in the TM chemistry.

Of note is that we do not consider the possibility of Li-Mn inversion (i.e., Mn disordering onto the tet sites) in this simulation to focus on the direct effects of Ti-substitution and Li-excess on breaking the 16d ordering. Because inversion removes TM from the oct sites, the 16c and 16d TM occupancies at elevated temperatures may differ from those seen here, especially if inversion occurs before the 16c/16d disordering temperature. However, we suspect that inversion may become less likely as the cation:anion ratios deviate further from
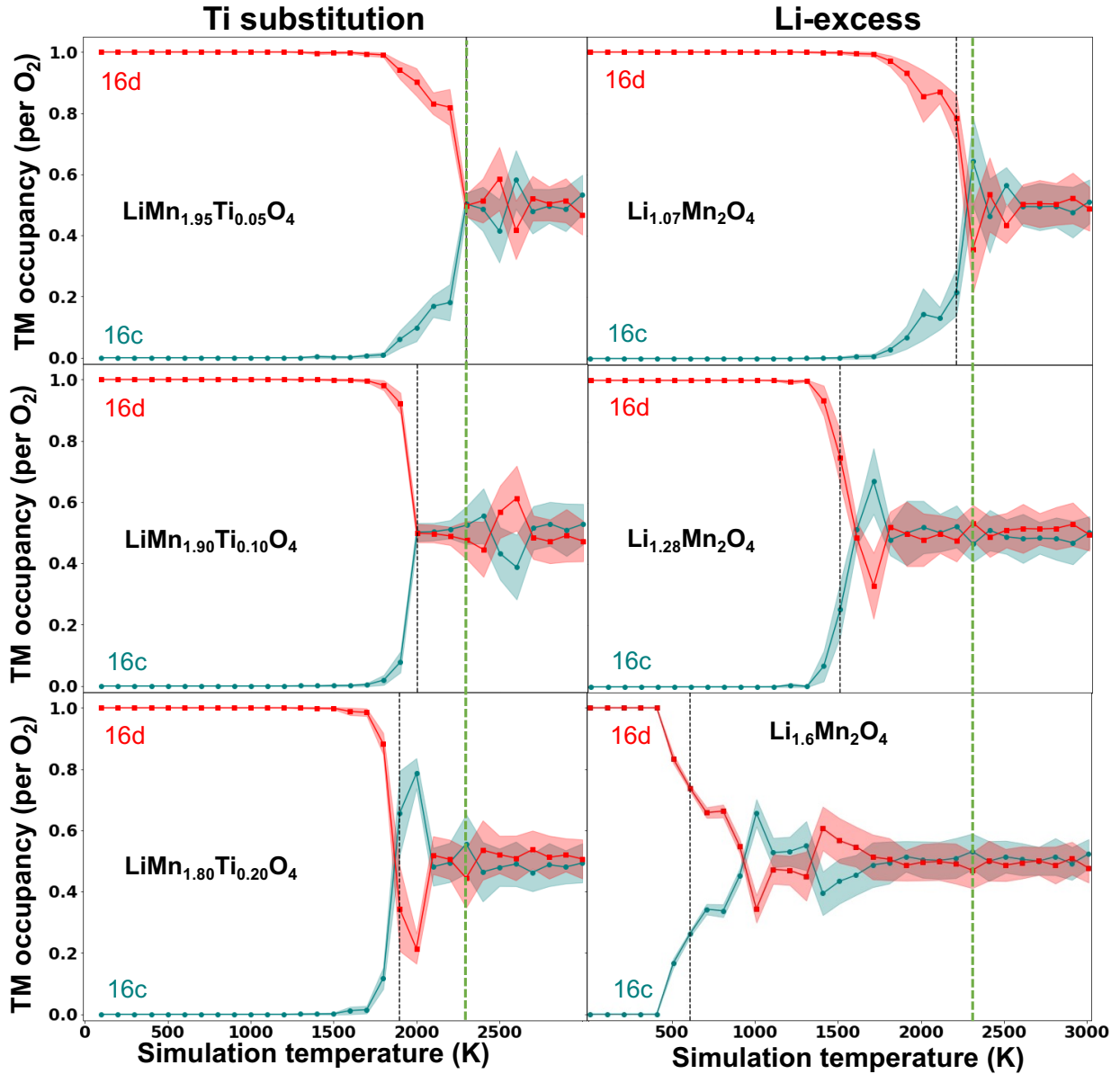
Figure 4.7: **TM-occupancies at increasing temperature with varying Li-excess and Ti-substitution** Average of sampled concentrations of TM-occupied 16d (teal) and 16c (red) sites during canonical MC heating of spinels with 0.05, 0.1, and 0.2 Ti^{4+} substituted for Mn^{4+} (left column) and 0.07, 0.28, and 0.60 Li-excess added to 16c sites (right column). Shaded regions indicate the standard deviation of the TM occupation concentrations sampled at each given temperature. Dashed black lines indicate the first temperature at which the TM occupancy of 16c sites exceeds $\langle x_{16c}^{TM} \rangle = 0.2$, while the dashed green line indicates the same for ordered $LiMn_2O_4$.

64

that of spinel (3:4) because there are fewer unoccupied, non-face-sharing tet sites onto which Mn can invert.

The exceedingly high temperatures required to disturb TM 16d ordering simulated here (>2000K) are reflected in the fact that PDS has, to this point, been mainly achieved by high-energy ball-milling.[195, 196] While high-energy ball-milling can transfer energies and achieve disordered configurations similar to those simulated at extremely elevated temperatures (up to 2500K based on previous work [103, 107]), it is not a scalable synthesis method for industry. Because the Li-excess and Ti^{4+}-substitution suggested here decrease the 16c/16d disordering temperature, we expect that these compositional adjustments should also make synthesis of PDS more facile, for example by lowering the required time for or speed of ball-milling or even enabling synthesis through solid-state methods.

4.4.3 Recommendations for partially disordered spinels

Based on simulated voltage curves, the two-phase region and $\sim$3 V voltage plateau disappear at $d = 0.25$, corresponding to 25% Mn occupancy on the 16c sites. Disordered spinels with higher levels of disorder also show no two-phase behavior, indicating that they would also display solid-solution behavior, but their spinel characteristics also decreases with disorder. Because the Mn begin to occupy 16c sites, the 8a-16c network that enables 3-D Li migration in spinel $LiMn_2O_4$ becomes increasingly obstructed with disorder. While Li can percolate through other tet sites (8b and 48f) that are stabilized by disorder [212], the excess loss of spinel character and its channels with facile Li migration impacts the overall Li mobility in, and thus the rate capability of, the highly disordered materials [195]. Therefore, we suggest that partially disordered spinels should not exceed disorders of $d = 0.25$.

However, disordered spinels with slightly lower levels of disorder ($d = 0.15$-0.20) likely maintain many of the advantages of the more disordered spinels. Disordered spinels with only $d = 0.15$-0.20 still show significantly shorter voltage plateaus (from $\sim x_{Li} = 0.85$ to 1.0 per O_2) compared to the ordered spinel ($x_{Li} = 0.5$ to 1.0 per O_2). Thus, most of the Li inserted through a two-phase region in the ordered spinel can lithiate instead through solid-solution in the $d = 0.15$-0.20 disordered spinels. 16c/16d disorder also breaks the 16d Mn ordering of the ordered spinel that is responsible for the collective Jahn-Teller distortion in the ordered spinel. Thus, partially disordered spinels with 15%-20% 16c Mn or TM occupancy are likely to show mostly solid-solution behavior without collective Jahn-Teller distortion as well as good rate capability due to higher spinel character.

Chapter 5

Concluding remarks

5.1 Conclusions

This dissertation utilized first-principles calculations and cluster expansion methods to analyze the thermodynamics associated with intercalation and the kinetics associated with migration of Li- and Mg-ions into spinel-based oxide frameworks as potential high energy density or high rate electrodes. Specifically, we investigated the intercalation of Mg-ions into the 8a sites of $Mg_x^{(8a)}Cr_2^{(16c)}O_4$ and Li-ions across the 8a-to-16c transition from $Li_3^{(8a)}(LiTi_5)^{(16d)}O_{12}$ to $Li_6^{(16c)}(LiTi_5)^{(16d)}O_{12}$, as well as their mobility at varying states of Mg and Li content. We then analyzed the effect of disordering the octahedral 16c and TM-occupied 16d sites of the spinel on the 8a-to-16c transition and intercalation voltage profile in $LiMn_2O_4$. The work presented in this dissertation offers valuable insights into potential barriers to Mg-ion intercalation, mechanisms for fast Li-ion diffusion, and pathways to optimizing electrochemical properties through framework disorder in spinel-based oxide materials.

Chapter 2 presented an investigation of the intercalation of Mg in the Cr_2O_4 spinel in order to better evaluate the $Mg_xCr_2O_4$ system as a potential Mg-ion cathode. This investigation focused on evaluating the associated thermodynamics of intercalation and kinetics of mobility of Mg in Cr_2O_4 by building a cluster expansion to evaluate the room temperature voltage curve and investigating the kinetics at strong intermediate Mg-Va ground state orderings. While the initial charge and deintercalation of the Mg is facile, the intermediate orderings at 33% Mg and 50% Mg concentrations do pose potential problems to intercalation due to the depth of the orderings and the high migration barrier of Mg at concentrations below 50% Mg. Doping on the transition metal site (with transition metals such as Mn or Ni) or on the anion sites (with F or S) is proposed to destabilize the deep intermediate orderings and decrease the high Mg migration barrier and large voltage steps. Given the recent improvements in cathodic stabilities of Mg electrolytes, further studies on removing the bottlenecks of reversible Mg intercalation in the high-voltage spinel-Cr_2O_4 cathode should enable the practical realization of high energy density Mg batteries.

In Chapter 3, we combined operando Li K-edge electron energy loss spectroscopy (Li-EELS) to characterize Li occupancy at high rate, simulated Li-EELS spectroscopy, and Li migration calculations to pinpoint the origins of fast Li kinetics in $Li_4Ti_5O_{12}$. Specifically, we carried out operando Li-EELS to probe Li-ion transport in a $Li_4Ti_5O_{12}$ electrode during galvanostatic discharge/discharge. First-principles computational spectroscopy was performed to identify the spectral signature of the intermediate arising from local distorted face-sharing Li polyhedra. Facile Li migration routes involving these face-sharing motifs were revealed in intermediate configurations. Many of these intermediate configurations are slightly higher in energy than the two-phase thermodynamic equilibrium but accessible with a small overpotential due to the Li defects on the 16d sites compared to typical LiM_2O_4 spinels, enabling high rate capability. These findings, which provide unique insights into the kinetics-controlled ionic transport in $Li_4Ti_5O_{12}$, may open new directions for designing electrode materials for fast-charging batteries.

Chapter 4 demonstrated how 16c/16d disordering can close the two-phase region between $LiMn_2O_4$ and $Li_2Mn_2O_4$ in $Li_xMn_2O_4$ spinel. Using a cluster expansion in combination with Monte Carlo calculations, we find that disorder shortens the two-phase region between $LiMn_2O_4$ and $Li_2Mn_2O_4$ by increasing Li solubility in $LiMn_2O_4$ with the plateau disappearing at 0.25 Mn occupancy on the 16c sites. While disorder also results in extreme voltages at the dilute Li limit, such effects are moderated by oxygen oxidation. Because 16c/16d disorder may be difficult to produce experimentally, we suggest that Ti substitution and Li-excess can aid in disrupting the 16d TM ordering. From this work, we demonstrate how disorder can elevate the overall energy landscape, making higher-energy solid-solution configurations more accessible, and can widen site energy distributions to reduce and even remove problematic two-phase regions. The removal of the rate- and cyclability-limiting two-phase region of the spinel through disorder provides an avenue by which to optimize the partially disordered spinels, bringing us another step closer to cheaper high-rate, energy-dense Li-ion cathodes.

5.2 Future directions for spinels as battery materials

While we investigated the spinel structure as possible Li-ion and Mg-ion electrodes, the spinel framework is also an attractive structure type for solid-state conductors due to its 3-D migration network. A number of Mg chalcogenide spinels have been proposed as Mg-ion solid-state conductors with surprisingly low migration barriers (as low as 360 meV).[52, 213] However, such chalcogenide-based materials tend to be unstable against the oxidizing and highly reducing conditions when in contact with the high voltage cathode and the Mg metal anode. Spinel frameworks (Li-substituted $MgAl_2O_4$)[214, 215] have also been considered for Li-ion solid-state conductors in order to build a lattice-matching solid-state battery without interfacial impedance. However, Li-ion mobility in oxide-based materials are generally somewhat lacking (with some exceptions) compared to the required Li mobility in a solid-state conductor. Halides, on the other hand, tend to have better stability against oxidation and reduction than chalcogenides and better ion mobility than oxides.[216] Indeed, the recently reported $Li_2Sc_{2/3}Cl_4$ spinel with Li-ion conductivity of 1.5 mS/cm [217] highlights that the halide spinels are an extremely promising class of materials worthy of a more thorough investigation.

In this dissertation, we considered intercalation from the empty spinel (B_2O_4, with a 1:2 cation:anion ratio) into the 8a sites (to AB_2O_4, with a 3:4 cation:anion ratio) and across the 8a-to-16c transition (to $A_2B_2O_4$ with a 1:1 cation:anion ratio). However, less investigation has been done on intercalation past the 1:1 cation:anion ratio. This is generally true in FCC oxides where the octahedral sites are usually fully filled at the 1:1 cation:anion ratio because cation insertion past the 1:1 cation:anion ratio requires tetrahedral occupancy. However, at dilute levels of insertion, cation insertion into the interstitial tetrahedral sites results in the face-sharing tetrahedral-octahedral configurations responsible for the fast Li-ion conduction in $Li_4Ti_5O_{12}$. Thus, if cation insertion in spinels past the 1:1 cation:anion ratio is possible, we expect that similar tetrahedral-octahedral face-sharing configurations may also facilitate high

cation mobility in these materials. Such face-sharing configurations and the low migration barrier of their cooperative migration have been shown in a disordered Li-ion vanadium rock salt oxide proposed as a fast-charging anode.[218] In spinel, cation insertion can be accommodated by the 8a sites, which face-share with four neighboring cation-occupied 16c sites and no (highly charged) transition metals. Similar local configurations (tetrahedral Li surrounded by four octahedral Li) also occurs in garnet $Li_7La_3Zr_2O_{12}$, a solid-state Li-ion conductor, further indicating such local configurations can be stabilized and conducive to fast Li-ion mobility. Thus, overlithiated spinels (with cation:anion ratio > 1:1) present an exciting opportunity for solid-state materials with fast Li-ion conduction.

Finally, further exploration of the partially disordered spinel (PDS) space is of great interest for realizing cheap high energy density, high rate Li-ion cathodes. While we mostly investigated partial disorder based on Mn disordering from the 16d sites onto the 16c sites, the nature of "partial disorder" in experimentally synthesized PDS may differ from the disordered spinel investigated here. For example, it is not quite clear whether the spinel-like order in PDS is short-, medium-, or long-range. Additionally, the disorder explored here (of the Mn onto the 16c sites) has infinite coherence due to the finite size of the supercell, which may not be true in the experimentally synthesized PDS. However, the disorder in PDS is currently evaluated based mainly on XRD refinement to the spinel structure.[195] While this type of characterization provides information regarding the level of disorder via the 16c and 16d TM occupancy, further experimental characterization with higher local and medium-range sensitivity could help to better determine the nature of the disorder. These types of detailed experimental characterizations, along with the larger-scale simulations enabled by cluster expansions, could facilitate navigation to the optimal material within the complex configurational space of PDS.

References

[1] Elsa A Olivetti et al. "Lithium-ion battery supply chain considerations: analysis of potential bottlenecks in critical metals". In: *Joule* 1.2 (2017), pp. 229–243.

[2] RJ Clément, Z Lun, and G Ceder. "Cation-disordered rocksalt transition metal oxides and oxyfluorides for high energy lithium-ion cathodes". In: *Energy & Environmental Science* 13.2 (2020), pp. 345–373.

[3] Naoki Nitta et al. "Li-ion battery materials: present and future". In: *Materials today* 18.5 (2015), pp. 252–264.

[4] John Reed and Gerbrand Ceder. "Role of electronic structure in the susceptibility of metastable transition-metal oxide structures to transformation". In: *Chemical reviews* 104.10 (2004), pp. 4513–4534.

[5] Yan Zhou et al. *Lithium-ion battery supply chain for E-drive vehicles in the United States: 2010–2020.* Tech. rep. Argonne National Lab.(ANL), Argonne, IL (United States), 2021.

[6] MM Thackeray et al. "Lithium insertion into manganese spinels". In: *Materials research bulletin* 18.4 (1983), pp. 461–472.

[7] Michael M Thackeray and Khalil Amine. "$LiMn_2O_4$ spinel and substituted cathodes". In: *Nature Energy* 6.5 (2021), pp. 566–566.

[8] Michael M Thackeray et al. "Review–From $LiMn_2O_4$ to Partially-Disordered Li_2MnNiO_4: The Evolution of Lithiated-Spinel Cathodes for Li-Ion Batteries". In: *Journal of The Electrochemical Society* 169.2 (2022), p. 020535.

[9] MM Thackeray et al. "Spinel electrodes from the Li-Mn-O system for rechargeable lithium battery applications". In: *Journal of the Electrochemical Society* 139.2 (1992), p. 363.

[10] Jerry Barker, René Koksbang, and M Yazid Saidi. "Lithium insertion in manganese oxides: A model lithium ion system". In: *Solid State Ionics* 82.3-4 (1995), pp. 143–151.

[11] Rui Wang et al. "A disordered rock-salt Li-excess cathode material with high capacity and substantial oxygen redox activity: $Li_{1.25}Nb_{0.25}Mn_{0.5}O_2$". In: *Electrochemistry Communications* 60 (2015), pp. 70–73.

[12] Jinhyuk Lee et al. "A new class of high capacity cation-disordered oxides for rechargeable lithium batteries: Li–Ni–Ti–Mo oxides". In: *Energy & Environmental Science* 8.11 (2015), pp. 3255–3265.

[13] Alexander Urban, Jinhyuk Lee, and Gerbrand Ceder. "The configurational space of rocksalt-type oxides for high-capacity lithium battery electrodes". In: *Advanced Energy Materials* 4.13 (2014), p. 1400478.

[14] Eunseok Lee and Kristin A Persson. "Structural and chemical evolution of the layered Li-excess Li_xMnO_3 as a function of Li content from first-principles calculations". In: *Advanced Energy Materials* 4.15 (2014), p. 1400498.

[15] Jinhyuk Lee et al. "Reversible Mn^{2+}/Mn^{4+} double redox in lithium-excess cathode materials". In: *Nature* 556.7700 (2018), pp. 185–190.

[16] Daniil A Kitchaev et al. "Design principles for high transition metal capacity in disordered rocksalt Li-ion cathodes". In: *Energy & Environmental Science* 11.8 (2018), pp. 2159–2171.

[17] Zhengyan Lun et al. "Design principles for high-capacity Mn-based cation-disordered rocksalt cathodes". In: *Chem* 6.1 (2020), pp. 153–168.

[18] Zhengyan Lun et al. "Cation-disordered rocksalt-type high-entropy cathodes for Li-ion batteries". In: *Nature materials* 20.2 (2021), pp. 214–221.

[19] Jakob Asenbauer et al. "The success story of graphite as a lithium-ion anode material–fundamentals, remaining challenges, and recent developments including silicon (oxide) composites". In: *Sustainable Energy & Fuels* 4.11 (2020), pp. 5387–5416.

[20] Thomas Waldmann, Björn-Ingo Hogg, and Margret Wohlfahrt-Mehrens. "Li plating as unwanted side reaction in commercial Li-ion cells–A review". In: *Journal of Power Sources* 384 (2018), pp. 107–124.

[21] Mickaël Holzapfel, Fannie Alloin, and Rachid Yazami. "Calorimetric investigation of the reactivity of the passivation film on lithiated graphite at elevated temperatures". In: *Electrochimica Acta* 49.4 (2004), pp. 581–589.

[22] Qingsong Wang et al. "Thermal stability of $LiPF_6$/EC + DEC electrolyte with charged electrodes for lithium ion batteries". In: *Thermochimica Acta* 437.1-2 (2005), pp. 12–16.

[23] Zonghai Chen et al. "Multi-scale study of thermal stability of lithiated graphite". In: *Energy & Environmental Science* 4.10 (2011), pp. 4023–4030.

[24] Xuning Feng et al. "Thermal runaway mechanism of lithium ion battery for electric vehicles: A review". In: *Energy Storage Materials* 10 (2018), pp. 246–267.

[25] Christian von Lüders et al. "Lithium plating in lithium-ion batteries investigated by voltage relaxation and in situ neutron diffraction". In: *Journal of Power Sources* 342 (2017), pp. 17–23.

[26] Thomas Waldmann and Margret Wohlfahrt-Mehrens. "Effects of rest time after Li plating on safety behavior—ARC tests with commercial high-energy 18650 Li-ion cells". In: *Electrochimica Acta* 230 (2017), pp. 454–460.

[27] Qianqian Liu et al. "Understanding undesirable anode lithium plating issues in lithium-ion batteries". In: *RSC advances* 6.91 (2016), pp. 88683–88700.

[28] Wenquan Lu et al. "Overcharge effect on morphology and structure of carbon electrodes for lithium-ion batteries". In: *Journal of the electrochemical society* 159.5 (2012), A566.

[29] KM Colbow, JR Dahn, and RR Haering. "Structure and electrochemistry of the spinel oxides $LiTi_2O_4$ and $Li_{4/3}Ti_{5/3}O_4$". In: *Journal of Power Sources* 26.3-4 (1989), pp. 397–402.

[30] Bote Zhao et al. "A comprehensive review of $Li_4Ti_5O_{12}$-based electrodes for lithium-ion batteries: The latest advancements and future perspectives". In: *Materials Science and Engineering: R: Reports* 98 (2015), pp. 1–71.

[31] Tao Yuan et al. "Challenges of spinel $Li_4Ti_5O_{12}$ for lithium-ion battery industrial applications". In: *Advanced energy materials* 7.12 (2017), p. 1601625.

[32] Norio Takami et al. "Electrochemical kinetics and safety of 2-volt class Li-ion battery system using lithium titanium oxide anode". In: *Journal of the electrochemical society* 156.2 (2008), A128.

[33] Ting-Feng Yi, Shuang-Yuan Yang, and Ying Xie. "Recent advances of $Li_4Ti_5O_{12}$ as a promising next generation anode material for high power lithium-ion batteries". In: *Journal of Materials Chemistry A* 3.11 (2015), pp. 5750–5777.

[34] Xu Jin et al. "Mesoporous Single-Crystal Lithium Titanate Enabling Fast-Charging Li-Ion Batteries". In: *Advanced Materials* (2022), p. 2109356.

[35] Tsutomu Ohzuku, Atsushi Ueda, and Norihiro Yamamoto. "Zero-strain insertion material of $Li[Li_{1/3}Ti_{5/3}]O_4$ for rechargeable lithium cells". In: *Journal of the Electrochemical Society* 142.5 (1995), p. 1431.

[36] AN Jansen et al. "Development of a high-power lithium-ion battery". In: *Journal of power sources* 81 (1999), pp. 902–905.

[37] Wu Xu et al. "Lithium metal anodes for rechargeable batteries". In: *Energy & Environmental Science* 7.2 (2014), pp. 513–537.

[38] Pieremanuele Canepa et al. "Odyssey of multivalent cathode materials: open questions and future challenges". In: *Chemical reviews* 117.5 (2017), pp. 4287–4341.

[39] Masaki Matsui. "Study on electrochemically deposited Mg metal". In: *Journal of Power Sources* 196.16 (2011), pp. 7048–7055.

[40] Albert L Lipson et al. "Practical stability limits of magnesium electrolytes". In: *Journal of The Electrochemical Society* 163.10 (2016), A2253.

[41] Matthew M Huie et al. "Cathode materials for magnesium and magnesium-ion based batteries". In: *Coordination Chemistry Reviews* 287 (2015), pp. 15–27.

[42] Doron Aurbach et al. "Prototype systems for rechargeable magnesium batteries". In: *Nature* 407.6805 (2000), pp. 724–727.

[43] Philip Lightfoot et al. "Structure of the cubic intercalate Mg_xTiS_2". In: *Journal of Materials Chemistry* 2.1 (1992), pp. 139–140.

[44] Xiaoqi Sun et al. "A high capacity thiospinel cathode for Mg batteries". In: *Energy & Environmental Science* 9.7 (2016), pp. 2273–2277.

[45] Xiaoqi Sun, Patrick Bonnick, and Linda F Nazar. "Layered TiS_2 positive electrode for Mg batteries". In: *ACS Energy Letters* 1.1 (2016), pp. 297–301.

[46] Ziqin Rong et al. "Materials design rules for multivalent ion mobility in intercalation structures". In: *Chemistry of Materials* 27.17 (2015), pp. 6016–6021.

[47] Chen Ling et al. "How general is the conversion reaction in Mg battery cathode: a case study of the magnesiation of α-MnO2". In: *Chemistry of Materials* 27.16 (2015), pp. 5799–5807.

[48] Ruigang Zhang and Chen Ling. "Unveil the chemistry of olivine $FePO_4$ as magnesium battery cathode". In: *ACS Applied Materials & Interfaces* 8.28 (2016), pp. 18018–18026.

[49] ID Brown. "What factors determine cation coordination numbers?" In: *Acta Crystallographica Section B: Structural Science* 44.6 (1988), pp. 545–553.

[50] Gopalakrishnan Sai Gautam et al. "Influence of inversion on Mg mobility and electrochemistry in spinels". In: *Chemistry of Materials* 29.18 (2017), pp. 7918–7930.

[51] Pieremanuele Canepa et al. "Role of point defects in spinel Mg chalcogenide conductors". In: *Chemistry of Materials* 29.22 (2017), pp. 9657–9667.

[52] Pieremanuele Canepa et al. "High magnesium mobility in ternary spinel chalcogenides". In: *Nature communications* 8.1 (2017), pp. 1–8.

[53] Sanjeev Krishna Kolli and Anton Van der Ven. "Elucidating the factors that cause cation diffusion shutdown in spinel-based electrodes". In: *Chemistry of Materials* 33.16 (2021), pp. 6421–6432.

[54] Alexandra Emly and Anton Van der Ven. "Mg intercalation in layered and spinel host crystal structures for Mg batteries". In: *Inorganic chemistry* 54.9 (2015), pp. 4394–4402.

[55] Yaosen Tian et al. "Promises and challenges of next-generation "beyond Li-ion" batteries for electric vehicles and grid decarbonization". In: *Chemical reviews* 121.3 (2020), pp. 1623–1669.

[56] Kohei Shimokawa and Tetsu Ichitsubo. "Spinel–rocksalt transition as a key cathode reaction toward high-energy-density magnesium rechargeable batteries". In: *Current Opinion in Electrochemistry* 21 (2020), pp. 93–99.

[57] Alexandra Michail, Begoña Silván, and Nuria Tapia-Ruiz. "Progress in high-voltage $MgMn_2O_4$ oxyspinel cathode materials for Mg batteries". In: *Current Opinion in Electrochemistry* 31 (2022), p. 100817.

[58] Shinya Okamoto et al. "Intercalation and Push-Out Process with Spinel-to-Rocksalt Transition on Mg Insertion into Spinel Oxides in Magnesium Batteries". In: *Advanced Science* 2.8 (2015), p. 1500072.

[59] Feilure Tuerxun et al. "Phase Transition Behavior of $MgMn_2O_4$ Spinel Oxide Cathode during Magnesium Ion Insertion". In: *Chemistry of Materials* 33.3 (2021), pp. 1006–1012.

[60] Zhenxing Feng et al. "Phase-controlled electrochemical activity of epitaxial Mg-spinel thin films". In: *ACS Applied Materials & Interfaces* 7.51 (2015), pp. 28438–28443.

[61] Chunjoong Kim et al. "Direct observation of reversible magnesium ion intercalation into a spinel oxide host". In: *Advanced materials* 27.22 (2015), pp. 3377–3384.

[62] Jiefu Yin et al. "Magnesium-ion battery-relevant electrochemistry of $MgMn_2O_4$: crystallite size effects and the notable role of electrolyte water content". In: *Chemical communications* 53.26 (2017), pp. 3665–3668.

[63] Miao Liu et al. "Spinel compounds as multivalent battery cathodes: a systematic evaluation based on ab initio calculations". In: *Energy & Environmental Science* 8.3 (2015), pp. 964–974.

[64] Chen Ling, Ruigang Zhang, and Fuminori Mizuno. "Quantitatively predict the potential of MnO_2 polymorphs as magnesium battery cathodes". In: *ACS applied materials & interfaces* 8.7 (2016), pp. 4508–4515.

[65] KS Irani, APB Sinha, and AB Biswas. "Effect of temperature on the structure of manganites". In: *Journal of Physics and Chemistry of Solids* 23.6 (1962), pp. 711–727.

[66] Lorenzo Malavasi et al. "Structural and transport properties of $Mg_{1-x}Mn_xMn_2O_4\pm\delta$ spinels". In: *Journal of Solid State Chemistry* 166.1 (2002), pp. 171–176.

[67] NK Radhakrishnan and AB Biswas. "A neutron diffraction study of the cation migration in $MgMn_2O_4$". In: *physica status solidi (a)* 37.2 (1976), pp. 719–722.

[68] M Rosenberg and P Nicolau. "Electrical properties and cation migration in $MgMn_2O_4$". In: *physica status solidi (b)* 6.1 (1964), pp. 101–110.

[69] J Reed, G Ceder, and A Van Der Ven. "Layered-to-spinel phase transition in Li_xMnO_2". In: *Electrochemical and Solid-State Letters* 4.6 (2001), A78.

[70] Jan N Reimers and JR Dahn. "Electrochemical and in situ X-ray diffraction studies of lithium intercalation in Li_xCoO_2". In: *Journal of the Electrochemical Society* 139.8 (1992), p. 2091.

[71] MM Thackeray et al. "Electrochemical extraction of lithium from $LiMn_2O_4$". In: *Materials Research Bulletin* 19.2 (1984), pp. 179–187.

[72] Byoungwoo Kang and Gerbrand Ceder. "Battery materials for ultrafast charging and discharging". In: *Nature* 458.7235 (2009), pp. 190–193.

[73] Rahul Malik, Fei Zhou, and Gerbrand Ceder. "Kinetics of non-equilibrium lithium incorporation in LiFePO$_4$". In: *Nature materials* 10.8 (2011), pp. 587–590.

[74] Michael M Thackeray. "Manganese oxides for lithium batteries". In: *Progress in Solid State Chemistry* 25.1-2 (1997), pp. 1–71.

[75] Fakui Luo et al. "Operando X-ray diffraction analysis of the degradation mechanisms of a spinel LiMn2O4 cathode in different voltage windows". In: *Journal of Energy Chemistry* 44 (2020), pp. 138–146.

[76] K Amine et al. "A New Three-Volt Spinel Li$_{1+x}$Mn$_{1.5}$Ni$_{0.5}$O$_4$ for Secondary Lithium Batteries". In: *Journal of The Electrochemical Society* 143.5 (1996), p. 1607.

[77] Xifei Li, Youlong Xu, and Chunlei Wang. "Suppression of Jahn–Teller distortion of spinel LiMn$_2$O$_4$ cathode". In: *Journal of Alloys and Compounds* 479.1-2 (2009), pp. 310–313.

[78] Gurpreet Singh et al. "Suppression of Jahn–Teller distortion by chromium and magnesium doping in spinel LiMn$_2$O$_4$: A first-principles study using GGA and GGA+U". In: *Journal of Physics and Chemistry of Solids* 70.8 (2009), pp. 1200–1206.

[79] Masashi Okubo et al. "Fast Li-ion insertion into nanosized LiMn$_2$O$_4$ without domain boundaries". In: *ACS nano* 4.2 (2010), pp. 741–752.

[80] Hui Xia, Zhentao Luo, and Jianping Xie. "Nanostructured LiMn$_2$O$_4$ and their composites as high-performance cathodes for lithium-ion batteries". In: *Progress in Natural Science: Materials International* 22.6 (2012), pp. 572–584.

[81] Liang Xiao et al. "Influence of particle sizes and morphologies on the electrochemical performances of spinel LiMn$_2$O$_4$ cathode materials". In: *Journal of Power Sources* 225 (2013), pp. 286–292.

[82] Renier Arabolla Rodríguez et al. "Structural defects in LiMn$_2$O$_4$ induced by gamma radiation and its influence on the Jahn-Teller effect". In: *Solid State Ionics* 324 (2018), pp. 77–86.

[83] Renier Arabolla Rodríguez et al. "Unveiling the role of Mn-interstitial defect and particle size on the Jahn-Teller distortion of the LiMn$_2$O$_4$ cathode material". In: *Journal of Power Sources* 490 (2021), p. 229519.

[84] Hao Li et al. "Toward high-energy Mn-based disordered-rocksalt Li-ion cathodes". In: *Joule* (2021).

[85] Pierre Hohenberg and Walter Kohn. "Inhomogeneous electron gas". In: *Physical review* 136.3B (1964), B864.

[86] Walter Kohn and Lu Jeu Sham. "Self-consistent equations including exchange and correlation effects". In: *Physical review* 140.4A (1965), A1133.

[87] Georg Kresse and Jürgen Furthmüller. "Efficient iterative schemes for ab initio total-energy calculations using a plane-wave basis set". In: *Physical review B* 54.16 (1996), p. 11169.

[88] Peter E Blöchl. "Projector augmented-wave method". In: *Physical review B* 50.24 (1994), p. 17953.

[89] Georg Kresse and Daniel Joubert. "From ultrasoft pseudopotentials to the projector augmented-wave method". In: *Physical review b* 59.3 (1999), p. 1758.

[90] Klaus Capelle. "A bird's-eye view of density-functional theory". In: *Brazilian journal of physics* 36 (2006), pp. 1318–1343.

[91] John P Perdew, Kieron Burke, and Matthias Ernzerhof. "Generalized gradient approximation made simple". In: *Physical review letters* 77.18 (1996), p. 3865.

[92] Jianwei Sun, Adrienn Ruzsinszky, and John P Perdew. "Strongly constrained and appropriately normed semilocal density functional". In: *Physical review letters* 115.3 (2015), p. 036402.

[93] Jianwei Sun et al. "Accurate first-principles structures and energies of diversely bonded systems from an efficient density functional". In: *Nature chemistry* 8.9 (2016), pp. 831–836.

[94] Julia H Yang, Daniil A Kitchaev, and Gerbrand Ceder. "Rationalizing accurate structure prediction in the meta-GGA SCAN functional". In: *Physical Review B* 100.3 (2019), p. 035132.

[95] MK Aydinol, AF Kohan, and Gerbrand Ceder. "Ab initio calculation of the intercalation voltage of lithium-transition-metal oxide electrodes for rechargeable batteries". In: *Journal of power sources* 68.2 (1997), pp. 664–668.

[96] Alexander Urban, Dong-Hwa Seo, and Gerbrand Ceder. "Computational understanding of Li-ion batteries". In: *npj Computational Materials* 2.1 (2016), pp. 1–13.

[97] ME Arroyo y de Dompablo, A Van der Ven, and G Ceder. "First-principles calculations of lithium ordering and phase stability on Li_xNiO_2". In: *Physical Review B* 66.6 (2002), p. 064112.

[98] Juan M Sanchez, Francois Ducastelle, and Denis Gratias. "Generalized cluster description of multicomponent systems". In: *Physica A: Statistical Mechanics and its Applications* 128.1-2 (1984), pp. 334–350.

[99] Didier De Fontaine. "Cluster approach to order-disorder transformations in alloys". In: *Solid state physics*. Vol. 47. Elsevier, 1994, pp. 33–176.

[100] Chris Wolverton and Didier de Fontaine. "Cluster expansions of alloy energetics in ternary intermetallics". In: *Physical Review B* 49.13 (1994), p. 8627.

[101] PD Tepesch, GD Garbulsky, and G Ceder. "Model for configurational thermodynamics in ionic systems". In: *Physical review letters* 74.12 (1995), p. 2272.

[102] Axel Van De Walle. "Multicomponent multisublattice alloys, nonconfigurational entropy and other additions to the Alloy Theoretic Automated Toolkit". In: *Calphad* 33.2 (2009), pp. 266–278.

[103] William D Richards et al. "Fluorination of lithium-excess transition metal oxide cathode materials". In: *Advanced Energy Materials* 8.5 (2018), p. 1701533.

[104] Atsuto Seko and Isao Tanaka. "Cluster expansion of multicomponent ionic systems with controlled accuracy: importance of long-range interactions in heterovalent ionic systems". In: *Journal of physics: Condensed matter* 26.11 (2014), p. 115403.

[105] Anton Van der Ven et al. "First-principles investigation of phase stability in Li_xCoO_2". In: *Physical Review B* 58.6 (1998), p. 2975.

[106] Daniil A Kitchaev et al. "Energetics of MnO_2 polymorphs in density functional theory". In: *Physical Review B* 93.4 (2016), p. 045132.

[107] Bin Ouyang et al. "Effect of Fluorination on Lithium Transport and Short-Range Order in Disordered-Rocksalt-Type Lithium-Ion Battery Cathodes". In: *Advanced Energy Materials* 10.10 (2020), p. 1903240.

[108] Lance J Nelson et al. "Compressive sensing as a paradigm for building physics models". In: *Physical Review B* 87.3 (2013), p. 035125.

[109] Peichen Zhong et al. "An l_0l_2-norm regularized regression model for construction of robust cluster expansions in multicomponent systems". In: *Physical Review B* 106.2 (2022), p. 024203.

[110] Julia H Yang et al. "Approaches for handling high-dimensional cluster expansions of ionic systems". In: *npj Computational Materials* 8.1 (2022), pp. 1–11.

[111] Gerbrand Ceder and Anton Van der Ven. "Phase diagrams of lithium transition metal oxides: investigations from first principles". In: *Electrochimica Acta* 45.1-2 (1999), pp. 131–150.

[112] Huiwen Ji et al. "Hidden structural and chemical order controls lithium transport in cation-disordered oxides for rechargeable batteries". In: *Nature communications* 10.1 (2019), pp. 1–9.

[113] Yoyo Hinuma, Ying S Meng, Gerbrand Ceder, et al. "Temperature-concentration phase diagram of $P2$-Na_xCoO_2 from first-principles calculations". In: *Physical Review B* 77.22 (2008), p. 224111.

[114] Tina Chen et al. "First-principles study of the voltage profile and mobility of Mg intercalation in a chromium oxide spinel". In: *Chemistry of Materials* 30.1 (2018), pp. 153–162.

[115] Miao Liu et al. "Evaluation of sulfur spinel compounds for multivalent battery cathode applications". In: *Energy & Environmental Science* 9.10 (2016), pp. 3201–3209.

[116] Mie Andersen, Chiara Panosetti, and Karsten Reuter. "A practical guide to surface kinetic Monte Carlo simulations". In: *Frontiers in chemistry* 7 (2019), p. 202.

[117] Keith James Laidler, J Keith, et al. *Chemical kinetics*. Vol. 2. McGraw-Hill New York, 1965.

[118] Graeme Henkelman and Hannes Jónsson. "Improved tangent estimate in the nudged elastic band method for finding minimum energy paths and saddle points". In: *The Journal of chemical physics* 113.22 (2000), pp. 9978–9985.

[119] Daniel Sheppard, Rye Terrell, and Graeme Henkelman. "Optimization methods for finding minimum energy paths". In: *The Journal of chemical physics* 128.13 (2008), p. 134106.

[120] C Glidewell. "Cation distribution in spinels: Lattice energy versus crystals field stabilisation energy". In: *Inorganica Chimica Acta* 19 (1976), pp. L45–L47.

[121] HK Mao and PM Bell. "Crystal-field effects in spinel: oxidation states of iron and chromium". In: *Chromium: its Physicochemical Behavior and Petrologic Significance*. Elsevier, 1976, pp. 865–874.

[122] Shou-Hang Bo et al. "Layered-to-rock-salt transformation in desodiated Na_xCrO_2 (x 0.4)". In: *Chemistry of Materials* 28.5 (2016), pp. 1419–1429.

[123] Ming-Hui Cao et al. "Suppressing the chromium disproportionation reaction in O3-type layered cathode materials for high capacity sodium-ion batteries". In: *Journal of Materials Chemistry A* 5.11 (2017), pp. 5442–5448.

[124] JS Stephens and DWJ Cruickshank. "The crystal structure of $(CrO3)_\infty$". In: *Acta Crystallographica Section B: Structural Crystallography and Crystal Chemistry* 26.3 (1970), pp. 222–226.

[125] Sian E Dutton et al. "Sensitivity of the magnetic properties of the $ZnCr_2O_4$ and $MgCr_2O_4$ spinels to nonstoichiometry". In: *Physical Review B* 83.6 (2011), p. 064407.

[126] H Ehrenberg et al. "Tetragonal low-temperature phase of $MgCr_2O_4$". In: *Powder diffraction* 17.3 (2002), pp. 230–233.

[127] Ch Kant et al. "Magnetic susceptibility of the frustrated spinels $ZnCr_2O_4$, $MgCr_2O_4$ and $CdCr_2O_4$". In: *Journal of Physics: Conference Series*. Vol. 200. 3. IOP Publishing. 2010, p. 032032.

[128] L Ortega-San-Martin et al. "Low temperature neutron diffraction study of $MgCr_2O_4$ spinel". In: *Journal of Physics: Condensed Matter* 20.10 (2008), p. 104238.

[129] MT Rovers et al. "Muon-spin-relaxation investigation of the spin dynamics of geometrically frustrated chromium spinels". In: *Physical Review B* 66.17 (2002), p. 174434.

[130] Hiroyuki Suzuki and Yorihiko Tsunoda. "Spinel-type frustrated system $MgCr_2O_4$ studied by neutron scattering and magnetization measurements". In: *Journal of Physics and Chemistry of Solids* 68.11 (2007), pp. 2060–2063.

[131] HJ Xiang et al. "Predicting the spin-lattice order of frustrated systems from first principles". In: *Physical Review B* 84.22 (2011), p. 224429.

[132]   Makoto Yoshida et al. "High field ESR study of three dimensional spin frustrated system $MgCr_2O_4$". In: *Journal of the Physical Society of Japan* 75.4 (2006), p. 044709.

[133]   C Wolverton and Alex Zunger. "First-principles prediction of vacancy order-disorder and intercalation battery voltages in Li_xCoO_2". In: *Physical review letters* 81.3 (1998), p. 606.

[134]   Gopalakrishnan Sai Gautam et al. "The intercalation phase diagram of Mg in V_2O_5 from first-principles". In: *Chemistry of Materials* 27.10 (2015), pp. 3733–3742.

[135]   Georg Kresse and Jürgen Hafner. "Ab initio molecular dynamics for liquid metals". In: *Physical review B* 47.1 (1993), p. 558.

[136]   Vladimir I Anisimov, Jan Zaanen, and Ole K Andersen. "Band theory and Mott insulators: Hubbard U instead of Stoner I". In: *Physical Review B* 44.3 (1991), p. 943.

[137]   Anubhav Jain et al. "Formation enthalpies by mixing GGA and GGA+U calculations". In: *Physical Review B* 84.4 (2011), p. 045115.

[138]   Fei Zhou et al. "First-principles prediction of redox potentials in transition-metal compounds with LDA+U". In: *Physical Review B* 70.23 (2004), p. 235121.

[139]   Hendrik J Monkhorst and James D Pack. "Special points for Brillouin-zone integrations". In: *Physical review B* 13.12 (1976), p. 5188.

[140]   A Van der Ven et al. "Phase transformations and volume changes in spinel $Li_xMn_2O_4$". In: *Solid State Ionics* 135.1-4 (2000), pp. 21–32.

[141]   G Ceder. "A derivation of the Ising model for the computation of phase diagrams". In: *Computational Materials Science* 1.2 (1993), pp. 144–150.

[142]   Anubhav Jain et al. "A high-throughput infrastructure for density functional theory calculations". In: *Computational Materials Science* 50.8 (2011), pp. 2295–2310.

[143]   Shyue Ping Ong et al. "Python Materials Genomics (pymatgen): A robust, open-source python library for materials analysis". In: *Computational Materials Science* 68 (2013), pp. 314–319.

[144]   Paul P Ewald. "Die Berechnung optischer und elektrostatischer Gitterpotentiale". In: *Annalen der physik* 369.3 (1921), pp. 253–287.

[145]   Tom Goldstein and Stanley Osher. "The split Bregman method for L1-regularized problems". In: *SIAM journal on imaging sciences* 2.2 (2009), pp. 323–343.

[146]   Wenxuan Huang et al. "Finding and proving the exact ground state of a generalized Ising model by convex optimization and MAX-SAT". In: *Physical Review B* 94.13 (2016), p. 134424.

[147]   A Van der Ven et al. "Linking the electronic structure of solids to their thermodynamic and kinetic properties". In: *Mathematics and computers in simulation* 80.7 (2010), pp. 1393–1410.

[148] Anton Van der Ven et al. "Nondilute diffusion from first principles: Li diffusion in Li_xTiS_2". In: *Physical Review B* 78.10 (2008), p. 104306.

[149] A vd van de Walle and Mark Asta. "Self-driven lattice-model Monte Carlo simulations of alloy thermodynamic properties and phase diagrams". In: *Modelling and Simulation in Materials Science and Engineering* 10.5 (2002), p. 521.

[150] Shyue Ping Ong, Vincent L Chevrier, and Gerbrand Ceder. "Comparison of small polaron migration and phase separation in olivine $LiMnPO_4$ and $LiFePO_4$ using hybrid density functional theory". In: *Physical Review B* 83.7 (2011), p. 075112.

[151] Thomas Maxisch, Fei Zhou, and Gerbrand Ceder. "Ab initio study of the migration of small polarons in olivine Li_xFePO_4 and their association with lithium ions and vacancies". In: *Physical review B* 73.10 (2006), p. 104301.

[152] Gopalakrishnan Sai Gautam et al. "First-principles evaluation of multi-valent cation insertion into orthorhombic V_2O_5". In: *Chemical Communications* 51.71 (2015), pp. 13619–13622.

[153] Jishnu Bhattacharya and Christopher Wolverton. "Relative stability of normal vs. inverse spinel for $3d$ transition metal oxides as lithium intercalation cathodes". In: *Physical Chemistry Chemical Physics* 15.17 (2013), pp. 6486–6498.

[154] Jae Chul Kim, Dong-Hwa Seo, and Gerbrand Ceder. "Theoretical capacity achieved in a $LiMn_{0.5}Fe_{0.4}Mg_{0.1}BO_3$ cathode by using topological disorder". In: *Energy & Environmental Science* 8.6 (2015), pp. 1790–1798.

[155] Fei Zhou, Thomas Maxisch, and Gerbrand Ceder. "Configurational electronic entropy and the phase diagram of mixed-valence oxides: the case of Li_xFePO_4". In: *Physical review letters* 97.15 (2006), p. 155704.

[156] A Van der Ven and G Ceder. "Lithium diffusion mechanisms in layered intercalation compounds". In: *Journal of power sources* 97 (2001), pp. 529–531.

[157] Chen Ling and Koji Suto. "Thermodynamic origin of irreversible magnesium trapping in chevrel phase Mo_6S_8: importance of magnesium and vacancy ordering". In: *Chemistry of Materials* 29.8 (2017), pp. 3731–3739.

[158] Anubhav Jain et al. "Commentary: The Materials Project: A materials genome approach to accelerating materials innovation". In: *APL materials* 1.1 (2013), p. 011002.

[159] Gopalakrishnan Sai Gautam et al. "Impact of intermediate sites on bulk diffusion barriers: Mg intercalation in $Mg_2Mo_3O_8$". In: *Journal of Materials Chemistry A* 4.45 (2016), pp. 17643–17648.

[160] James C Hunter. "Preparation of a new crystal form of manganese dioxide: λ-MnO_2". In: *Journal of Solid State Chemistry* 39.2 (1981), pp. 142–147.

[161] A Mosbah, A Verbaere, and M Tournoux. "Phases Li_xMnO_2 λ rattachees au type spinelle". In: *Materials research bulletin* 18.11 (1983), pp. 1375–1381.

[162] C Bellitto et al. "The effect of doping $LiMn_2O_4$ spinel on its use as a cathode in Li-ion batteries: neutron diffraction and electrochemical studies". In: *Journal of Physics and Chemistry of Solids* 65.1 (2004), pp. 29–37.

[163] G Pistoia et al. "Doped Li-Mn Spinels: physical/chemical characteristics and electrochemical performance in Li batteries". In: *Chemistry of materials* 9.6 (1997), pp. 1443–1450.

[164] Jeffrey W Fergus. "Recent developments in cathode materials for lithium ion batteries". In: *Journal of power sources* 195.4 (2010), pp. 939–954.

[165] Yang-Kook Sun et al. "Effect of sulfur and nickel doping on morphology and electrochemical performance of $LiNi_{0.5}Mn_{1.5}O_{4-x}S_x$ spinel material in 3-V region". In: *Journal of power sources* 161.1 (2006), pp. 19–26.

[166] Ting-Feng Yi et al. "Recent developments in the doping of $LiNi_{0.5}Mn_{1.5}O_4$ cathode material for 5 V lithium-ion batteries". In: *Ionics* 17.5 (2011), pp. 383–389.

[167] C Choodamani, B Rudraswamy, and GT Chandrappa. "Structural, electrical, and magnetic properties of Zn substituted magnesium ferrite". In: *Ceramics International* 42.9 (2016), pp. 10565–10571.

[168] Akinori Kan et al. "Influence of Zn substitution for Mg on microwave dielectric properties of spinel-structured $(Mg_{1-x}Zn_x)Ga_2O_4$ solid solutions". In: *Japanese Journal of Applied Physics* 53.9S (2014), 09PB03.

[169] Hao Liu et al. "Capturing metastable structures during high-rate cycling of $LiFePO_4$ nanoparticle electrodes". In: *Science* 344.6191 (2014), p. 1252817.

[170] S Scharner, W Weppner, and P Schmid-Beurmann. "Evidence of Two-Phase Formation upon Lithium Insertion into the $Li_{1.33}Ti_{1.67}O_4$ Spinel". In: *Journal of the Electrochemical Society* 146.3 (1999), p. 857.

[171] Marnix Wagemaker et al. "A kinetic two-phase and equilibrium solid solution in spinel $Li_{4+x}Ti_5O_{12}$". In: *Advanced Materials* 18.23 (2006), pp. 3169–3173.

[172] Benedikt Ziebarth et al. "Lithium diffusion in the spinel phase $Li_4Ti_5O_{12}$ and in the rocksalt phase $Li_7Ti_5O_{12}$ of lithium titanate from first principles". In: *Physical Review B* 89.17 (2014), p. 174301.

[173] Holger Hain et al. "Study of local structure and Li dynamics in $Li_{4+x}Ti_5O_{12}$ ($0 \leq x \leq 5$) using ^{6}Li and ^{7}Li NMR spectroscopy". In: *Solid state nuclear magnetic resonance* 42 (2012), pp. 9–16.

[174] Walter Schmidt et al. "Small Change—Great Effect: Steep Increase of Li Ion Dynamics in $Li_4Ti_5O_{12}$ at the Early Stages of Chemical Li Insertion". In: *Chemistry of Materials* 27.5 (2015), pp. 1740–1750.

[175] Martin Wilkening et al. "Microscopic Li self-diffusion parameters in the lithiated anode material $Li_{4+x}Ti_5O_{12}$ ($0 \leq x \leq 3$) measured by 7 Li solid state NMR". In: *Physical Chemistry Chemical Physics* 9.47 (2007), pp. 6199–6202.

[176]   Swapna Ganapathy et al. "The fine line between a two-phase and solid-solution phase transformation and highly mobile phase interfaces in spinel $Li_{4+x}Ti_5O_{12}$". In: *Advanced energy materials* 7.9 (2017), p. 1601781.

[177]   Wei Zhang et al. "Multi-stage structural transformations in zero-strain lithium titanate unveiled by in situ X-ray absorption fingerprints". In: *Journal of the American Chemical Society* 139.46 (2017), pp. 16591–16603.

[178]   CP Grey and JM Tarascon. "Sustainability and in situ monitoring in battery development". In: *Nature materials* 16.1 (2017), pp. 45–56.

[179]   Feng Wang et al. "Excess lithium storage and charge compensation in nanoscale $Li_{4+x}Ti_5O_{12}$". In: *Nanotechnology* 24.42 (2013), p. 424006.

[180]   Feng Wang et al. "Tracking lithium transport and electrochemical reactions in nanoparticles". In: *Nature communications* 3.1 (2012), pp. 1–8.

[181]   Michel Armand et al. "Ionic-liquid materials for the electrochemical challenges of the future". In: *Materials for sustainable energy: a collection of peer-reviewed research and review articles from Nature Publishing Group* (2011), pp. 129–137.

[182]   Feng Wang et al. "Chemical distribution and bonding of lithium in intercalated graphite: Identification with optimized electron energy loss spectroscopy". In: *ACS nano* 5.2 (2011), pp. 1190–1197.

[183]   Keith Robinson, GV Gibbs, and PH Ribbe. "Quadratic elongation: a quantitative measure of distortion in coordination polyhedra". In: *Science* 172.3983 (1971), pp. 567–570.

[184]   Takashi Yamamoto. "Assignment of pre-edge peaks in K-edge x-ray absorption spectra of 3d transition metal compounds: Electric dipole or quadrupole?" In: *X-Ray Spectrometry: An International Journal* 37.6 (2008), pp. 572–584.

[185]   Marnix Wagemaker, Fokko M Mulder, and Anton Van der Ven. "The role of surface and interface energy on phase stability of nanosized insertion compounds". In: *Advanced Materials* 21.25-26 (2009), pp. 2703–2709.

[186]   Swapna Ganapathy and Marnix Wagemaker. "Nanosize storage properties in spinel $Li_4Ti_5O_{12}$ explained by anisotropic surface lithium insertion". In: *ACS nano* 6.10 (2012), pp. 8702–8712.

[187]   Oleksandr Dolotko et al. "Neutron diffraction study of $Li_4Ti_5O_{12}$ at low temperatures". In: *Solid state sciences* 36 (2014), pp. 101–106.

[188]   V Janovec, V Dvořák, and J Petzelt. "Symmetry classification and properties of equitranslation structural phase transitions". In: *Czechoslovak Journal of Physics B* 25.12 (1975), pp. 1362–1396.

[189]   Jianping Huang et al. "Non-topotactic reactions enable high rate capability in Li-rich cathode materials". In: *Nature Energy* 6.7 (2021), pp. 706–714.

[190] Xinye Zhao et al. "Design principles for zero-strain Li-ion cathodes". In: *Joule* 6.7 (2022), pp. 1654–1671.

[191] Jinhyuk Lee et al. "Mitigating oxygen loss to improve the cycling performance of high capacity cation-disordered cathode materials". In: *Nature communications* 8.1 (2017), pp. 1–10.

[192] Zhengyan Lun et al. "Improved cycling performance of Li-excess cation-disordered cathode materials upon fluorine substitution". In: *Advanced Energy Materials* 9.2 (2019), p. 1802959.

[193] Jia-yan Luo et al. "Ordered mesoporous spinel $LiMn_2O_4$ by a soft-chemical process as a cathode material for lithium-ion batteries". In: *Chemistry of Materials* 19.19 (2007), pp. 4791–4795.

[194] Kuthanapillil M Shaju and Peter G Bruce. "A stoichiometric nano-$LiMn_2O_4$ spinel electrode exhibiting high power and stable cycling". In: *Chemistry of Materials* 20.17 (2008), pp. 5557–5562.

[195] Zijian Cai et al. "Realizing continuous cation order-to-disorder tuning in a class of high-energy spinel-type Li-ion cathodes". In: *Matter* 4.12 (2021), pp. 3897–3916.

[196] Huiwen Ji et al. "Ultrahigh power and energy density in partially ordered lithium-ion cathode materials". In: *Nature Energy* 5.3 (2020), pp. 213–221.

[197] Alexander Urban et al. "Electronic-structure origin of cation disorder in transition-metal oxides". In: *Physical review letters* 119.17 (2017), p. 176402.

[198] Yubo Zhang et al. "Efficient first-principles prediction of solid stability: Towards chemical accuracy". In: *npj Computational Materials* 4.1 (2018), pp. 1–6.

[199] Wenxuan Huang et al. "Construction of ground-state preserving sparse lattice models for predictive materials simulations". In: *npj Computational Materials* 3.1 (2017), pp. 1–9.

[200] Noah Simon and Robert Tibshirani. "Standardization and the group lasso penalty". In: *Statistica Sinica* 22.3 (2012), p. 983.

[201] Tom FW Barth and E Posnjak. "Spinel structures: with and without variate atom equipoints". In: *Zeitschrift Für Kristallographie-Crystalline Materials* 82.1-6 (1932), pp. 325–341.

[202] Atsuto Seko et al. "Prediction of ground-state structures and order-disorder phase transitions in II-III spinel oxides: A combined cluster-expansion method and first-principles study". In: *Physical Review B* 73.18 (2006), p. 184117.

[203] David Santos-Carballal, Phuti E Ngoepe, and Nora H De Leeuw. "Ab initio investigation of the thermodynamics of cation distribution and of the electronic and magnetic structures in the $LiMn_2O_4$ spinel". In: *Physical Review B* 97.8 (2018), p. 085126.

[204] MK Aydinol and Gerbrand Ceder. "First-principles prediction of insertion potentials in Li-Mn oxides for secondary Li batteries". In: *Journal of the Electrochemical Society* 144.11 (1997), p. 3832.

[205] Sergei L Dudarev et al. "Electron-energy-loss spectra and the structural stability of nickel oxide: An LSDA+U study". In: *Physical Review B* 57.3 (1998), p. 1505.

[206] Lei Wang, Thomas Maxisch, and Gerbrand Ceder. "Oxidation energies of transition metal oxides within the GGA+U framework". In: *Physical Review B* 73.19 (2006), p. 195107.

[207] Bo Xu and Shirley Meng. "Factors affecting Li mobility in spinel $LiMn_2O_4$—A first-principles study by GGA and GGA+U methods". In: *Journal of Power Sources* 195.15 (2010), pp. 4971–4976.

[208] Arup Chakraborty et al. "Predicting accurate cathode properties of layered oxide materials using the SCAN meta-GGA density functional". In: *npj Computational Materials* 4.1 (2018), pp. 1–9.

[209] Wei Zhang et al. "Kinetic pathways of ionic transport in fast-charging lithium titanate". In: *Science* 367.6481 (2020), pp. 1030–1034.

[210] Tina Chen and Gerbrand Ceder. "Solid solution pathways through spinel's phase transition by topological analysis". Manuscript in preparation.

[211] Robert A House et al. "Lithium manganese oxyfluoride as a new cathode material exhibiting oxygen redox". In: *Energy & Environmental Science* 11.4 (2018), pp. 926–932.

[212] Julia Yang and Gerbrand Ceder. "Activated internetwork pathways in partially-disordered spinel cathode materials with ultrahigh rate performance". Manuscript in preparation.

[213] Julius Koettgen, Christopher J Bartel, and Gerbrand Ceder. "Computational investigation of chalcogenide spinel conductors for all-solid-state Mg batteries". In: *Chemical Communications* 56.13 (2020), pp. 1952–1955.

[214] Fabio Rosciano et al. "Towards a lattice-matching solid-state battery: synthesis of a new class of lithium-ion conductors with the spinel structure". In: *Physical Chemistry Chemical Physics* 15.16 (2013), pp. 6107–6112.

[215] Jan L Allen et al. "Fast Li-Ion Conduction in Spinel-Structured Solids". In: *Molecules* 26.9 (2021), p. 2625.

[216] Austin D Sendek et al. "Quantifying the search for solid Li-ion electrolyte materials by anion: a data-driven perspective". In: *The Journal of Physical Chemistry C* 124.15 (2020), pp. 8067–8079.

[217] Laidong Zhou et al. "A new halospinel superionic conductor for high-voltage all solid state lithium batteries". In: *Energy & Environmental Science* 13.7 (2020), pp. 2056–2063.

[218] Haodong Liu et al. "A disordered rock salt anode for fast-charging lithium-ion batteries". In: *Nature* 585.7823 (2020), pp. 63–67.

[219] Georg Kresse and Jürgen Furthmüller. "Efficiency of ab-initio total energy calculations for metals and semiconductors using a plane-wave basis set". In: *Computational materials science* 6.1 (1996), pp. 15–50.

[220] C Elsässer and S Köstlmeier. "Density-functional modelling of core-hole effects in electron energy-loss near-edge spectra". In: *Ultramicroscopy* 86.3-4 (2001), pp. 325–337.

[221] Paolo Giannozzi et al. "QUANTUM ESPRESSO: a modular and open-source software project for quantum simulations of materials". In: *Journal of physics: Condensed matter* 21.39 (2009), p. 395502.

[222] Edwin E Salpeter and Hans Albrecht Bethe. "A relativistic equation for bound-state problems". In: *Physical Review* 84.6 (1951), p. 1232.

[223] J Vinson et al. "Theoretical optical and x-ray spectra of liquid and solid H_2O". In: *Physical Review B* 85.4 (2012), p. 045101.

[224] YC Chen et al. "Lithium ion diffusion in $Li_{4+x}Ti_5O_{12}$: from ab initio studies". In: *Electrochimica Acta* 56.17 (2011), pp. 6084–6088.

[225] Wei Kong Pang et al. "Lithium migration in $Li_4Ti_5O_{12}$ studied using in situ neutron powder diffraction". In: *Chemistry of Materials* 26.7 (2014), pp. 2318–2326.

[226] Yiyang Li et al. "Current-induced transition from particle-by-particle to concurrent intercalation in phase-separating battery electrodes". In: *Nature materials* 13.12 (2014), pp. 1149–1156.

[227] R Brydson. "Probing the local structure and bonding at interfaces and defects using EELS in the TEM". In: *Journal of Microscopy* 180.3 (1995), pp. 238–249.

Appendix A

Supplemental information for investigating Mg$_x$Cr$_2$O$_4$ as a Mg-ion cathode

Further details on the cluster expansion ECI and the 33% Mg and 50% Mg ground state orderings are provided. An explanation of the free energy integration performed to remove hysteresis in the voltage profile is also provided. The change in unit cell during Mg intercalation is provided and discussed. The 60°C (333 K) voltage profile is plotted along with the DFT, CE-predicted, and 20°C (293 K) voltage profiles shown in the main text. The migration path of an additional Mg in the 50% Mg structure for which migration barriers were calculated is shown. Direct comparisons between NEB migration barriers and the convex hulls of the Mg$_x$Cr$_2$O$_4$ system using the GGA vs. GGA+U functionals are also displayed.

A.1   Cluster expansion ECI information

The cluster expansion is fit to a $Mg_2Cr_4O_8$ primitive cell with Mg at fractional coordinates
(0.375 0.875 0.875) and (0.625 0.125 0.125) in a lattice of matrix:

$$\begin{pmatrix} 4.16384 & 4.16384 & 0 \\ 4.16384 & 0 & -4.16384 \\ 0 & 4.16384 & -4.16384 \end{pmatrix}$$
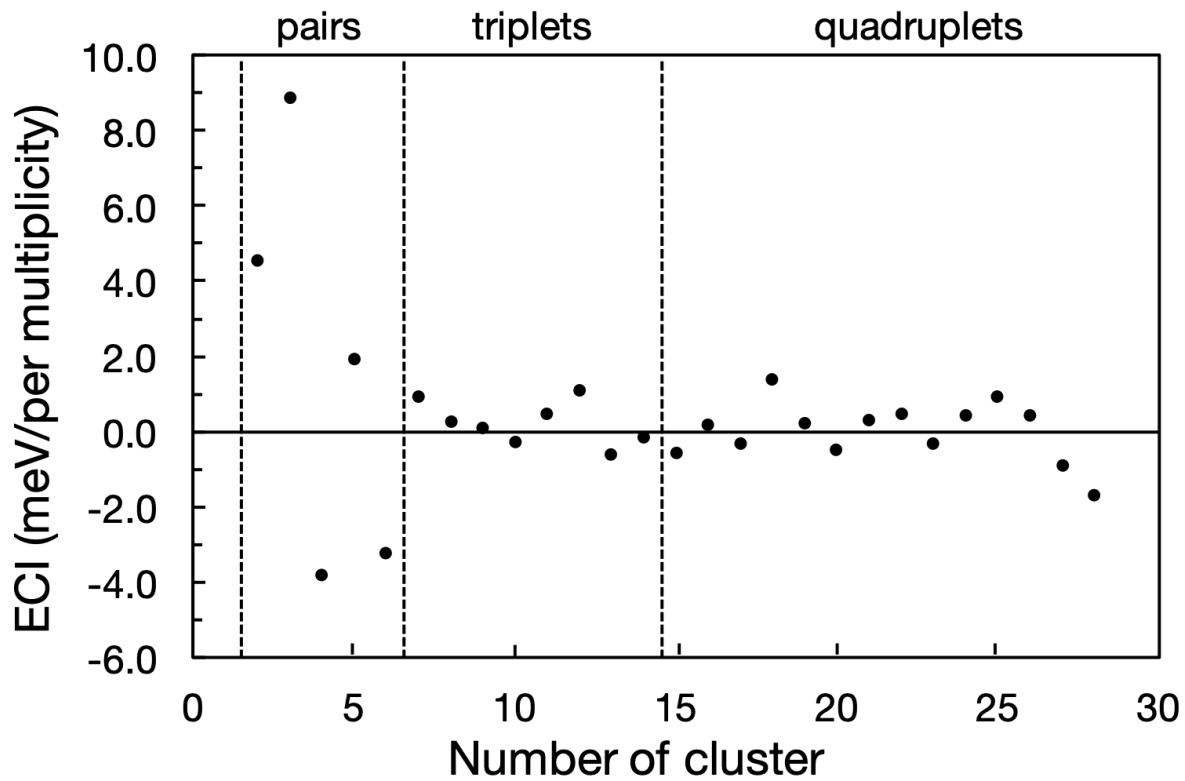
Figure A.1: Fitted ECI for formation energy, with cluster number corresponding to clusters
in Table S1. The zero- and point-cluster terms are not shown, and the pairs, triplets, and
quadruplets ECI's are separated by dashed lines.

A.2 $x = 0.33$ and $x = 0.5$ ground state orderings of $\mathbf{Mg}_x\mathbf{Cr}_2\mathbf{O}_4$

$\mathbf{Mg_2Cr_8O_{16}}$

Lattice parameters

$\mathbf{a} = 5.889, \mathbf{b} = 5.889, \mathbf{c} = 10.199$

Lattice angles

$\boldsymbol{\alpha} = 73.221, \boldsymbol{\beta} = 90.000, \boldsymbol{\gamma} = 120.000$

Cell volume $= 288.763$

Atom	Fractional coordinates		
	x	y	z
Mg	0.375	0.75	0.875
Mg	0.25	0.5	0.25
Cr	0.5625	0.125	0.3125
Cr	0.0625	0.125	0.8125
Cr	0.8125	0.125	0.0625
Cr	0.3125	0.125	0.5625
Cr	0.8125	0.625	0.0625
Cr	0.3125	0.625	0.5625
Cr	0.3125	0.125	0.0625
Cr	0.8125	0.125	0.5625
O	0.94185	0.8837	0.17445
O	0.44185	0.8837	0.67445
O	0.18315	0.3663	0.45055
O	0.68315	0.3663	0.95055
O	0.67445	0.8837	0.44185
O	0.17445	0.8837	0.94185
O	0.45055	0.3663	0.18315
O	0.95055	0.3663	0.68315
O	0.67445	0.3489	0.44185
O	0.17445	0.3489	0.94185
O	0.45055	0.9011	0.183150
O	0.95055	0.9011	0.68315
O	0.20925	0.8837	0.44185
O	0.70925	0.8837	0.94185
O	0.91575	0.3663	0.183150
O	0.41575	0.3663	0.68315

Mg₂Cr₁₂O₂₄

Lattice parameters

$\mathbf{a} = 5.889, \mathbf{b} = 13.167, \mathbf{c} = 5.889$

Lattice angles

$\boldsymbol{\alpha} = 77.079, \boldsymbol{\beta} = 90.000, \boldsymbol{\gamma} = 77.079$

Cell volume $= 433.145$

Atom	Fractional coordinates		
	x	y	z
Mg	0.916667	0.166667	0.416667
Mg	0.166667	0.666667	0.166667
Cr	0.375	0.25	0.125
Cr	0.708333	0.583333	0.458333
Cr	0.041667	0.916667	0.791667
Cr	0.708333	0.083333	0.958333
Cr	0.041667	0.416667	0.291667
Cr	0.375	0.75	0.625
Cr	0.375	0.25	0.625
Cr	0.708333	0.583333	0.958333
Cr	0.041667	0.916667	0.291667
Cr	0.208333	0.083333	0.958333
Cr	0.541667	0.416667	0.291667
Cr	0.875	0.75	0.625
O	0.294567	0.410867	0.527167
O	0.6279	0.442	0.8605
O	0.961233	0.077533	0.193833
O	0.788767	0.422467	0.056167
O	0.1221	0.7558	0.3895
O	0.455433	0.089133	0.722833
O	0.938033	0.589133	0.705433
O	0.271367	0.922467	0.038767
O	0.6047	0.2558	0.3721
O	0.1453	0.2442	0.8779
O	0.478633	0.577533	0.211233
O	0.811967	0.910867	0.544567
O	0.294567	0.410867	0.061967
O	0.6279	0.7442	0.3953
O	0.961233	0.077533	0.728633
O	0.788767	0.422467	0.521367
O	0.1221	0.7558	0.8547
O	0.455433	0.089133	0.188033
O	0.472833	0.589133	0.705433
O	0.806167	0.922467	0.038767
O	0.1395	0.2558	0.3721
O	0.6105	0.2442	0.8779
O	0.943833	0.577533	0.211233
O	0.277167	0.910867	0.544567
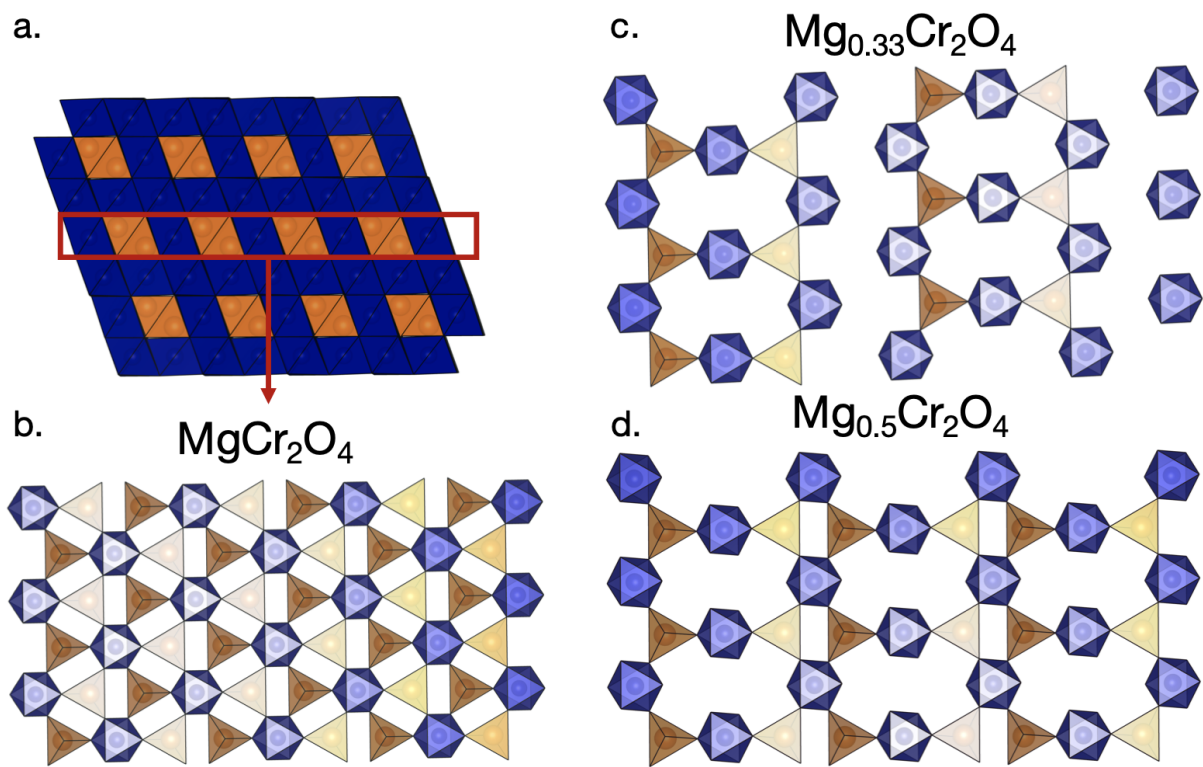
Figure A.2: Orderings of Mg in the Mg-Cr layer in various states of Mg concentration x in $Mg_xCr_2O_4$, with Mg represented by orange tetrahedral and Cr represented by blue octahedral and O at the vertices of the polyhedra. (a) Mg-Cr layer outlined in red in fully magnesiated $MgCr_2O_4$. Mg-Cr layer in the (111) direction of (b) $MgCr_2O_4$, (c) $Mg_{0.33}Cr_2O_4$, and (d) $Mg_{0.5}Cr_2O_4$.

A.3 Free energy integration
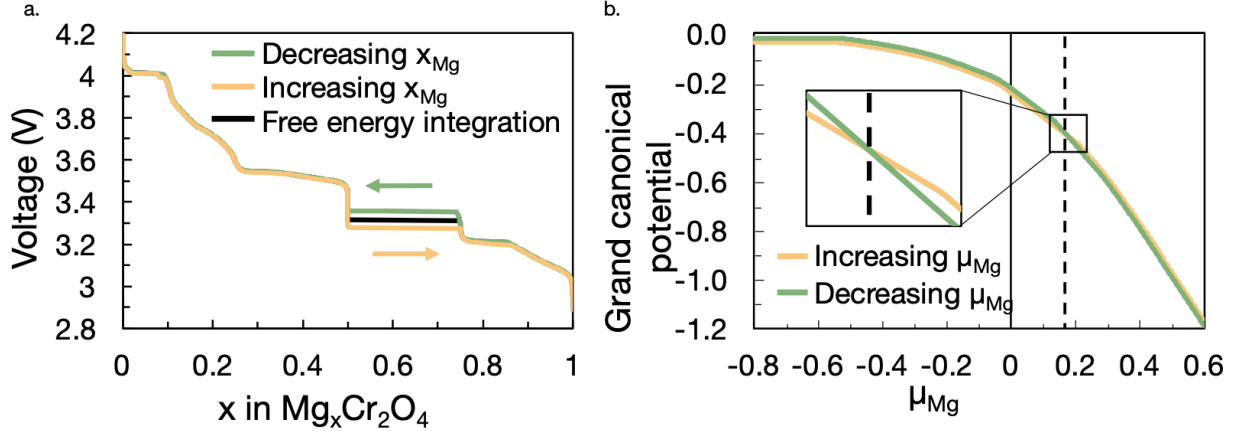
Figure A.3: (a) Demonstration of free energy integration from Grand canonical Monte Carlo scans over decreasing x_{Mg} (green) and increasing x_{Mg} (yellow) to obtain the free energy-integrated curve (black). (b) The Grand canonical Monte Carlo scans from (a) plotted in the Grand canonical potential-μ_{Mg} space, with the Grand canonical potential (ϕ) calculated from Equation A.1. Yellow and green lines in (b) represent scans in increasing and decreasing μ_{Mg}, respectively. The free-energy-integrated voltage curve in (a) is the lower envelope of the green and yellow lines in (b). The vertical black dashed line marks the μ_{Mg} where the yellow and green lines intersect ($\mu_{Mg} \sim 1.9$), while the inset shows a zoom-in of the intersection.

Hysteresis can be observed in Monte Carlo simulations, leading to quantitatively differ-ent voltage profiles and transition temperatures while simulating phase transitions.[113] For example, from Figure A.3a, the voltage curves calculated from an increasing x_{Mg} (yellow line) and a decreasing x_{Mg} (green) Monte Carlo scans differ significantly at $x_{Mg} \sim 0.5$ (3.27 V in the increasing x_{Mg} scan and 3.36 V in the decreasing x_{Mg} scan). Such hysteresis can be removed via free energy integration. Figure A.33 demonstrates free energy integration between $x_{Mg} \sim 0$ and $x_{Mg} \sim 1$, which corresponds to $\mu_{Mg} \sim -0.8$ and $\mu_{Mg} \sim 0.6$, re-spectively. The free energy integration is calculated by performing Grand canonical Monte Carlo scans in both increasing (yellow line in Figure A.3b) and decreasing (green) μ_{Mg} and subsequently taking the lower envelope of free energy obtained from the two scans in the Grand canonical potential-μ_{Mg} space. As in Hinuma, *et al.* [113], we calculate the Grand canonical potential at a given μ_{Mg} and temperature ($T = 293$ K) based on the integral of the average concentration $\langle N(T = 293\text{K}, \mu) \rangle$ over $d\mu$, from an initial reference state where the Grand canonical potential is known (at $\mu{=}\mu_0$) as

$$\phi(293\text{K}, \mu_{Mg}) = \phi(293\text{K}, \mu_0) - \int_{\mu_0}^{\mu_{Mg}} \langle N(293\text{K}, \mu) \rangle \, d\mu \qquad (A.1)$$

91

For the yellow curve in Figure A.3b, $\mu_0 \sim -0.8$ ($x_{Mg} = 0$) and $d\mu > 0$, while the green curve has $\mu_0 \sim 0.6$) ($x_{Mg} = 1$) and $d\mu < 0$. In Figure A.3b, the lower envelope of the yellow and green lines corresponds to the true minimum of the Grand-canonical potential at each μ_{Mg}, i.e., the yellow line from $\mu_0 \sim -0.8$ to $\mu_0 \sim 1.9$ and the green line from $\mu_0 \sim 1.9$ to $\mu_0 \sim 0.6$, which in turn leads to the voltage curve without any numerical hysteresis (black in Figure A.3a). The dashed black line in Figure A.3b corresponds to the μ_{Mg} at which the green and yellow line intersect in the Grand canonical potential-μ_{Mg} space (Figure A.3b). After free energy integration, the voltage plateau from $x_{Mg} \sim 0.5$ to $x_{Mg} \sim 0.75$ is 3.31 V.

From Figure A.3a (black), we note that we are missing a 33% Mg voltage step in the free energy-integrated voltage curve. However, we consider the 33% Mg ground state to be important due to its high depth (Figure 2.2 in main text). Further, canonical Monte Carlo scans (at constant x_{Mg}) and increasing temperature indicate that the 33% Mg structure should be a ground state at both 0 K and 293 K. Thus, to obtain an accurate voltage curve including the 33% Mg ground state, we use a free energy integration scheme between 25% and 50% Mg and initiate Monte Carlo scans from the missing 33% Mg configuration.

Figure A.4 demonstrates free energy integration between 25% and 50% Mg ($\mu_{Mg} \sim -0.3$ to $\mu_{Mg} \sim 0.2$), analogous to Figure A.3. Here, we start from the free energy-integrated curve of Figure A.3 (also black in Figure A.4a-b) and perform Grand canonical Monte Carlo scans from an initial $\mu_0 = 0$ ($x_{Mg} \sim 33\%$, the ground state at 293 K) with, separately, increasing (yellow in Figure A.4b) and decreasing (green) μ_{Mg}. The voltage curve from the free energy integration (red curve in Figure A.4a) is given by the lower envelope of the yellow, green, and black curves in Figure A.4b, which is composed of the black curve from $\mu_{Mg} \sim -0.3$ to $\mu_{Mg} \sim -0.15$, the green curve from $\mu_{Mg} \sim -0.15$ to $\mu_{Mg} \sim 0$, the yellow curve from $\mu_{Mg} \sim 0$ to $\mu_{Mg} \sim 0.07$, and the black curve from $\mu_{Mg} \sim 0.07$ to $\mu_{Mg} \sim 0.2$. Thus, the configurations along the lower envelope of Figure A.4b are $\sim 25\%$ Mg from $\mu_{Mg} \sim -0.3$ to $\mu_{Mg} \sim -0.15$, 33% Mg from $\mu_{Mg} \sim -0.15$ to $\mu_{Mg} \sim 0.07$, and 50% Mg from $\mu_{Mg} \sim 0.07$ to $\mu_{Mg} \sim 0.17$. The voltage curve in Figure A.4a exhibits a voltage jump at 33% Mg from 3.46 V to 3.66 V due to the second free energy integration we perform between 25% Mg and 50% Mg.
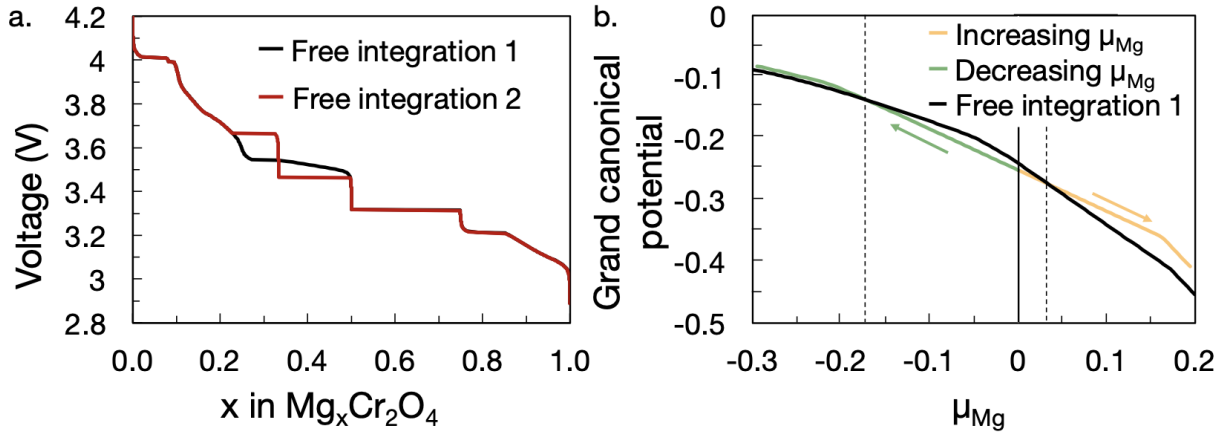
Figure A.4: (a) Plot of the voltage curve before (black) and after (red) free energy integration to obtain a voltage curve with the 33% Mg voltage step starting from the voltage profile obtained over the entire Mg composition range obtained in Figure A.3 (black line in Figure A.3). (b) Grand canonical Monte Carlo scans starting from $\mu_0 = 0$ and increasing (yellow) and decreasing (green) in μ_{Mg}. We additionally show the curve from the first free energy integration (from Figure A.3) in the Grand chemical potential-μ_{Mg} space (panel b). The red curve in (a) is obtained by taking the lower envelope of the yellow, green, and black curves in (b). The vertical dashed black lines in (b) show where the green and black curves intersect ($\mu_{Mg} \sim -1.5$) and where the yellow and black curves intersect ($\mu_{Mg} \sim 0.07$).

A.4 Volume change during Mg intercalation
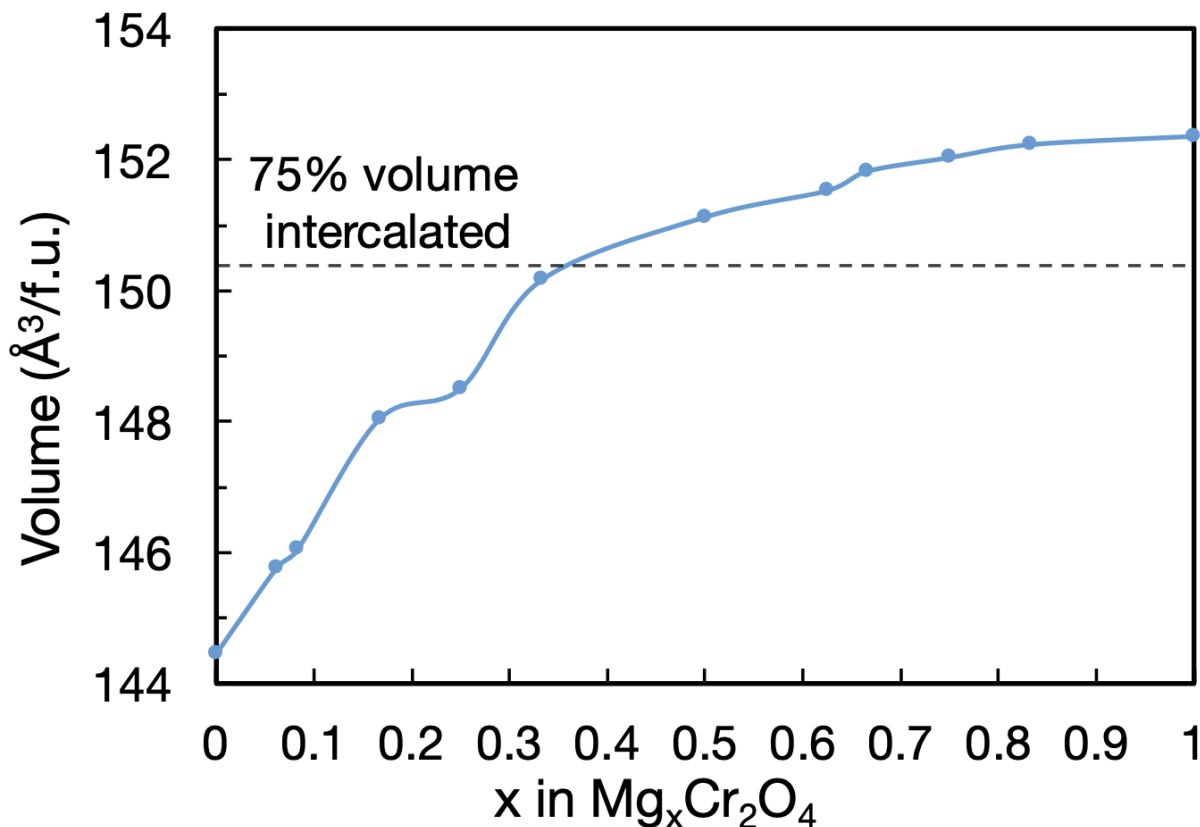
Figure A.5: Volume expansion of $Mg_xCr_2O_4$ ground states as Mg is intercalated from the system is shown through a plot of the volume/f.u. of the DFT ground states against the Mg concentration. The dashed line indicates where 75% of the volume increase occurs during Mg intercalation into the charged-Cr_2O_4.

Figure A.5 plots the volume/f.u. of the ground states at the corresponding Mg concentrations of the ground states to investigate the volume change during intercalation. From the fully charged to the fully discharged states, the structure experiences a total volume expansion of 5.2%. Interestingly, the spinel lattice expands most rapidly at low levels of magnesiation, leading to a 4.0% volume increase from the 0% Mg (at 144.5 $Å^3$/f.u.) to the 33% Mg (at 150.2 $Å^3$/f.u.). Beyond 33% Mg, the spinel expands to a lesser extent, further increasing 1.5% in volume (up to 152.4 $Å^3$/f.u.) at 100% Mg. Thus, 72.5% of the total volume expansion occurs between 0% Mg and 33% Mg while the remaining 27.5% of the total volume expansion occurs between 33% Mg and 100% Mg content.

A.5 Voltage curve at elevated temperature

Figure A.6 plots the 333 K voltage curve calculated from Monte-Carlo simulations of the CE (solid blue). Note that the 333 K voltage curve lies directly on top of the 293 K CE-predicted voltage curve (solid black line), indicating that there should be negligible change in the voltage profile with the increase in temperature from 293 K to 333 K.
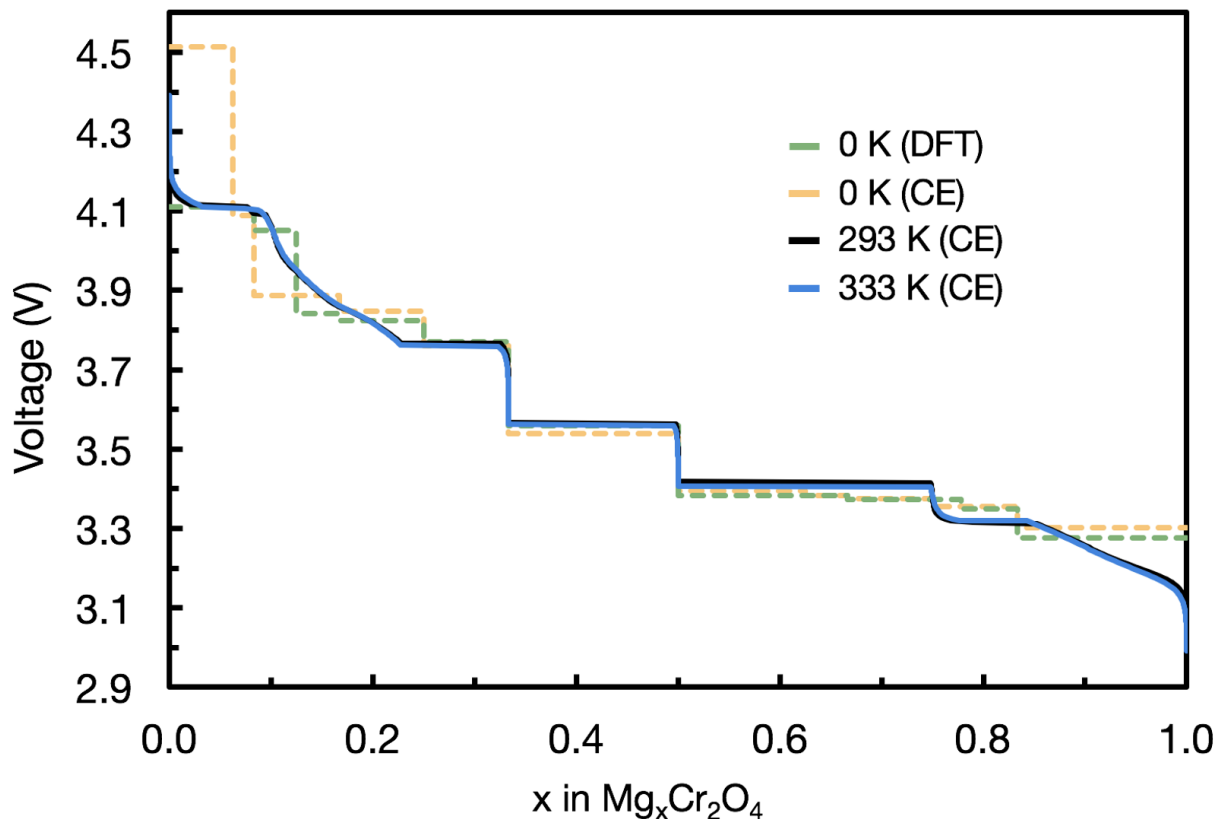
Figure A.6: Voltage curves calculated from the DFT convex hull (green dashed), from the CE-predicted convex hull at 0 K (yellow dashed), from Monte Carlo calculations using the CE at room temperature (293 K, black), and from Monte Carlo calculations using the CE at 60°(333 K, blue).

A.6 Migration path of additional Mg in $Mg_{0.5}Cr_2O_4$ ground state ordering
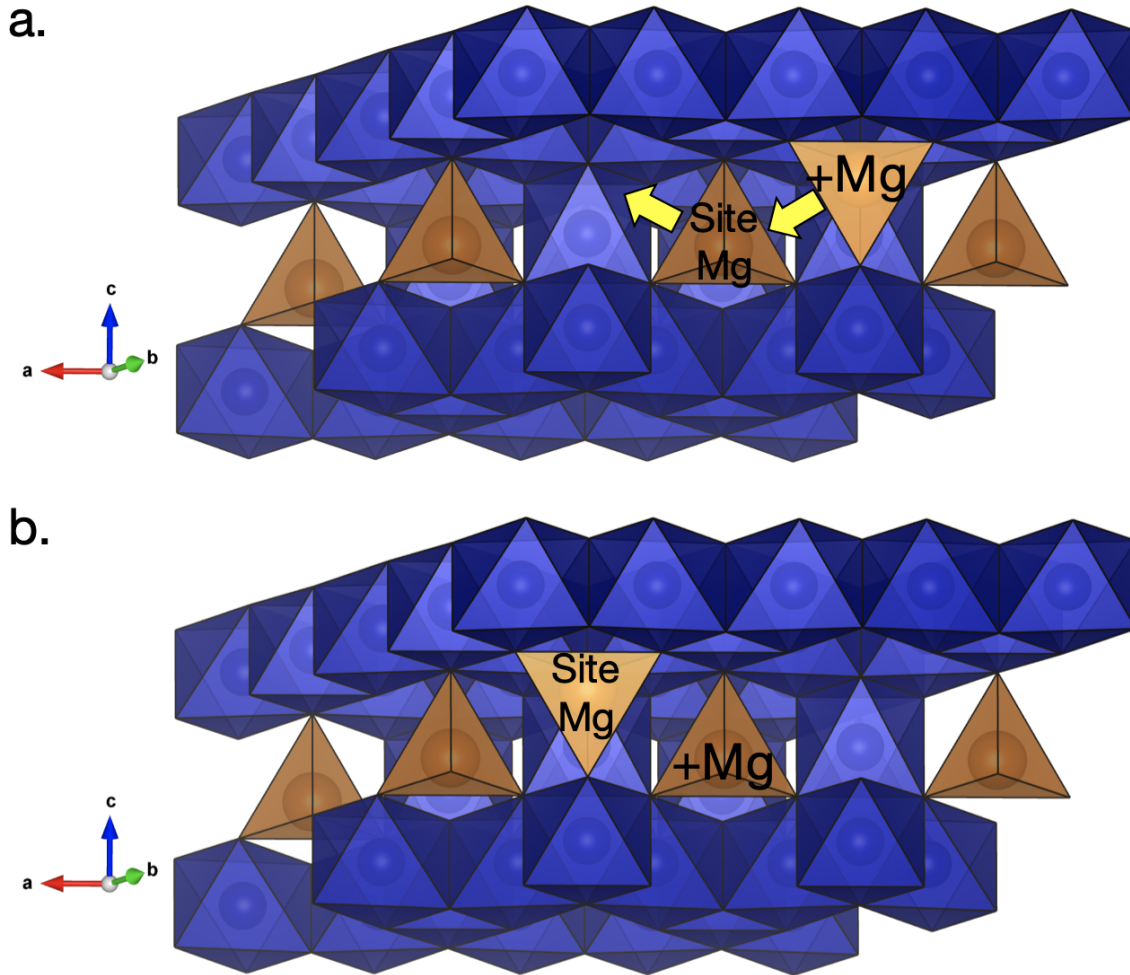
Figure A.7: (a) Initial and (b) final states of the considered migration path for the 50% Mg with additional Mg configuration. The added Mg, labeled "+Mg", is inserted in a site that is not occupied in the 50% Mg ground state ordering. "+Mg" migrates to an adjacent Mg site which is occupied in the 50% Mg ground state ordering, labeled "Site Mg". Because the adjacent site is occupied in (a) by "Site Mg", the migration of "+Mg" from inserted site to adjacent site is accompanied by the migration of "Site Mg" from the adjacent site to a site equivalent to the inserted site.

A.7 Comparison between GGA+U and GGA NEB barriers
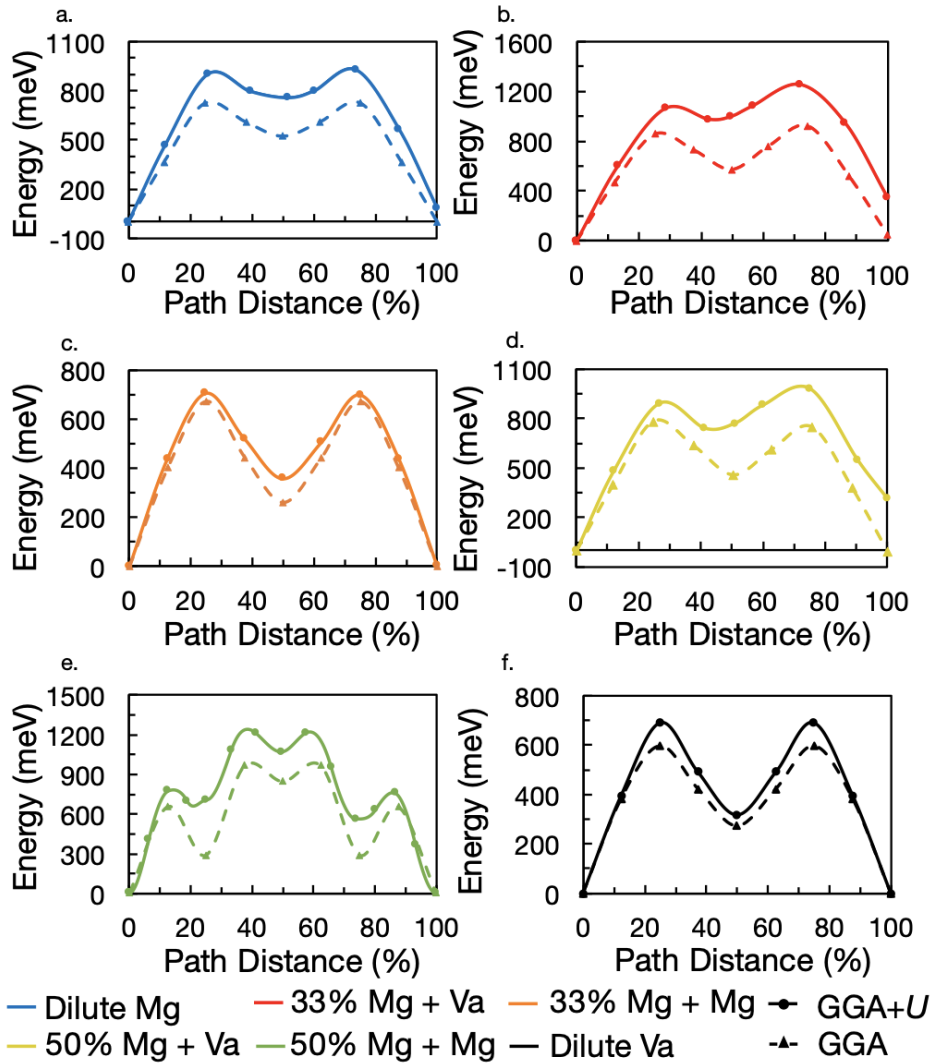
Figure A.8: Comparison between the activation migration barriers using the GGA (dashed) vs. GGA+U (solid) functionals in DFT-based NEB. The migration barriers are shown at the dilute Mg (blue), 33% Mg with additional vacancy (red), 33% Mg with additional Mg (orange), 50% Mg with additional vacancy (yellow), 50% Mg with additional Mg (green), and dilute vacancy (black) configurations.

Figure A.8 shows in each plot a comparison between the migration barriers calculated using DFT with GGA (solid) and GGA+U (solid). Migration barriers were calculated for the

dilute Mg, 33% Mg (with both additional vacancy and additional Mg), 50% Mg (with both additional vacancy and additional Mg), and dilute vacancy configurations (see Figures 2.5 and 2.6 in Chapter 2). In all cases, the GGA+U barriers are higher than the GGA barriers for the same configuration. The dilute Va and 33% Mg with additional Mg barriers are the most similar between GGA and GGA+U, with a barrier increases of only $\sim$90 meV and $\sim$30 meV respectively with GGA+U compared to the GGA barrier. However, the barriers of the dilute vacancy, 33% Mg with additional Mg, 50% Mg with additional vacancy, and 50% Mg with additional Mg configurations increase considerably, by $\sim$200 meV, $\sim$320 meV, $\sim$200 meV, and $\sim$250 meV respectively, when GGA+U is employed instead of GGA. Also, the migration energy profiles at 33% Mg and 50% Mg with additional vacancies demonstrate a large difference in energy (300-350 meV) between the initial site (0% path distance) and final site (100% path distance) when using GGA+U instead of GGA.

A.8 Comparison between GGA vs. GGA+U convex ground state hulls

Figure A.9 shows a comparison between the convex hulls of the $Mg_xCr_2O_4$ when calculating energies of configurations using DFT using the GGA vs. GGA+U functionals. In order to demonstrate the difference in functionals, we consider only the GGA+U ground states when calculating both of the convex hulls. Notably, 8.3%, 25%, 62.5%, and 75% ground states in GGA+U are no longer ground states when the energies are calculated using GGA. Further, the 16% Mg and 66% Mg ground states are much deeper (from $E_{\text{tie-line}} < 5$ meV to $E_{\text{tie-line}} > 10$ meV). Thus, both the shape of the ground state hulls (which affects the voltage) and the depths of ground state configurations (which indicate the important Mg-Va orderings that may lead to high Mg migration barriers) are evaluated differently in GGA compared to GGA+U.
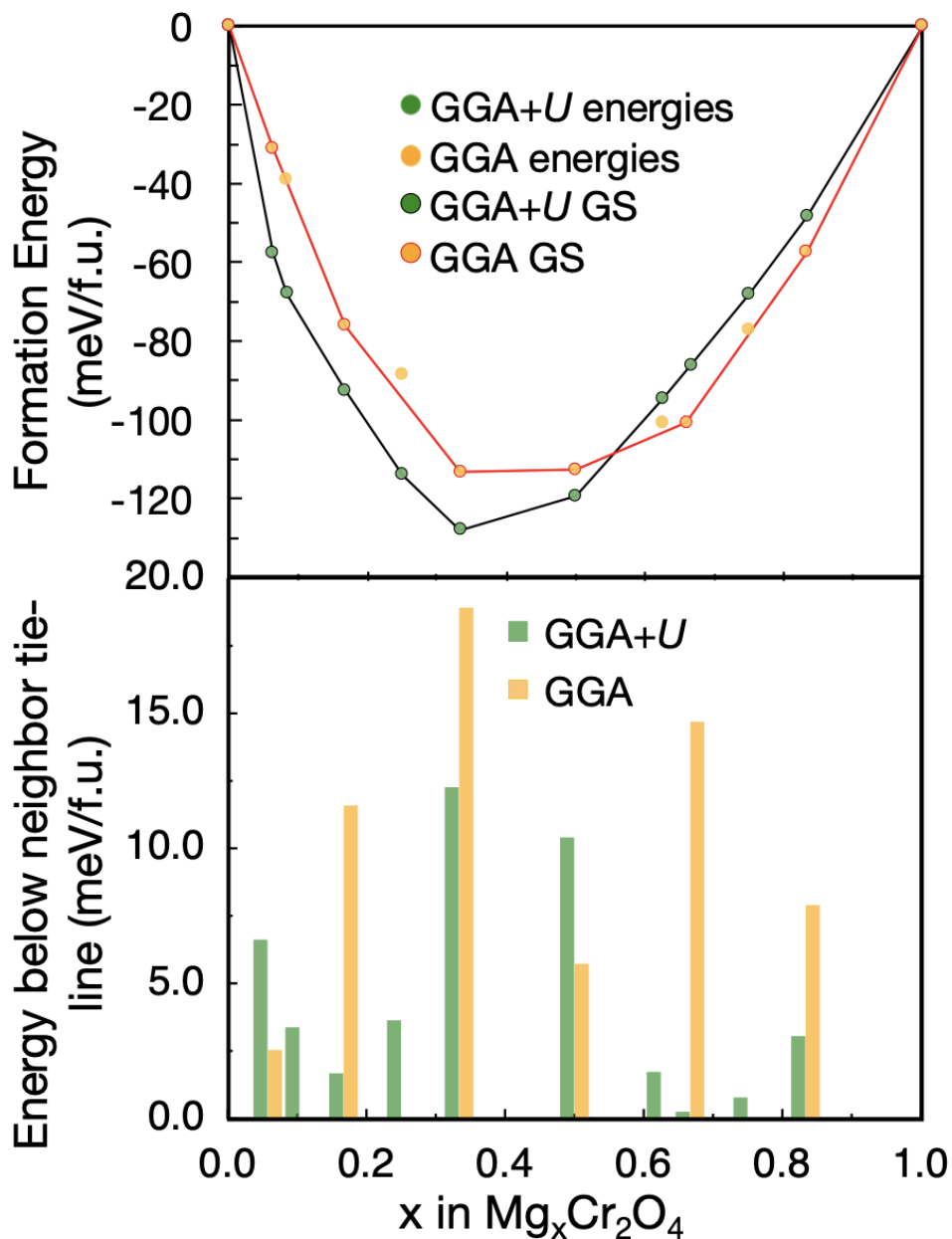
Figure A.9: Comparison between the convex hulls of the $Mg_xCr_2O_4$ system with configurations calculated in DFT using the GGA (yellow circles) vs. GGA+U (green circles) functionals. The GGA+U convex hull is delineated in black (with ground states outlined in black), while the GGA convex hull is delineated in red (and ground states outlined in red). The GGA convex hull was constructed by calculating the energies of the GGA+U ground states within the GGA framework.

Appendix B

Supplemental information for investigating the kinetics of $\mathbf{Li_{4+x}Ti_5O_{12}}$

The materials and methods are described. Further details describing the local reaction in the LTO electrodes, the redox of Ti during (dis)charge, on the Li-EELS spectra (from ex situ measurements and its rate dependence) are provided. We also analyze the calculated Li-EELS pre-edge fine structure of the atomic configurations and Li polyhedral distortions in the low-energy intermediate configurations. We identify the correlation between the pre-peak M and the local distortion in the Li polyhedra. We additionally provide the detailed calculated migration paths not shown in the main text. More detailed experimental characterization of the electrochemical cell and its components is also provided.

B.1 Materials and methods

B.1.1 Phase stability calculation details

All first-principles calculations were performed with the Perdew–Burke–Ernzerhof exchange-correlation parameterization to density functional theory (DFT) using the spin-polarized generalized gradient approximation [91]. The projector-augmented wave pseudopotentials were used as implemented in the Vienna ab initio simulation package (VASP) version 5.3.5 [219]. We used a plane-wave basis set with an energy cutoff of 520 eV and sampled $5 \times 2 \times 5$ gamma-centered k-point meshes for $1 \times 3 \times 1$ supercells of a primitive cell of spinel $Li_4Ti_4O_8$ to find stable configurations of $Li_{4+x}Ti_5O_{12}$ ($x = 0, 1, 2,$ and 3).

B.1.2 Calculation of Li-EELS spectra

The $Z+1$ approximation was employed to calculate the Li-EELS spectra [220] of $Li_{4+x}Ti_5O_{12}$. We used large supercells of $2 \times 3 \times 2$ primitive unit cells of spinel $Li_{2.67+x}Ti_{3.33}O_8$ with a gamma-centered $1 \times 1 \times 1$ k-point grid and a large number of unoccupied bands (three times the number of occupied bands) to accurately predict EELS spectra [220]. At each configuration of $Li_{4+x}Ti_5O_{12}$ ($x = 0, 1, 2,$ and 3), EELS spectra were computed for all symmetrically inequivalent Li-ions within supercells and summed with weighting by their multiplicities. The computed total EELS spectra were aligned at 61.5 eV (the main peak position of the experimental spectra). The resolution of the computed total EELS intensities in Figure B.5A was reduced by convolution with the Gaussian distribution and a full width at half maximum (FWHM) of 1 eV in order to consider the effect of instrumental broadening of operando EELS spectra. To clearly see the differences between the spectra of individual Li ions at the 8a, 16c, and 16d sites, we used a FWHM of 0.5 eV for individual EELS peaks.

To validate the $Z+1$ method used for computing the Li-EELS spectra, we compared them with the spectra obtained using the Obtaining Core Excitations from Ab initio Electronic Structure and NBSE (OCEAN) package version 2.5.2.[220] Ground-state wave functions and orbital energies, which are used as inputs for OCEAN calculations, were obtained from plane-wave norm-conserving (NC) pseudopotential calculations using Quantum ESPRESSO package version 6.3 [221] with a kinetic energy cutoff of 100 Ry. We verified that the total density of states of $Li_7Ti_5O_{12}$ is almost identical for VASP and Quantum ESPRESSO calculations. The electron–core hole interaction was treated using the Bethe–Salpeter equation [222]. A total of 1600 bands were included (approximately 100 eV above the Fermi level) to compute the screened core-hole potential in the OCEAN calculations. In the OCEAN calculations, the reference Li 1s core hole energy level was set to 8.54 eV. Relative core level shifts were calculated according to the procedure described in Ref. [223]. All OCEAN spectra were shifted by a constant energy of 47.9 eV to align with experimental spectra and broadened with a Gaussian broadening with a FWHM of 1.2 eV. Figure B.4 shows that both computational methods predict similar energy positions of pre-peak S and relative intensities

compared with those of the main peak for both $Li_4Ti_5O_{12}$ and $Li_7Ti_5O_{12}$, which is in good agreement with the experiments, further validating our method to predict Li-EELS spectra.

B.1.3   Calculation of Li migration barriers

Li migration barriers were calculated using the nudged-elastic band (NEB) method [118, 119] within a supercell containing 8 formula units of $Li_{4+x}Ti_5O_{12}$ ($Li_{33}Ti_{40}O_{96}$), $Li_{5+x}Ti_5O_{12}$ ($Li_{41}Ti_{40}O_{96}$), and $Li_{7-x}Ti_5O_{12}$ ($Li_{55}Ti_{40}O_{96}$). Compared to previously considered migration pathways, the proposed migration pathway considers interstitial Li at the $Li_4Ti_5O_{12}$ and $Li_5Ti_5O_{12}$ concentrations rather than vacancies in the $Li_4Ti_5O_{12}$ structure [172, 224]. The use of interstitial Li^+ as the percolating defect at these compositions is consistent with the high Li^+ chemical potential applied to insert Li^+ into $Li_4Ti_5O_{12}$ and also with the sudden increase in Li^+ diffusivity observed at $Li_{4.1}Ti_5O_{12}$ [174].

In situ neutron powder diffraction analysis revealed that the main hopping mechanism of Li in $Li_4Ti_5O_{12}$ is from the 8a sites to 16c sites and vice versa.[225] Thus, for the NEB method for calculations with interstitial Li, we stitched together a series of 5 hops that resulted in symmetrically equivalent beginning and end configurations to ensure that the stitched-together pathway was percolating. For each of the hops, we used three replicas of the systems, except for the last hop of the $Li_{4+x}Ti_5O_{12}$ calculation, which used five replicas because of the length of the hop. The $Li_{7-x}Ti_5O_{12}$ pathway is a simpler 16c-8a-16c path compared to the complex configurations involving the interstitials, so we calculate a simple pair of 16c-8a and 8a-16c hops using 7 replicas total. The replicas were initiated by linear interpolation between the initial and final configurations of each individual hop. All the lattice parameters were fixed as before with one interstitial lithium or lithium vacancy added. The atomic positions within the supercell were relaxed to an energy convergence criterion of 10^{-5} eV and a force convergence criterion of 0.05 eV $Å^{-1}$. A plane wave energy cutoff of 520 eV and a gamma-centered $1 \times 1 \times 1$ k-point grid was used.

B.1.4   Experimental methods and materials

Electrochemical measurements

The electrodes for coin cells were prepared by casting slurry of 60 wt.% $Li_4Ti_5O_{12}$, 20 wt% Super P carbon, and 20 wt.% polyvinylidene difluoride. These cathodes were assembled into 2032-type coin cells in an Ar glovebox, with a metallic lithium foil (MTI Crop.) as the counter electrode and glass microfiber (Whatman, GF/D) as the separator. Ionic liquid (IL) containing 1.0 M lithium bis(trifluoromethanesulfonyl)imide (LiTFSI) in 1-butyl-1-methylpyrrolidinium bis(trifluoromethylsulfonyl)imide was used as the electrolyte. Organic liquid electrolyte with 1 M $LiPF_6$ in a 1:1 volume ratio of dimethyl carbonate and ethylene carbonate was also used for comparison. The electrochemical charge-discharge tests were performed in galvanostatic mode between 1.0 and 2.5 V at different C-rates, using a battery cycler (Arbin Instrument, BT-2400). The theoretical capacity of the lithium titanate (LTO)

electrode was set to 175 mA h g^{-1} (i.e., the specific current corresponding to 1 C is 175 mA g^{-1}). Cyclic voltammetry (CV) curves of LTO electrodes were recorded at a scanning rate of 0.1 mV s^{-1} between 1.0 and 2.5 V.

Transmission electron microscopy – electron energy-loss spectroscopy characterization

Transmission electron microscopy (TEM) images, electron energy-loss spectroscopy (EELS) data, high-angle annular dark-field (HAADF) images, and selected area electron diffraction (SAED) patterns were obtained using a JEOL ARM 200F microscope equipped with two spherical-aberration correctors, a cold-field-emission electron source, and a high-resolution dual-EELS spectrometer. The energy resolution of the EELS spectra is about 0.5 eV (estimated by the full width of the half magnitude (FWHM) of the zero-loss peak). The coin cells for the ex situ TEM measurements were disassembled in a glovebox, immediately after completing the electrochemical tests. The electrodes were dispersed in dimethyl carbonate and loaded onto a copper grid, and then sealed in an Ar glovebox bag for transferring into the TEM column. All the EELS measurements were performed in diffraction mode. The electron beam was spread to the greatest extent possible to minimize electron beam irradiation.

Operando TEM-EELS experiments

Operando EELS measurements were performed using an electrochemical cell designed for operation in a TEM, using a similar configuration as a real battery system and consisting of a TEM-grid-based electrode loaded with active materials (working electrode), a Li metal plate (counter electrode), and added IL electrolyte to enable electrochemical functionality analogous to a real battery system.

To prepare the working electrode, a dilute solution with LTO nanoparticles in isopropanol alcohol was first sonicated for approximately 10 minutes and then dripped over an amorphous carbon film supported on a TEM half grid. The carbon film fulfilled a similar role as the carbon black used in general electrodes, acting as the media for transporting electrons and ions. A thin layer of IL was applied to the carbon film as electrolyte. The Li metal plate was directly connected to the IL. After assembling the cell, it was loaded onto a TEM holder suitable for electrical biasing (Nanofactory), which was sealed in an Ar-filled bag and transferred to the TEM column. A Biologic SP-200 potentiostat was used for the operando measurements in galvanostatic mode, and with a low current option, precisely controlled current (1–30 nA) was applied to the cell to trigger Li-ion migration between the TEM-grid-based electrode and Li metal, similar to the process that occurs in a real battery system. To estimate the cycling rates (C-rates), the electrochemical cells were galvanostatically cycled under a wide range of currents. The global C-rates were estimated based on the applied current and elapsed time for the full discharging/charging processes.

EELS spectra were acquired in TEM diffraction mode from local regions selected using an

aperture with a diameter of 180 nm, allowing for fast data acquisition under the prerequisite low-dose irradiation condition. By taking advantage of the small characteristic angle of Li K-edge ($\sim$0.1 mrad) a small collection angle was used (with a semi-angle $\sim$ 0.9 mrad) to lower the plasmon plural scattering. Li K-edge EELS (Li-EELS) data were recorded at a rate of 0.1 s/spectrum, and Ti L-edge and O K-edge spectra were recorded at 2 s/spectrum. Hundreds of Li-EELS spectra were recorded as the (de)lithiation progressed for real-time tracking of the occupancy and migration of Li ions in the LTO nanoparticles. All EELS spectra were deconvoluted to remove the multiple-scattering components. The area intensities I_M and I_S were measured by Lorentzian fitting of pre-peaks M and S of numerous operando EELS spectra.

B.2 Local reaction in LTO electrodes

Based on the operando EELS experiments with a spatial resolution limit of 180 nm (based on the diameter of selected area aperture), the reaction in LTO is likely to differ from the particle-by-particle behavior observed in $LiFePO_4$ (LFP) [226]. When the particle-by-particle reaction occurs in LFP, only a small number of particles carry most of the current and will be (de)lithiated [226]. Therefore, the time to (dis)charge an individual particle is less than the full electrode (dis)charging time [226]. In the case of LTO, the appearance of pre-peak M was detected throughout the whole (dis)charging process in all the sampled regions, regardless of the applied cycling rate (Figure 3.2E), indicating that in LTO the lithiation is mostly homogeneous.

Furthermore, if we assume the particle-by-particle reaction occurs in LTO, lithiation should occur in a sequential order in the selected regions, i.e. first in one particle, and then in the second particle after completing lithiation in the first particle, and so forth. Therefore, if the particle-by-particle reaction were to take place in local regions, pre-peak M would appear during lithiation in the first particle and then reduce in peak intensity when lithiation finishes in the first particle, appear again when the reaction occurs in the second particle, and then disappear again when the reaction is completed in the second particle, and so forth. However, no such intensity oscillation of pre-peak M is observed in Figure 3.2E. Instead, the intensity of pre-peak M continuously increases at the beginning of (dis)charge, remains almost constant in the middle of (dis)charge, and then decreases at the end of (dis)charge (Figure 3.2E). Therefore, the absence of the peak intensity oscillation does not support the particle-by-particle reaction in LTO. It is instead more likely that the LTO system follows the occurrence of (de)lithiation, which may result from the very low energy barrier for nucleation and growth of a new phase due to the negligible strain energy and interfacial energy at the phase boundaries.

B.3 Redox of Ti in LTO during charging/discharging

As illustrated in Figure B.1A, the Ti L-edge slightly shifted to a lower energy by approximately 0.5 eV after discharge because of the reduction of Ti to Ti^{3+} in LTO. The Ti L-edge shifted back upon charge indicating oxidation of Ti to Ti^{4+}. Correspondingly, the intensity of the pre-peak at the O K-edge decreased in the spectrum of the discharged sample and then increased in the spectra of the charged sample (Figure B.1B). All of these features are related to the formation of $Li_7Ti_5O_{12}$ after discharge [179], which transforms back into $Li_4Ti_5O_{12}$ after charge.
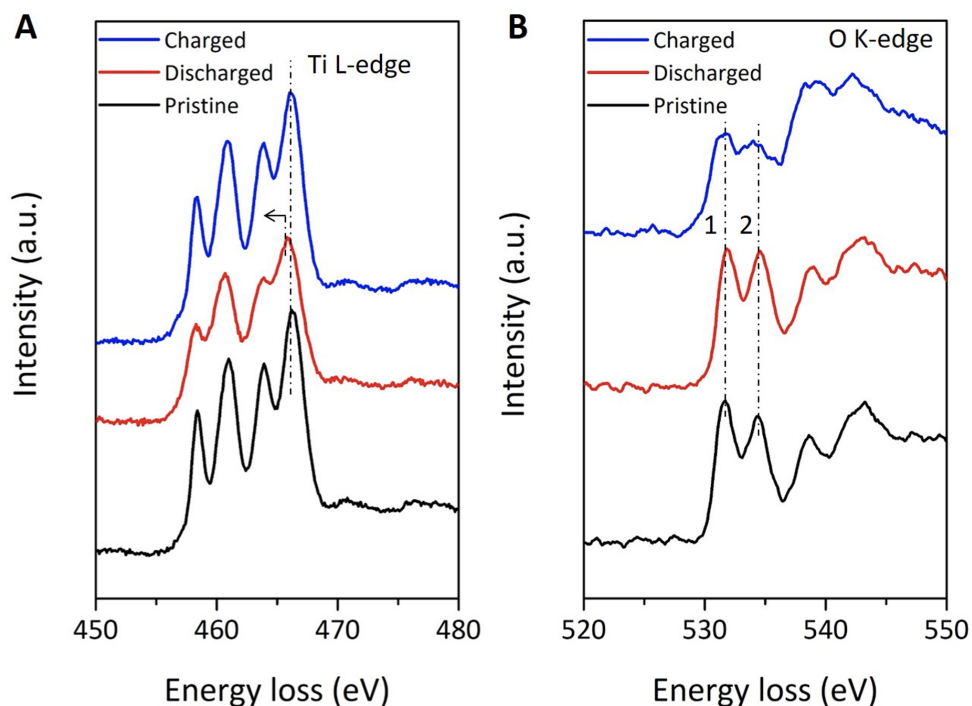
Figure B.1: Evolution of (A) Ti L-edge, and (B) O K-edge spectra for pristine (black line), discharged (red line), and charged (blue line) states during galvanostatic cycling of the nanoparticles shown in Fig. 3.2A. Four distinct peaks in Ti L_{23} (A) representing the e_g and t_{2g} electron orbitals of the Ti L_2 and L_3 energy positions were clearly visible in pristine and charged samples. The peaks became broader and peak separation of e_g and t_{2g} were less pronounced in the discharged sample, indicating the decreased valence state in discharged sample. The intensity of pre-peak 1 in (B) was reduced and became similar to that of pre-peak 2 after discharge; however, it increased and became higher than that of pre-peak 2 after charge.

B.4 Li-K-edge EELS (Li-EELS) spectra from ex situ measurements

Ex situ Li-EELS measurements were performed on pristine, half-discharged, and fully charged electrodes, with the main results shown in Figure B.2 for comparison with the operando results (Figure 3.2C). A pre-peak S in Li-EELS spectra was observed in the pristine sample as well as in the half- and fully discharged samples, arising from Li^+ in 8a and 16c sites in $Li_4Ti_5O_{12}$ and $Li_7Ti_5O_{12}$ phases as previously reported [179]. However, pre-peak M, which was observed in operando EELS experiments (Figure 3.2C), was not detected in the half-discharged sample, further confirming that pre-preak M originates from Li in the metastable intermediates $Li_{4+x}Ti_5O_{12}$.
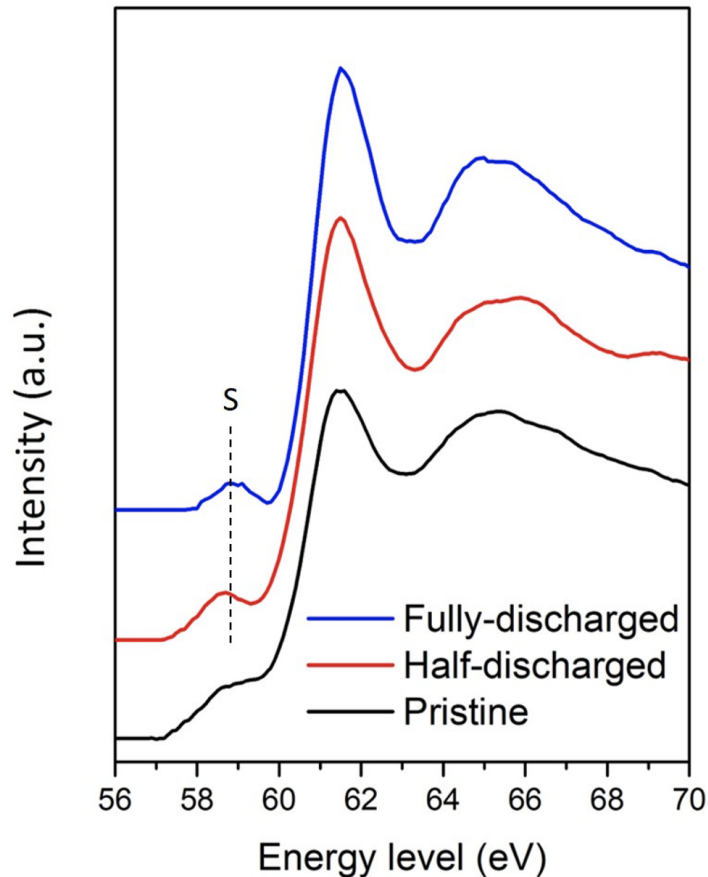
Figure B.2: Ex situ Li-EELS spectra obtained from the pristine (black), half-discharged (red), and fully discharged electrodes (blue). Only pre-peak S was observed in the spectra of the half- and fully discharged samples.

B.5 Rate dependence of pre-edge fine structure in Li-EELS spectra

Li-EELS spectra were recorded from LTO nanoparticles during cycling at different rates. The main results are presented in Figure B.3, showing the strong dependence of the intensity of pre-peak M on cycling rate. Specifically, the intensity of pre-peak M is very weak at low rates (i.e., 1C, 2C) and becomes significantly stronger at higher rates (3C, 8C). Quantitative analysis of the intensity of pre-peak M relative to that of S was performed by extracting the ratio of the integrated intensity of the two peaks (I_M/I_S). The evolution of I_M/I_S as a function of Li concentration (x) is shown in Figure 3.2E. At a low rate of 1C, the intensity ratio I_M/I_S was ~0.2 but increased abruptly with increasing rates to 2 and 2.4 at rates of 3C and 8C, respectively. Note that only pre-peak S was present at the end of discharge regardless of rate because the $Li_7Ti_5O_{12}$ phase was re-formed. As pre-peak M mainly originates from the metastable configurations and increasing the cycling rates results in elevated overpotentials, the formation of metastable configurations is strongly linked to the amplitude of the overpotentials.
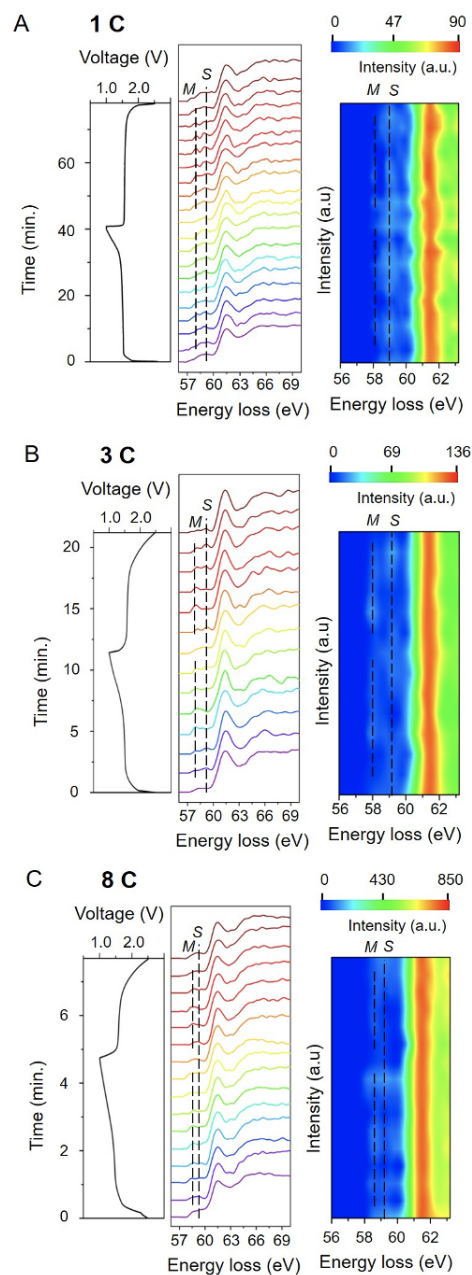
Figure B.3: Intensity profiles and maps of Li-EELS spectra during the first cycle at a series of current rates (A) 1C, (B) 3C, and (C) 8C, with the voltage profiles presented on the left side of each intensity map. The positions of the pre-peaks are marked by black dashed lines. The intensity ratios of pre-peak M to that of S as a function of Li concentration x during discharge and charge, I_M/I_S, where I_M and I_S are the integrated intensities of pre-peaks M and S, respectively, are presented in Fig. 3.2

B.6 Pre-edge fine structure in Li-EELS by computations
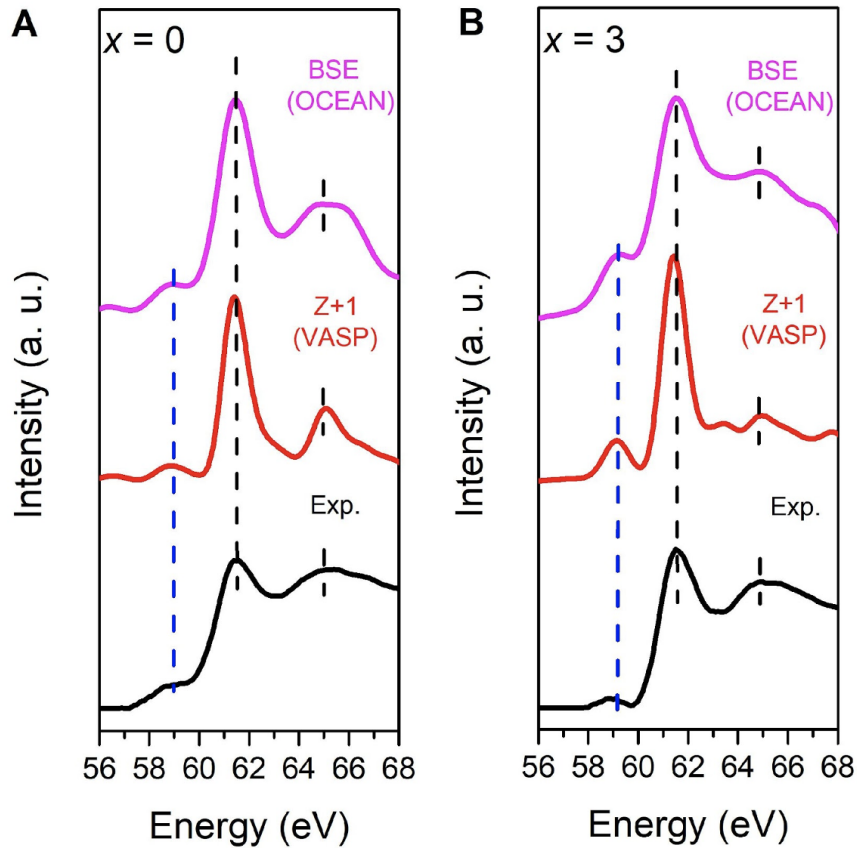
Figure B.4: Computed Li-EELS spectra of (A) $Li_4Ti_5O_{12}$ and (B) $Li_7Ti_5O_{12}$ using two different methods, the $Z+1$ method (red) and Bethe-Salpeter equation (BSE) method (purple), in comparison to experimental spectra (black). The good agreement between the experimental and calculated spectra validates the use of the $Z+1$ method to predict Li-EELS spectra.
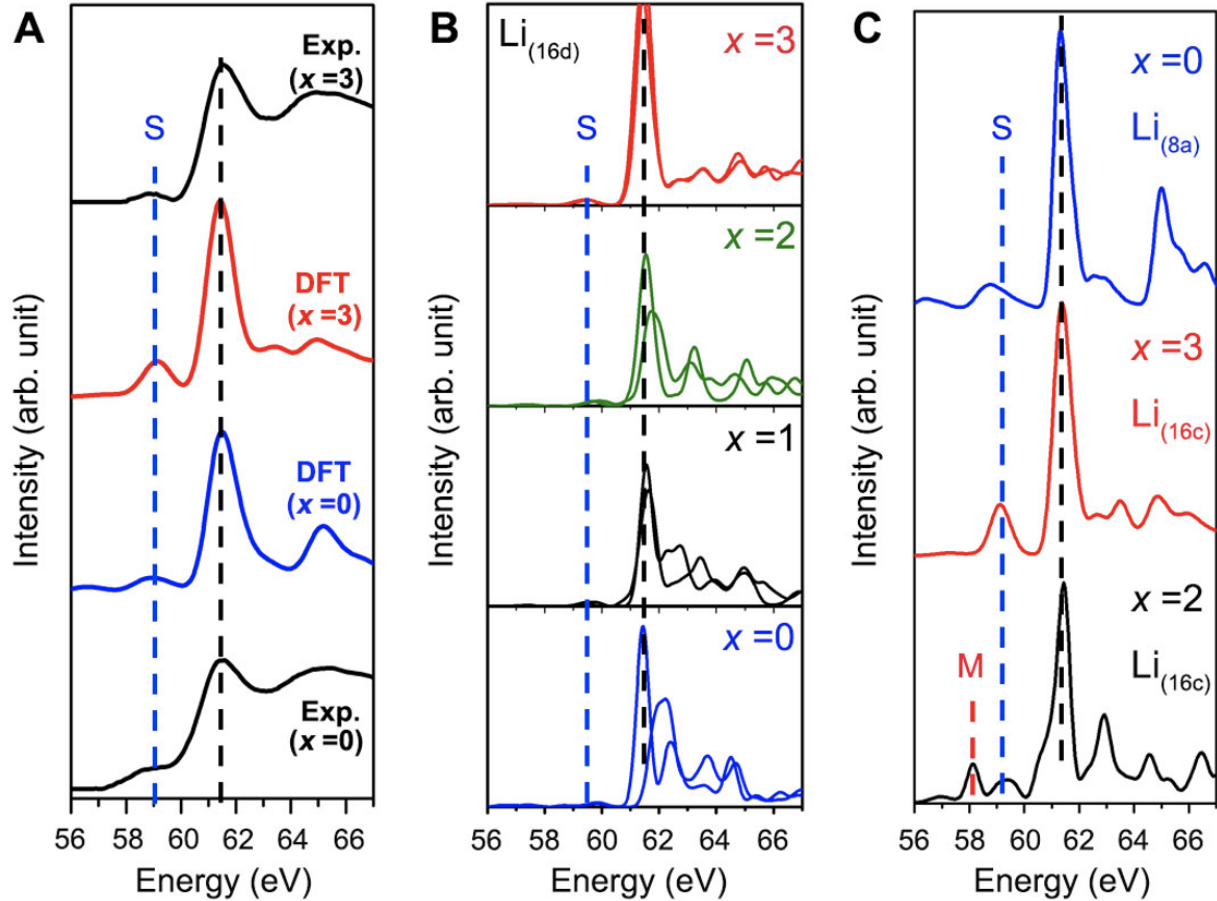
Figure B.5: Calculated Li-EELS spectra. (A) Spectra for pristine $Li_4Ti_5O_{12}$ (blue) and $Li_7Ti_5O_{12}$ (red), in good agreement with the experiments (black), (B) Spectra from individual Li ion at $Li_{(16d)}$ in $Li_{4+x}Ti_5O_{12}$ ($x = 0$, 1, 2, and 3), showing only pre-peak S in the pre-edge region. The black and blue dashed lines mark the energy positions of the main peaks and pre-peak S, respectively. Note that the changes of the computed EELS spectra of $Li_{(16d)}$ in $Li_{4+x}Ti_5O_{12}$ ($x = 0$, 1, 2, and 3) are negligible in the energy ranges between the pre-peak S and main peak. (C) Average spectra of $Li_{(8a)}$ in $Li_4Ti_5O_{12}$, $Li_{(16c)}$ in $Li_7Ti_5O_{12}$ and highly distorted $Li_{(16c)}$ in $Li_6Ti_5O_{12}$. The black, blue and red dashed lines mark the energy positions of the main peak, pre-peak S and pre-peak M, respectively. Only $Li_{(8a)}$ in $Li_4Ti_5O_{12}$ contributes to the pre-peak S, and it appears that a broader pre-peak S is present in $Li_4Ti_5O_{12}$ than that in $Li_7Ti_5O_{12}$.
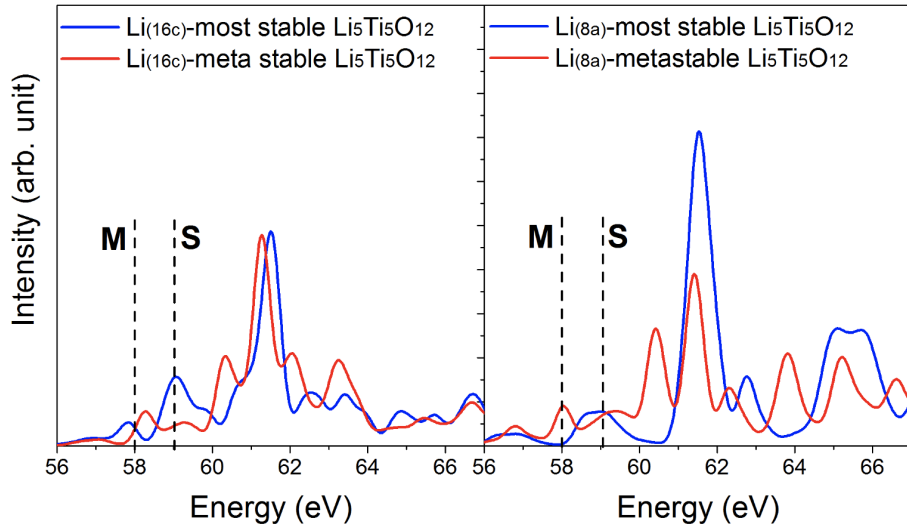
Figure B.6: Computed Li-EELS spectra of individual $Li_{(16c)}$ and $Li_{(8a)}$ in the most stable $Li_5Ti_5O_{12}$ and a metastable $Li_5Ti_5O_{12}$ configuration. The I_M/I_S ratios of $Li_{(16c)}$ in the most stable $Li_5Ti_5O_{12}$ and the metastable $Li_5Ti_5O_{12}$ are 0.30 and 1.48, respectively, while the I_M/I_S ratios of $Li_{(8a)}$ are 0 and 1.15, respectively.
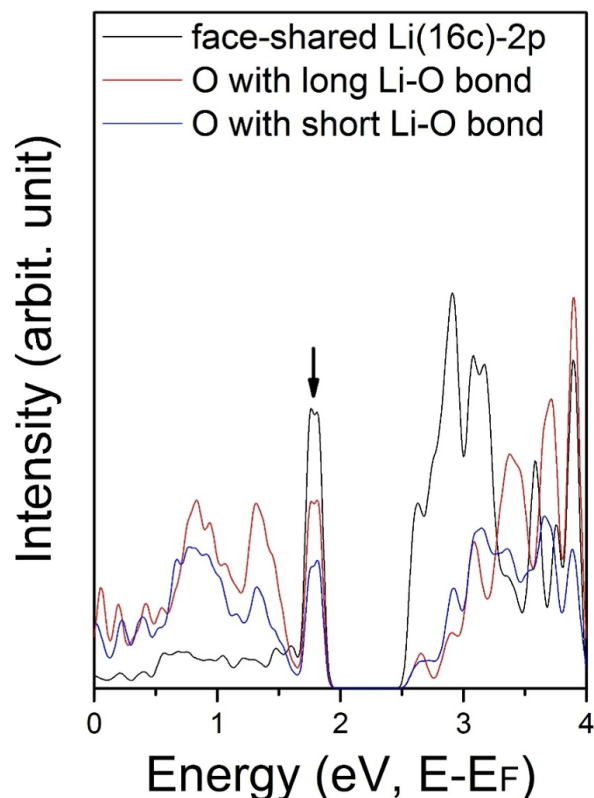
Figure B.7: Projected DOS on a 2p orbital of face-sharing $Li_{(16c)}$ (black), a neighboring oxygen with a long Li-O bond (red), and a neighboring oxygen with a short Li-O bond (blue). Note that the oxygen with a long Li-O bond has more overlap with $Li_{(16c)}$-2p orbital within 2 eV of the Fermi level, especially the peak at 1.78 eV indicated by the arrow. In contrast, at higher energies (> 2 eV above the Fermi level), contributions from O show a weak dependence on the bond length. This is in line with the different spatial charge distribution with energy range, as shown in Fig. 3.4C. The projected DOS and spatial charge distribution demonstrate that the electronic origin of pre-peak M is the splitting of Li-O anti-bonding states associated with the local distortion of face-sharing Li polyhedra.

The small peak at around 57 eV in the computed Li-EELS is mainly from $Li_{(8a)}$ and its intensity varies from 0.02 and 0.09 (Figure 3.4A and Figure B.8B) which is smaller than the intensities of pre-peak S ($\sim$0.14-0.31) at 59 eV in $Li_4Ti_5O_{12}$ and $Li_7Ti_5O_{12}$ and pre-peak M ($\sim$0.12-0.24) at 58 eV in the most stable $Li_5Ti_5O_{12}$ and $Li_6Ti_5O_{12}$ configurations (Figure 3.4B) and less stable intermediate $Li_6Ti_5O_{12}$ configuration (Figure B.8A). Previous work on Li-EELS calculations of $Li_{(8a)}$ in $Li_4Ti_5O_{12}$ also reported a small peak below 57 eV,[179] in agreement with our results using DFT/Z+1 and BSE/OCEAN. Although both calculations in our study predict the same peak positions of pre-peak S and the peak below 57 eV, it is likely that the BSE calculation predicts more accurate relative peak intensity because it has

113
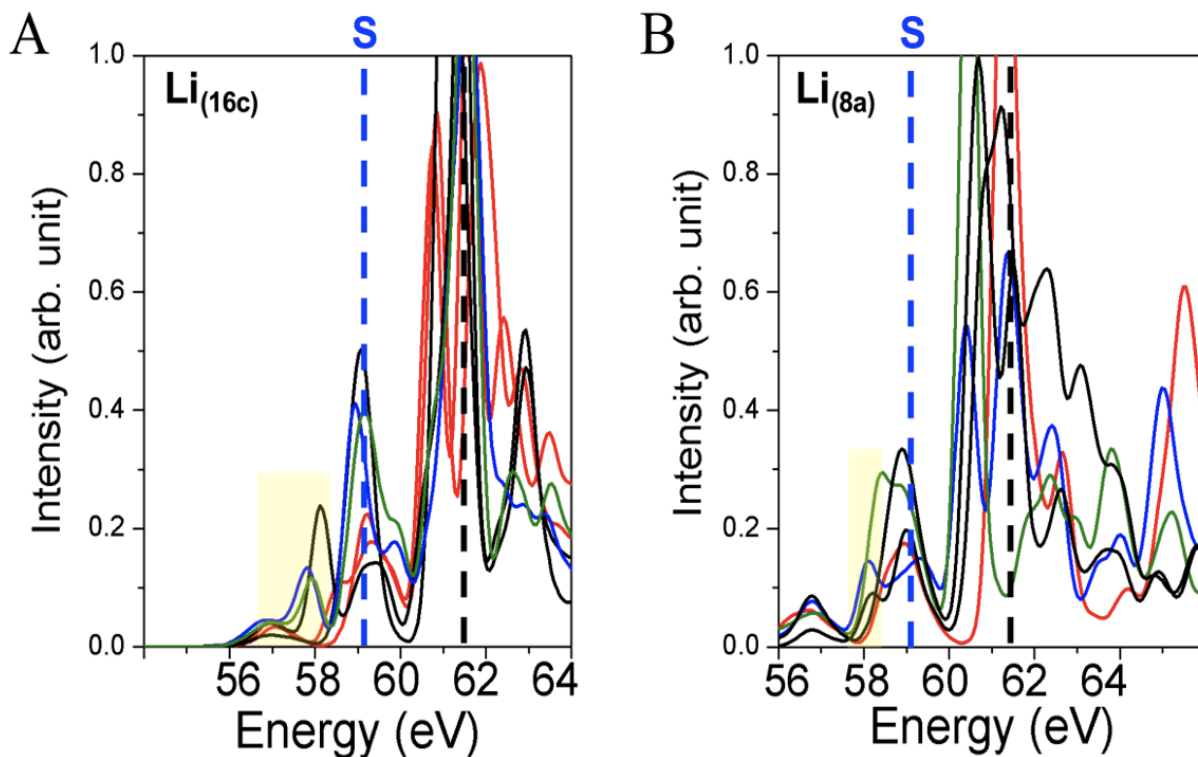
Figure B.8: Full computed Li-EELS spectra of individual Li ion at $Li_{(16c)}$ and $Li_{(8a)}$ for various $Li_5Ti_5O_{12}$ and $Li_6Ti_5O_{12}$ intermediates. The black and blue dashed lines mark the energy positions of the main peaks and pre-peak S, respectively. The yellow shaded boxes highlight the newly appearing pre-peak M with different intensities and energy positions, which was not observed in $Li_4Ti_5O_{12}$ and $Li_7Ti_5O_{12}$.

a more accurate description of the core-hole effects in the many-body perturbation theory framework. In fact, the intensity of the peak at 57 eV is 20% that of pre-peak S at 59 eV in BSE, while that ratio increases to 40% in $Z+1$ calculation (Figure B.4). Therefore, the peak intensity of the peak below 57 eV will be very small compared to the other pre-peaks, rendering it difficult to distinguish from background noise in experiments. In fact, we can observe a small peak at around 56 eV with a background range of $\sim$55-57 eV (Figure B.9A) with a relative intensity that is 20% of peak S at 59 eV, which agrees with the BSE/OCEAN calculation. However, this peak disappears when we use a background range of $\sim$56-57.5 eV (Figure B.9B). This indicates that the peak signals below 57 eV vary with the energy range selected for background subtraction.
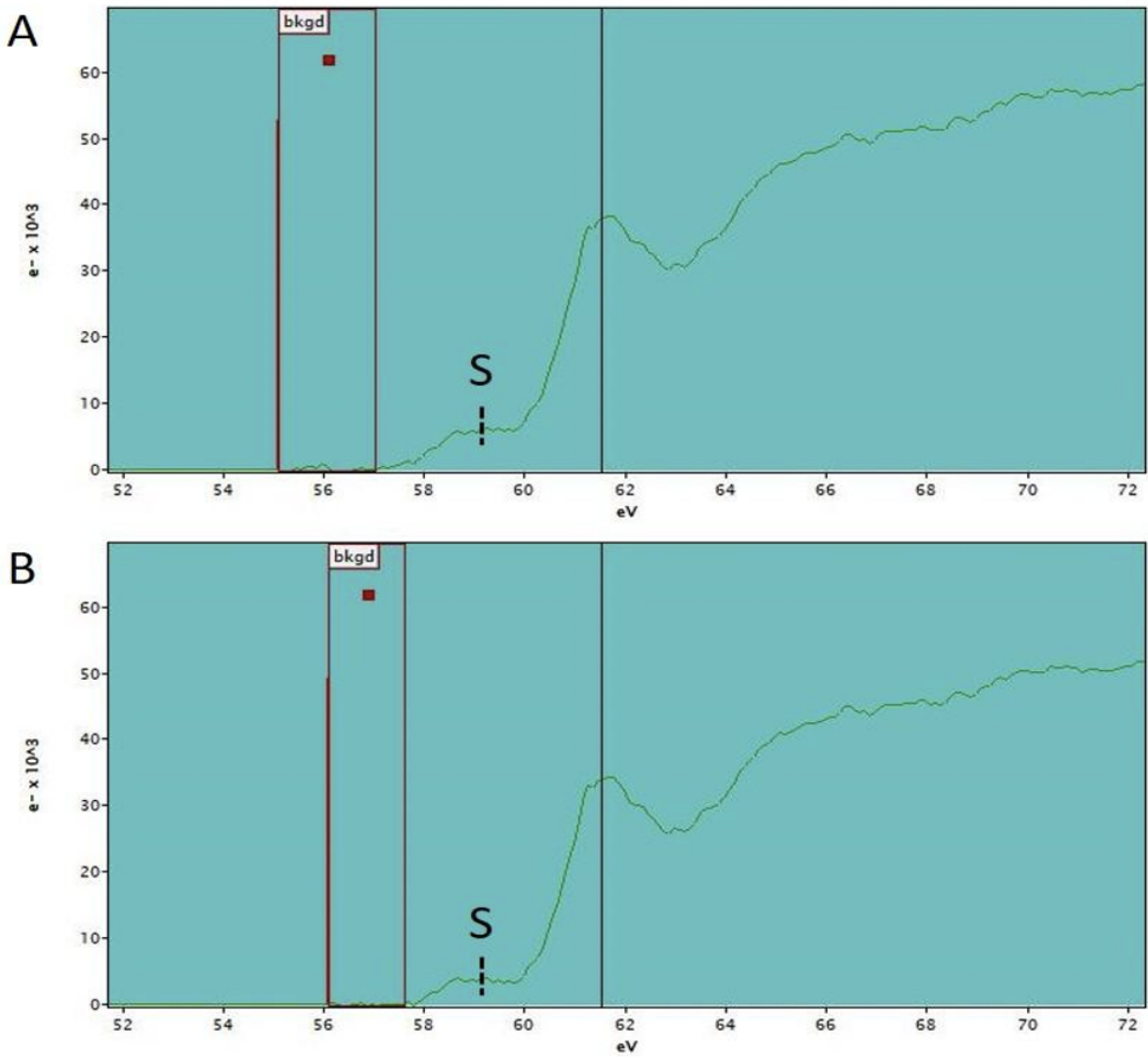
Figure B.9: Li-EELS spectra from pristine $Li_4Ti_5O_{12}$, with background subtraction from different ranges (shown by the red rectangles), (A) $\sim$55-57 eV and (B) $\sim$56-57.5 eV. The spectra after background subtraction were shown in green.

We have further examined the electronic origin of the peak at 57 eV in the $Z+1$ method, and the corresponding charge density iso-surface of this peak in $Li_{(8a)}$ in $Li_4Ti_5O_{12}$ is shown in Figure B.10. From the charge density plot, the charge density around $Li_{(8a)}$ within the energy range of $\sim$56.0-57.8 eV (left) is negligible compared to that within the energy of $\sim$57.8-60.6 eV corresponding to pre-peak S (right). Note that the charge density located on $Li_{(8a)}$ from the small pre-peak within $\sim$56.0-57.8 eV in $Li_4Ti_5O_{12}$ is negligible compared to that from pre-peak M and S on $Li_{(16c)}$ in $Li_5Ti_5O_{12}$ (Figure 3.4C). Therefore, peaks M and S are important spectral features that are sensitive to the chemical environment of Li, but the peak at around 57 eV is not.
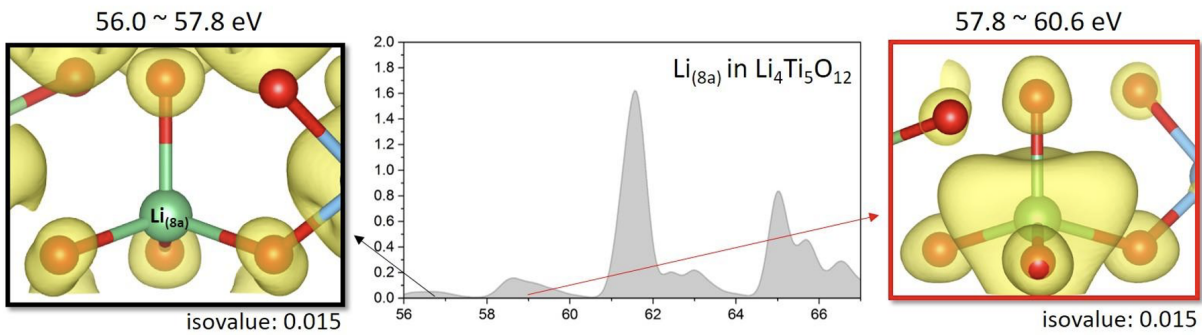
Figure B.10: Isosurface of partial charge density around $Li_{(8a)}$ in $Li_4Ti_5O_{12}$ within the energy range of $\sim$56.0-57.8 eV (left) and $\sim$57.8-60.6 eV (right) with an isovalue of 0.015.

B.7   Li polyhedra distortions in low-energy intermediate states
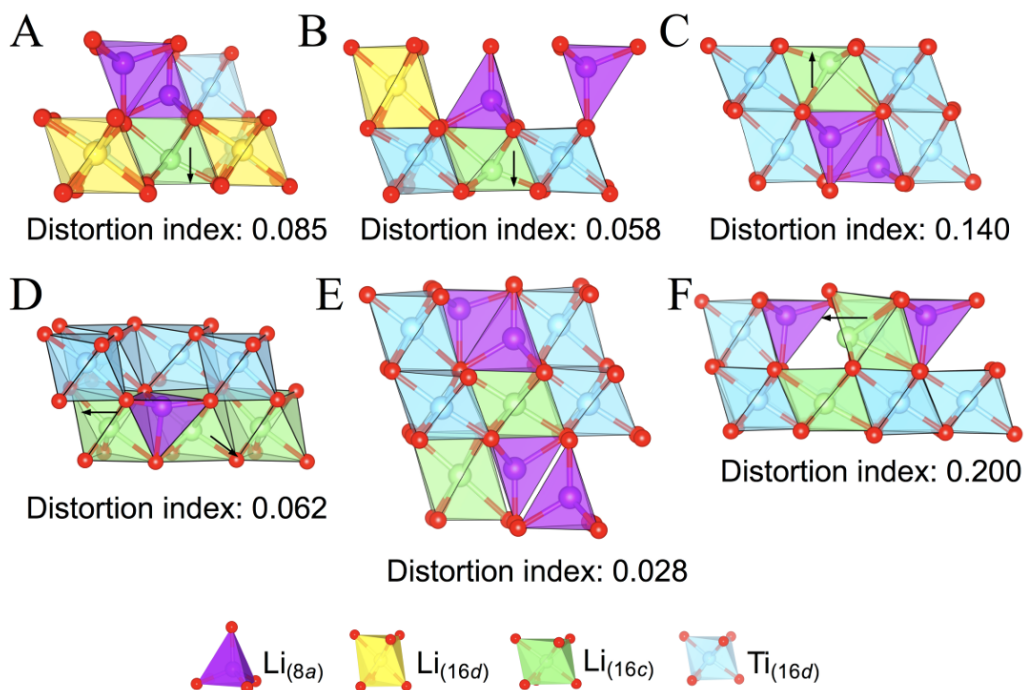
Figure B.11: **Local face-sharing configurations in LTO intermediates** Various configurations of face-sharing $Li_{(16c)}$ and $Li_{(8a)}$ in $Li_5Ti_5O_{12}$, with different levels of distortion (A-F). The black arrows indicate shifting of a Li atom from the center of $Li_{(16c)}$. The face-sharing $Li_{(16c)}$ polyhedra become highly distorted at a wide range of levels, as indicated by the distortion index below each configuration.

The distances between face-sharing $Li_{(8a)}$ and $Li_{(16c)}$ in the lowest-energy states of $Li_5Ti_5O_{12}$ (2.445 Å) and $Li_6Ti_5O_{12}$ (2.418 Å) were much longer than those in normal spinel $Li_{1+x}Ti_2O_4$ (1.807 Å). However, they were still much shorter than the distances between nearest-neighbor Li ions within $Li_4Ti_5O_{12}$ (3.475 Å) and $Li_7Ti_5O_{12}$ (2.884 Å). The nearest neighbor proximity of two Li-ions (as close as 2.445 Å) resulted in a distortion that pushed the $Li_{(8a)}$ and $Li_{(16c)}$ off-center in their polyhedra (Figure B.11). In the lowest-energy $Li_5Ti_5O_{12}$ and $Li_6Ti_5O_{12}$ configurations, the face-sharing $Li_{(8a)}$ and $Li_{(16c)}$ polyhedra have neighboring $Li_{(16d)}$ octahedra. Because the $Li_{(16d)}$ octahedra are larger than the $Ti_{(16d)}$ octahedra, Li ions in $Li_{(8a)}$ and $Li_{(16c)}$ polyhedra with neighboring $Li_{(16d)}$ octahedron have more space to accommodate the repulsion between face-sharing Li ions than those without $Li_{(16d)}$ neighbors.

B.8 Correlation between the pre-peak M and distortion in Li polyhedra
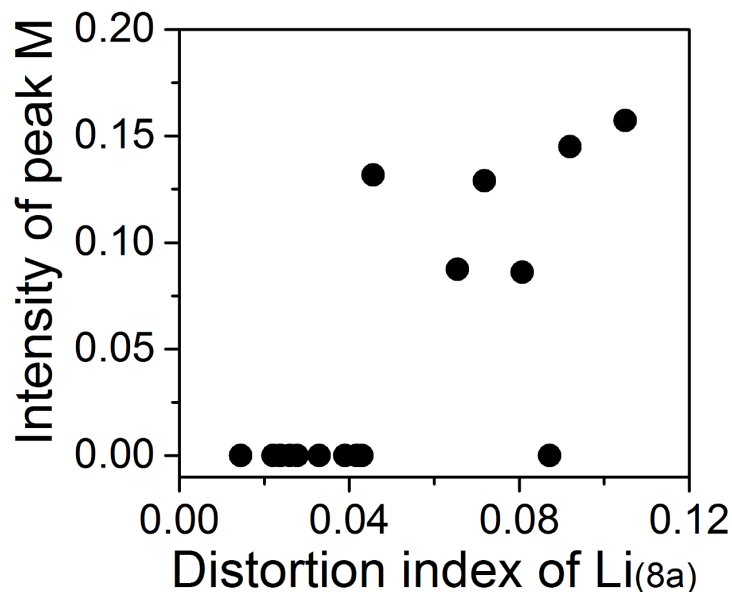
Figure B.12: Intensity of pre-peak M as a function of the distortion index of $Li_{(8a)}$ for various metastable configurations in $Li_5Ti_5O_{12}$ and $Li_6Ti_5O_{12}$. The intensity rapidly increased with increasing distortion index.

Face-sharing $Li_{(16c)}$ and $Li_{(8a)}$ in some of the higher-energy (less stable) $Li_5Ti_5O_{12}$ and $Li_6Ti_5O_{12}$ resulted in different peak intensities and energy positions of pre-peak M (Figures B.8 and B.12). Therefore, the experimentally observed pre-peak M should be sums of the M pre-peaks that appear at different energies. Some of the face-sharing $Li_{(16c)}$ and $Li_{(8a)}$ spectra did not have a peak at approximately 58 eV, whereas others had larger M pre-peaks than those from the lowest-energy $Li_5Ti_5O_{12}$ and $Li_6Ti_5O_{12}$ intermediates. In addition, pre-peak M was located at a slightly higher energy ($\sim$58.4 eV at 8C) than at 1C, 2C, and 3C ($\sim$58 eV) (Figure B.3). This difference may originate from the less stable $Li_{4+x}Ti_5O_{12}$ structures becoming dominant under the high overpotential at 8C, which can generate spectra with pre-peak M at higher energies, similar to the red spectrum with a shoulder peak at $\sim$58.4 eV in Figure B.8A.

As the presence of pre-peaks in EELS spectra is generally attributed to the local structural distortion of polyhedra [227], the intensity and energy positions of pre-peak M should be related to the distortion of $Li_{(16c)}$ and $Li_{(8a)}$ polyhedra. Therefore, we investigated the relation between their distortion index (d) values and intensities. The d values for Li polyhedra were determined using the following equation:
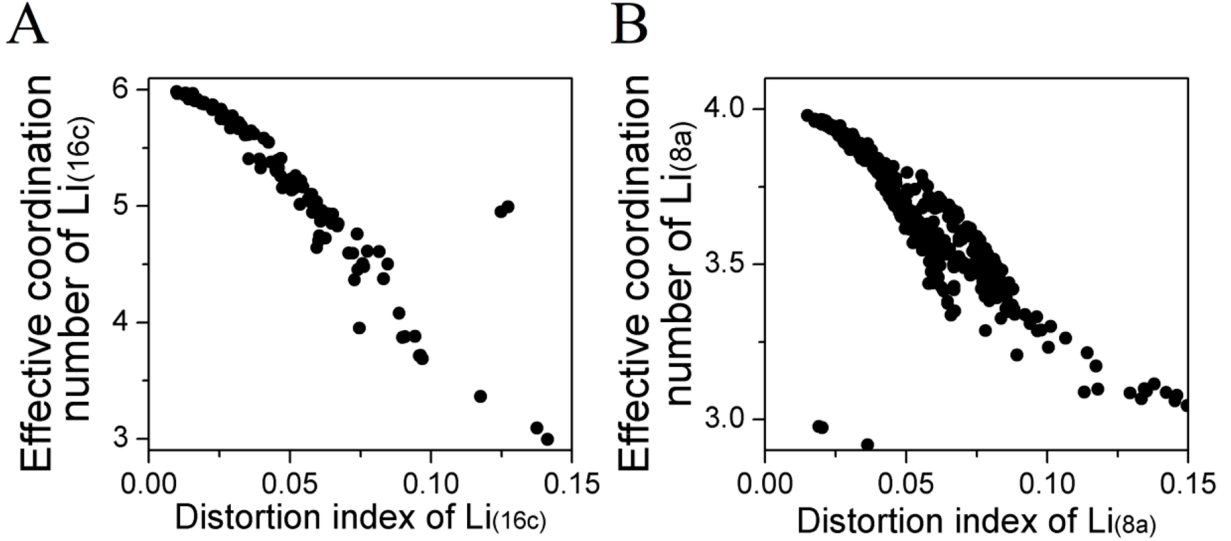
Figure B.13: Effective coordination numbers of (A) $Li_{(16c)}$ and (B) $Li_{(8a)}$ as a function of their distortion indices. The effective Li coordination number is reduced while local distortion in Li polyhedra is increased.

$$d = \frac{1}{n} \sum_{i=1}^{n} \frac{|l_i - l_{av}|}{l_{av}} \tag{B.1}$$

where l_i is the distance from the central Li atom to the ith O atom. l_{av} is the average bond length, and n is the number of bonded O atoms.

The highly distorted $Li_{(16c)}$ ($d = 0.106$) of the most stable $Li_5Ti_5O_{12}$ has three short Li–O bonds (< 2.00 Å) and three long Li–O bonds (> 2.34 Å) because of the repulsion with face-sharing $Li_{(8a)}$ and thus effectively exhibits a lower coordination than $Li_{(16c)}$ octahedra in $Li_7Ti_5O_{12}$. The effective coordination numbers (ECoNs) of $Li_{(16c)}$ were determined by summing the coordination numbers of all the surrounding O atoms using a weighting scheme [183]. ECoN of Li polyhedra linearly decreased with increasing d (Figure B.13). Because the elongated Li-O bond of Li polyhedra with low ECoN induces splitting of the anti-bonding Li-O state (Figure 3.4C and Figure B.7), Li polyhedra with high d (low ECoN) will result in the appearance of pre-peak M in Li-EELS. For example, in the most stable $Li_5Ti_5O_{12}$ configuration, a $Li_{(16c)}$ with $d = 0.106$ has an ECoN of 3.63 and results in the appearance of pre-peak M in Li-EELS, whereas a $Li_{(16c)}$ with $d = 0.057$ in the second-lowest-energy $Li_5Ti_5O_{12}$ configuration has ECoN of 5.15 and no pre-peak M is seen in the Li-EELS, even though this $Li_{(16c)}$ shares a face with a $Li_{(8a)}$. Moreover, the intensity of pre-peak M tends to increase with d of Li polyhedra, as shown in Figure 3.4D and Figure B.12.

119

This approach thus provides a strategy to estimate the intensity of pre-peak M based on the d of Li polyhedra in a large number of $Li_5Ti_5O_{12}$ and $Li_6Ti_5O_{12}$ configurations without the need for EELS calculations. Note that Li polyhedra can be distorted even when not face-sharing with a neighbor Li in the intermediate $Li_{4+x}Ti_5O_{12}$ compositions. However, the distortion index of non-face-sharing Li polyhedra are typically much smaller than those with face-sharing Li, as shown in Figure 3.4E, B.14, and B.15. As most of the distortion indices of non-face-sharing Li below 100 meV/O_4 are less than the approximate value of d above which pre-peak M appears (0.06), the contribution of Li polyhedra without face-sharing Li on the intensity of pre-peak M is generally much less than that of face-sharing Li polyhedra.
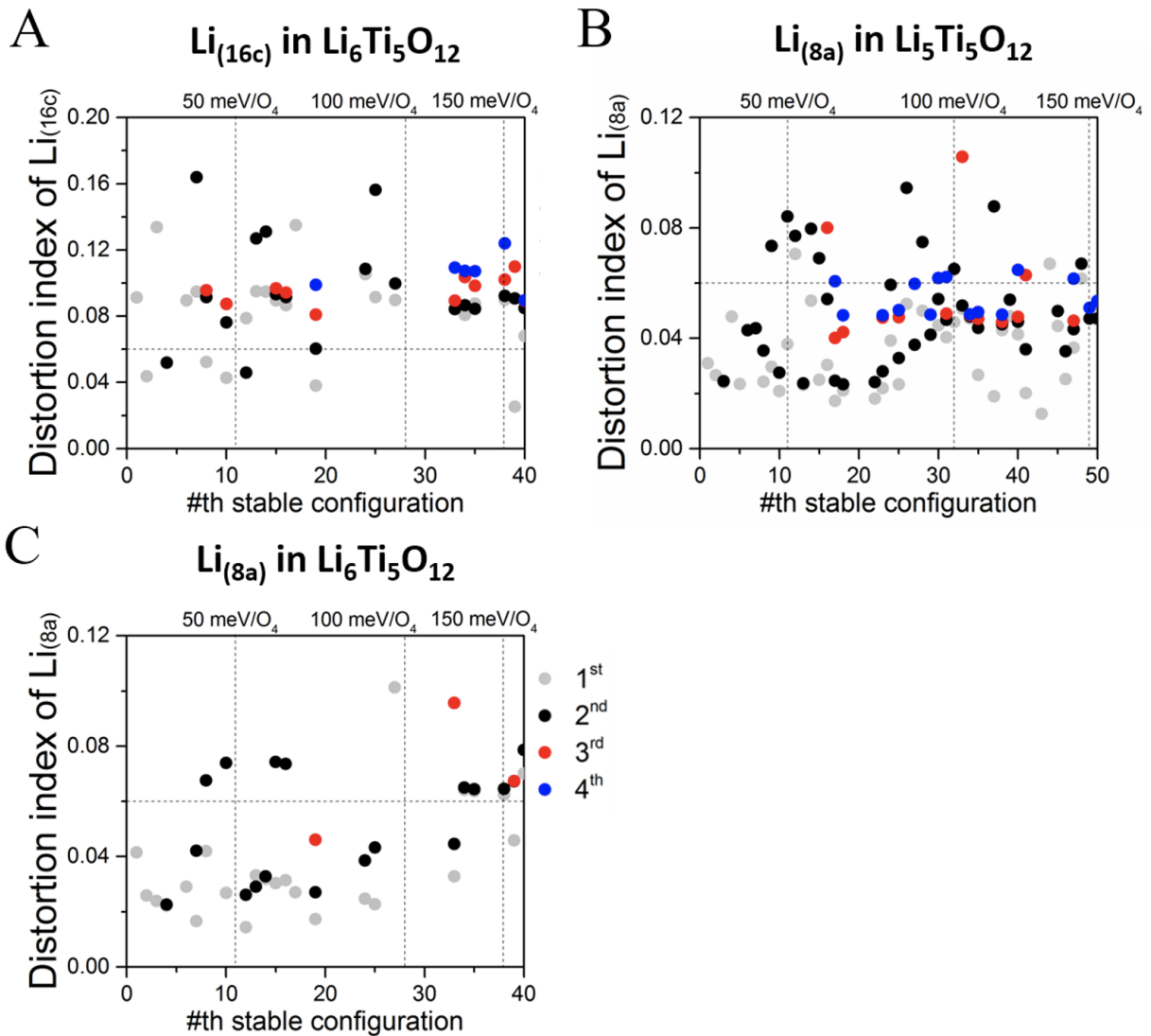
Figure B.14: Distortion indices of (A) $Li_{(16c)}$ in $Li_6Ti_5O_{12}$, (B) $Li_{(8a)}$ in $Li_5Ti_5O_{12}$, and (C) $Li_{(8a)}$ in $Li_6Ti_5O_{12}$. The horizontal and vertical dashed lines indicate the approximate value of d above which pre-peak M appears and the formation energy of the nth stable configuration at 50, 100, and 150 meV/O_4. When a single configuration contains multiple face-sharing $Li_{(16c)}$, the different face-sharing $Li_{(16c)}$ are labeled as different colored points according to their d values in the ascending order: grey (first lowest distortion index), black (second), red (third), and blue (fourth).
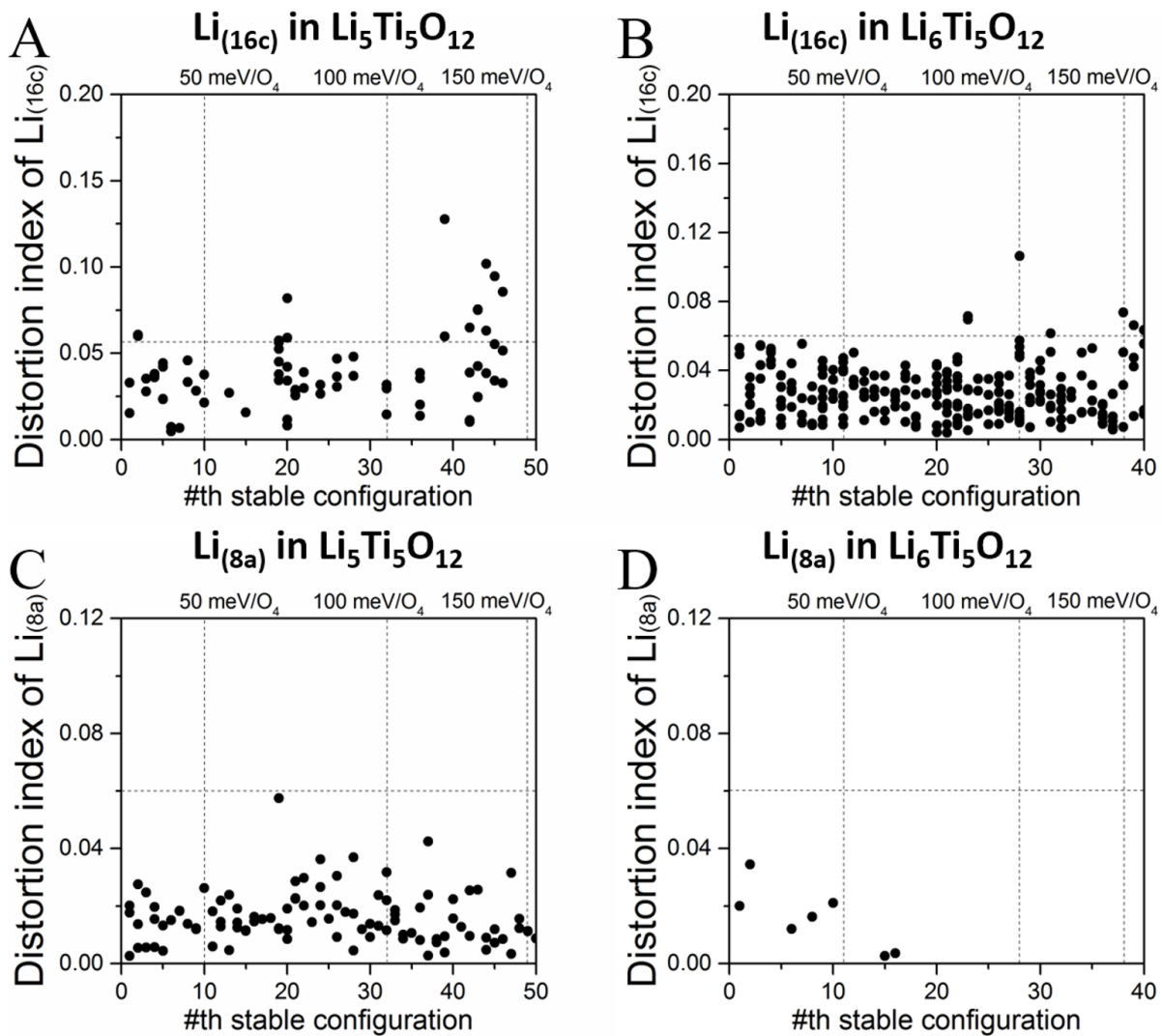
Figure B.15: Distortion indices of Li polyhedra which are not face-sharing with neighbor Li. (A) $Li_{(16c)}$ in $Li_5Ti_5O_{12}$, (B) $Li_{(16c)}$ in $Li_6Ti_5O_{12}$, (c) $Li_{(8a)}$ in $Li_5Ti_5O_{12}$, and (D) $Li_{(8a)}$ in $Li_6Ti_5O_{12}$. The horizontal and vertical dashed lines indicate the approximate value of d above which pre-peak M appears and the formation energy of the nth stable configuration at 50, 100, and 150 meV/O_4.

B.9 Detailed migration paths of $Li_{4+\delta}Ti_5O_{12}$ and $Li_{7-\delta}Ti_5O_{12}$
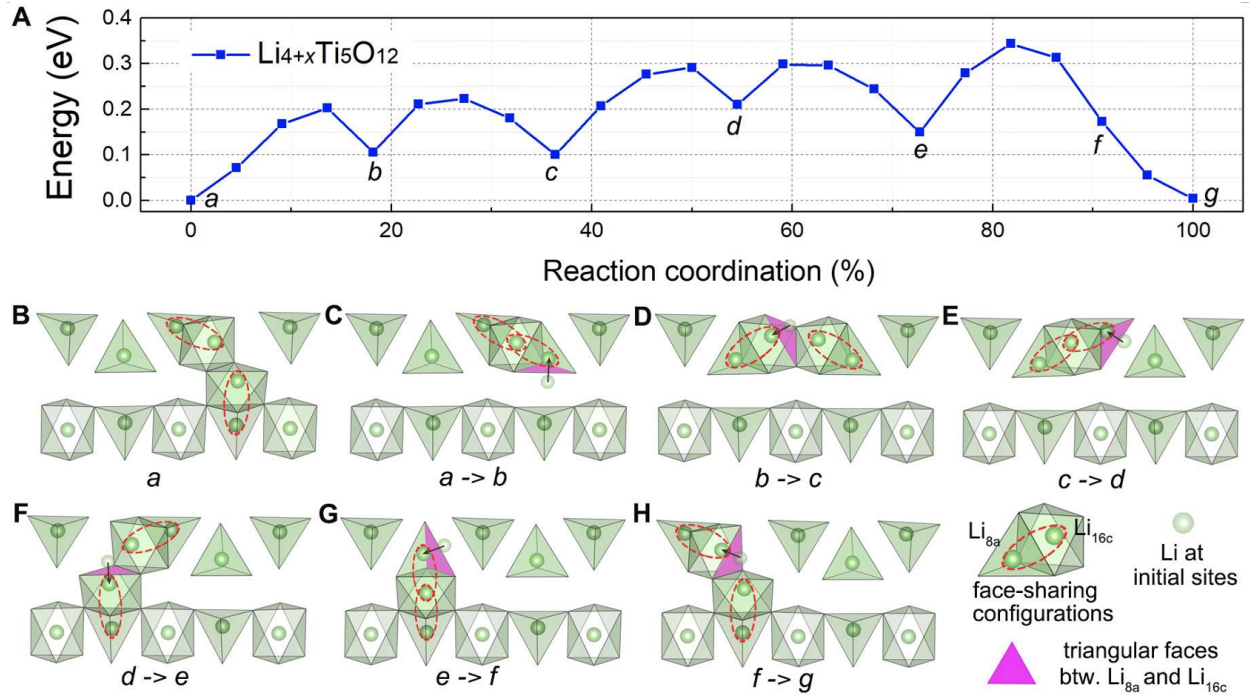
Figure B.16: Nudged-elastic band (NEB) calculations of Li migration in the $Li_{4+\delta}Ti_5O_{12}$ structure. (A) Energy profile of the pathways as a plot of energy vs. reaction coordinate. (B–H) Sub-step pathways of Li migration corresponding to the energy profile in (A). The translucent green spots mark the initial Li sites during every sub-step of migration. The migration direction of each sub-step is labeled by black arrows. The three-coordinated oxygen face between a $Li_{(8a)}$ tetrahedron and a $Li_{(16c)}$ octahedron is colored purple.
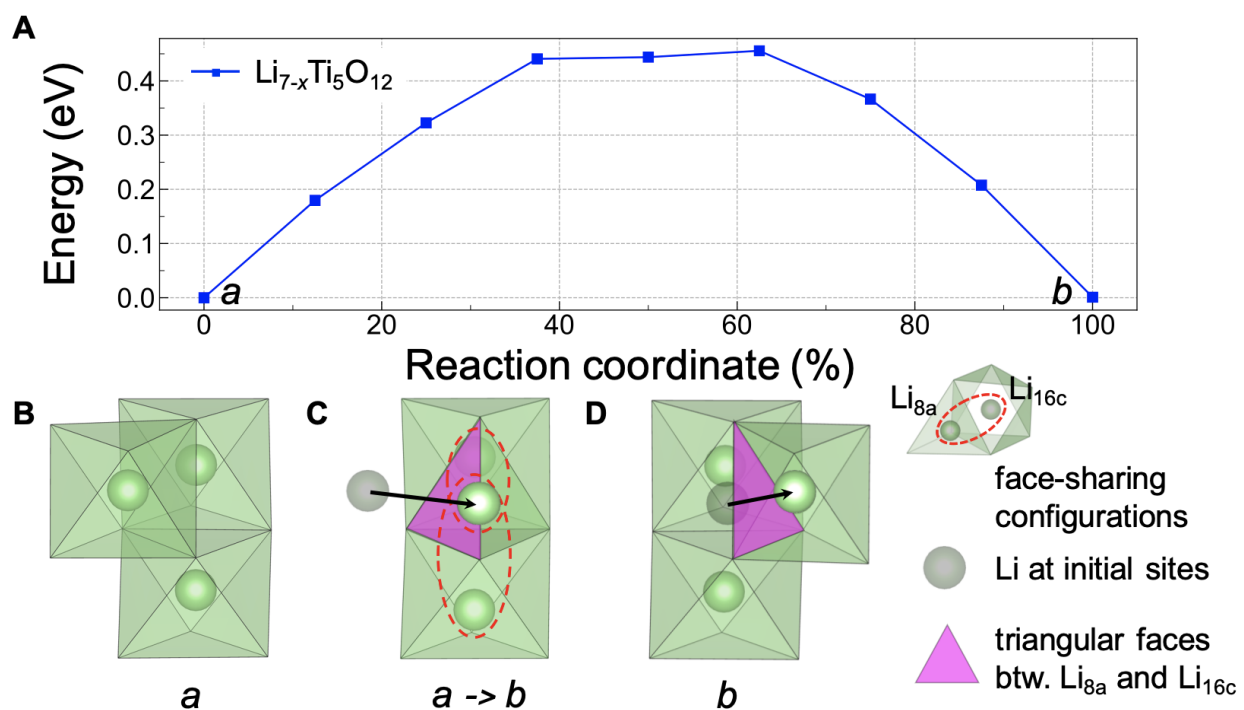
Figure B.17: Nudged-elastic band (NEB) calculations of Li migration in the $Li_{7-\delta}Ti_5O_{12}$ structure. (A) Energy profile of the pathways as a plot of energy vs. reaction coordinate. (B–D) Sub-step pathways of Li migration corresponding to the energy profile in (A). The translucent green spots mark the initial Li sites during each sub-step of migration. The migration direction of each sub-step is labeled by black arrows. The three-coordinated oxygen face between a $Li_{(8a)}$ tetrahedron and a $Li_{(16c)}$ octahedron is colored purple.

B.10 Experimental characterization of IL-based cell and LTO electrode
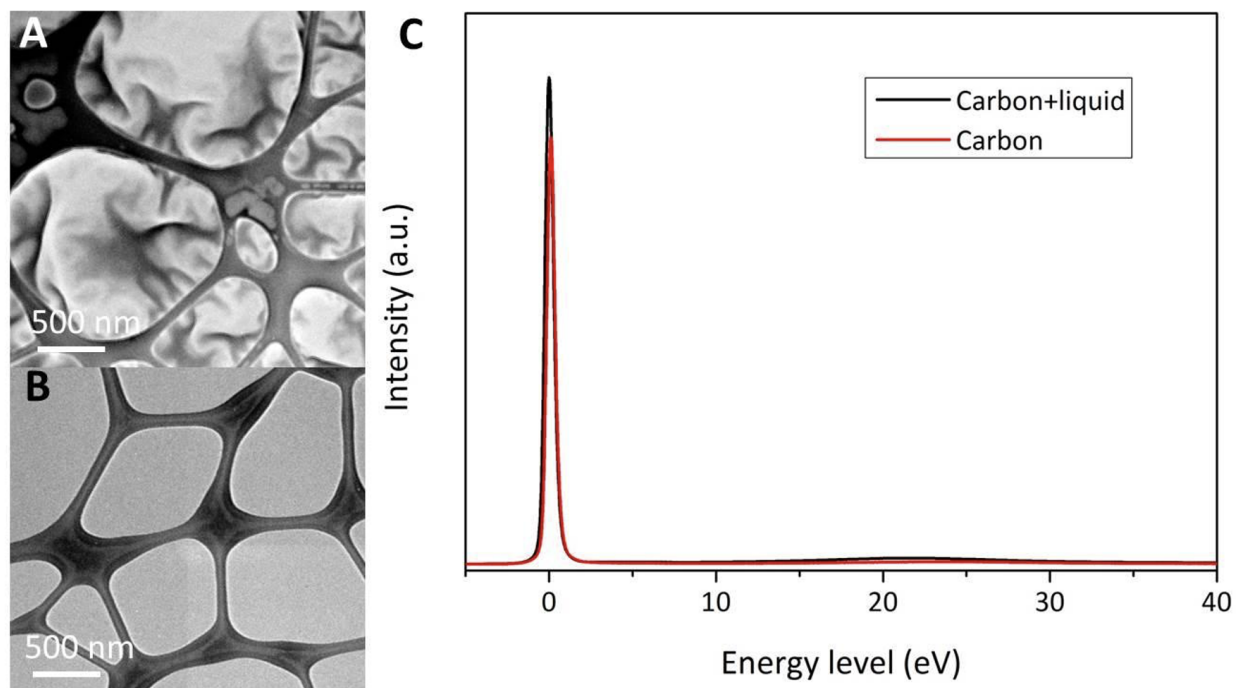
Figure B.18: Thickness of IL layer estimated from low-loss EELS spectra. (A) Typical TEM image of the ionic liquid covered on the carbon film, shown by the mass-thickness contrast inside the holes. (B) TEM image of a blank carbon film. No contrast was observed inside the holes. (C) Low-loss EELS spectra obtained from the regions shown in (A) in black color and (B) in red, respectively. Based on the intensities of the plasmon peaks two curves, the thicknesses of (A) and (B) were estimated to be 21 and 28 nm, respectively, indicating that the average thickness of the IL layer is approximately 7 nm.
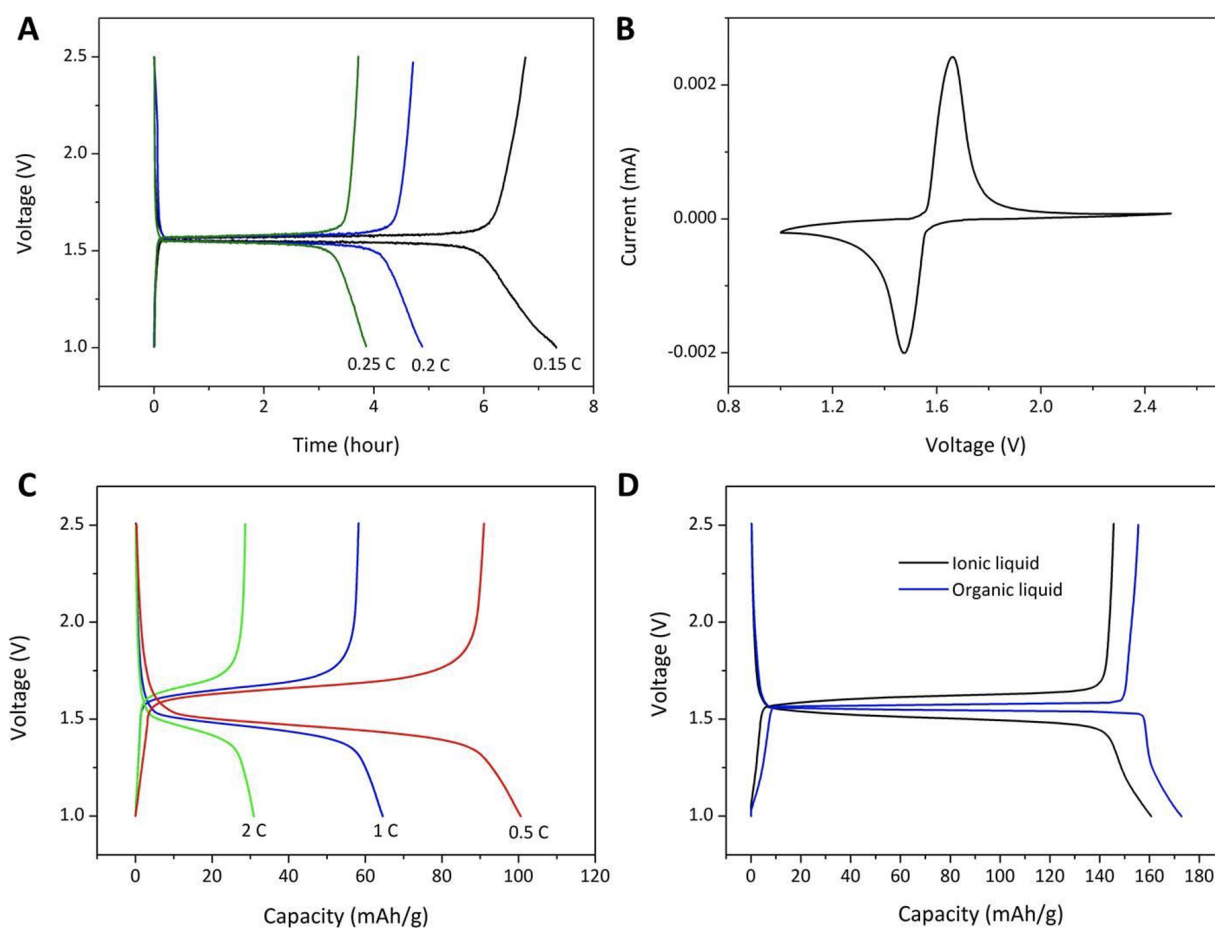
Figure B.19: Electrochemical tests of the functionality of the in situ electrochemical cells in comparison to that of normal coin cells. (A, B) Voltage profiles at different rates (from 0.15C to 0.25C) and CV curve (at a scan rate of 0.1 mV/s) of LTO nanoparticles cycled in the in situ electrochemical cell. (C) Capacity–voltage profiles of the LTO electrodes in IL-based coin cells cycled at different rates (from 0.5C to 2C). (D) Capacity–voltage profiles of LTO electrodes in IL (black curve) and organic liquid (blue curve) cycled at 0.1C.
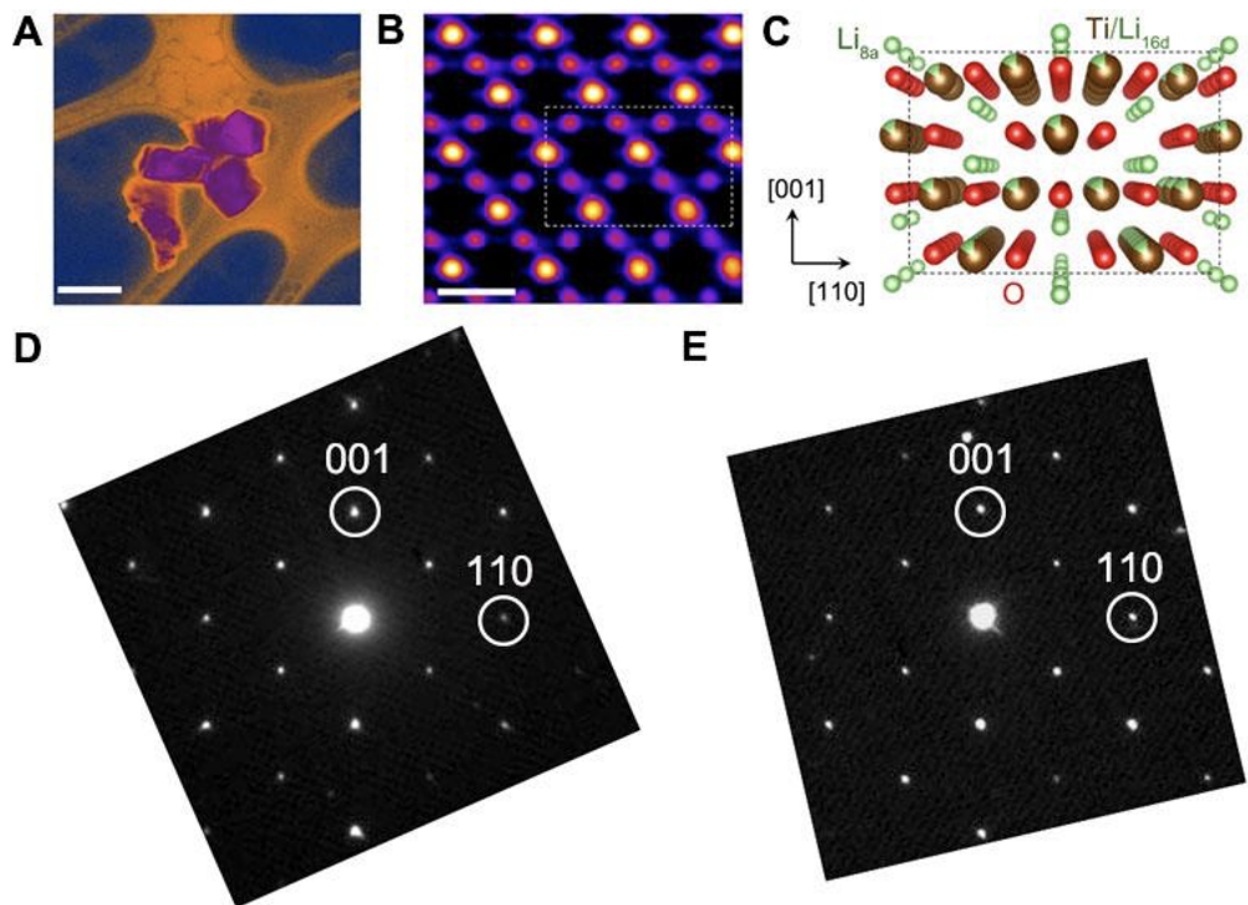
Figure B.20: Structural analysis of the LTO nanoparticles in IL electrolyte. (A) Bright-field TEM image showing the LTO nanoparticles (purple) immersed in a thin layer of IL electrolyte (light brown). Scale bar: 200 nm. (B) High-angle annual dark-field image of LTO viewed along the [1-10] direction, showing the atomic arrangements Ti. Scale bar: 0.5 nm. (C) Schematic illustration of the atomic arrangement of the unit structure enclosed by the rectangular box in B. (D, E) Electron diffraction patterns of $Li_4Ti_5O_{12}$ and $Li_7Ti_5O_{12}$ nanoparticles, respectively, both being along the [1-10] direction. No structural difference between $Li_4Ti_5O_{12}$ and $Li_7Ti_5O_{12}$ was detected by these diffraction patterns because of the negligible change in the lattice parameter (only ~ 0.005 Å) before and after lithiation.
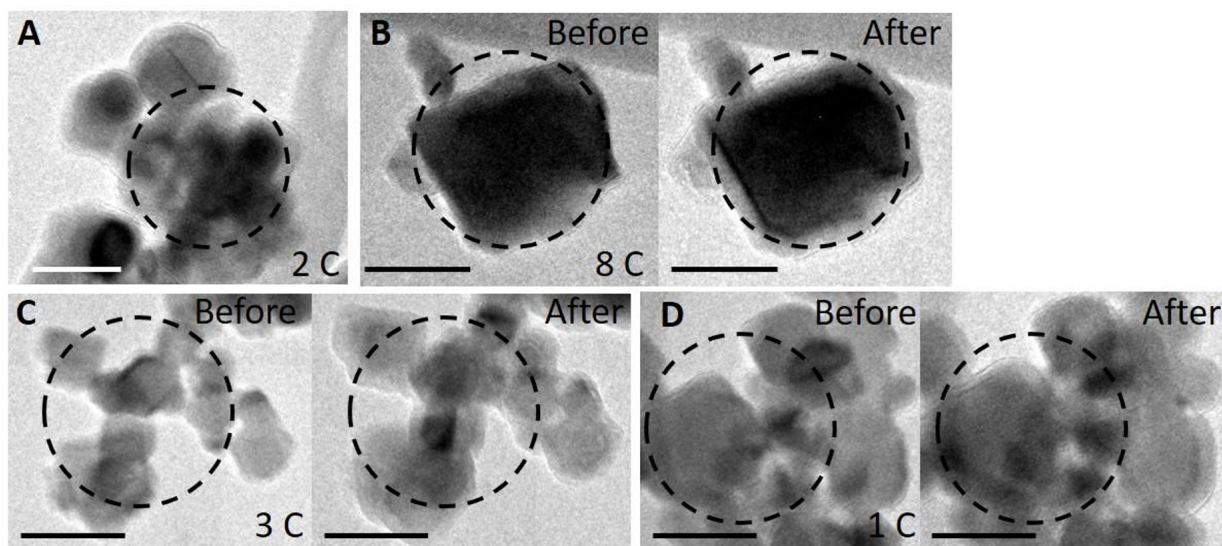
Figure B.21: Bright-field TEM images of LTO nanoparticles selected for operando Li-EELS measurements. (A) after one cycle at 2C, (B - D) before and after one cycle at 8C, 3C, 1C. Scale bars: 100 nm. The black dashed circles mark the region selected for obtaining Li-EELS spectra.
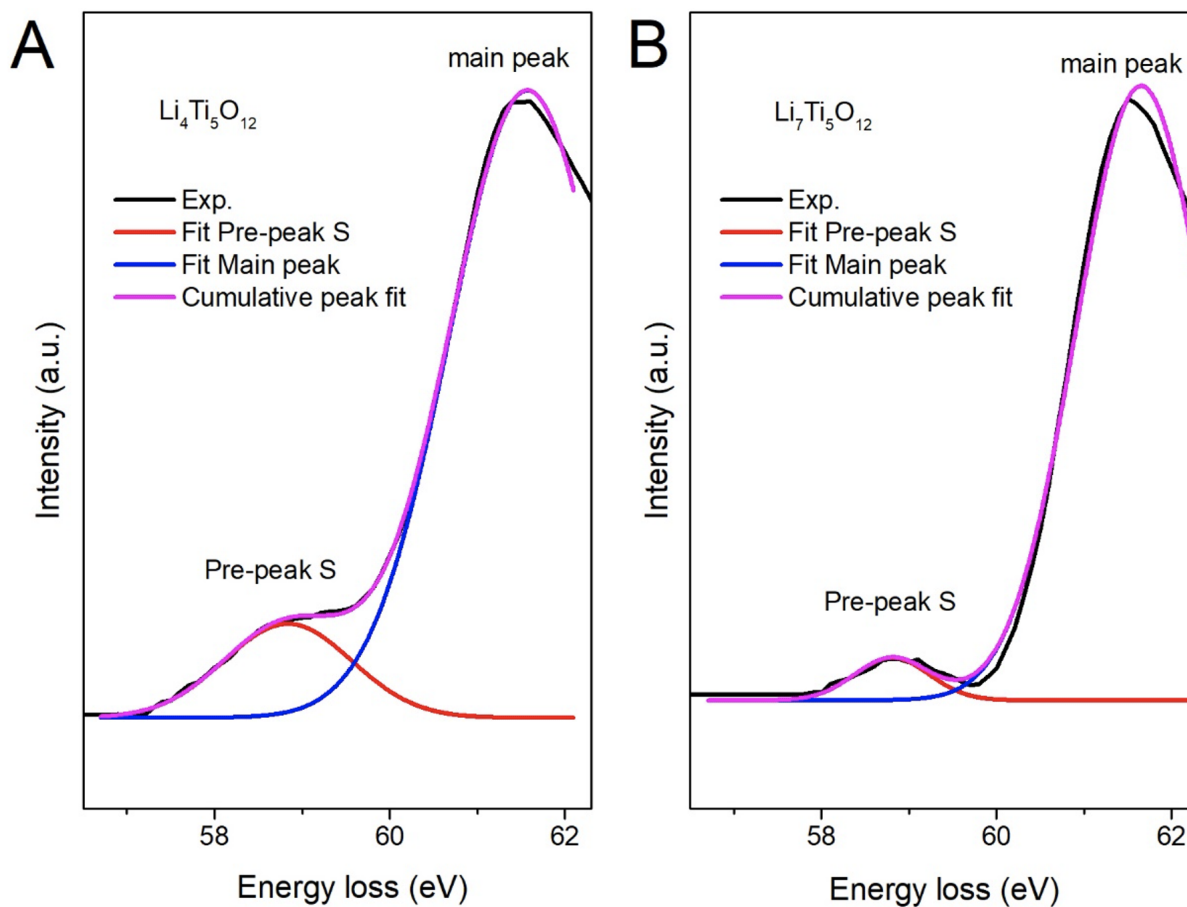
Figure B.22: Positions of pre-peak S in $Li_4Ti_5O_{12}$ and $Li_7Ti_5O_{12}$ from Li-EELS, at 58.84 ± 0.03 eV and 58.80 ± 0.08 eV respectively. Both spectra were fitted using Gaussian functions.

Appendix C

Supplemental information on disordering of spinel LiMn$_2$O$_4$

We provide the simplified voltage curve of LiMn$_2$O$_4$ using Li pseudopotentials including more electrons and with varying DFT functional and application of the Hubbard U correction. More details regarding the effects of oxygen oxidation on the simulated voltage curves of LiMn$_2$O$_4$ at each level of disorder, the dependence of the CE-evaluated energies of the disordered spinel on tetrahedral Li occupancy, and the transition metal occupancies in stoichiometric LiMn$_2$O$_4$ at increasing temperature are also provided. Finally, we describe further the method by which the solid-solution configurations of the ordered LiMn$_2$O$_4$ across the two-phase LiMn$_2$O$_4$-Li$_2$Mn$_2$O$_4$ reaction are sampled.

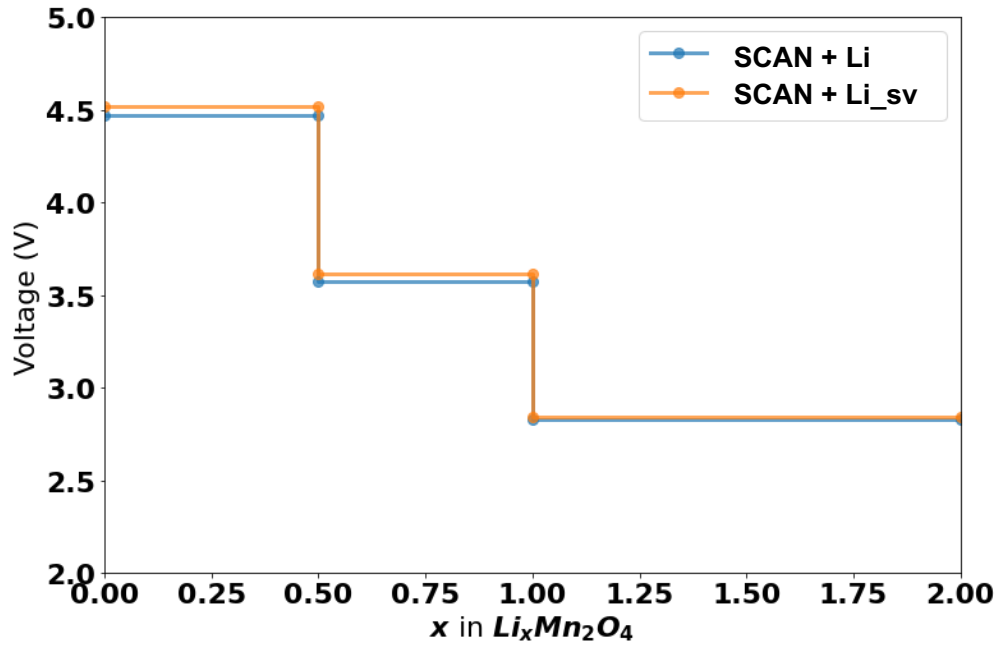## C.1 Pseudopotential and Hubbard U effects on simple spinel voltage curve

Figure C.1: Estimated voltage curves based on average voltages between known ground state Li orderings in $Li_xMn_2O_4$ spinel, calculated using DFT using the SCAN meta-GGA functional with the Li pseudopotential (blue) and the Li_sv pseudopotential (orange), using the Li_sv for bcc Li.
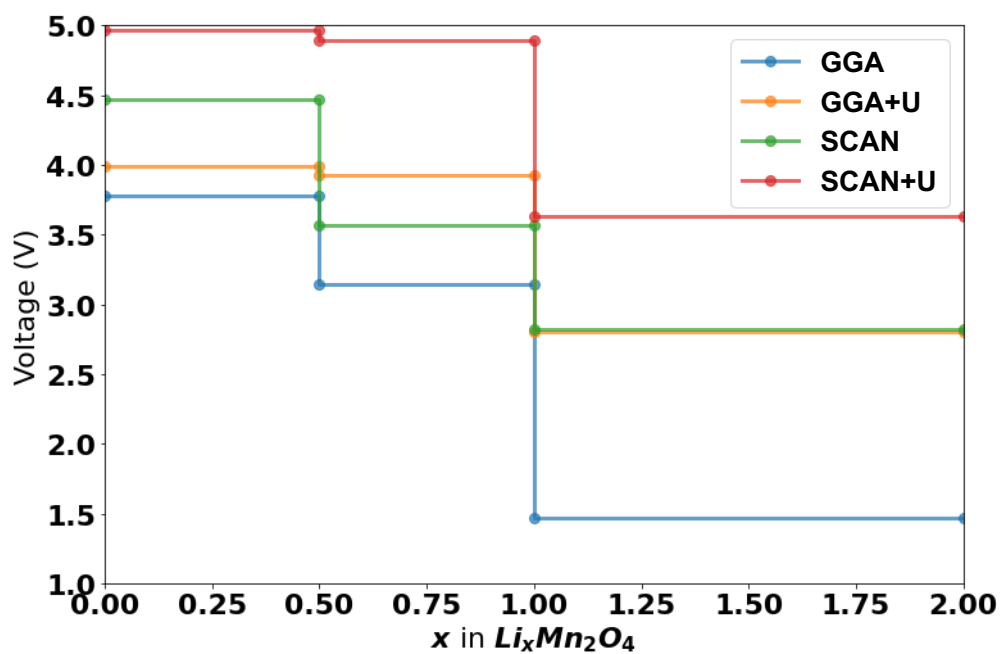
Figure C.2: Estimated voltage curves based on average voltages between known ground state Li orderings in $Li_xMn_2O_4$ spinel, calculated using DFT with GGA (blue), GGA with the Hubbard U correction (GGA+U, orange), SCAN meta-GGA functional (green), and SCAN with Hubbard U correction (SCAN+U, red).

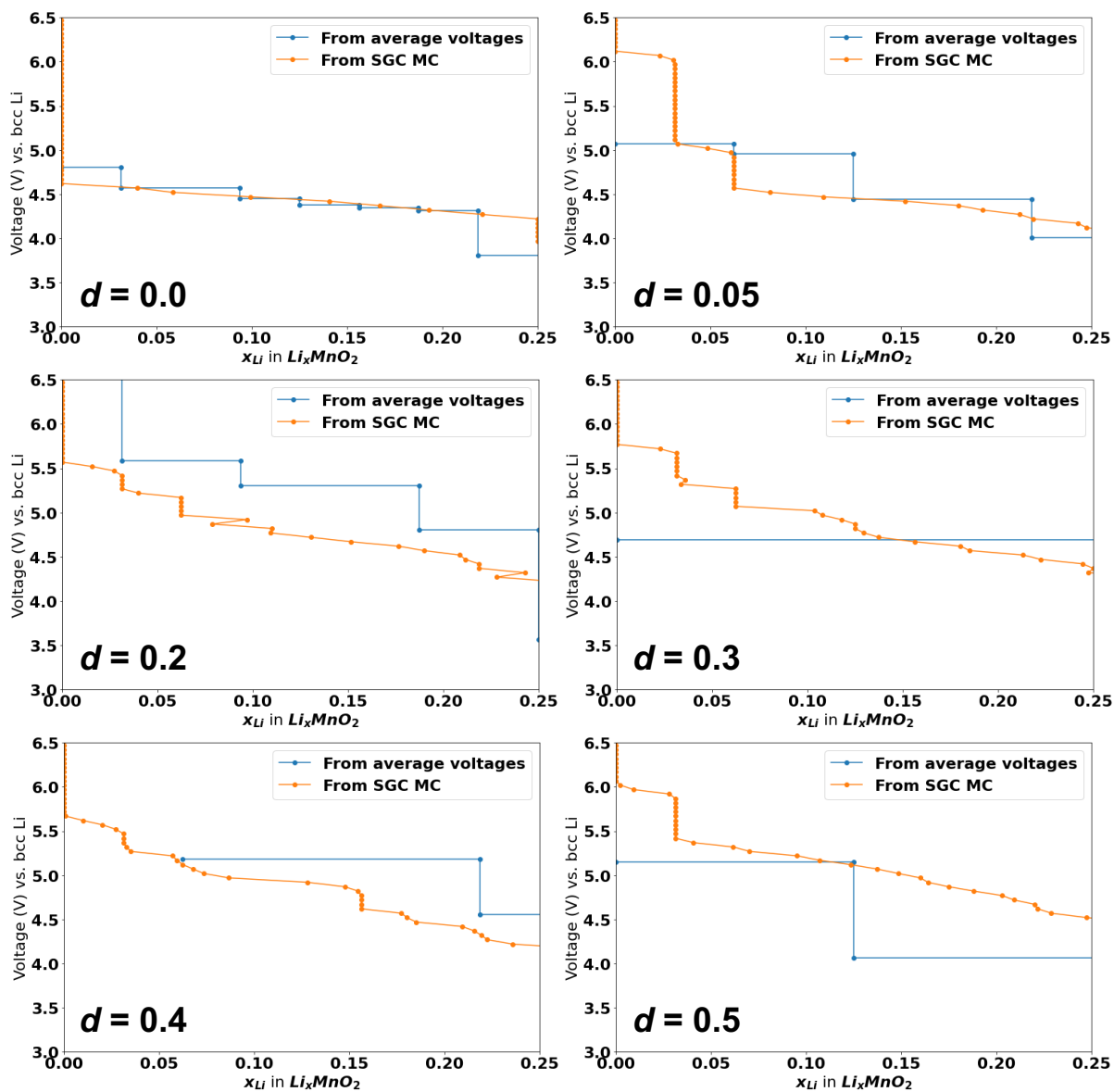## C.2 Effects of oxygen oxidation on disordered LiMn$_2$O$_4$ voltage curves

Figure C.3: Comparison between sgc-MC-simulated voltage curves, which do not explicitly include oxygen oxidation, and average voltages based on DFT-SCAN calculations of structures sampled at low x_{Li} for LiMn$_2$O$_4$ with varying levels of disorder, excluding $d = 0.1$, which is shown in Chapter 4.

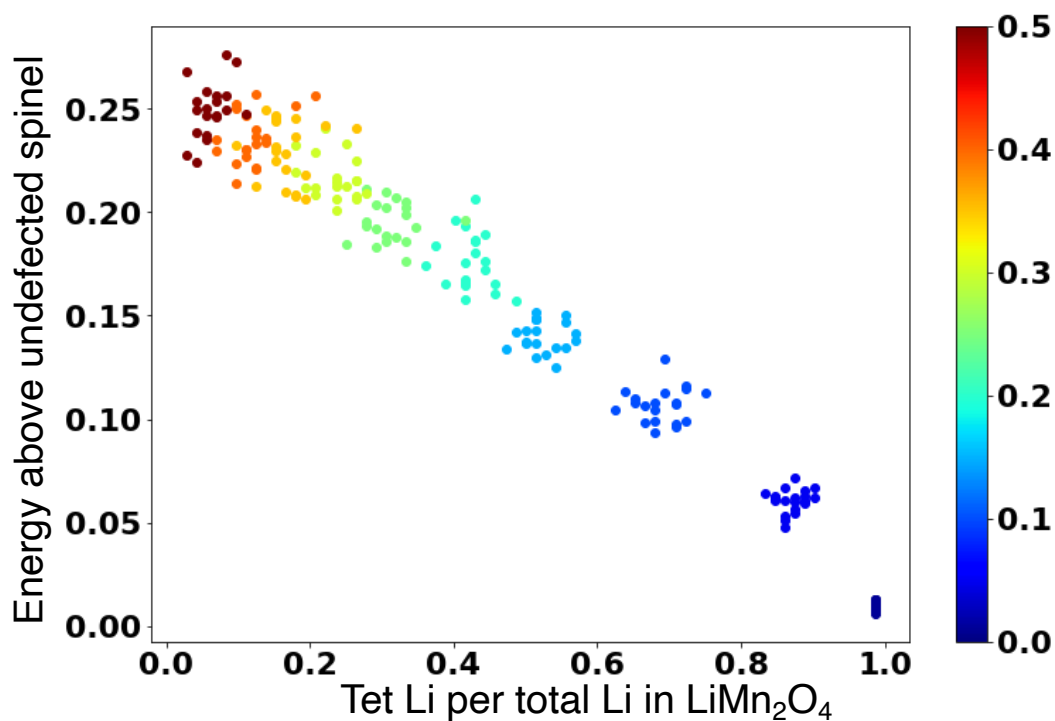## C.3 Dependence of disordered spinel energy on tetrahedral Li occupancy

Figure C.4: Cluster expansion energy above the ordered spinel $LiMn_2O_4$ of disordered $LiMn_2O_4$ configurations as a function of the fraction of tetrahedral Li in the configuration. Points are colored by the amount of disorder applied to the spinel to create the configuration.

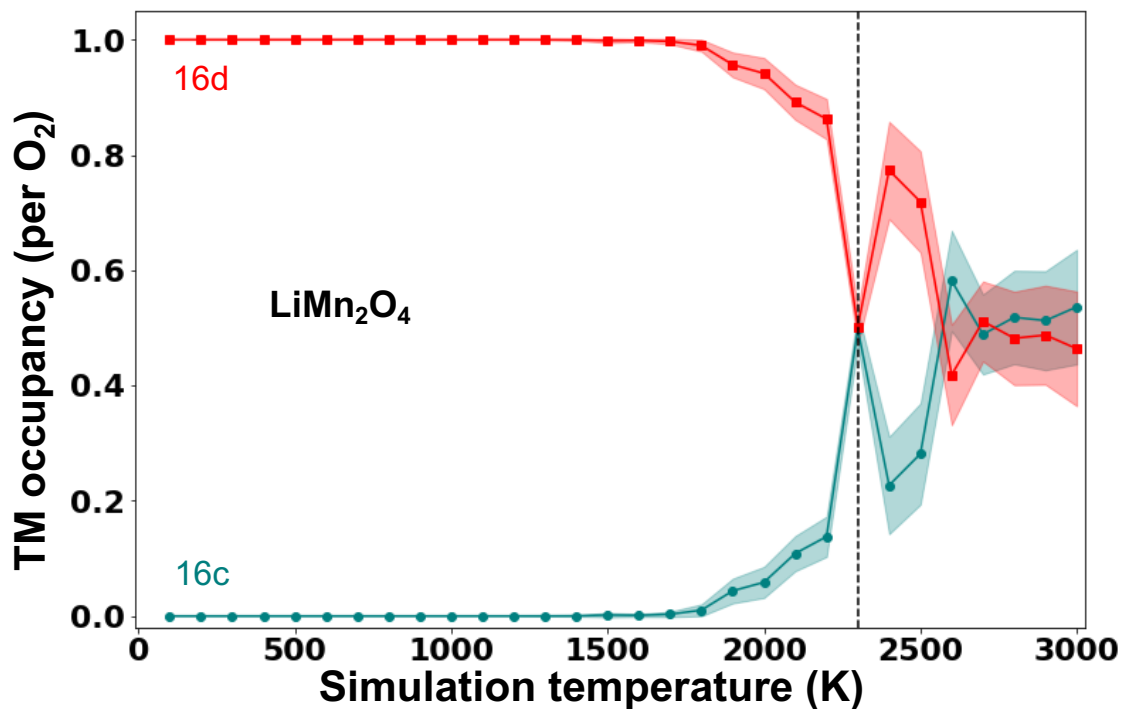## C.4 TM occupancies of stoichiometric LiMn₂O₄ with temperature

Figure C.5: Sampled concentrations of TM-occupied 16d (teal) and 16c (red) sites during canonical MC heating of spinel LiMn$_2$O$_4$ when allowing Mn swaps among octahedral sites and Li rearrangement over tetrahedral and octahedral sites (i.e., suppressing inversion). The dashed line indicates the first temperature at which the average 16c occupancy exceeds $\langle x_{16c}^{TM} \rangle = 0.2$ per O$_2$.

C.5 Sampling of solid-solution configurations in ordered ($d = 0.0$) system

Strong two-phase behavior is observed in the ordered ($d = 0.0$) system between spinel $LiMn_2O_4$ spinel and lithiated spinel $Li_2Mn_2O_4$. To estimate the energies of the solid-solution configurations above the two-phase tie-line, we calculate the cluster expansion energies of possible solid-solution configurations under a number of constraints. These constraints are:

1. Full octahedral Li occupancy

2. Full tetrahedral Li occupancy

3. Octahedral Li insertion into spinel $LiMn_2O_4$

4. Tetrahedral and octahedral Li occupation based on the ideal $\Delta x_{Li}^{tet} : \Delta x_{Li}^{oct}$ ratio of -1:2, which transforms $(Li_{0.5})^{tet}MnO_2$ to $(Li)^{oct}MnO_2$. The resulting structures are of the composition $(Li_{0.5-x})^{tet}(Li_{2x})^{oct}MnO_2$, where $0 \leq x \leq 0.5$.

We construct 200 random structures adhering to each of these constraints at 5 equally space x_{Li} in Li_xMnO_2 between $Li_{0.5}MnO_4$ and $LiMnO_2$. To maintain charge neutrality, an equal number of Mn are reduced from charge state of 4+ to 3+ as the number of Li. After evaluating all sampled structures using the CE, the competing solid-solution pathway is then taken to be the set of lowest-energy configurations at each x_{Li}. The formation energies of all of the sampled solid-solution configurations, plotted with the sgc MC-simulated formation energies for the ordered $d = 0.0$ and the disordered d = 0.1 systems, is shown in Figure C.6. Structures constructed to have only oct Li occupancy, only tet Li occupancy, modeling oct Li insertion into spinel, and both tet and oct occupancy where $(Li_{0.5-x})^{tet}(Li_{2x})^{oct}MnO_2$ are plotted as light blue, orange, green, and purple crosses.
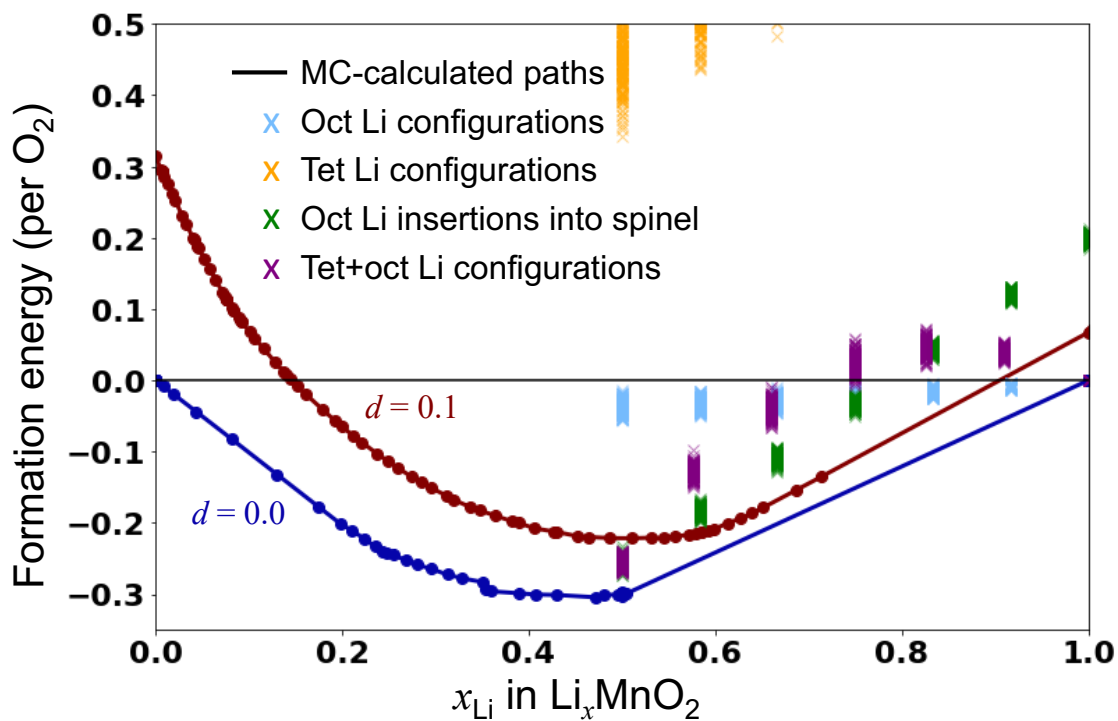
Figure C.6: CE-evaluated formation energies of possible solid-solution configurations in the d = 0.0 ordered spinel system. Solid-solution configurations are constructed as described above. Also plotted for comparison are the averaged formation energies of sampled configurations from sgc MC for the $d = 0.0$ ordered spinel (dark blue) and the $d = 0.1$ disordered spinel (maroon).